

TRAJECTORY DESIGN IN THE SPATIAL CIRCULAR RESTRICTED  
THREE-BODY PROBLEM EXPLOITING  
HIGHER-DIMENSIONAL POINCARÉ MAPS

A Dissertation

Submitted to the Faculty

of

Purdue University

by

Amanda F. Haapala

In Partial Fulfillment of the

Requirements for the Degree

of

Doctor of Philosophy

December 2014

Purdue University

West Lafayette, Indiana

In loving memory of Guy Denniston and Mariana Lippa.

## ACKNOWLEDGMENTS

I must first and foremost thank my husband, Gary. Your unconditional love and endless support have carried me through the past six years. I can never express all the gratitude and love I have for you. I would also like to thank my parents, Kate and Dan, and my brother, Andrew, for their constant love and encouragement. To all of my family and friends, your support is something I have come to rely upon and I am very lucky to have each of you in my life. Thank you so much for your love and encouragement.

Professor Howell, I am so thankful for each of the opportunities you have given me and for your guidance, patience, and support. I have loved learning from you, and am grateful for the freedom you have given me to pursue my ambitions. I would additionally like to thank my committee members, Professor Longuski, Professor Corless, and Professor Marchand. I have enjoyed having each of you as my professors, and am grateful to you for your time reviewing this dissertation.

During my time at Purdue, I have also had the great privilege of working with Mr. David Folta and Dr. Donald Dichmann at Goddard Space Flight Center. I have truly enjoyed learning from your expertise, and it has been an honor to have been included in your discussions and meetings.

For the funding without which I could not pursue this work, I must thank the Purdue Graduate School and the Purdue Doctoral Fellowship, as well as the School of Aeronautics and Astronautics. I am most grateful for additional support from the Zonta Amelia Earhart Fellowship and NASA Goddard Space Flight Center Internal Research And Development (IRAD) grants NNX12AC57G and NNX13AE55G.

I would finally like to express my gratitude to all of the past and current members of my research group. Your suggestions and support have been vital throughout

my time at Purdue, and especially in the preparation of this dissertation. Most importantly, you have made graduate school fun! Working with each of you has been both humbling and uplifting, and it is a privilege to be counted amongst you in this research group.

## TABLE OF CONTENTS

	Page
LIST OF TABLES . . . . .	viii
LIST OF FIGURES . . . . .	ix
ABSTRACT . . . . .	xx
1 PROBLEM AND MOTIVATION . . . . .	1
1.1 Historical Overview of the Three-Body Problem . . . . .	2
1.2 Motion in the Vicinity of the Collinear Libration Points . . . . .	4
1.3 Trajectory Design Employing Poincaré Maps . . . . .	4
1.4 Present Work . . . . .	7
2 BACKGROUND — CIRCULAR RESTRICTED THREE-BODY PROBLEM . . . . .	11
2.1 Equations of Motion Relative to an Inertial Observer . . . . .	11
2.2 Equations of Motion Relative to the Rotating Frame . . . . .	13
2.3 Symmetry Properties . . . . .	18
2.4 Integral of the Motion . . . . .	19
2.5 Equilibrium Solutions . . . . .	19
2.6 Zero-Velocity Surfaces . . . . .	23
3 FUNDAMENTAL MOTION IN THE RESTRICTED PROBLEM . . . . .	26
3.1 Linearized Motion near the Libration Points . . . . .	26
3.2 Stability of the Collinear Libration Points and Invariant Manifolds .	28
3.3 Local Invariant Manifolds . . . . .	32
3.3.1 Local Hyperbolic Manifold . . . . .	33
3.3.2 Local Center Manifold . . . . .	34
3.3.3 Hyperbolic Manifolds Asymptotic to the Local Center Manifold	35
3.4 Global Invariant Manifolds . . . . .	37
3.4.1 Global Hyperbolic Manifold . . . . .	37
3.4.2 Global Center Manifold . . . . .	39
3.4.3 Hyperbolic Manifolds Asymptotic to the Global Center Manifold	54
3.5 Invariant Manifolds as Separatrices and Transit . . . . .	58
4 POINCARÉ MAPS AND TRAJECTORY DESIGN . . . . .	60
4.1 Poincaré Maps . . . . .	60
4.1.1 Identification of Structures within Poincaré Maps . . . . .	62

	Page
4.1.2 Dimensionality of Poincaré Maps . . . . .	64
4.2 Existing Design Techniques Employing Poincaré Maps in the Planar Problem . . . . .	66
4.3 Existing Design Techniques Employing Poincaré Maps in the Spatial Problem . . . . .	69
<b>5 NEW APPLICATIONS FOR EXISITNG DESIGN TECHNIQUES . . . . .</b>	<b>76</b>
5.1 Analysis of the Temporary Capture of Jupiter-Family Comets . . . . .	76
5.1.1 Comet 39P/Oterma . . . . .	77
5.1.2 Comet 111P/Helin-Roman-Crockett . . . . .	80
5.2 Locating Periodic Orbits in the Spatial Problem . . . . .	83
5.2.1 Periapse Maps . . . . .	84
5.2.2 Perpendicular Crossing Maps . . . . .	87
<b>6 REPRESENTING HIGHER-DIMENSIONAL POINCARÉ MAPS . . . . .</b>	<b>96</b>
6.1 Data Display Techniques from Multidimensional Data Visualization	96
6.2 Visual Representations for Higher-Dimensional Poincaré Maps . . .	100
6.3 Employing Maps to Compute Libration Point Orbit Transfers . . . .	103
6.4 Differential Corrections Algorithms to Compute Transfers between Periodic Libration Point Orbits . . . . .	108
6.4.1 Free Transfers Between Periodic Orbits . . . . .	112
6.4.2 Low-Cost Transfers Between Periodic Orbits . . . . .	114
6.5 Transfers Between Libration Point Orbits in Different Systems . . .	117
<b>7 EXPLORING THE ROLE OF POINCARÉ MAPS IN AN INTERACTIVE TRAJECTORY DESIGN ENVIRONMENT . . . . .</b>	<b>128</b>
7.0.1 Transfer Design Environment . . . . .	130
7.0.2 Differential Corrections Environment . . . . .	140
<b>8 CATALOG OF FREE AND LOW-COST TRANSFERS BETWEEN LIBRATION POINT ORBITS IN THE EARTH-MOON SYSTEM . . . . .</b>	<b>145</b>
8.1 Catalog Taxonomy . . . . .	145
8.2 Homoclinic Connections Associated with Vertical Orbits . . . . .	151
8.3 Homoclinic Connections Associated with Halo Orbits . . . . .	164
8.4 Homoclinic Connections Associated with Axial Orbits . . . . .	176
8.5 Heteroclinic Connections between Northern and Southern Halo/Axial Orbits . . . . .	178
8.6 Low-Cost Transfers . . . . .	186
8.6.1 Transfers between $L_1$ Vertical and $L_2$ Vertical Orbits . . . .	187
8.6.2 Transfers between $L_1$ Halo and $L_2$ Halo Orbits . . . . .	189
8.6.3 Transfers between $L_1$ Axial and $L_2$ Axial Orbits . . . . .	191
8.6.4 Transfers between $L_1$ Vertical and $L_2$ Halo Orbits . . . . .	192

	Page
8.6.5 Transfers between $L_1$ Halo and $L_2$ Vertical Orbits . . . . .	193
8.7 Catalog Observations and Discussion . . . . .	194
8.7.1 General Observations about Heteroclinic/Homoclinic Connections . . . . .	194
8.7.2 General Observations about Low-Cost Transfers . . . . .	194
8.7.3 Existence of Partner Transfers . . . . .	196
8.7.4 Computation of Vertical Homoclinic Transfers in the Hill Problem . . . . .	201
8.7.5 Groupings of Transfers of Similar Geometry . . . . .	204
8.7.6 Charting the Solution Space to Locate Transfers . . . . .	216
8.7.7 Evolution of Low-Cost Transfers with Mass Parameter . . . . .	219
8.8 Existence of Transfers in an Ephemeris Model . . . . .	222
8.8.1 Transitioning to an Ephemeris Model . . . . .	222
8.8.2 Transitioning Solutions to GMAT . . . . .	226
8.9 Catalog Conclusions . . . . .	231
9 CONCLUDING REMARKS . . . . .	233
9.1 Incorporating Higher-Dimensional Poincaré Maps into the Trajectory Design Process . . . . .	233
9.2 Interactive Design Environments and a Catalog of Libration Point Orbit Transfers . . . . .	235
9.3 Recommendations for Future Work . . . . .	237
LIST OF REFERENCES . . . . .	239
A DERIVING THE CR3B EQUATIONS OF MOTION . . . . .	247
B DERIVING THE JACOBI CONSTANT . . . . .	249
B.1 Derivation of the Jacobi Integral . . . . .	249
B.2 Second Partial Derivatives of the Pseudo-Potential . . . . .	250
C EIGENSTRUCTURE ASSOCIATED WITH THE LIBRATION POINTS . . . . .	251
C.1 Eigenvalues Associated with the Collinear Points . . . . .	251
C.2 General Solution for a Center . . . . .	254
C.3 General Solution for a Saddle Point . . . . .	254
D HILL'S THREE-BODY PROBLEM . . . . .	256
D.1 Deriving Hill's Equations of Motion . . . . .	256
D.2 Equilibrium Points and the Jacobi Constant . . . . .	258
D.3 Symmetry Properties . . . . .	259
VITA . . . . .	262

## LIST OF TABLES

Table	Page
2.1 System Constants and Characteristic Quantities . . . . .	15
2.2 Locations of the Collinear Libration Points of Various Systems . . . . .	21
2.3 Jacobi Constant Values for the Libration Points in Various Systems . .	22
5.1 Properties of Periodic Orbits . . . . .	93
6.1 Approximate cost for transfers 1→4 . . . . .	106
8.1 Catalog of Libration Point Orbit Transfers . . . . .	148
8.2 Vertical Orbit Homoclinic Connections . . . . .	151
8.3 Halo Orbit Homoclinic Connections . . . . .	164
8.4 Axial Orbit Homoclinic Connections . . . . .	176
8.5 Heteroclinic Connections between Northern and Southern Orbits . . . .	178
8.6 Low-Cost Transfers . . . . .	186
8.7 Vertical Orbit Homoclinic Connections in the Hill Problem . . . . .	202
8.8 Transfer Groupings 1–5 . . . . .	210
8.9 Transfer Groupings 6–11 . . . . .	211

## LIST OF FIGURES

Figure	Page
2.1 Rotating coordinate frame . . . . .	14
2.2 Libration points in the rotating frame. . . . .	21
2.3 Regions of position space delineated by the ZVCs for $C_{L_3} < C < C_{L_2}$ (Earth and Moon $2\times$ actual size) . . . . .	24
2.4 Zero-velocity surfaces in for $C_{L_2} < C < C_{L_1}$ . . . . .	24
2.5 Zero-velocity curves for varying values of Jacobi constant. (Earth and Moon $2\times$ actual size) . . . . .	25
3.1 Stable and unstable manifolds asymptotic to a collinear libration point	34
3.2 Sample periodic and quasi-periodic orbits in the vicinity of a collinear libration point . . . . .	36
3.3 Sample unstable manifold (red) departing a Lissajous orbit . . . . .	37
3.4 Global stable and unstable manifolds associated with the $L_1$ point in the Earth-Moon system ( $L_1$ -centered view) . . . . .	40
3.5 Sample members from the families of Lyapunov orbits in the Earth-Moon system . . . . .	41
3.6 Sample members from the families of vertical orbits in the Earth-Moon system . . . . .	42
3.7 Stability information for Lyapunov orbits in the Earth-Moon system .	47
3.8 Sample members from the families of halo orbits in the Earth-Moon system . . . . .	49
3.9 Sample members from the families of axial orbits in the Earth-Moon system . . . . .	50
3.10 Stability information for halo and axial orbits in the Earth-Moon system	51
3.11 Quasi-periodic tori associated with an $L_1$ halo orbit in the Earth-Moon system for $C = 3.15$ . . . . .	54

Figure	Page
3.12 Quasi-periodic tori associated with an $L_2$ vertical orbit in the Earth-Moon system for $C = 3.15$ . . . . .	54
3.13 Sample stable (blue) and unstable (red) manifolds associated with periodic orbits and quasi-periodic tori with in the Earth-Moon system for $C = 3.15$ . . . . .	58
4.1 Schematic of a one-sided Poincaré map . . . . .	61
4.2 Illustrative Poincaré map . . . . .	63
4.3 Heteroclinic connections are determined from the intersection of manifold contours on a Poincaré map for the planar problem; Earth-Moon system for $C = 3.15$ (Moon-centered view) . . . . .	67
4.4 A transit solution is computed from initial conditions within the manifold contours on a Poincaré map for the planar problem; Earth-Moon system for $C = 3.15$ (Moon-centered view) . . . . .	68
4.5 Reducing $y = 0$ map of invariant manifolds to 1D contours in $\mathbb{R}^2$ for $C = 3.15$ in the Earth-Moon system, (a) projection of map onto $y$ - $z$ plane, (b) reducing to 2D surfaces by selecting $z = z_0$ reveals black contour defining intersection of manifolds, (c) $\dot{z} = \dot{z}_0$ plane intersects surfaces to form contours, (d) maps reduced to 1D by constraining $z \approx z_0$ , $\dot{z} \approx \dot{z}_0$ . . . . .	72
4.6 Heteroclinic connections and a transit trajectory located using maps in the Earth-Moon system (Moon-centered views) . . . . .	74
4.7 Trajectories with map crossings outside of the intersection of the manifold contours do not transit both gateways (Moon-centered views) . . . . .	75
5.1 Ephemeris path of comet OTR as viewed in the Jupiter-centered Sun-Jupiter rotating frame . . . . .	78
5.2 Location of OTR state relative to invariant manifolds at $\Sigma_{P_2}$ for $C = 3.02$ . . . . .	79
5.3 Ephemeris path of comet HRC as viewed in the Jupiter-centered Sun-Jupiter rotating frame; Jupiter 10 $\times$ actual size . . . . .	80
5.4 Location of HRC transit relative to invariant manifolds for $C = 3.029$ . . . . .	82

Figure	Page
5.5 Planar periapse map for $C = 3.172$ in the Earth-Moon system, (a) first, second, and third periapses along $L_1$ temporary capture trajectories plotted in orange, cyan, magenta, and periapses along $L_1$ unstable manifold plotted in black, (b) first, second, and third periapses along $L_2$ temporary capture trajectories plotted in orange, cyan, magenta, and periapses along $L_2$ unstable manifold plotted in black, (c) periapses along transit (magenta) and nontransit (cyan) trajectories . . . . .	86
5.6 A pair of sample periodic orbits is computed via an initial guess from the cyan region of the periapse map for $C = 3.172$ in the Earth-Moon system . . . . .	87
5.7 Planar periapse map for $C = 3.15$ in the Earth-Moon system, (a) first, second, and third periapses along $L_1$ temporary capture trajectories plotted in orange, cyan, magenta, and periapses along $L_1$ unstable manifold plotted in black, (b) first, second, and third periapses along $L_2$ temporary capture trajectories plotted in orange, cyan, magenta, and periapses along $L_2$ unstable manifold plotted in black, (c) periapses along transit (magenta) and nontransit (cyan) trajectories . . . . .	88
5.8 Maps representing perpendicular crossings associated with periodic orbits in the Earth-Moon system, (a) returns to $y = 0$ surface with $ \dot{x} ,  \dot{z}  < \delta$ , (b) returns to map with periodic orbit crossings overplotted and colored consistent with linear stability (c) sorted crossings of sample periodic orbits, (d) crossings, colored consistent with linear stability, displayed with crossings of invariant manifolds in black; initial conditions corresponding to transit (cyan) and long-term capture (magenta) also displayed . . . . .	91
5.9 Maps corresponding to surfaces $\Sigma_\perp$ and $\Sigma_r$ in the Earth-Moon system	92
5.10 Projection of sample periodic orbits onto the $x$ - $y$ plane in the Earth-Moon system . . . . .	94
5.11 Projection of sample periodic orbits onto the $x$ - $z$ plane in the Earth-Moon system . . . . .	95
6.1 Star, face, and stick-figure representations for sample Chevrolet vehicle data . . . . .	98
6.2 Glyph representation for a four-dimensional data point . . . . .	101
6.3 Manifolds are employed to search for a transfer between $L_1$ vertical and $L_2$ northern halo orbits in the Earth-Moon system, $C = 3.0555$ . . . . .	104

Figure	Page
6.4 Searching for transfers between $L_1$ vertical and $L_2$ northern halo orbits in the Earth-Moon system . . . . .	106
6.5 Locally optimal transfer in the Earth-Moon system, $C_1 = 3.0571$ , $C_2 = 3.0468$ , TOF = 40.5559 days, $\Delta v = 7.9048$ m/s . . . . .	107
6.6 Defining the variables employed in targeting algorithms for transfers between periodic orbits . . . . .	109
6.7 Defining the lunar angle from $\Sigma_{\theta_1}$ and $\Sigma_{\theta_2}$ . . . . .	121
6.8 Unstable manifold arcs departing $L_2$ Lyapunov orbits in the Earth-Moon system . . . . .	121
6.9 Stable manifold arcs approaching $L_1$ Lyapunov orbits in the Sun-Earth system . . . . .	122
6.10 Glyph representation for a three-dimensional data point . . . . .	123
6.11 Employing a Poincaré map to locate a low-cost transfer between libration point orbits in the Earth-Moon and Sun-Earth systems . . . . .	123
6.12 Constructing an initial guess for the system-to-system transfer . . . . .	125
6.13 Converged transfer in the Sun-Earth-Moon ephemeris model with $\Delta v = 0$ . . . . .	127
7.1 Transfer Design Environment . . . . .	130
7.2 Transfer properties are selected . . . . .	132
7.3 Poincaré map properties are defined . . . . .	134
7.4 Poincaré map display properties are specified . . . . .	136
7.5 Transfer orbits are computed and manifold crossings of the Poincaré map are displayed . . . . .	137
7.6 The Poincaré map is explored for transfer opportunities . . . . .	138
7.7 Transfer arcs are interactively selected from the Poincaré map . . . . .	139
7.8 The initial guess for the transfer is displayed in the Differential Corrections Environment . . . . .	141
7.9 Output from the differential corrections algorithms . . . . .	142
7.10 A transfer corresponding to $\Delta v = 0$ is computed . . . . .	143
8.1 V1-1, $C = 3.1775$ , TOF = 52.5825 days . . . . .	152
8.2 V1-2, $C = 3.1580$ , TOF = 53.1241 days . . . . .	152

Figure	Page
8.3 V1-3, $C = 3.1565$ , TOF = 50.5069 days . . . . .	152
8.4 V1-5, $C = 3.1389$ , TOF = 51.1528 days . . . . .	153
8.5 V1-7, $C = 3.1316$ , TOF = 50.4070 days . . . . .	153
8.6 V1-8, $C = 3.1271$ , TOF = 60.7297 days . . . . .	153
8.7 V1-9, $C = 3.1201$ , TOF = 53.1732 days . . . . .	154
8.8 V1-10, $C = 3.1126$ , TOF = 63.9845 days . . . . .	154
8.9 V1-12, $C = 3.1060$ , TOF = 66.0469 days . . . . .	154
8.10 V1-13, $C = 3.1059$ , TOF = 39.9676 days . . . . .	155
8.11 V1-14, $C = 3.1008$ , TOF = 51.4635 days . . . . .	155
8.12 V1-15, $C = 3.0947$ TOF = 67.9682 days . . . . .	155
8.13 V1-16, $C = 3.0897$ , TOF = 55.3035 days . . . . .	156
8.14 V1-17, $C = 3.0885$ , TOF = 38.7444 days . . . . .	156
8.15 V1-18, $C = 3.0870$ , TOF = 47.0461 days . . . . .	156
8.16 V1-19, $C = 3.0825$ , TOF = 51.4976 days . . . . .	157
8.17 V1-20, $C = 3.0768$ , TOF = 73.6204 days . . . . .	157
8.18 V1-21, $C = 3.0760$ , TOF = 72.0903 days . . . . .	157
8.19 V2-4, $C = 3.1450$ , TOF = 72.2670 days . . . . .	158
8.20 V2-7, $C = 3.1416$ , TOF = 59.5273 days . . . . .	158
8.21 V2-6, $C = 3.1361$ , TOF = 61.8870 days . . . . .	158
8.22 V2-5, $C = 3.1288$ , TOF = 62.5025 days . . . . .	159
8.23 V2-8, $C = 3.1198$ , TOF = 63.4957 days . . . . .	159
8.24 V2-11, $C = 3.1093$ , TOF = 58.1397 days . . . . .	159
8.25 V2-12, $C = 3.1054$ , TOF = 76.3231 days . . . . .	160
8.26 V2-15, $C = 3.1045$ , TOF = 70.6015 days . . . . .	160
8.27 V2-13, $C = 3.1053$ , TOF = 46.9066 days . . . . .	160
8.28 V2-14, $C = 3.0999$ , TOF = 58.4020 days . . . . .	161
8.29 V2-16, $C = 3.0876$ , TOF = 60.1932 days . . . . .	161

Figure		Page
8.30	V2-17, $C = 3.0852$ , TOF = 45.2766 days . . . . .	161
8.31	V2-18, $C = 3.0827$ , TOF = 52.7960 days . . . . .	162
8.32	V2-20, $C = 3.0798$ TOF = 79.5223 days . . . . .	162
8.33	V2-22, $C = 3.0707$ , TOF = 71.3786 days . . . . .	162
8.34	V2-19, $C = 3.0697$ , TOF = 59.1197 days . . . . .	163
8.35	V2-21, $C = 3.0618$ , TOF = 79.4076 days . . . . .	163
8.36	V2-23, $C = 3.0315$ , TOF = 69.6960 days . . . . .	163
8.37	H1-1, $C = 3.1685$ , TOF = 62.9075 days . . . . .	165
8.38	H1-3, $C = 3.1658$ , TOF = 44.5716 days . . . . .	165
8.39	H1-4, $C = 3.1638$ , TOF = 69.2250 days . . . . .	165
8.40	H1-6, $C = 3.1453$ , TOF = 45.3983 days . . . . .	166
8.41	H1-7, $C = 3.1352$ , TOF = 61.7935 days . . . . .	166
8.42	H1-8, $C = 3.1051$ TOF = 73.5694 days; Note that this connection impacts the Moon . . . . .	166
8.43	H1-9, $C = 3.0837$ , TOF = 60.1211 days . . . . .	167
8.44	H1-10, $C = 3.0766$ , TOF = 65.1147 days . . . . .	167
8.45	H1-11, $C = 3.0763$ , TOF = 52.9703 days . . . . .	167
8.46	H1-12, $C = 3.0726$ , TOF = 59.7869 days . . . . .	168
8.47	H1-13, $C = 3.0725$ , TOF = 64.6227 days . . . . .	168
8.48	H1-14, $C = 3.0723$ , TOF = 65.9529 days . . . . .	168
8.49	H1-15, $C = 3.0701$ , TOF = 72.4875 days . . . . .	169
8.50	H1-16, $C = 3.0600$ , TOF = 71.7162 days . . . . .	169
8.51	H1-17, $C = 3.0584$ , TOF = 70.6021 days . . . . .	169
8.52	H1-18, $C = 3.0498$ , TOF = 62.5695 days . . . . .	170
8.53	H1-19, $C = 3.0366$ , TOF = 63.1381 days . . . . .	170
8.54	H2-2, $C = 3.1517$ , TOF = 45.0669 days . . . . .	170
8.55	H2-5, $C = 3.1510$ , TOF = 57.1765 days . . . . .	171

Figure	Page
8.56 H2-8, $C = 3.1013$ , TOF = 78.4380 days . . . . .	171
8.57 H2-9, $C = 3.0892$ , TOF = 65.4246 days . . . . .	171
8.58 H2-11, $C = 3.0820$ , TOF = 58.3090 days . . . . .	172
8.59 H2-15, $C = 3.0790$ , TOF = 74.7334 days . . . . .	172
8.60 H2-12, $C = 3.0775$ , TOF = 64.9840 days . . . . .	172
8.61 H2-16, $C = 3.0764$ , TOF = 73.6022 days . . . . .	173
8.62 H2-10, $C = 3.0746$ , TOF = 72.0334 days . . . . .	173
8.63 H2-14, $C = 3.0687$ , TOF = 75.1186 days . . . . .	173
8.64 H2-17, $C = 3.0663$ , TOF = 75.1945 days . . . . .	174
8.65 H2-13, $C = 3.0618$ , TOF = 78.4496 days . . . . .	174
8.66 H2-18, $C = 3.0616$ , TOF = 66.4187 days . . . . .	174
8.67 H2-19, $C = 3.0485$ , TOF = 65.5675 days . . . . .	175
8.68 A1-1, $C = 3.0048$ , TOF = 71.2748 days . . . . .	176
8.69 A1-2, $C = 3.0028$ TOF = 68.6406 days . . . . .	176
8.70 A2-1, $C = 2.9862$ TOF = 83.8149 days . . . . .	177
8.71 A2-2, $C = 2.9818$ TOF = 79.6937 days . . . . .	177
8.72 HH1-1, $C = 3.1694$ , TOF = 74.7445 days . . . . .	179
8.73 HH1-2, $C = 3.1635$ , TOF = 42.3206 days . . . . .	179
8.74 HH1-3, $C = 3.1625$ , TOF = 51.6166 days . . . . .	179
8.75 HH1-4, $C = 3.1589$ , TOF = 54.2482 days . . . . .	180
8.76 HH1-5, $C = 3.1580$ , TOF = 57.1155 days . . . . .	180
8.77 HH1-6, $C = 3.1422$ , TOF = 41.5511 days . . . . .	180
8.78 HH1-8, $C = 3.1189$ , TOF = 41.1956 days . . . . .	181
8.79 HH1-9, $C = 3.0779$ , TOF = 65.9390 days . . . . .	181
8.80 HH1-10, $C = 3.0768$ , TOF = 43.9812 days . . . . .	181
8.81 HH1-11, $C = 3.0723$ , TOF = 40.1881 days . . . . .	182
8.82 HH1-12, $C = 3.0497$ , TOF = 61.8061 days . . . . .	182

Figure	Page
8.83 HH2-7, $C = 3.1395$ , TOF = 65.6368 days . . . . .	182
8.84 HH2-8, $C = 3.1267$ , TOF = 46.5733 days . . . . .	183
8.85 HH2-9, $C = 3.0850$ , TOF = 70.6057 days . . . . .	183
8.86 HH2-10, $C = 3.0742$ , TOF = 50.6271 days . . . . .	183
8.87 HH2-11, $C = 3.0686$ , TOF = 47.7498 days . . . . .	184
8.88 HH2-12, $C = 3.0551$ , TOF = 66.4160 days . . . . .	184
8.89 AA1-1, $C = 3.0037$ , TOF = 56.2121 days . . . . .	185
8.90 AA2-1, $C = 2.984$ , TOF = 66.8773 days . . . . .	185
8.91 V1V2-1, $C_1 = 3.1616$ , $C_2 = 3.1536$ , TOF = 40.1034 days, $\Delta v = 4.7099$ m/s . . . . .	187
8.92 V1V2-2, $C_1 = 3.1564$ , $C_2 = 3.1504$ , tof = 39.5552 days, $\Delta v = 16.0344$ m/s . . . . .	187
8.93 V1V2-3, $C_1 = 3.1265$ , $C_2 = 3.1147$ , tof = 35.9293 days, $\Delta v = 7.9431$ m/s . . . . .	187
8.94 V1V2-4, $C_1 = 3.1139$ , $C_2 = 3.1073$ , tof = 54.9474 days, $\Delta v = 5.733$ m/s	188
8.95 V1V2-5, $C_1 = 3.0986$ , $C_2 = 3.0951$ , tof = 41.2976 days, $\Delta v = 9.854$ m/s	188
8.96 V1V2-6, $C_1 = 3.0949$ , $C_2 = 3.1039$ , tof = 53.0685 days, $\Delta v = 19.5612$ m/s . . . . .	188
8.97 V1V2-7, $C_1 = 3.0898$ , $C_2 = 3.0875$ , tof = 49.5468 days, $\Delta v = 4.653$ m/s	189
8.98 V1V2-8, $C_1 = 3.0849$ , $C_2 = 3.0884$ , tof = 33.1433 days, $\Delta v = 5.254$ m/s	189
8.99 H1H2-1, $C_1 = 3.1681$ , $C_2 = 3.1468$ , TOF = 43.003 days, $\Delta v = 7.9742$ m/s . . . . .	189
8.100 H1H2-2, $C_1 = 3.1469$ , $C_2 = 3.1317$ , TOF = 28.9771 days, $\Delta v = 18.2642$ m/s . . . . .	190
8.101 H1H2-3, $C_1 = 3.1269$ , $C_2 = 3.1158$ , TOF = 51.0004 days, $\Delta v = 13.915$ m/s . . . . .	190
8.102 H1H2-4, $C_1 = 3.0930$ , $C_2 = 3.0972$ , TOF = 59.7738 days, $\Delta v = 3.5776$ m/s . . . . .	190
8.103 H1H2-5, $C_1 = 3.0698$ , $C_2 = 3.0717$ , tof = 62.1769 days, $\Delta v = 5.1442$ m/s . . . . .	191

Figure	Page
8.104 H1H2-6, $C_1 = 3.0537$ , $C_2 = 3.0795$ , tof = 51.1918 days, $\Delta v = 11.8545$ m/s . . . . .	191
8.105 A1A2-1, $C_1 = 3.0058$ , $C_2 = 2.9835$ , TOF = 52.0105 days, $\Delta v = 25.7533$ m/s . . . . .	191
8.106 V1H2-2, $C_1 = 3.1604$ , $C_2 = 3.1223$ , TOF = 37.5423 days, $\Delta v = 17.8769$ m/s . . . . .	192
8.107 V1H2-3, $C_1 = 3.0571$ , $C_2 = 3.0468$ , TOF = 40.5559 days, $\Delta v = 7.9048$ m/s . . . . .	192
8.108 V1H2-4, $C_1 = 3.0542$ , $C_2 = 3.0544$ , TOF = 62.8318 days, $\Delta v = 0.24305$ m/s; Note that this solution is not optimal - the required $\Delta v$ is reduced using fmincon but an optimal solution is not reached. . . . .	192
8.109 H1V2-1, $C_1 = 3.1636$ , $C_2 = 3.1666$ , TOF = 40.529 days, $\Delta v = 4.5$ m/s; Note that this solution is not optimal - reducing the required $\Delta v$ causes the halo orbit to approach the $x - y$ plane, and the vertical orbit to approach the $L_2$ point, thus, reducing the $z$ -amplitude and approaching a transfer between an $L_1$ Lyapunov orbit and the $L_2$ libration point. . . . .	193
8.110 H1V2-2, $C_1 = 3.1327$ , $C_2 = 3.1517$ , TOF = 36.7461 days, $\Delta v = 11.7682$ m/s . . . . .	193
8.111 H1V2-3, $C_1 = 3.0338$ , $C_2 = 3.0538$ , TOF = 41.1473 days, $\Delta v = 16.5722$ m/s . . . . .	193
8.112 Low-cost transfer associated with an $L_2$ vertical orbit possessing geometry similar to V1-10, $C_1 = C_2 = 3.1131$ , TOF = 71.5102 days, $\Delta v = 18.218$ m/s . . . . .	197
8.113 Locally optimal transfer of geometry similar to V2-23, $C_1 = C_2 = 3.0469$ , tof = 65.2842 days, $\Delta v = 21.3015$ m/s . . . . .	198
8.114 Homoclinic connection possessing geometry similar to V2-23 but incorporating an additional revolution about $L_2$ , $C = 3.0492$ , TOF = 76.5048 days . . . . .	198
8.115 Low-cost transfer associated with an $L_2$ halo orbit and of geometry similar to H1-6, $C_1 = 3.1496$ , $C_2 = 3.1495$ , TOF = 53.52 days, $\Delta v = 20$ m/s . . . . .	199
8.116 Poincaré maps at $y = 0$ for various energy levels . . . . .	199

Figure	Page
8.117 Low-cost transfer associated with an $L_2$ halo orbit and of geometry similar to H1-7, $C_1 = 3.1477$ , $C_2 = 3.1478$ , TOF = 65.6326 days, $\Delta v = 20$ m/s . . . . .	201
8.118 V1-9/V1-22 in the Hill problem, $C = 2.7141$ , TOF = 19.4363 nd . . .	203
8.119 HH1-11, $C = 3.0723$ , TOF = 40.1881 days . . . . .	205
8.120 H1-11, $C = 3.0763$ , TOF = 52.9703 days . . . . .	205
8.121 HH1-9, $C = 3.0779$ , TOF = 65.9390 days . . . . .	205
8.122 H1-14, $C = 3.0723$ , TOF = 65.9529 days . . . . .	206
8.123 Homoclinic connection associated with an $L_1$ halo orbit in the Earth-Moon system, $C = 3.0787$ , TOF = 79.0007 days . . . . .	206
8.124 Transfer from an $L_1$ halo orbit to a distant prograde orbit in the Earth-Moon system, $C_1 = 3.0727$ , $C_2 = 3.0776$ , TOF = 41.5601 days, $\Delta v = 6.6609$ m/s . . . . .	207
8.125 HH2-11, $C = 3.0686$ , TOF = 47.7498 days . . . . .	207
8.126 H2-11, $C = 3.0820$ , TOF = 58.3090 days . . . . .	207
8.127 HH2-9, $C = 3.0850$ , TOF = 70.6057 days . . . . .	208
8.128 H2-14, $C = 3.0687$ , TOF = 75.1186 days . . . . .	208
8.129 Homoclinic connection associated with an $L_2$ halo orbit in the Earth-Moon system, $C = 3.0865$ , TOF = 83.1477 days . . . . .	208
8.130 Transfer from an $L_1$ halo orbit to a distant prograde orbit in the Earth-Moon system, $C_1 = 3.0848$ , $C_2 = 3.0898$ , tof = 41.3846 days, $\Delta v = 19.4659$ m/s (not optimized) . . . . .	209
8.131 Catalog transfers are represented via their associated time-of-flight and Jacobi constant values . . . . .	212
8.132 H1-19 Group 2, $C = 3.0366$ , period = 31.4358 days . . . . .	213
8.133 V2-17 Group 7, $C = 3.0852$ , period = 18.359 days . . . . .	214
8.134 H1-10 Group 9, $C = 3.0766$ , period = 42.2254 days . . . . .	214
8.135 H1-17 Group 11, $C = 3.0663$ , period = 43.1169 days . . . . .	215
8.136 H2-2 Group 12, $C = 3.1518$ , period = 28.4862 days . . . . .	215
8.137 V1-9, $C = 3.1201$ , period = 38.0188 days . . . . .	215

Figure	Page
8.138 Heat map for transfers of type V1 . . . . .	218
8.139 Heat map for transfers of type V2 . . . . .	218
8.140 H1H2-2 in the (a),(c) Sun-Earth CR3BP, $C_1 = 3.0007425$ , $C_2 = 3.0007387$ , TOF = 401.9274 days, $\Delta v = 2.2331$ m/s; (b),(d) Hill 3BP, $C = 3.6156$ TOF = 11.2451 dimensionless, $\Delta v = 0$ . . . . .	219
8.141 V1V2-8 in the (a),(c) Sun-Earth system, $C_1 = 3.0005$ , $C_2 = 3.0005$ , TOF = 464.4181 days, $\Delta v = 0.6859$ m/s; (b),(d) V1V2-8 in the Hill problem, $C = 2.5296$ , TOF = 13.061 dimensionless, $\Delta v = 0$ . . . . .	220
8.142 V1-19 in the Sun-Earth-Moon ephemeris model for initial epoch July 31 2020 23:37:26.4 . . . . .	224
8.143 HH2-11 in the Sun-Earth-Moon ephemeris model for initial epoch June 30 2020 23:23:50.5 . . . . .	225
8.144 H1H2-2 in the Sun-Earth-Moon ephemeris model for initial epoch December 1 2020 0:42:48.2 . . . . .	225
8.145 V1H2-3 in the Sun-Earth-Moon ephemeris model for initial epoch August 31 2020 23:14:58.9 . . . . .	225
8.146 H1V2-3 in the Sun-Earth-Moon ephemeris model for initial epoch November 1 2020 1:13:52.1 . . . . .	226
8.147 Transfers are transitioned to GMAT assuming a Sun-Earth-Moon ephemeris model with SRP . . . . .	228
8.148 Transfers are transitioned to GMAT assuming a Sun-Earth-Moon ephemeris model with SRP . . . . .	229

## ABSTRACT

Haapala, Amanda F. Ph.D., Purdue University, December 2014. Trajectory Design in the Spatial Circular Restricted Three-Body Problem Exploiting Higher-Dimensional Poincaré Maps. Major Professor: Kathleen C. Howell.

In this investigation, the role of higher-dimensional Poincaré maps in facilitating trajectory design is explored for a variety of applications. To begin, existing strategies to implement Poincaré maps for applications in the spatial CR3BP are evaluated. New applications for these strategies are explored, including an analysis of the natural motion of Jupiter-family comets that experience temporary capture about Jupiter, and the search for periodic orbits in the vicinity of the primary bodies. Because current strategies to represent higher-dimensional maps, generally, lead to a loss of information, new approaches to represent all information contained in higher-dimensional Poincaré maps are sought.

The field of data visualization offers many options to visually represent multivariate data sets, including the use of glyphs. A glyph is any graphical object whose physical attributes are determined by the variables of a data set. In this investigation, the role of glyphs in representing higher-dimensional Poincaré maps is explored, and the resulting map representations are demonstrated to search for maneuver-free and low-cost transfers between libration point orbits. A catalog of libration point orbit transfers is developed in the Earth-Moon system, and observations about the catalog solutions yields insight into the existence of these transfers. The application of Poincaré maps to compute transfers between libration point orbits in different three-body systems is additionally considered. Finally, an interactive trajectory design environment that incorporates Poincaré maps into the design process is demonstrated.

Such an environment offers a unique opportunity to explore the available trajectory options and to gain intuition about the solution space.

## 1. PROBLEM AND MOTIVATION

The natural dynamics that emerge in the three-body problem yield a complex solution space and an expanded range of trajectory options. In particular, the symmetry properties and analytical insight available in the Circular Restricted Three-Body Problem (CR3BP) produce an effective framework for preliminary trajectory design in a multi-body force environment. Within this context, an infinite number of periodic and quasi-periodic orbits exist, both in the vicinity of equilibrium or *libration* points, and centered on the primary bodies. Many of these orbits are unstable and, therefore, possess stable and unstable invariant manifolds that offer a means of free transport. Solutions, such as libration point orbits and their associated invariant manifolds, have been incorporated into trajectory design scenarios in support of various missions. In the Sun-Earth system, observatories delivered to the vicinity of  $L_1$  include ISEE-3 [1], SOHO [2], ACE [3], WIND [3], Genesis [3]. Missions to the Sun-Earth  $L_2$  point have also been demonstrated, including WMAP [4] as well as the Herschel and Planck Space Observatories [5]. ARTEMIS was the first libration point mission in the Earth-Moon system; two spacecraft were maintained in large quasi-periodic orbits about the Earth-Moon  $L_1$  and  $L_2$  points before entering long-term lunar orbits [6]. While the available solutions within the CR3BP are generally well understood, the process to incorporate them into the trajectory design concept in support of a mission is nontrivial. Thus, new strategies to explore and represent the design space are essential to improve the mission design process.

A map on a Poincaré surface of section is a powerful tool both to analyze and represent the solution space, as well as to locate and compute trajectories with specified behavior. Incorporation of maps into trajectory design strategies improves the tractability of mission design in multi-body regimes and offers the opportunity for im-

lementation within an interactive mission design environment. Poincaré maps are frequently higher-dimensional and are difficult to represent visually. Thus, strategies to represent higher-dimensional maps are required.

## 1.1 Historical Overview of the Three-Body Problem

With the publication of the *Principia* in 1687, Sir Isaac Newton inspired a search for an analytical solution to the problem of  $n$ -bodies moving under the Newtonian Universal Law of Gravitation. Newton had supplied a geometrical solution to the relative two-body problem (2BP) and, in 1710, Johann Bernoulli demonstrated that all relative motions of two bodies are described by a conic sections. Interest was refocused toward an understanding of the motion of the Moon in the Sun-Earth-Moon three-body problem (3BP), offering a framework for formulation of the problem of lunar theory.

In 1722, Leonhard Euler, a student of Bernoulli, proposed the formulation of the restricted three-body problem (R3BP) in which one of the bodies is assumed massless and the remaining ‘primary’ bodies are assumed to move on conic sections. Euler approached the R3BP from the perspective of a synodic, or rotating, coordinate frame for application to his lunar theories. This synodic frame later became essential for the qualitative exploration of behavior in the 3BP. In the same year, the existence of five equilibrium solutions in the restricted Sun-Jupiter 3BP was demonstrated by Joseph Louis Lagrange. Lagrange’s findings predicted the existence of the Trojan asteroids in the vicinity of the linearly stable equilateral libration points in the Sun-Jupiter system. It was not until 1906, however, that the first of the Trojan asteroids, 588 Achilles, was discovered near the  $L_5$  point. Currently, 6075 Jupiter Trojan asteroids have been catalogued [7]. In addition, one Earth Trojan, four Mars Trojans, one Uranus Trojan, and nine Neptune Trojans have been discovered. By framing the 3BP within a synodic frame, Carl Gustav Jacob Jacobi demonstrated in 1836 that

an integral of the motion exists. This integral is known as the Jacobi integral or Jacobi constant and is the only known quantity that is conserved for the circular restricted three-body problem. The existence of the Jacobi constant has qualitative implications for solutions in the 3BP. One consequence of the existence of this integral is the zero-velocity surfaces (ZVSs) and zero-velocity curves (ZVCs) which define the regions of space that are accessible to the third body. In 1877–1878, George William Hill considered a simplified version of the Sun-Earth 3BP in which the assumptions of zero solar parallax, zero solar eccentricity, and zero lunar inclination were imposed to search for particular solutions [8]. All solutions within this simplified system are symmetric with respect to the  $x$ - and  $y$ -axes in the rotating coordinate frame. Hill discovered one periodic solution, identified as Hill’s variation orbit, with period equal to that of the Moon. Prior to Hill’s discovery, all solutions in the 3BP were obtained by solving the 2BP and adding perturbations to the conic solution. A significant contribution from Hill is his introduction of the zero-velocity curves, derived using the Jacobi integral, to define limiting boundaries in the solution space. Through the use of the ZVCs, Hill could demonstrate that there exist limits on the radius of the Moon’s orbit, thereby demonstrating that the Moon cannot escape its orbit about the Earth.

The first-return map, or Poincaré map, was introduced in 1881, by Jules Henri Poincaré as a tool to examine the stability of periodic orbits [9]. Later, in 1899, Poincaré completed the three volume set *Les Méthodes Nouvelles de la Mécanique Céleste*. Within the second volume, Poincaré proved that no new transcendental, or nonalgebraic, integrals of the motion exist in the R3BP. Two years prior, Heinrich Bruns had proved the nonexistence of any new algebraic integrals of motion for the general 3BP. Also within the second volume, Poincaré then applied the theory of asymptotic solutions to the R3BP, and produced doubly asymptotic solutions that he would later label as homoclinic solutions [9, 10]. The behavior of these homoclinic connections was difficult to describe and was sensitive to perturbations in the

initial conditions, thereby prompting Poincaré’s discussion of chaos. In 1912, Karl Sundman, a Finnish mathematical astronomer, produced a solution in the 3BP in terms of a convergent power series. However, computing solutions using this convergent series is not computationally practical and, because the solution does not supply any qualitative intuition about the problem, further study of the problem is clearly warranted.

## 1.2 Motion in the Vicinity of the Collinear Libration Points

In 1968, Charles C. Conley demonstrated the existence of several classifications of trajectories in the vicinity of the collinear libration points within the context of the Circular Restricted Three-Body Problem (CR3BP), where the two primary bodies are assumed to move on circular orbits about their barycenter [11]. A proof is developed that implicates the stable and unstable invariant manifolds, asymptotic to solutions in the center subspace associated with the collinear libration points, as separatrices that distinguish two distinct classifications of trajectories: transit orbits that cross through the equilibrium region between adjoining regions of the ZVCs, in the planar problem, and nontransit orbits that are bounded to their region of origin. Building on the results of Conley, Koon et al. (2000) and Gómez et al. (2004) demonstrate the application of these invariant manifolds for trajectory design [12, 13].

## 1.3 Trajectory Design Employing Poincaré Maps

The successful use of Poincaré maps has been demonstrated for trajectory design and analysis by various researchers. Employing a Poincaré map, in combination with a constraint on the energy level, i.e., the value of the Jacobi constant, offers a reduction in dimension by two. In the planar CR3BP, the system is, thus, reduced to two dimensions and the map is fully represented by the projection onto a plane.

In the spatial problem, however, Poincaré maps are at least four-dimensional and strategies to facilitate their application to trajectory design are required.

In 2000, Koon et al. explored the application of Poincaré maps for the design of transit trajectories in the planar CR3BP by exploiting the separatrix structure of the invariant manifolds asymptotic to the center manifold associated with the collinear points [12]. These authors additionally employed maps to investigate the temporary capture and transit of the comet Oterma in the Sun-Jupiter system. In 2003, Villac and Scheeres employed the periapse Poincaré map to identify regions of escape and capture in the planar Hill three-body problem (H3BP). Haapala [14] and Davis [15] later investigate these regions in the CR3BP, and demonstrate the relationship between the escape/capture regions and the invariant manifold structures. While these investigations represent analyses in problems with two degrees-of-freedom, the application of Poincaré maps in the three degree-of-freedom (spatial) problem has also been explored.

To employ Poincaré maps for trajectory design in the full spatial CR3BP, strategies to employ higher-dimensional Poincaré maps are necessary. These strategies generally either serve to reduce the dimension of the map, or to offer strategies for visually representing the higher-dimensional data set. As a third option, the map may be projected into a lower-dimensional space so that, while some information is lost, insight into the solution space might still be gained. Early work with higher-dimensional maps generally employed this latter method, where various orthographic projections are employed to gain insight into the higher dimensional space, e.g. Froeschlé [16,17], Martinet and Magnenat [18] as well as Contopoulos et al. [19]. Froeschlé [17] additionally considers “slices” of the three-dimensional projection of a map. Here, he plots numerous stereoscopic projections, each of which include only the crossings of the map within some tolerance of a prescribed value of one of the state variables. Later, Patsis and Zachilas employ rotation of a three-dimensional image so that all projections may be considered, and include color to represent the fourth dimension [20]. Geisel [21]

applies this method to investigate structures within the CR3BP. While the strategies employed by Patsis, Zachilas, and Geisel serve to represent the full map, rotation of the view is required to consider all possible orthographic projections.

Alternatively to considering projections of a higher-dimensional map, the dimension of the map may be reduced by applying additional constraints. For example, Jorba and Masdemont [22] as well as Gómez et al. [23] demonstrate the use of Poincaré maps to represent the crossings of periodic and quasi-periodic orbits that exist within the center manifold associated with a collinear point. These authors develop a higher-order normal form expansion of the Hamiltonian in the vicinity of the equilibrium point to decouple the stable and unstable motion. A change in variables allows for the removal of the unstable behavior via a reduction to the center manifold and yields a system with two degrees of freedom. Thus, two-dimensional Poincaré maps associated with periodic and quasi-periodic orbits in the spatial problem, for a particular energy level, are represented using two nonphysical coordinates. In 2001, Gómez et al. [24] define multiply constrained surfaces of section to reduce the dimension of Poincaré maps in the spatial problem. For a surface of section defined by three constraints, a three-dimensional map may be computed. Including a constraint on the value of the Jacobi constant, the dimension is reduced to two, and the maps are fully represented using two state variables. While the application of multiple constraints yields a reduction in the dimension of the map, it may not be obvious which additional constraints are most useful. In addition, only the subset of the higher-dimensional map that satisfies the selected constraints is considered using this strategy. Thus, techniques to represent the entire map are sought to facilitate an exploration of the entire solution space.

Strategies to visualize the full higher-dimensional map include the afore mentioned techniques employing three-dimensional scatter plots including color to represent the fourth dimension by Patsis and Zachilas [20], as well as Geisel [21]. Alternatively to the use of scatter plots, new symbols may be employed to represent crossings

of the map. Paskowitz and Scheeres [25] classify trajectory behavior in the spatial H3BP problem using periapse maps. These authors represent the region of periapses corresponding to immediate escape from the vicinity of the smaller primary using a vector. The basepoint of the vector represents the position in three-dimensional configuration space, and the length and orientation of the vector indicate the velocity magnitude and direction at periapsis. Thus, the full six-dimensional state is represented for each crossing of the map. Again, while the use of vectors allows the full map to be represented, rotation of the view is required to consider all possible orthographic projections. In this investigation, alternative representations are considered for higher-dimensional maps that allow the map to be viewed in one plane. Thus, all of the information is represented in a single image without requiring rotation of the view.

#### 1.4 Present Work

In this investigation, the role of higher-dimensional Poincaré maps in facilitating trajectory design is explored for a variety of applications. To begin, existing strategies to implement Poincaré maps for trajectory design applications in the spatial CR3BP are evaluated. New applications for these strategies are explored, including an analysis of the natural motion of Jupiter-family comets that experience temporary capture about Jupiter, and the search for periodic orbits in the vicinity of the primary bodies in the spatial problem. Because current strategies tend to be computationally intensive, new approaches to represent the information contained in higher-dimensional Poincaré maps are sought. The field of data visualization offers many options to visually represent multivariate data sets, including the use of glyphs. A glyph is any graphical object whose physical attributes are determined by the variables of a data set. For example, the vectors employed by Paskowitz and Scheeres [25] to represent crossings of the periapse map in the spatial Hill's problem are a glyph representation.

In this investigation, the role of glyphs in representing higher-dimensional Poincaré maps is explored, and the resulting map representations are demonstrated to search for maneuver-free and low-cost transfers between libration point orbits. A catalog of libration point orbit transfers is developed in the Earth-Moon system, and observations about the catalog solutions yields insight into the existence of these transfers. The application of Poincaré maps to compute transfers between libration point orbits in different three-body systems is additionally considered. Finally, interactive trajectory design environments incorporating Poincaré maps into the design process are demonstrated. Such design environments offer a unique opportunity to explore the available trajectory options and to gain intuition about the solution space.

The organization of this study is as follows:

- Chapter 2: Background — Circular Restricted Three-Body Problem

In this chapter, the equations of motion are derived for the CR3BP. The single integral of the motion, as well as the zero-velocity surfaces, and equilibrium solutions are discussed.

- Chapter 3: Fundamental Motion in the Restricted Problem

Examination of the variational system in the vicinity of the three collinear points reveals the existence of periodic and quasi-periodic, as well as hyperbolic, solutions. Invariant manifold theory is introduced in connection with the collinear libration points, and the role of the invariant manifolds in determining the evolution of nearby solutions is developed. Finally, the state-transition matrix is defined and is utilized in the development of targeting algorithms.

- Chapter 4: Poincaré Maps and Trajectory Design

Poincaré maps are discussed as a means of representing higher-dimensional systems, and their role in trajectory design is evaluated. The representation of

invariant manifolds using maps is introduced, and proves useful in the location of heteroclinic and homoclinic trajectories.

- Chapter 5: New Applications for Existing Design Techniques

Trajectory design techniques demonstrated by previous researchers are applied for new scenarios. The paths of comets Oterma and Helin-Roman-Crockett during temporary capture about Jupiter are analyzed, and temporary capture events are demonstrated to be facilitated by the stable and unstable invariant manifolds asymptotic to the center manifold associated with the  $L_1$  and  $L_2$  libration points.

- Chapter 6: Representing Higher-Dimensional Poincaré Maps

Tools from the field of data visualization are discussed and their relevance to trajectory design strategies is explored. In particular, the role of glyphs as a visual tool to display crossings of higher-dimensional Poincaré maps is demonstrated.

- Chapter 7: Exploring the Role of Poincaré Maps in an Interactive Trajectory Design Environment

Trajectory design tools employing Poincaré maps within a visual environment are demonstrated for the design of transfers between periodic libration point orbits. Graphical environments prove useful to explore the available solution space and to locate an initial guess for a transfer. An interactive differential corrections environment is demonstrated to locate feasible solutions and to apply constraints on any maneuvers.

- Chapter 8: Catalog of Free and Low-Cost Transfers Between Libration Point Orbits in the Earth-Moon System

A visual design environment, demonstrated in Chapter 6, is employed to compute a catalog of available maneuver-free and low-cost transfers between various libration point orbits in the Earth-Moon system. The constraints on the cata-

log are defined, and the computed trajectories are displayed. Observations are offered about the relationship between the primary system mass ratio and the available transfers.

- Chapter 9: Concluding Remarks and Recommendations for Future Work  
The results of this investigation are summarized, and a proposal for future work is discussed.

## 2. BACKGROUND — CIRCULAR RESTRICTED THREE-BODY PROBLEM

Within the context of the Circular Restricted Three-Body Problem (CR3BP), the motion of a particle,  $P_3$ , in the vicinity of two primary bodies,  $P_1$  and  $P_2$ , is investigated. While no closed-form solution is known to exist in the CR3BP, qualitative observations and numerical exploration offer much insight into the problem. To facilitate numerical integration, the equations of motion are derived for the CR3BP. The equations of motion admit a single integral of the motion, that is, the Jacobi integral. The existence of the Jacobi integral allows the definition of zero-velocity surfaces, from which qualitative observations about the accessible solutions are available. Five equilibrium points exist, in the CR3BP, including three collinear points and two equilateral points. The three collinear points are determined to be linearly unstable, with a four-dimensional center manifold, a one-dimensional stable manifold and a one-dimensional unstable manifold. Thus, a study of the variational system in the vicinity of the collinear points reveals the existence of periodic and quasi-periodic, as well as hyperbolic, solutions.

### 2.1 Equations of Motion Relative to an Inertial Observer

Derivation of the differential equations governing the motion of  $P_3$  as viewed by an inertial observer is based on Newton's second law. Assuming that  $P_3$  is too small to influence the motion of  $P_1$  and  $P_2$ , the primary orbits are conics, assumed to be circular for the CR3BP. In the spatial problem,  $P_3$  is free to move with respect to the rotating primary system in all three spatial dimensions. Define the distance between the primary bodies as  $\ell^*$ , and the masses of the larger and smaller primary

bodies as  $m_1$  and  $m_2$ , respectively. Let  $\hat{X}, \hat{Y}, \hat{Z}$  represent inertial unit vectors. The inertial  $\hat{X}$ - $\hat{Y}$  plane is defined as the plane of primary motion and  $\hat{Z}$  is parallel to the angular momentum vector associated with the primary system. Consistent with circular orbits, the mean motion,  $N$ , of the primary system is defined such that  $N = \sqrt{\frac{G(m_1 + m_2)}{\ell^*^3}}$ , and the angle orienting the rotating line connecting  $P_1$  and  $P_2$  with respect to the inertial  $\hat{X}$ -axis is  $N \cdot \tau$ , where  $\tau$  is the independent time variable. Let  $\bar{R}_i$  be defined as the position vector that locates  $P_i$  relative to the inertially fixed barycenter,  $B$ , and  $R_i = ||\bar{R}_i||$ . The distances between each primary and the system barycenter are evaluated as  $R_1 = \frac{m_2 l^*}{(m_1 + m_2)}$  and  $R_2 = \frac{m_1 l^*}{(m_1 + m_2)}$ . The position vector representing the location of  $P_3$  relative to  $B$  is defined as  $\bar{R}_3 = \bar{R}$ , where, written in terms of inertial unit vectors,  $\bar{R} = X\hat{X} + Y\hat{Y} + Z\hat{Z}$ . The vectors that represent the positions of the third body relative to the primaries are defined in terms of the inertial unit vectors as

$$\bar{R}_{13} = (X - R_1 \cos(N \cdot \tau))\hat{X} + (Y - R_1 \sin(N \cdot \tau))\hat{Y} + Z\hat{Z}, \quad (2.1)$$

$$\bar{R}_{23} = (X + R_2 \cos(N \cdot \tau))\hat{X} + (Y + R_2 \sin(N \cdot \tau))\hat{Y} + Z\hat{Z}, \quad (2.2)$$

where the relative position vectors are defined as  $\bar{R}_{ij} = \bar{R}_j - \bar{R}_i$ . The equations of motion as viewed by an inertial observer are derived using Newton's second law. As a consequence, the acceleration of the third particle,  $P_3$ , is derived from the gradient of the gravitational potential function, such that  $\bar{R}_I'' = \bar{\nabla}U$ , where the scalar potential function  $U$  is defined as  $U = -G \left( \frac{m_1}{R_{13}} + \frac{m_2}{R_{23}} \right)$ . Thus, the acceleration is evaluated as

$$\bar{R}_I'' = -\frac{Gm_1}{R_{13}^3}\bar{R}_{13} - \frac{Gm_2}{R_{23}^3}\bar{R}_{23}, \quad (2.3)$$

where a prime indicates the time derivative with respect to time  $\tau$  and subscript  $I$  indicates that the derivative is with respect to the inertial frame. Note that the line connecting  $P_1$  and  $P_2$  is oriented such that its angle with respect to  $\hat{X}$  is  $N \cdot \tau$ .

Decomposing the vector equation (2.3) into its scalar components, the scalar equations of motion relative to the inertial frame become:

$$X''_I = \frac{m_1(X - R_1 \cos(N \cdot \tau))}{R_{13}^3} + \frac{m_2(X + R_2 \cos(N \cdot \tau))}{R_{23}^3}, \quad (2.4)$$

$$Y''_I = \frac{m_1(Y - R_1 \sin(N \cdot \tau))}{R_{13}^3} + \frac{m_2(Y + R_2 \sin(N \cdot \tau))}{R_{23}^3}, \quad (2.5)$$

$$Z''_I = \frac{m_1 Z}{R_{13}^3} + \frac{m_2 Z}{R_{23}^3}, \quad (2.6)$$

where  $R_{ij} = \|\bar{R}_{ij}\|$ . The equations of motion with respect to the inertial frame in equations (2.4)–(2.6) are nonautonomous. Because, in the *restricted* three-body problem, the total energy of the system is not conserved, the system of differential equations is not Hamiltonian and, therefore, possesses an energy integral which is time-varying. Describing the motion of  $P_3$  from the perspective of a synodic frame rotating with the primary system produces autonomous equations of motion that are Hamiltonian in nature and yield a constant integral of the motion.

## 2.2 Equations of Motion Relative to the Rotating Frame

The concept of a synodic or rotating coordinate system was first introduced by Euler in 1772 for application to his lunar theory. Because the equations of motion in the CR3BP possess a constant integral of the motion when written with respect to a synodic reference frame, it is advantageous to define such a synodic frame and derive the associated equations of motion. The second-order vector differential equation (2.3) is rewritten to exploit the rotating frame defined by unit vectors  $\hat{x}$ ,  $\hat{y}$ ,  $\hat{z}$ . The rotating frame is illustrated in Figure 2.1. The rotating  $\hat{x}$ -axis is defined to be directed from the larger primary to the smaller, the  $\hat{z}$ -axis is parallel to the direction of the orbital angular velocity of the primary system with respect to the inertial frame, and the  $\hat{y}$ -axis completes the dextral, orthonormal triad. To remove the dependence of the differential equations on system quantities such as the distance between primaries or the specific primary masses, characteristic quantities are defined for use in

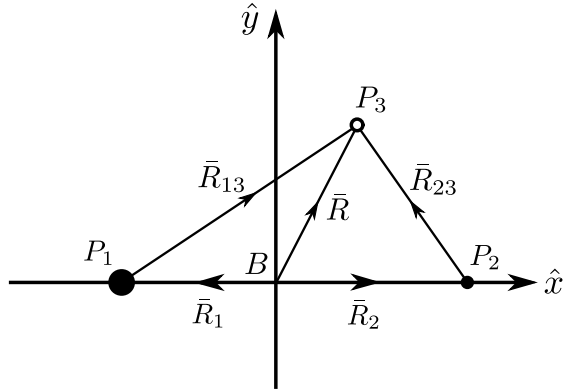


Figure 2.1. Rotating coordinate frame

nondimensionalization. If the total mass of the two primary bodies,  $m^* = m_1 + m_2$ , the distance between the two primaries,  $l^* = R_1 + R_2$ , and the independent time variable,  $t^* = \sqrt{\frac{l^{*3}}{Gm^*}} = \frac{1}{N}$ , are defined as characteristic quantities, then

$$\mu = m_2/m^*,$$

$$1 - \mu = m_1/m^*,$$

$$t = \tau/t^*.$$

The system mass parameter,  $\mu$ , varies between 0 and  $\frac{1}{2}$ , and solutions of the CR3BP vary qualitatively for differing values of  $\mu$ . The angular frequency of the primary system is  $2\pi/t^*$ , and the nondimensional system completes one revolution in  $t = 2\pi$ . The nondimensional mean motion,  $n = Nt^*$ , is normalized to unity. Due to the assumption of circular orbits for the primary bodies,  $\ell^*$  is a constant. The values of the constants for the systems employed in this investigation appear in Table 2.1. The

Table 2.1 System Constants and Characteristic Quantities

System	$\mu$	$m^*$ (kg)	$\ell^*$ (km)	$2\pi t^*$
Earth-Moon	$1.21506 \times 10^{-2}$	$6.04680 \times 10^{24}$	$3.85693 \times 10^5$	27.4223 days
Sun-Jupiter	$9.53816 \times 10^{-4}$	$1.99042 \times 10^{30}$	$7.78412 \times 10^8$	1.88833 years
Sun-Earth	$3.00390 \times 10^{-6}$	$1.98853 \times 10^{30}$	$1.49598 \times 10^8$	1.00009 years

nondimensional position vectors are defined in terms of rotating coordinates as

$$\bar{r}_1 = \bar{R}_1/\ell^* = -\mu\hat{x}, \quad (2.7)$$

$$\bar{r}_2 = \bar{R}_2/\ell^* = (1-\mu)\hat{x}, \quad (2.8)$$

$$\bar{r}_{13} = \bar{R}_{13}/\ell^* = (x + \mu)\hat{x} + y\hat{y} + z\hat{z}, \quad (2.9)$$

$$\bar{r}_{23} = \bar{R}_{23}/\ell^* = (x - 1 + \mu)\hat{x} + y\hat{y} + z\hat{z}, \quad (2.10)$$

$$\bar{r} = \bar{R}_3/\ell^* = x\hat{x} + y\hat{y} + z\hat{z}. \quad (2.11)$$

Equation (2.3) may then be rewritten in its nondimensional form:

$$\ddot{\bar{r}}_I = -\frac{1-\mu}{r_{13}^3}\bar{r}_{13} - \frac{\mu}{r_{23}^3}\bar{r}_{23}, \quad (2.12)$$

where, for some quantity  $q$ ,  $\dot{q}$  represents the derivative of  $q$  with respect to nondimensional time,  $t$ . To express the left side of equation (2.12) as a derivative relative to the rotating frame, the kinematic expansion for acceleration  $\ddot{\bar{r}}_I$  is required. The kinematic expansion relates derivatives as viewed by different observers, that is,

$$\ddot{\bar{r}}_I = (\ddot{x}_R - 2\dot{y}_R - x)\hat{x} + (\ddot{y}_R + 2\dot{x}_R - y)\hat{y} + \ddot{z}_R\hat{z},^1 \quad (2.13)$$

---

<sup>1</sup>See Appendix A for details.

where subscript  $R$  indicates a derivative with respect to the rotating frame. Thus, the three second-order nondimensional scalar equations of motion are expressed in terms of rotating coordinates as

$$\ddot{x} - 2n\dot{y} - n^2x = -\frac{(1-\mu)(x+\mu)}{r_{13}^3} - \frac{\mu(x-1+\mu)}{r_{23}^3}, \quad (2.14)$$

$$\ddot{y} + 2n\dot{x} - n^2y = -\frac{(1-\mu)y}{r_{13}^3} - \frac{\mu y}{r_{23}^3}, \quad (2.15)$$

$$\ddot{z} = -\frac{(1-\mu)z}{r_{13}^3} - \frac{\mu z}{r_{23}^3}, \quad (2.16)$$

where  $n = 1$  and subscripts  $R$  have been removed.

While the general three-body problem is conservative, the restricted problem is not. In the inertial frame, there exists a potential function  $U = -G\left(\frac{m_1}{R_{13}} + \frac{m_2}{R_{23}}\right)$ , such that  $\bar{R}_I'' = \bar{\nabla}U$ . Because,  $R_{13}$  and  $R_{23}$  vary with time, the total energy of the system is not constant. In the rotating frame it is not possible to write the equations of motion in terms of the gradient of a potential function. However, a similar quantity,  $\Omega$ , exists such that

$$\Omega(x, y, z) = \frac{1-\mu}{r_{13}} + \frac{\mu}{r_{23}} + \frac{1}{2}n^2(x^2 + y^2), \quad (2.17)$$

and is typically labeled the *pseudo-potential* function. Note that  $\Omega$  is a function of the position of  $P_3$  only, and is independent of the velocity of  $P_3$ . The pseudo-potential can be used to simplify the equations of motion (2.14)–(2.16). The partial derivatives,

$$\Omega_x = n^2x - \frac{(1-\mu)(x+\mu)}{r_{13}^3} - \frac{\mu(x-1+\mu)}{r_{23}^3}, \quad (2.18)$$

$$\Omega_y = n^2y - \frac{(1-\mu)y}{r_{13}^3} - \frac{\mu y}{r_{23}^3}, \quad (2.19)$$

$$\Omega_z = -\frac{(1-\mu)z}{r_{13}^3} - \frac{\mu z}{r_{23}^3}, \quad (2.20)$$

where  $\Omega_q = \frac{\partial\Omega}{\partial q}$  are substituted into the differential equations, resulting in the nondimensionalized equations of motion for the CR3BP:

$$\ddot{x} = 2n\dot{y} + \Omega_x, \quad (2.21)$$

$$\ddot{y} = -2n\dot{x} + \Omega_y, \quad (2.22)$$

$$\ddot{z} = \Omega_z. \quad (2.23)$$

It is convenient to rewrite equations (2.21)–(2.23) in first-order form. Let  $\bar{x}$  be defined as the six-dimensional state vector, that is,  $\bar{x} = [x \ y \ z \ \dot{x} \ \dot{y} \ \dot{z}]^T$ . Then, the second-order scalar equations (2.21)–(2.23) are rewritten as a first-order vector equation of motion,

$$\dot{\bar{x}} = \bar{f}(\bar{x}), \quad (2.24)$$

where

$$\bar{f} = \left[ \dot{x}, \ \dot{y}, \ \dot{z}, \ 2n\dot{y} + \Omega_x, \ -2n\dot{x} + \Omega_y, \ \Omega_z \right]^T. \quad (2.25)$$

Written with respect to rotating coordinates, these nonlinear equations of motion are now autonomous and Hamiltonian. Note that for an initial state that is solely in the  $x$ - $y$  plane, the trajectory evolves with time to remain solely in the  $x$ - $y$  plane. Thus, the *planar* Circular Restricted Three-Body Problem (PCR3BP) may be explored independently of the spatial problem (SCR3BP).

Because no closed-form solution for the CR3BP is available, trajectories are computed via numerical integration of the first-order equations of motion (2.24). Given an initial state  $\bar{x}_0 = \bar{x}(t_0)$ , an explicit integration scheme is employed to propagate the associated trajectory for a given time interval or until a desired stopping condition is met. In this investigation, all numerical propagation is achieved with a Prince-Dormand (8, 9) method via the publicly available GNU Scientific Library [26].

### 2.3 Symmetry Properties

Inherent in the CR3B equations of motion is a symmetry in time. Given a solution

$$[x(t), y(t), z(t), \dot{x}(t), \dot{y}(t), \dot{z}(t)]^T,$$

the symmetry properties of the system equations also yield a solution of the form

$$[x(-t), -y(-t), z(-t), -\dot{x}(-t), \dot{y}(-t), -\dot{z}(-t)]^T.$$

This result is apparent if the equations are allowed to evolve in negative time, that is,  $t \rightarrow -t$ . Consider the second-order equations (2.21)–(2.23). The time transformation yields  $\frac{d}{d(-t)} = -\frac{d}{dt}$ , and  $\frac{d^2}{d(-t)^2} = \frac{d^2}{dt^2}$ , thus,

$$\frac{d^2x}{d(-t)^2} = 2\frac{d(-y)}{d(-t)} + \frac{\partial\Omega}{\partial x}, \quad (2.26)$$

$$\frac{d^2(-y)}{d(-t)^2} = -2\frac{dx}{d(-t)} + \frac{\partial\Omega}{\partial(-y)}, \quad (2.27)$$

$$\frac{d^2z}{d(-t)^2} = \frac{\partial\Omega}{\partial z}. \quad (2.28)$$

The form of these solutions is exactly the same as the previously derived equations of motion, equations (2.21)–(2.23), with suitable substitutions. Therefore, given any solution, a second solution, reflected across the  $\hat{x}$ -axis, also exists. This symmetry property is frequently exploited in trajectory design. One consequence of this symmetry property is the mirror theorem:

**Theorem 2.3.1 (The Mirror Theorem)** *If  $n$  point masses are acted upon by their mutual gravitational forces only, and at a certain epoch each radius vector from the center of mass of the system is perpendicular to every velocity vector, then the orbit of each mass after that epoch is a mirror image of its orbit prior to that epoch. Such a configuration of radius and velocity vectors is called a mirror configuration [29].*

If a mirror configuration occurs at two distinct times along a trajectory in the CR3BP, the trajectory must be periodic. The mirror theorem is frequently employed in the search for periodic solutions in the CR3BP.

## 2.4 Integral of the Motion

In 1836, Jacobi formulated the restricted three-body problem in terms of a synodic coordinate frame to derive what is now labeled the Jacobi integral or the Jacobi constant. The Jacobi integral is the only integral of the motion that is known to exist in the CR3BP. The Hamiltonian for a time-independent system represents an integral of the dynamical system [10]. The Hamiltonian,  $H$ , for the system described by equations (2.21)–(2.23) is written in terms of rotating coordinates as

$$H = \frac{1}{2} (\dot{x}^2 + \dot{y}^2 + \dot{z}^2) - \frac{1}{2} (x^2 + y^2) - \frac{(1 - \mu)}{r_{13}^3} - \frac{\mu}{r_{23}^3}, \quad (2.29)$$

and represents an energy-like quantity associated with the motion of  $P_3$  relative to the rotating frame. The Jacobi constant is related to the Hamiltonian as  $C = -2H$ , (see Appendix B.1 for details) and is, thus, represented as

$$C = 2\Omega(x, y, z) - v^2, \quad (2.30)$$

where  $v = \sqrt{\dot{x}^2 + \dot{y}^2 + \dot{z}^2}$ . The Jacobi constant provides a relationship between the speed of  $P_3$  and its position. While there is no closed-form solution for the behavior in the CR3BP, the Jacobi constant yields much qualitative insight into the available solutions. Because the Jacobi constant is defined as a negative quantity, increasing  $C$  corresponds to decreasing the energy of  $P_3$  in the rotating frame.

## 2.5 Equilibrium Solutions

The search for particular solutions to the equations of motion (2.21)–(2.23) yields five equilibrium points. These equilibrium points, often denoted the *libration* or *La-grange* points, are locations in the rotating system where the combined gravitational forces of the two primary bodies exactly equal the centripetal force required for the third body to rotate with the primary system. The libration points are, therefore, stationary from the perspective of a rotating observer, and placing  $P_3$  at any of the

five equilibrium points, with zero velocity and acceleration relative to the rotating frame, results in zero motion relative to the rotating system.

The five libration points are frequently categorized into two types. The *collinear* points lie along the rotating  $\hat{x}$ -axis, and the *triangular* or *equilateral* points are positioned off the  $\hat{x}$ -axis. To compute the locations of the libration points, solutions of the form  $x(t) = x(0)$ ,  $y(t) = y(0)$ ,  $z(t) = z(0)$  are sought. Such solutions occur when the rotating velocities and accelerations are zero, thus, the equilibrium solutions are located where  $\Omega_x = \Omega_y = \Omega_z = 0$ . Recall equations (2.18)–(2.20). Because  $\left(\frac{(1-\mu)}{r_{13}^3} + \frac{\mu}{r_{23}^3}\right)$  is nonzero,  $z$  must be zero for all equilibrium solutions. Thus, all five equilibrium points lie in the  $x$ - $y$  plane.

To determine the positions of the libration points, begin with the second equilibrium condition, that is,  $\Omega_y = 0$ . There are three solutions to this condition, namely  $y = 0$ , corresponding to the three collinear points, and  $y = \pm\sqrt{3}/2$ , reflecting the  $y$ -coordinates of the two equilateral points. Selecting  $y = 0$ ,  $\Omega_x$  is reduced and the three solutions to the first equilibrium condition,  $\Omega_x = 0$ , are the roots of the following expressions,

$$x_{L_1} - \frac{1-\mu}{(x_{L_1}+\mu)^2} + \frac{\mu}{(x_{L_1}-1+\mu)^2} = 0, \quad (2.31)$$

$$-x_{L_2} + \frac{1-\mu}{(x_{L_2}+\mu)^2} + \frac{\mu}{(x_{L_2}-1+\mu)^2} = 0, \quad (2.32)$$

$$-x_{L_3} - \frac{1-\mu}{(x_{L_3}+\mu)^2} - \frac{\mu}{(x_{L_3}-1+\mu)^2} = 0. \quad (2.33)$$

The solutions to these three equations define the positions,  $x_{L_1}$ ,  $x_{L_2}$ , and  $x_{L_3}$ , corresponding to the collinear libration points,  $L_1$ ,  $L_2$ , and  $L_3$ . Solving equations (2.31)–(2.33) for a given value of  $\mu$  yields the locations of the collinear libration points for a particular system. Given  $y = \pm\sqrt{3}/2$  and solving the second equilibrium condition,  $\Omega_y = 0$ , produces the locations of the two triangular libration points,  $L_4$  and  $L_5$ , as follows,

$$x_{L_{4,5}} = \frac{1}{2} - \mu \quad y_{L_{4,5}} = \pm \frac{\sqrt{3}}{2}. \quad (2.34)$$

The relative positions of the five libration points in the rotating frame are displayed in Figure 2.2. The collinear libration points appear in red along the rotating  $x$ -axis, and the triangular points are plotted in green.

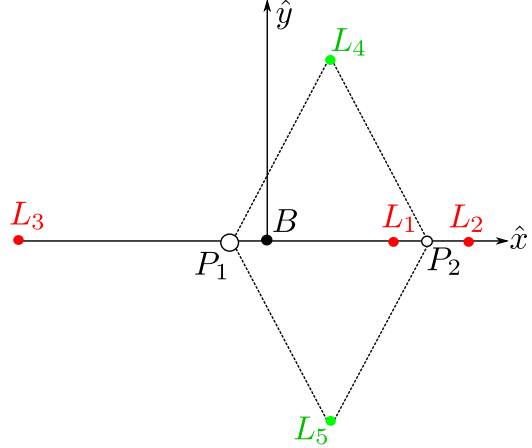


Figure 2.2. Libration points in the rotating frame.

and the triangular points are plotted in green. As evidenced by equations (2.31)–(2.33), the positions of each of the collinear libration points vary with the system mass parameter,  $\mu$ . The nondimensional (nd) locations of the collinear points for the systems that appear in this analysis are listed in Table 2.2. The values of the Jacobi

Table 2.2 Locations of the Collinear Libration Points of Various Systems

System	$x_{L_1}(nd)$	$x_{L_2}(nd)$	$x_{L_3}(nd)$
Earth-Moon	0.836915	1.155682	-1.005063
Sun-Jupiter	0.932367	1.068829	-1.000397
Sun-Earth	0.990026	1.010035	-1.000001

constant ( $C_{L_i}$ ) associated with each libration point for the three systems that appear in this investigation are included in Table 2.3. Clearly, the value of Jacobi constant varies across the different libration points. This variation is not unexpected because, while relative velocity is zero at all equilibrium points, the positions of the libration

Table 2.3 Jacobi Constant Values for the Libration Points in Various Systems

System	$C_{L_1}$	$C_{L_2}$	$C_{L_3}$	$C_{L_4} = C_{L_5}$
Earth-Moon	3.188341	3.172160	3.012147	2.987997
Sun-Jupiter	3.038759	3.037487	3.000954	2.999047
Sun-Earth	3.000891	3.000887	3.000003	2.999997

points differ. The values of Jacobi constant,  $C_{L_i}$ , corresponding to the individual libration points additionally vary as a function of the system parameter  $\mu$ . However, a relationship among the various values of Jacobi constant for the different libration points is maintained regardless of the system . Values for  $C_{L_i}$  descend as  $i$  increases from 1 to 4, and are equal for  $i = 4, 5$ , i.e.,  $C_{L_1} \geq C_{L_2} \geq C_{L_3} \geq C_{L_4} = C_{L_5}$ .

## 2.6 Zero-Velocity Surfaces

While an analytical solution for the behavior of  $P_3$  does not exist, its motion is bounded under certain conditions. From the expression for Jacobi constant in equation (2.30), a rearrangement, such that  $v^2 = 2\Omega(x, y, z) - C$ , suggests possible restrictions on the allowable positions of  $P_3$ . Clearly, when  $C > 2\Omega(x, y, z)$ , the speed,  $v$ , is imaginary. The position components,  $x, y, z$ , are therefore constrained such that  $2\Omega(x, y, z) \geq C$ . The inaccessible regions where the speed of  $P_3$  is imaginary are denoted the *forbidden* regions. The boundary of the forbidden region in position space is a set of three-dimensional *zero-velocity* surfaces that vary as a function of  $C$ . Through a projection of the zero-velocity surfaces onto the  $x$ - $y$  plane, the zero-velocity curves (ZVCs) emerge. The ZVCs were first introduced by Hill and applied to a special case of the R3BP known as Hill's problem [10]. An example of the ZVCs in the Earth-Moon system, for a value of Jacobi constant such that  $C_{L_3} < C < C_{L_2}$ , appears in Figure 2.3. From these curves, the delineation of different available regions is apparent. Here, the region surrounding the larger primary is defined as the *interior* region, the region in the vicinity of the smaller primary is labeled the  $P_2$  region, and the region beyond the ZVCs is denoted the *exterior* region. The entire three-dimensional zero-velocity surface in the Earth-Moon system appears in Figure 2.4, with the ZVCs plotted as the dashed black line. Inner surfaces that bound the interior and  $P_2$  regions are apparent. The outer surface serves as the boundary of the exterior region. The volume between the inner and outer surfaces is the forbidden region.

For a given system, as the Jacobi constant value decreases, the qualitative characteristics of the ZVCs in the plane of motion of the primaries evolve. Higher values of  $C$  correspond to lower energies, and a larger volume of space is restricted as the forbidden region expands. Some examples of ZVCs for varying values of Jacobi constant in the Earth-Moon system appear in Figure 2.5. At the greatest values of  $C$ , the regions surrounding  $P_1$  and  $P_2$  are bounded such that  $P_3$  cannot pass between

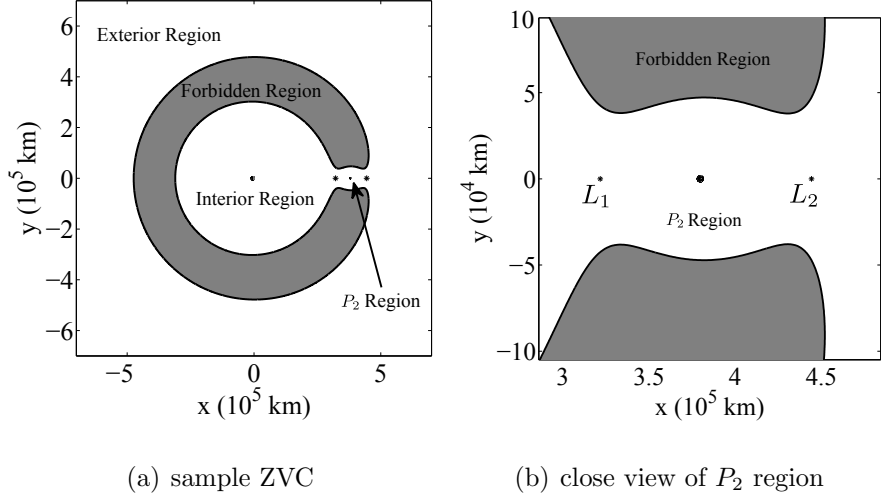


Figure 2.3. Regions of position space delineated by the ZVCs for  $C_{L_3} < C < C_{L_2}$  (Earth and Moon 2× actual size)

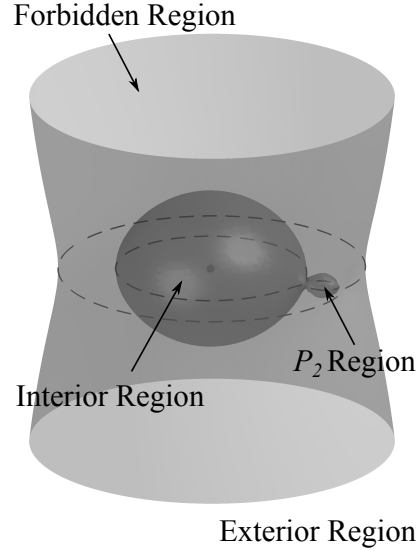


Figure 2.4. Zero-velocity surfaces in for  $C_{L_2} < C < C_{L_1}$

the primary bodies, as seen in Figure 2.5(a). As  $C$  decreases, the ZVCs open at  $L_1$  and the  $L_1$  gateway emerges, through which  $P_3$  may pass between the interior and  $P_2$  regions. Further decreasing  $C$ , the ZVCs open at  $L_2$ , and eventually  $C$  reaches a

value such that the  $L_2$  gateway opens and  $P_3$  may pass between the  $P_2$  and exterior regions. Once a value of  $C$  is achieved such that  $C \leq C_{L_2}$ ,  $P_3$  may access all regions, excluding, of course, the forbidden region. For  $C < C_{L_4,L_5}$ , the zero-velocity surfaces are entirely out-of-plane.

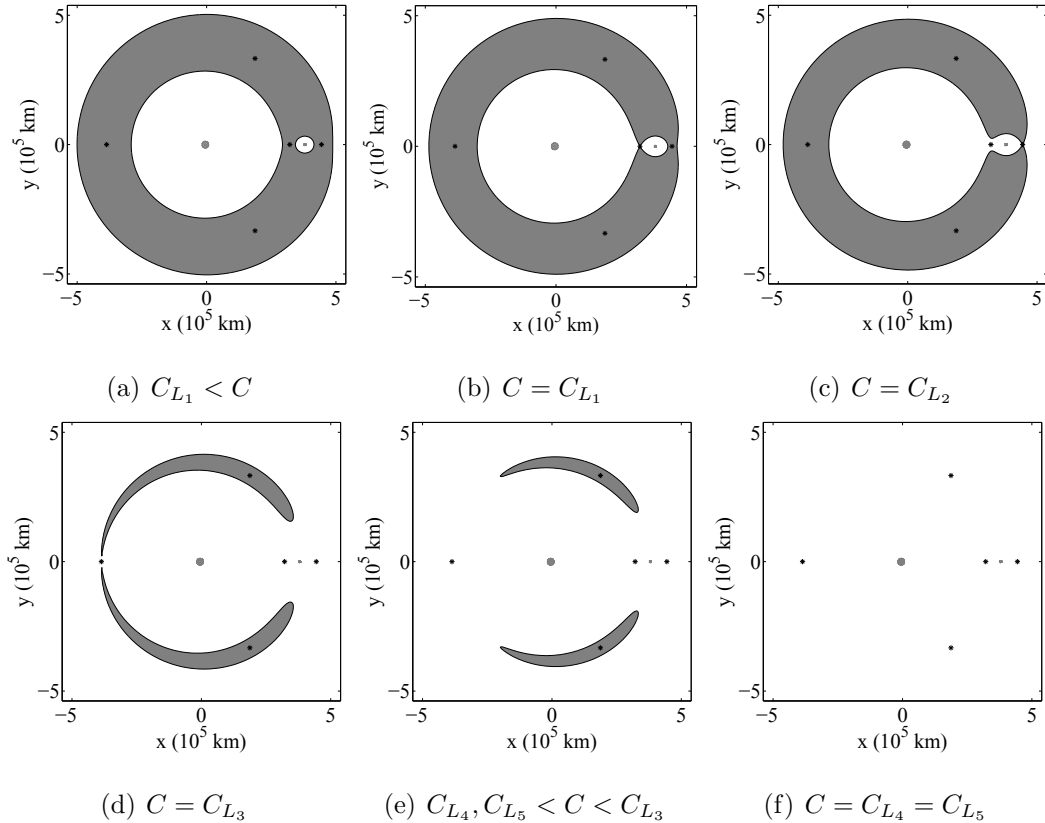


Figure 2.5. Zero-velocity curves for varying values of Jacobi constant.  
(Earth and Moon  $2\times$  actual size)

While no closed-form solution is known to exist in the CR3BP, the Jacobi integral and zero-velocity surfaces provide a great deal of qualitative insight into the behavior of  $P_3$ . Further, analysis of the five equilibrium points yields information about the behavior near these points. In the upcoming chapter, the variational equations are explored to determine the available solution types in the vicinity of the libration points, and techniques to extend these solutions to the nonlinear problem are discussed.

### 3. FUNDAMENTAL MOTION IN THE RESTRICTED PROBLEM

A rich solution space exists in the vicinity of the equilibrium points of the CR3BP, offering a number of solution types that are valuable for mission design. To understand the behavior of solutions in the vicinity of the libration points, it is useful to investigate the stability of the equilibrium points via linearization relative to any of the five Lagrange solutions. From an examination of the behavior in the linearized system, a phase portrait of the flow in the vicinity of a particular solution may be developed for the nonlinear system.

#### 3.1 Linearized Motion near the Libration Points

To develop a phase portrait of the flow in the vicinity of the libration points, it is useful to consider the variational equations of motion. Consider a general  $n$ -dimensional system for which the dynamics are governed by a nonlinear, autonomous, continuous-time, first-order vector differential equation,

$$\dot{\bar{x}} = \bar{f}(\bar{x}). \quad (3.1)$$

Here,  $\bar{f}$  is a smooth function that defines a vector field in  $\mathbb{R}^n$ . For the CR3BP, the function  $\bar{f}$  is defined as in equation (2.25). The flow,  $\phi_t$ , as the differential equation evolves is defined by  $\bar{f}$  so that  $\phi_t(\bar{x}) = \phi(\bar{x}, t)$  is smooth and  $\frac{d}{dt}(\phi(\bar{x}, t))|_{t=\tau} = \bar{f}(\phi(\bar{x}, \tau))$ .

Let  $\bar{x}_r$  represent the state along some reference solution, and consider a linearization relative to  $\bar{x}_r$  such that the linear vector variational equation is

$$\delta\dot{\bar{x}} = A(t)\delta\bar{x}, \quad (3.2)$$

where the variation,  $\delta\bar{x} = \bar{x} - \bar{x}_r = [\delta x \ \delta y \ \delta z \ \delta \dot{x} \ \delta \dot{y} \ \delta \dot{z}]^T$ , is an  $n$ -dimensional perturbation from the reference solution. Here,  $A(t) = D\bar{f}(\bar{x}_r)$  is the  $n \times n$  Jacobian matrix of first partial derivatives of  $\bar{f}$ , and is not constant, in general. The general solution to equation (3.2), obtained through integration via separation of variables, is of the form

$$\delta\bar{x}(t) = \Phi(t, t_0)\delta\bar{x}(t_0), \quad (3.3)$$

where the state transition matrix,  $\Phi(t, t_0)$ , is defined as

$$\Phi(t, t_0) \equiv e^{A(t-t_0)}. \quad (3.4)$$

Defining the reference solution to be an equilibrium point of the CR3BP, the state along a nearby trajectory is written as follows,

$$\bar{x} = \bar{x}_{eq} + \delta\bar{x}, \quad (3.5)$$

where  $\bar{x}_{eq}$  represents the state associated with the libration point. Linearization of the system relative to the equilibrium point yields equation (3.2), where

$$A = \begin{bmatrix} A_1 & A_2 \\ A_3 & A_4 \end{bmatrix} \quad (3.6)$$

is a constant matrix. The submatrices,  $A_i$ , are defined as follows:  $A_1 = 0_{3 \times 3}$  is the  $3 \times 3$  submatrix of zeroes,  $A_2 = I_{3 \times 3}$  is the  $3 \times 3$  identity matrix, and

$$A_3 = \begin{bmatrix} \Omega_{xx0} & \Omega_{xy0} & 0 \\ \Omega_{yx0} & \Omega_{yy0} & 0 \\ 0 & 0 & \Omega_{zz0} \end{bmatrix}, \quad A_4 = \begin{bmatrix} 0 & 2 & 0 \\ -2 & 0 & 0 \\ 0 & 0 & 0 \end{bmatrix}, \quad (3.7)$$

where  $\Omega_{pq} = \frac{\partial^2 \Omega}{\partial p \partial q}$  are the second partial derivatives (listed in Appendix B.2), and  $\Omega_{pq0} = \Omega_{pq}|_{\bar{x}_{eq}}$  indicates that the expression is evaluated at the libration point. Note that  $\Omega_{xz0} = \Omega_{yz0} = \Omega_{zx0} = \Omega_{zy0} = 0$ . The resulting set of linear differential equations

relative to the equilibrium point and with constant coefficients represents the variational equations of motion for the CR3BP. Expressing these equations in second-order form yields

$$\delta\ddot{x} - 2\delta\dot{y} = \Omega_{xx0}\delta x + \Omega_{xy0}\delta y, \quad (3.8)$$

$$\delta\ddot{y} + 2\delta\dot{x} = \Omega_{yx0}\delta x + \Omega_{yy0}\delta y, \quad (3.9)$$

$$\delta\ddot{z} = \Omega_{zz0}\delta z. \quad (3.10)$$

It is clear that, for the *linearized* system, the out-of-plane motion is decoupled from the planar motion. The term  $\Omega_{zz0}$  is negative for each of the five libration points. The motion in  $\hat{z}$  is therefore simple harmonic with frequency  $\omega = \sqrt{|\Omega_{zz0}|}$ . Submatrix  $A_3$  further reduces for the collinear libration points, where  $\Omega_{xy0} = \Omega_{yx0} = 0$ .

### 3.2 Stability of the Collinear Libration Points and Invariant Manifolds

The eigenvalues and eigenvectors of  $A$  are useful to explore the stability of the libration point  $\bar{x}_{eq}$ . The linear state matrix,  $A$ , is diagonalized by exploiting the eigenstructure of  $A$  and rewriting  $A$  in the form  $A = S\Lambda S^{-1}$ , where matrix  $S$  contains columns equal to the eigenvectors,  $\bar{v}_i$ , of  $A$ , and matrix  $\Lambda$  is diagonal with elements equal to the corresponding eigenvalues,  $\lambda_i$ . Then, assuming  $t_0 = 0$ , equation (3.3) is rewritten as

$$\delta\bar{x}(t) = Se^{\Lambda t}S^{-1}\delta\bar{x}(0). \quad (3.11)$$

For matrices  $A$  with  $n$  distinct eigenvalues, equation (3.11) is expanded as

$$\delta\bar{x}(t) = \sum_{i=1}^n \alpha_i e^{\lambda_i t} \bar{v}_i. \quad (3.12)$$

It is clear from this equation that the eigenvalues,  $\lambda_i$ , govern the behavior of  $\delta\bar{x}(t)$  over time and the eigenvectors determine the direction of the subsequent motion. The eigenstructure for Hamiltonian systems is symmetric about both the real and imaginary axes of the complex plane. Thus, for the matrix,  $A$ , eigenvalues occur

in real pairs  $\pm\lambda$ , purely imaginary pairs  $\pm i|\lambda|$ , or quartets of complex eigenvalues  $\pm Real(\lambda) \pm iImag(\lambda)$  [30]. When  $Real(\lambda) < 0$  for all eigenvalues, then, as time progresses, each term  $e^{\lambda_i t}$  approaches zero,  $\bar{x}$  approaches  $\bar{x}_{eq}$ , and the solution is asymptotically stable. Note that this condition is not feasible for equilibrium points in the CR3BP as the eigenvalues of  $A$  occur in opposite pairs. If  $Real(\lambda) > 0$  for any eigenvalue, then  $\delta\bar{x}$  grows exponentially with time and the solution is unstable. A critical point with eigenvalues,  $\lambda_i, \lambda_j$ , such that  $Real(\lambda_i) < 0$  and  $Real(\lambda_j) > 0$ , is nonstable and is termed a saddle point. The solution is considered neutrally stable when  $Real(\lambda) \leq 0$  for all eigenvalues, and one or more eigenvalues possesses a zero real part and are nondefective. In this case, the linear solution is bounded with respect to  $\bar{x}_{eq}$ , but does not naturally return to equilibrium.

The eigenvectors,  $\bar{v}_i$ , associated with  $\lambda_i$  are linearly independent and span  $\mathbb{R}^n$ . Let  $n_S$  be the number of eigenvalues  $\lambda_{S,i}$  with positive real parts,  $n_U$  be the number of eigenvalues  $\lambda_{U,i}$  with negative real parts,  $n_C$  be the number of eigenvalues  $\lambda_{C,i}$  with zero real parts; let  $\bar{v}_i^S, \bar{v}_i^U, \bar{v}_i^C$  be the associated eigenvectors. Then,  $E^S = span\{\bar{v}_i^S\}_{i=1}^{n_S}$ ,  $E^U = span\{\bar{v}_i^U\}_{i=1}^{n_U}$ ,  $E^C = span\{\bar{v}_i^C\}_{i=1}^{n_C}$  are defined as the stable, unstable, and center subspaces of dimension  $n_S$ ,  $n_U$ , and  $n_C$ , respectively. The  $\mathbb{R}^n$  space is defined by the union  $E^S \cup E^U \cup E^C$  such that  $n = n_S + n_U + n_C = \text{rank}(A)$ . These subspaces are invariant under  $e^{\lambda_i t}$ , that is, a solution originating from a point  $c_i \bar{v}_i$  within one of these subspaces remains within  $span\{\bar{v}_i\}$  for all time [31]. The notion of invariance implies that any solution which is initially in an invariant subspace will remain in that subspace for all past and future times. From the stable, unstable, and center subspaces, the notion of stable, unstable, and center manifolds may be defined. An equilibrium point is said to be hyperbolic if all eigenvalues have nonzero real parts, that is,  $n_C = 0$ .

**Theorem 3.2.1 (Stable Manifold Theorem)** *Suppose that  $\dot{\bar{x}} = \bar{f}(\bar{x})$  has a hyperbolic equilibrium point,  $\bar{x}_{eq}$ . Then there exist local stable and unstable manifolds,  $W_{loc}^S(\bar{x}_{eq}), W_{loc}^U(\bar{x}_{eq})$ , of the same dimension,  $n_S, n_U$ , as the eigenspaces,  $E^S, E^U$ , of*

the linearized system (3.2), and tangent to  $E^S$  and  $E^U$  at  $\bar{x}_{eq}$ .  $W_{loc}^S(\bar{x}_{eq})$ ,  $W_{loc}^U(\bar{x}_{eq})$  are smooth, as is function  $\bar{f}$  [31].

The local manifolds,  $W_{loc}^S(\bar{x}_{eq})$ ,  $W_{loc}^U(\bar{x}_{eq})$ , have global analogs,  $W^S(\bar{x}_{eq})$ ,  $W^U(\bar{x}_{eq})$ , obtained by allowing points in  $W_{loc}^S(\bar{x}_{eq})$  to flow backward in time and points in  $W_{loc}^U(\bar{x}_{eq})$  to flow forward in time [31], that is,

$$W^S(\bar{x}_{eq}) = \bigcup_{t \leq 0} \phi_t(W_{loc}^S(\bar{x}_{eq})) \quad (3.13)$$

$$W^U(\bar{x}_{eq}) = \bigcup_{t \geq 0} \phi_t(W_{loc}^U(\bar{x}_{eq})). \quad (3.14)$$

An important property of the invariant manifolds is established by the existence and uniqueness of solutions of equation (3.1).

**Theorem 3.2.2 (The Fundamental Existence-Uniqueness Theorem)** *Let  $E$  be an open subset of  $\mathbb{R}^n$  containing  $\bar{x}_0$ , and assume that  $\bar{f} \in C^1(E)$ . Then there exists an  $a > 0$  such that the initial value problem  $\dot{\bar{x}} = \bar{f}(\bar{x})$ ,  $\bar{x}(0) = \bar{x}_0$  has a unique solution  $\bar{x}(t)$  on the interval  $[-a, a]$  [32].*

By this theorem, the stable manifolds associated with distinct equilibrium points,  $\bar{x}_{eq1}$ ,  $\bar{x}_{eq2}$ , can neither intersect one another, nor can they self-intersect. Likewise, the unstable manifolds emanating from distinct equilibrium points,  $\bar{x}_{eq1}$ ,  $\bar{x}_{eq2}$ , cannot intersect one another or themselves. However, the stable manifold and the unstable manifold associated with two distinct equilibrium points, or even with one equilibrium point, can intersect [31]. Such intersections yield heteroclinic and homoclinic connections. For nonhyperbolic equilibria,  $n_C \neq 0$  and a center manifold exists.

**Theorem 3.2.3 (Center Manifold Theorem)** *Let  $\bar{f}$  be a  $C^r$  vector field on  $\mathbb{R}^n$  vanishing at the origin so that  $\bar{f}(\bar{x}_{eq}) = \bar{0}$ , and let  $A = D\bar{f}(\bar{x}_{eq})$ . The matrix  $A$  may be divided into its stable, center and unstable parts,  $n_S$ ,  $n_C$ , and  $n_U$ , respectively, with*

$$Real(\lambda) \left\{ \begin{array}{l} < 0; \lambda \in n_S \\ = 0; \lambda \in n_C \\ > 0; \lambda \in n_U \end{array} \right\}.$$

Let the generalized eigenspaces be  $E^S$ ,  $E^C$ , and  $E^U$ , respectively. Then there exist  $C^r$  stable and unstable invariant manifolds,  $W^S$  and  $W^U$ , tangent to  $E^S$  and  $E^U$  at  $\bar{x}_{eq}$ , and a  $C^{r-1}$  center manifold,  $W^C$ , tangent to  $E^C$  at  $\bar{x}_{eq}$ . The manifolds  $W^S$ ,  $W^U$ , and  $W^C$  are all invariant for the flow  $\bar{f}$ . The stable and unstable manifolds are unique, but the center manifold need not be. If  $\bar{f}$  is  $C^\infty$ , then there exists a  $C^r$  center manifold for any  $r < \infty$  [31].

Thus, the notion of invariance extends to the global manifolds associated with an equilibrium point. Any trajectory which is initially on an invariant manifold must remain on that manifold for all past and future times. Because the manifolds are invariant, no trajectory can ever cross such structures in the six-dimensional state space [33].

Consider a linearization relative to a collinear libration point. Evaluating the matrix  $A$  from equation (3.2), three eigenvalue pairs emerge. A pair of real roots,  $\pm\rho$ , indicates that the collinear points are nonstable saddle points, and possess one-dimensional stable and unstable manifolds. Two pairs of imaginary roots,  $\pm i\nu$  and  $\pm i\omega$ , indicate that the center subspace is four-dimensional and oscillatory behavior exists, for the linear system, in the vicinity of the libration point. The complete set of eigenvalues and eigenvectors from the linear matrix  $A$  are of the form

$$\lambda_1 = \rho, \quad \bar{v}_1 = \begin{bmatrix} 1 & \sigma & 0 & \rho & \rho\sigma & 0 \end{bmatrix}^T, \quad (3.15)$$

$$\lambda_2 = -\rho, \quad \bar{v}_2 = \begin{bmatrix} 1 & -\sigma & 0 & -\rho & \rho\sigma & 0 \end{bmatrix}^T, \quad (3.16)$$

$$\lambda_4 = i\nu, \quad \bar{v}_4 = \begin{bmatrix} 1 & i\tau & 0 & i\nu & -\nu\tau & 0 \end{bmatrix}^T, \quad (3.17)$$

$$\lambda_5 = -i\nu, \quad \bar{v}_5 = \begin{bmatrix} 1 & -i\tau & 0 & -i\nu & -\nu\tau & 0 \end{bmatrix}^T, \quad (3.18)$$

$$\lambda_3 = i\omega, \quad \bar{v}_3 = \begin{bmatrix} 0 & 0 & 1 & 0 & 0 & i\omega \end{bmatrix}^T, \quad (3.19)$$

$$\lambda_6 = -i\omega, \quad \bar{v}_6 = \begin{bmatrix} 0 & 0 & 1 & 0 & 0 & -i\omega \end{bmatrix}^T, \quad (3.20)$$

where

$$\sigma = 2\rho / (\Omega_{yy0} - \rho^2) = (\rho^2 - \Omega_{xx0}) / 2\rho < 0, \quad (3.21)$$

$$\tau = 2\nu / (\Omega_{yy0} + \nu^2) = (\Omega_{xx0} + \nu^2) / 2\nu > 0. \quad (3.22)$$

Details on the derivation of these quantities appear in Appendix C.1.

### 3.3 Local Invariant Manifolds

The eigenvalues corresponding to the constant matrix  $A$ , as evaluated at the collinear libration points, indicate that these points possess a topological structure of the type saddle  $\times$  center  $\times$  center. This serves as a framework for the types of solutions that exist in the vicinity of  $L_1$ ,  $L_2$ , and  $L_3$ . Expressing the general solution as a combination of the eigenmodes from the linear system, such as in equation (3.12), unique behaviors are apparent. The first term,  $\alpha_1 e^{\rho t} \bar{v}_1$ , represents the unstable eigenmode that drives the solution,  $\delta\bar{x}(t)$  from equation (3.12), to diverge from the equilibrium solution. The second term,  $\alpha_2 e^{-\rho t} \bar{v}_2$ , represents the eigenmode yielding asymptotically stable motion. The terms  $(\alpha_4 e^{i\nu t} \bar{v}_4 + \alpha_5 e^{-i\nu t} \bar{v}_5)$  and  $(\alpha_3 e^{i\omega t} \bar{v}_3 + \alpha_6 e^{-i\omega t} \bar{v}_6)$  represent the planar and out-of-plane center eigenmodes of the solution, respectively, that produce oscillatory behavior. By proper selection of  $\alpha_i$ , it is possible to isolate specific desired behaviors. Assuming  $t_0 = 0$ , the initial conditions are represented in terms the constants  $\alpha_i$  via the expression

$$\delta\bar{x}(0) = \sum_{i=1}^n \alpha_i \bar{v}_i. \quad (3.23)$$

Define the vector of constants as  $\bar{\alpha} = [\alpha_1 \ \alpha_2 \ \alpha_3 \ \alpha_4 \ \alpha_5 \ \alpha_6]^T$ , and the matrix with columns equal to the eigenvectors of  $A$  as

$$S = \begin{bmatrix} \bar{v}_1 & \bar{v}_2 & \bar{v}_3 & \bar{v}_4 & \bar{v}_5 & \bar{v}_6 \end{bmatrix}. \quad (3.24)$$

Then, equation (3.23) can be rewritten as

$$\delta\bar{x}(0) = S\bar{\alpha}, \quad (3.25)$$

and the constants  $\alpha_i$  are determined by inverting this expression, yielding

$$\bar{\alpha} = S^{-1}\delta\bar{x}(0). \quad (3.26)$$

The initial conditions are defined explicitly as follows,

$$\alpha_1 = \frac{1}{2} \left[ \frac{\nu\tau\delta x_0 + \delta\dot{y}_0}{\rho\sigma + \nu\tau} + \frac{\tau\delta\dot{x}_0 - \nu\delta y_0}{\rho\tau - \nu\sigma} \right], \quad (3.27)$$

$$\alpha_2 = \frac{1}{2} \left[ \frac{\nu\tau\delta x_0 + \delta\dot{y}_0}{\rho\sigma + \nu\tau} - \frac{\tau\delta\dot{x}_0 - \nu\delta y_0}{\rho\tau - \nu\sigma} \right], \quad (3.28)$$

$$\alpha_3 = \frac{1}{2} [\delta z_0 - i\omega\delta\dot{z}_0], \quad (3.29)$$

$$\alpha_4 = \frac{1}{2} \left[ \frac{\rho\sigma\delta x_0 - \delta\dot{y}_0}{\rho\sigma + \nu\tau} + i\frac{\sigma\delta\dot{x}_0 - \rho\delta y_0}{\rho\tau - \nu\sigma} \right], \quad (3.30)$$

$$\alpha_5 = \frac{1}{2} \left[ \frac{\rho\sigma\delta x_0 - \delta\dot{y}_0}{\rho\sigma + \nu\tau} - i\frac{\sigma\delta\dot{x}_0 - \rho\delta y_0}{\rho\tau - \nu\sigma} \right], \quad (3.31)$$

$$\alpha_6 = \frac{1}{2} [\delta z_0 + i\omega\delta\dot{z}_0]. \quad (3.32)$$

By careful selection of the constants  $\bar{\alpha}$ , trajectories with specific behavior in the vicinity of the libration point are isolated.

### 3.3.1 Local Hyperbolic Manifold

To isolate solutions within the one-dimensional local stable or unstable manifolds associated with a collinear point, all oscillatory motion should be eliminated. For example, selecting the coefficients so that  $\alpha_2 = \alpha_3 = \alpha_4 = \alpha_5 = \alpha_6 = 0$ , the unstable, divergent behavior is isolated and the solution is of the form

$$\delta\bar{x}(t) = \alpha_1 e^{\rho t} \bar{v}_1. \quad (3.33)$$

Thus, equation (3.33) represents the local unstable manifold associated with the collinear points,

$$W_{loc}^{U-} = \alpha_1 e^{\rho t} \bar{v}_1, \quad \alpha_1 < 0, \quad (3.34)$$

$$W_{loc}^{U+} = \alpha_1 e^{\rho t} \bar{v}_1, \quad \alpha_1 > 0. \quad (3.35)$$

Likewise, by selecting  $\alpha_1 = \alpha_3 = \alpha_4 = \alpha_5 = \alpha_6 = 0$ , only stable solutions that converge to the libration point are located and the solution is written as

$$\delta\bar{x}(t) = \alpha_2 e^{-\rho t} \bar{v}_2. \quad (3.36)$$

The result in equation (3.36) represents the local stable manifold of the collinear points,

$$W_{loc}^{S-} = \alpha_2 e^{-\rho t} \bar{v}_2, \quad \alpha_2 < 0, \quad (3.37)$$

$$W_{loc}^{S+} = \alpha_2 e^{-\rho t} \bar{v}_2, \quad \alpha_2 > 0. \quad (3.38)$$

The local stable and unstable manifolds are plotted for the linear system in Figure 3.1.

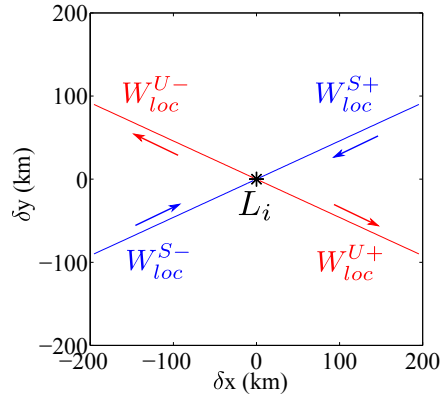


Figure 3.1. Stable and unstable manifolds asymptotic to a collinear libration point

### 3.3.2 Local Center Manifold

To isolate solutions within the four-dimensional local center manifold associated with a collinear point, all unstable and asymptotically stable motion should be eliminated. Selection of  $\alpha_1 = \alpha_2 = 0$  satisfies this requirement and yields oscillatory mo-

tion in the vicinity of  $\bar{x}_{eq}$ . The resulting trajectories are periodic and quasi-periodic orbits of the form

$$\delta\bar{x}(t) = 2\text{Real}(\alpha_4 e^{i\nu t} \bar{v}_4) + 2\text{Real}(\alpha_3 e^{i\omega t} \bar{v}_3). \quad (3.39)$$

Details of the derivation of equation (3.39) are outlined in Appendix C.2. The position states are represented as

$$\delta x(t) = \delta x_0 \cos(\nu t) + (\delta y_0/\tau) \sin(\nu t), \quad (3.40)$$

$$\delta y(t) = -\tau \delta x_0 \sin(\nu t) + \delta y_0 \cos(\nu t), \quad (3.41)$$

$$\delta z(t) = \delta z_0 \cos(\omega t) + \omega \delta \dot{z}_0 \sin(\omega t). \quad (3.42)$$

Defining the initial velocities such that  $\delta\dot{x}(0) = -\delta y(0)\frac{\nu}{\tau}$ ,  $\delta\dot{y}(0) = -\nu\tau\delta x(0)$ , the constants  $\alpha_1 = \alpha_2 = 0$  and trajectories within the local center manifold are isolated. Both periodic and quasi-periodic orbits exist within the four-dimensional center subspace associated with the collinear libration points. Note that selecting  $\alpha_3 = \alpha_6 = 0$  constrains these orbits to planar oscillations only, yielding elliptical orbits centered on the libration point, i.e., the planar Lyapunov orbits. Selecting  $\alpha_4 = \alpha_5 = 0$  yields orbits with oscillations only in the  $\hat{z}$  direction. These orbits are labeled the vertical Lyapunov orbits. The quasi-periodic orbits that emerge when both planar and vertical oscillations are introduced are denoted as Lissajous orbits. Sample planar and vertical Lyapunov orbits (black), and a Lissajous orbit (gray) appear in Figure 3.2 for the linear system.

### 3.3.3 Hyperbolic Manifolds Asymptotic to the Local Center Manifold

Similar to the stable and unstable manifolds asymptotic to the libration point, manifolds also exist that are asymptotic to the periodic and quasi-periodic orbits in the vicinity of the libration point. These manifolds are computed by perturbing an orbit within the center manifold in the stable or unstable direction. Perturbing in the

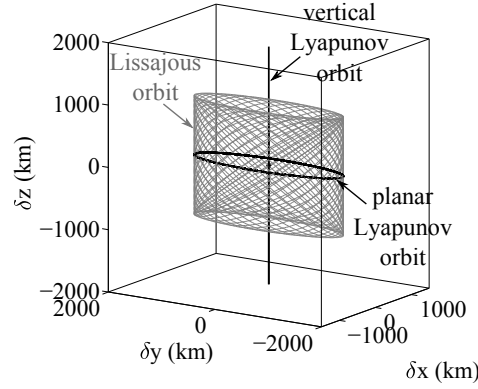


Figure 3.2. Sample periodic and quasi-periodic orbits in the vicinity of a collinear libration point

unstable direction yields the unstable manifold asymptotic to a libration point orbit in the linear system:

$$W_{LPO,loc}^{U-} = \alpha_1 e^{\rho t} \bar{v}_1 + 2\text{Real}(\alpha_4 e^{i\nu t} \bar{v}_4) + 2\text{Real}(\alpha_3 e^{i\omega t} \bar{v}_3), \quad \alpha_1 < 0, \quad (3.43)$$

$$W_{LPO,loc}^{U+} = \alpha_1 e^{\rho t} \bar{v}_1 + 2\text{Real}(\alpha_4 e^{i\nu t} \bar{v}_4) + 2\text{Real}(\alpha_3 e^{i\omega t} \bar{v}_3), \quad \alpha_1 > 0. \quad (3.44)$$

Likewise, the local stable manifolds convergent to a libration point orbit are isolated by perturbing in the stable direction:

$$W_{LPO,loc}^{S-} = \alpha_2 e^{-\rho t} \bar{v}_2 + 2\text{Real}(\alpha_4 e^{i\nu t} \bar{v}_4) + 2\text{Real}(\alpha_3 e^{i\omega t} \bar{v}_3), \quad \alpha_2 < 0, \quad (3.45)$$

$$W_{LPO,loc}^{S+} = \alpha_2 e^{-\rho t} \bar{v}_2 + 2\text{Real}(\alpha_4 e^{i\nu t} \bar{v}_4) + 2\text{Real}(\alpha_3 e^{i\omega t} \bar{v}_3), \quad \alpha_2 > 0. \quad (3.46)$$

To locate manifolds such that the value of Jacobi constant associated with the orbit is preserved,  $\alpha_1$  and  $\alpha_2$  should be selected to be small. A sample unstable manifold associated with a Lissajous orbit appears in red in Figure 3.3. In negative time, this manifold approaches the quasi-periodic orbit as demonstrated by the black arc.

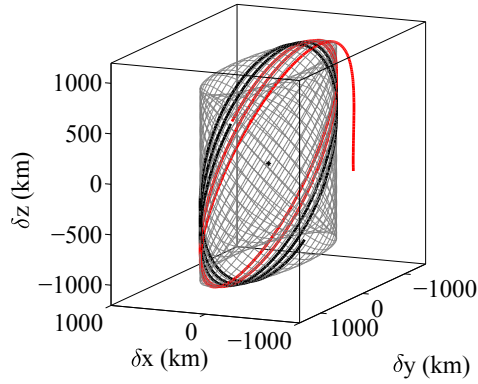


Figure 3.3. Sample unstable manifold (red) departing a Lissajous orbit

### 3.4 Global Invariant Manifolds

To study the evolution of the invariant manifolds in the *nonlinear* system as they depart the vicinity of  $\bar{x}_{eq}$ , it is necessary to compute the global invariant manifolds from the local manifold approximations.

#### 3.4.1 Global Hyperbolic Manifold

In Section 3.3.1, the local unstable and stable invariant manifolds asymptotic to a collinear libration point are computed by perturbing the state associated with the libration point in the direction of the unstable and stable eigendirections. The resulting trajectories in the *linear* variational model are summarized in equations (3.33) and (3.36). Recall from equations (3.15)–(3.20) that  $\lambda_1 = \rho > 0$  and  $\lambda_2 = -\rho$  are the stable and unstable eigenvalues of the constant linear state matrix,  $A$ , and  $\bar{v}_1$  and  $\bar{v}_2$  are their associated eigenvectors, computed by solving the equations  $A\bar{v}_1 = \lambda_1\bar{v}_1$ ,  $A\bar{v}_2 = \lambda_2\bar{v}_2$ . Define  $\bar{v}^+$  as possessing a positive  $\hat{x}$  component, and  $\bar{v}^-$  as possessing a negative  $\hat{x}$  component. Based on the Stable Manifold Theorem 3.2.1 and consistent with equations (3.34), (3.37), the local half-manifolds,  $W_{loc}^{U-}$  and  $W_{loc}^{S-}$ , are approximated by introducing a perturbation relative to the equilibrium point,  $\bar{x}_{eq}$ , in the

direction of the unstable and stable eigenvector directions,  $\bar{v}_U^- = -\bar{v}_1$  and  $\bar{v}_S^- = -\bar{v}_2$ , respectively. Likewise, a perturbation relative to  $\bar{x}_{eq}$  in the direction of the unstable and stable eigenvector directions,  $\bar{v}_U^+ = \bar{v}_1$  and  $\bar{v}_S^+ = \bar{v}_2$ , respectively, produces the local half-manifolds  $W_{loc}^{U+}$  and  $W_{loc}^{S+}$ , consistent with equations (3.35), (3.38). The initial states from equations (3.34)–(3.35) and (3.37)–(3.38) represent perturbations relative to the equilibrium point in the direction of the unstable and stable eigenvectors. Alternatively, the following procedure is employed to compute these initial perturbations. Define the stable eigenvector as  $\bar{v}_S^+ = [x_S \ y_S \ z_S \ \dot{x}_S \ \dot{y}_S \ \dot{z}_S]^T$ , where  $x_S > 0$  and  $\bar{v}_S^+$  is of unit length. Note that, from equation (3.16),  $z_S = \dot{z}_S = 0$ . The magnitude of the eigenvector is adjusted such that

$$\bar{w}_{S,eq}^+ = \bar{v}_S^+ / \sqrt{x_S^2 + y_S^2 + z_S^2}. \quad (3.47)$$

The position components of the eigenvector  $\bar{w}_{S,eq}^+$  are now of unit length. Then, the step along the direction of the eigenvector is computed as

$$\bar{x}_{eq}^{S+} = \bar{x}_{eq} + d \cdot \bar{w}_{S,eq}^+, \quad (3.48)$$

$$\bar{x}_{eq}^{S-} = \bar{x}_{eq} - d \cdot \bar{w}_{S,eq}^+, \quad (3.49)$$

where  $d$  may be interpreted as a distance away from the equilibrium point. Likewise, the unstable eigenvector is defined as  $\bar{v}_U^+ = [x_U \ y_U \ z_U \ \dot{x}_U \ \dot{y}_U \ \dot{z}_U]^T$ , where  $x_U > 0$  and  $\bar{v}_U^+$  is of unit length. Then, the eigenvector employed to compute the unstable manifold direction is

$$\bar{w}_{U,eq}^+ = \bar{v}_U^+ / \sqrt{x_U^2 + y_U^2 + z_U^2}, \quad (3.50)$$

and the step along the direction of the eigenvector is defined as

$$\bar{x}_{eq}^{U+} = \bar{x}_{eq} + d \cdot \bar{w}_{U,eq}^+, \quad (3.51)$$

$$\bar{x}_{eq}^{U-} = \bar{x}_{eq} - d \cdot \bar{w}_{U,eq}^+. \quad (3.52)$$

The result is an approximation for the local manifolds,  $W_{eq,loc}^{S+}$ ,  $W_{eq,loc}^{S-}$ , and  $W_{eq,loc}^{U+}$ ,  $W_{eq,loc}^{U-}$ , associated with the equilibrium point. The value of  $d$  is critical because it

determines the accuracy with which the local manifolds are approximated. If  $d$  is too large, the perturbation is not a close approximation to a state that actually exists along the manifold. If  $d$  is too small, long integration times are required to compute the global manifold, due to the asymptotic nature of the manifolds, leading to the accumulation of numerical error. The local manifolds are globalized by propagating the states  $\bar{x}_{eq}^{S+}$  and  $\bar{x}_{eq}^{S-}$  in the nonlinear model. This process yields the numerical approximation for the global manifolds  $W_{eq}^{S+}$  and  $W_{eq}^{S-}$ , respectively, where  $i = 1, 2$ , or 3. The same procedure is employed to approximate the unstable global manifolds,  $W_{eq}^{U+}$  and  $W_{eq}^{U-}$ . As an example, the global stable and unstable manifolds corresponding to the  $L_1$  equilibrium point appear in Figure 3.4.1 in blue and red, respectively, for the Earth-Moon system. The thick blue and red arrows in Figure 3.4(b) represent the local manifolds, and are aligned with the stable and unstable eigenvector directions,  $\bar{v}_S^-$ ,  $\bar{v}_S^+$  and  $\bar{v}_U^-$ ,  $\bar{v}_U^+$ . The zoomed view near the libration point in Figure 3.4(b) demonstrates that the global and local manifolds are initially equivalent. As the manifolds are propagated in the nonlinear problem, the global manifolds depart from the approximation supplied by the local manifolds.

### 3.4.2 Global Center Manifold

The existence of both periodic and quasi-periodic libration point orbits is demonstrated for the linear system in Section 3.3.2. These solutions persist in the nonlinear model, and additional families of orbits are located via bifurcations from known families.

#### Periodic Lyapunov Orbits

From a linear analysis, the existence of both planar and vertical Lyapunov orbits is demonstrated. Using an orbit from the linear system as an initial guess, a periodic orbit is converged in the nonlinear model using a differential corrections or targeting

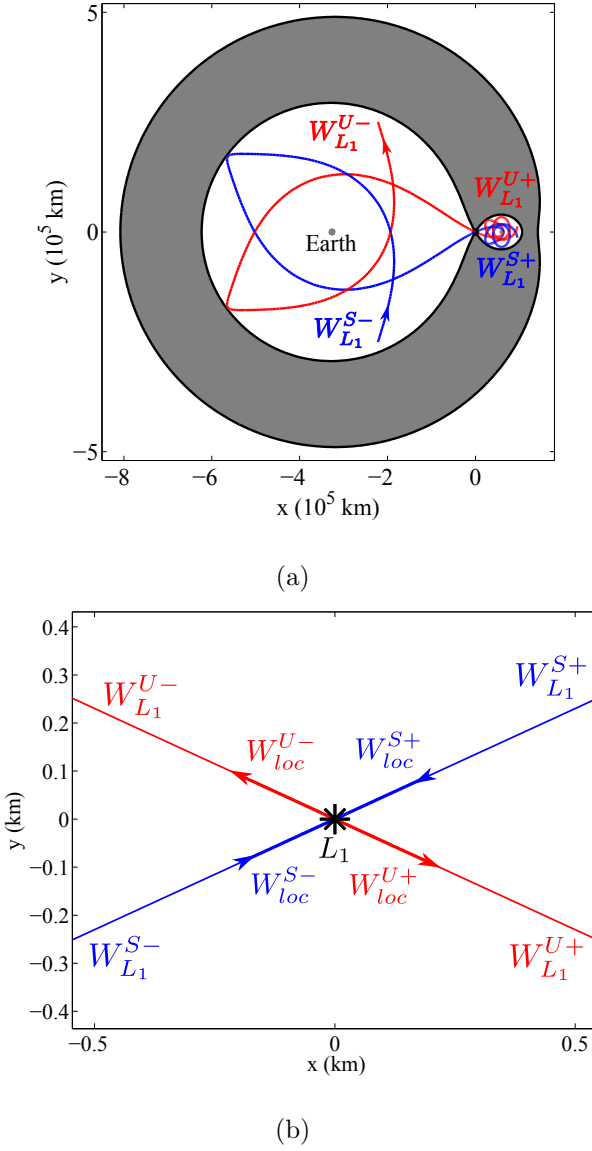


Figure 3.4. Global stable and unstable manifolds associated with the  $L_1$  point in the Earth-Moon system ( $L_1$ -centered view)

algorithm. From the converged solution in the nonlinear model, families of the planar and vertical Lyapunov orbits are computed via numerical continuation methods [34]. Thus, solutions within the global center manifold associated with a libration point are located. Sample members from the families of planar and vertical Lyapunov

orbits appear for the Earth-Moon system in Figures 3.5 and 3.6. The orbits within the families are colored according to the associated value of Jacobi constant so that red→blue corresponds to higher→lower values of Jacobi constant. Note that the color mapping is not the same among the different families.

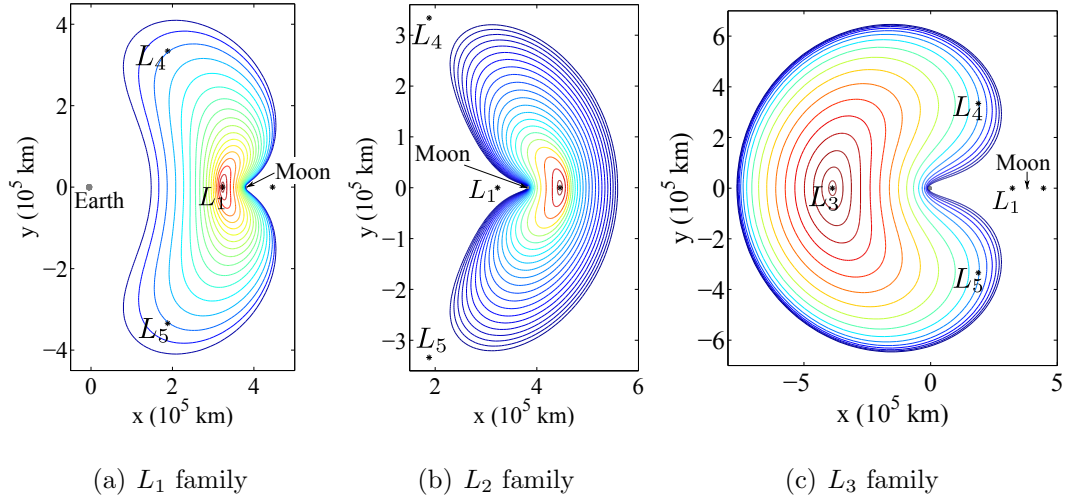


Figure 3.5. Sample members from the families of Lyapunov orbits in the Earth-Moon system

### Stability of Periodic Orbits and the Monodromy Matrix

In addition to the families of Lyapunov orbits, the families of halo and axial orbits also exist in the nonlinear model. These families bifurcate from the families of Lyapunov orbits, that is, the originating member of the halo family is also a member from the planar Lyapunov family. Two ‘originating’ members of the axial family also exist and emerge as members of the planar and vertical Lyapunov families. To compute bifurcations within the Lyapunov families, the stability of the orbits within these families is assessed.

Recall the linear system defined in equation (3.2), i.e.,  $\delta\dot{\bar{x}} = A(t)\delta\bar{x}$ , where  $\delta\bar{x} = \bar{x} - \bar{x}_r$ , and  $\bar{x}_r$  is some reference solution,  $A(t) = D\bar{f}(\bar{x}_r)$  and  $\bar{f}$  is defined by equation

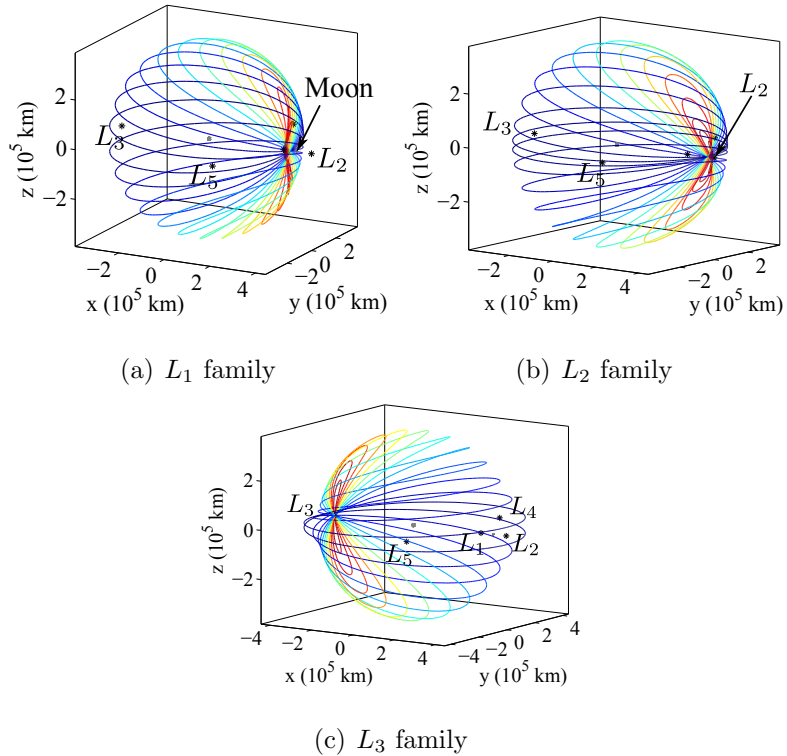


Figure 3.6. Sample members from the families of vertical orbits in the Earth-Moon system

(2.25) for the CR3BP. The general solution to equation (3.2) is of the form  $\delta\bar{x}(t) = e^{A(t-t_0)}\delta\bar{x}(t_0)$ , and the state transition matrix (STM),  $\Phi(t, t_0) \equiv e^{A(t-t_0)}$ , is defined as in equation (3.4). Associated with the STM are the following identities:

$$\Phi(t_0, t_0) = I, \quad (3.53)$$

$$\Phi(t_2, t_0) = \Phi(t_2, t_1)\Phi(t_1, t_0), \quad (3.54)$$

$$\Phi(t_0, t_1) = \Phi(t_1, t_0)^{-1}. \quad (3.55)$$

Selecting  $\bar{x}_r = \bar{x}^*$  to be some state along a periodic orbit and defining  $T = t - t_0$  as the period of that orbit, then, a stroboscopic mapping  $P_T : \delta\bar{x}(kT) \rightarrow \delta\bar{x}((k+1)T)$  is defined that maps the state  $\delta\bar{x}(kT) = \delta\bar{x}_k$  to  $\delta\bar{x}((k+1)T) = \delta\bar{x}_{k+1}$ , where  $k = 0, 1, \dots$  represents subsequent intersections of the map  $P_T$ . From this mapping,  $\bar{x}^*$  appears

as a single fixed point at the origin  $\delta\bar{x} = \bar{0}$ , that is,  $\bar{x}^*(kT) = \bar{x}^*(0)$  on the map  $P_T$ . The map is linearized relative to  $\bar{x}^*$  as

$$\delta\bar{x}_{k+1} = \Phi(T, 0)\delta\bar{x}_k. \quad (3.56)$$

Equation (3.56) is a discrete time representation of the evolution of solutions nearby  $\bar{x}^*$ , and the matrix  $\Phi(T, 0)$  is defined as the *monodromy matrix* associated with the fixed point. For initial conditions originating near  $\bar{x}^*$  on  $P_T$ , the linear map in equation (3.56) describes the behavior of subsequent intersections of  $P_T$  relative to the fixed point. Assuming that  $\Phi(T, 0)$  is not defective, the evolution of  $\delta\bar{x}$  is described as

$$\delta\bar{x}_k = \Phi(kT, 0)\delta\bar{x}_0, \quad (3.57)$$

where, by equation (3.54),  $\Phi(kT, 0) = \Phi(T, 0)^k$ . The eigenvalues,  $\lambda_i$ , of  $\Phi(T, 0)$  are the characteristic multipliers associated with the fixed point, and  $\bar{v}_i$  are the associated eigenvectors. Then, the general solution representing subsequent intersections of the map is

$$\delta\bar{x}_k = \sum_{i=1}^n c_i \lambda_i^k \bar{v}_i. \quad (3.58)$$

It is clear from this equation that the characteristic multipliers,  $\lambda_i$ , govern the behavior of  $\delta\bar{x}_k$  with time.

The eigenvalue structure of the monodromy matrix can be predicted by Lyapunov's theorem.

**Theorem 3.4.1 (Lyapunov's Theorem)** *If  $\lambda$  is an eigenvalue of the monodromy matrix,  $\Phi(t_0 + T, t_0)$ , of a time-invariant system, then  $\lambda^{-1}$  is also an eigenvalue. The spectrum of the monodromy matrix of a real time-invariant system is symmetric with respect to both the unit circle and the real axis [35].*

The monodromy matrix associated with a periodic orbit, then, possesses characteristic multipliers that occur in reciprocal pairs. For a complex number with magnitude equal to unity, the reciprocal is equal to the complex conjugate. The eigenvectors,

$\bar{v}_i$ , associated with  $\lambda_i$  are linearly independent and span  $\mathbb{R}^n$ . The space is, therefore, defined by the union of three invariant subspaces,  $E_S$ ,  $E_U$ , and  $E_C$ . Let  $n_S$  be the number of characteristic multipliers with real parts of magnitude  $> 1$ ,  $n_U$  be the number with real parts of magnitude  $< 1$ , and  $n_C$  be the number for which  $|\lambda| = 1$ , so that  $n = n_S + n_U + n_C = \text{rank}(\Phi(T, 0))$ . Then, the dimensions of the invariant subspaces  $E_S$ ,  $E_U$ , and  $E_C$  are  $n_S$ ,  $n_U$ , and  $n_C$ , respectively. In the CR3BP, the monodromy matrix is a real matrix that possesses three pairs of eigenvalues. The monodromy matrix associated with any periodic solution possesses at least one unit eigenvalue. Consequently, for Hamiltonian systems, the monodromy matrix associated with a periodic solution possesses at least one pair of eigenvalues equal to unity, and the associated eigenvectors are tangent to the periodic solution at the fixed point [36]. That is, for an initial state  $\bar{x}(0)$  along the periodic orbit, the eigenvectors corresponding to the unit eigenvalues are in the direction  $\dot{\bar{x}}(0)$ . Thus, for periodic solutions that exist within the context of the CR3BP,  $n_C \geq 2$  is always true.

The general solution for the discrete time system evolves with the term  $\lambda_i^k$ , as is apparent in equation (3.58). For  $\lambda_i = 1$ ,  $\lambda_i^k$  remains equal to unity and the general solution neither grows nor decays with time relative to the fixed point. Stability and boundedness for the discrete system are, therefore, determined by comparing the magnitude of the eigenvalues to one. If all eigenvalues possess a magnitude less than one, then, as time progresses, each term  $\lambda_i^k$  approaches zero, and subsequent intersections of  $P_T$  approach the fixed point,  $\delta\bar{x} = 0$ . The fixed point is, then, defined as asymptotically stable. Note that a fixed point along a periodic orbit in the CR3BP cannot be asymptotically stable, as the eigenvalues of the monodromy matrix occur in reciprocal pairs. If any one of the eigenvalues possesses magnitude greater than one, then  $\delta\bar{x}$  grows over subsequent iterations of the map and the fixed point is unstable. If  $\Phi(T, 0)$  possesses eigenvalues,  $\lambda_i, \lambda_j$ , such that  $|\lambda_i| < 1$  and  $|\lambda_j| > 1$ , then the fixed point is nonstable and is identified as a saddle point. The fixed point is considered neutrally stable when  $|\lambda| \leq 1$  for all eigenvalues, but at least one eigenvalue has

magnitude equal to one and is nondefective. In this case, subsequent intersections of the map are bounded with respect to  $\bar{x}^*$ , but will not naturally return to the fixed point. Because  $\bar{x}^*$  fully represents the periodic orbit, the stability of the fixed point determines the stability of the periodic solution [37].

A fixed point is said to be hyperbolic if all characteristic multipliers possess magnitude greater than one, except for the pair of unit eigenvalues, that is,  $n_C = 2$ . Then, the following theorem defines the stable and unstable manifolds associated with hyperbolic fixed points:

**Theorem 3.4.2 (The Stable Manifold Theorem for Periodic Orbits)** *Consider the  $n$ -dimensional autonomous system of equations (2.24), where  $\bar{f} \in C^1(E)$  and  $E$  is an open subset of  $\mathbb{R}^n$  containing a periodic orbit,  $\gamma^*$  of period  $T$ . Let  $\phi_t$  be the flow of the system, and  $\gamma^*(t) = \phi_t(\bar{x}^*)$ . Suppose  $m$ ,  $0 \leq m \leq n - 1$ , of the characteristic multipliers of  $\gamma^*$  have magnitude  $< 1$ , and  $n - m - 1$  have magnitude  $> 1$ . Then, the stable manifold of  $\gamma^*(t)$ , denoted as  $W_{\gamma^*}^S$ , is defined as the set of all points,  $\bar{x}^S$ , such that  $P_T^k(\bar{x}^S)$  approaches  $\gamma^*$  as  $k \rightarrow \infty$ . The stable manifold is of dimension  $(m + 1)$ , is differentiable, and is positively invariant under the flow  $\phi_t$ . The unstable manifold of  $\gamma^*(t)$ , denoted as  $W_{\gamma^*}^U$ , is defined as the set of all points,  $\bar{x}^U$ , such that  $P_T^k(\bar{x}^U)$  approaches  $\gamma^*$  as  $k \rightarrow -\infty$ . The unstable manifold is of dimension  $(n - m)$ , is differentiable, and is negatively invariant under the flow  $\phi_t$  [32, 37].*

For nonhyperbolic fixed points,  $n_C \geq 4$  and a nontrivial center manifold exists.

**Theorem 3.4.3 (The Center Manifold Theorem for Periodic Orbits)** *Consider the  $n$ -dimensional autonomous system of equations (2.24), where  $\bar{f} \in C^r(E)$  with  $r \geq 1$  and  $E$  is an open subset of  $\mathbb{R}^n$  containing a periodic orbit,  $\gamma^*$  of period  $T$ . Let  $\phi_t$  be the flow of the system, and  $\gamma^*(t) = \phi_t(\bar{x}^*)$ . If  $m$  of the characteristic multipliers of  $\gamma^*$  have magnitude  $< 1$ ,  $\ell$  have magnitude  $> 1$ , and  $n - m - \ell$  have unit magnitude, then there exists an  $m$ -dimensional center manifold,  $W_{\gamma^*}^C$ , of  $\gamma^*$  of class*

$C^r$  which is invariant under the flow  $\phi_t$ , and is tangent to the center subspace,  $E^C$ , of  $\gamma^*$  at  $\bar{x}^*$  [32].

For stable periodic orbits in the CR3BP,  $n_C = 6$  and stable and unstable manifolds associated with the periodic solution do not exist. For unstable periodic orbits, at least one reciprocal pair of real eigenvalues exists and the stable and unstable manifolds associated with the fixed point are defined using the same techniques as those applied for equilibrium points in Section 3.2. Because a periodic solution can be defined by an infinite number of fixed points along the orbit, an infinite number of stable and unstable manifolds are associated with an unstable periodic orbit.

### Periodic Halo and Axial Orbits

Stepping along the families of Lyapunov orbits in Figures 3.5 and 3.6, parameters such as the orbital period or Jacobi constant value evolve continuously. Orbital stability also evolves along a family and stability changes may occur. The location at which a stability change occurs within a family of periodic orbits is identified as a *bifurcation point*. Different types of stability changes are possible, and the type of stability change determines any qualitative changes that occur as a result of the bifurcation [38]. By tracking changes in stability along a particular family of planar Lyapunov orbits, bifurcations to other distinct orbit families may be located. For the planar and vertical families of Lyapunov orbits, plots depicting the stability of individual orbits within each family appear in Figure 3.7.

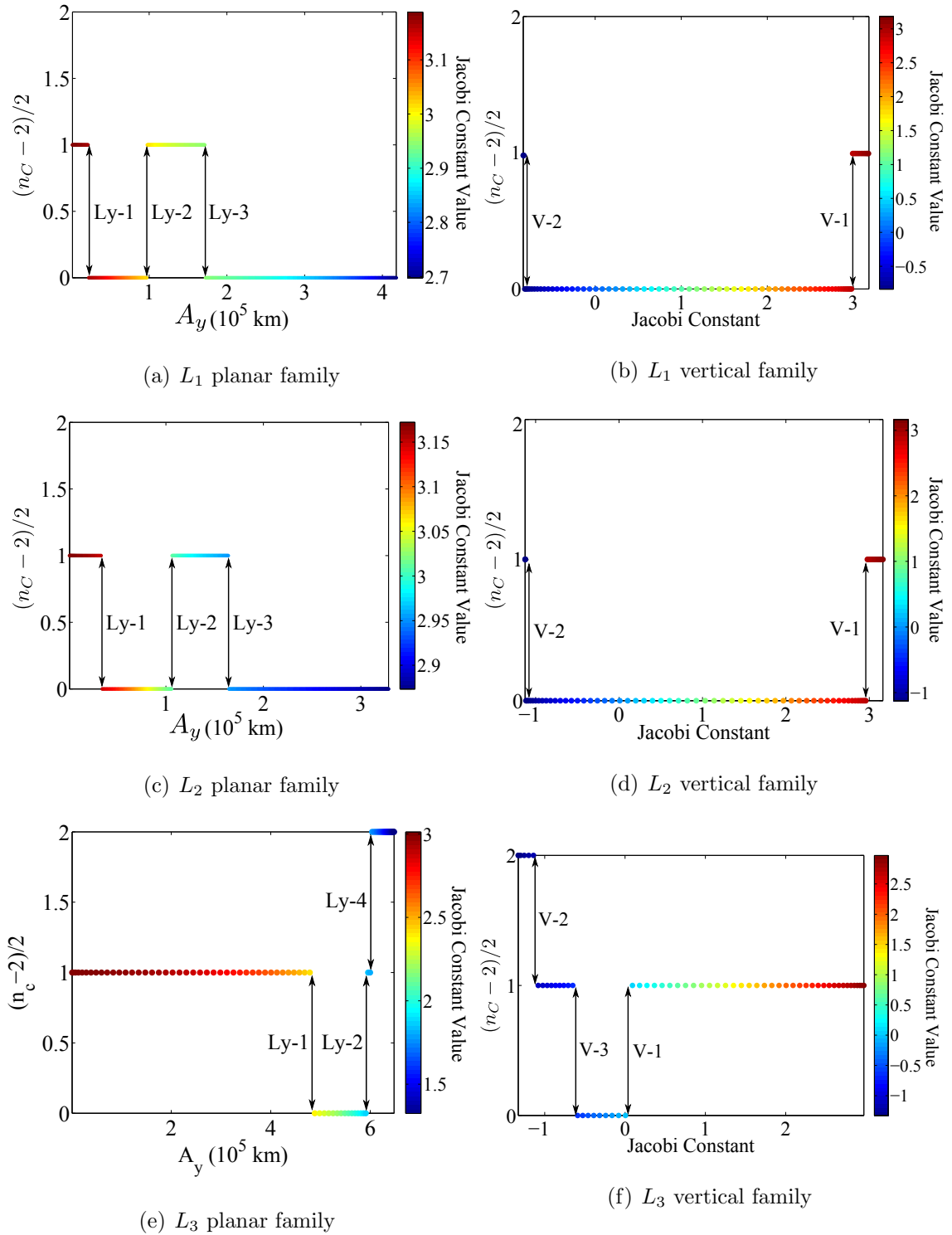


Figure 3.7. Stability information for Lyapunov orbits in the Earth-Moon system

For each representative orbit from Figures 3.5 and 3.6, the number of eigenvalue pairs for which  $|\lambda| = 1/|\lambda| = 1$  is recorded, not including the trivial pair of unit eigenvalues that exist for any periodic orbit. When  $(n_C - 2)/2 = 0$ , the orbit is unstable with stable and unstable manifolds of dimension  $n_S = n_U = 2$  and there exists no center manifold except for that associated with the pair of unit eigenvalues. If  $(n_C - 2)/2 = 1$ , the orbit possesses stable and unstable manifolds of dimension  $n_S = n_U = 1$ , and a nontrivial center manifold of dimension  $n_C - 2 = 2$ . Orbits corresponding to  $(n_C - 2)/2 = 2$  are stable and possess no stable or unstable manifolds. These orbits are associated with a center manifold of dimension  $n_C - 2 = 4$ . Examining the stability of the planar Lyapunov families, the first bifurcations, labeled Ly-1, yield out-of-plane families of orbits labeled halo orbits. Thus, the originating member of a halo family is also a member emerging from the planar Lyapunov family and is the bifurcating orbit linking the two families. The second bifurcation in the planar Lyapunov families, labeled Ly-2, leads to the axial orbits. The  $L_1$  and  $L_2$  planar Lyapunov families possess a third bifurcation, Ly-3, which corresponds to a period-doubling bifurcation. The third bifurcation in the  $L_3$  planar Lyapunov family, Ly-4, links this family to families of planar orbits that originate from the equilateral points,  $L_4$  and  $L_5$  [34]. Examination of the stability plots for the vertical families, several additional bifurcations are apparent. The first bifurcation in each family is labeled V-1, and corresponds to a bifurcation to the respective axial families. Thus, two distinct ‘originating’ members of each axial family exist and are also members from the planar and vertical Lyapunov families. In the  $L_1$  and  $L_2$  vertical families, the second bifurcation, labeled V-2, corresponds to a period-halving bifurcation [39]. The  $L_3$  family also experiences this bifurcation as its third bifurcation. The second bifurcation V-3 in the  $L_3$  vertical family connects this family to the  $L_4$  and  $L_5$  families of vertical orbits [34].

Sample orbits from northern halo families are plotted for the Earth-Moon system in Figure 3.8. Southern families also exist and are computed by reflecting the northern

families across the  $x$ - $y$  plane. Portions of the axial families appear in Figure 3.9. Only those orbits for which  $z > 0$  at the maximal value of  $y$  are plotted and are termed the ‘northern’ axial orbits in this investigation. The southern families are computed by reflecting these members across the  $x$ - $y$  plane. Again, the individual orbits within the families in Figures 3.8–3.9 are colored consistent with the associated value of Jacobi constant, however, the color mapping is not the same among the different families. Other families of libration point orbits exist in the nonlinear system, e.g., period multiplying families of halo orbits [40], but are not employed in this investigation.

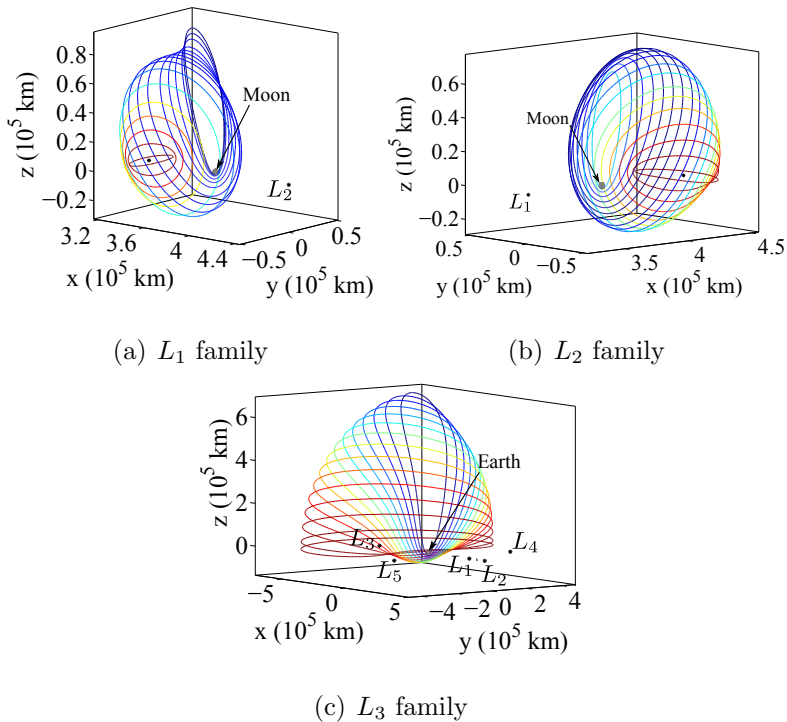


Figure 3.8. Sample members from the families of halo orbits in the Earth-Moon system

Plots representing the stability of the halo and axial families of orbits appear in Figure 3.10. For the halo families, the number of complex eigenvalue pairs is represented as a function of orbit amplitude ratio  $A_z/A_y$ . At the points H-1, H-2 and H-4, the  $L_1$  and  $L_2$  families experience period doubling bifurcations. The

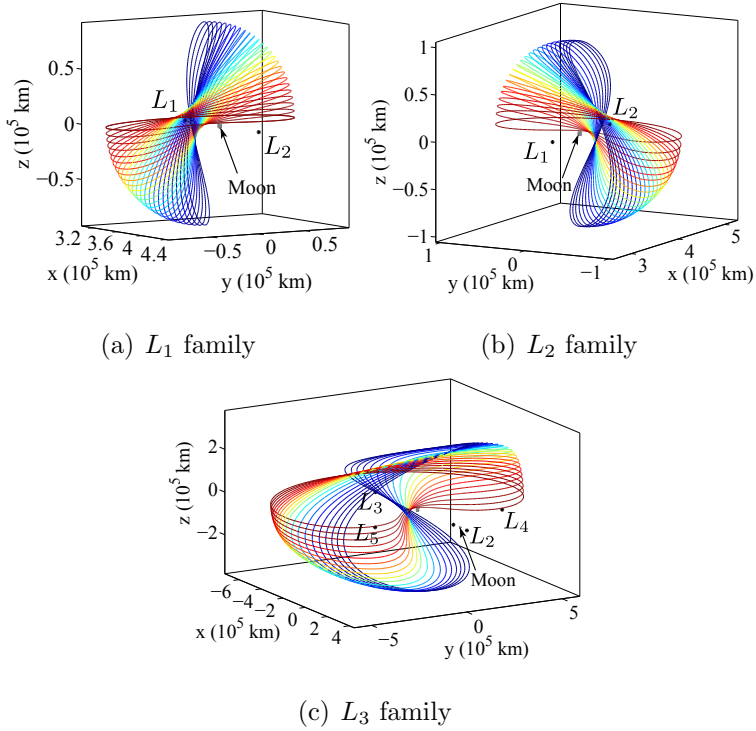


Figure 3.9. Sample members from the families of axial orbits in the Earth-Moon system

bifurcations labeled H-3 and H-3 represent a stability change in the family, however, these bifurcations do not lead to any new orbit families [40]. The  $L_2$  halo family undergoes a period-doubling bifurcation, H-6, that yields the family of  $L_2$  butterfly orbits [34]. Only those orbits with perilune above the surface of the Moon are included in the plots, thus, a bifurcation from the  $L_1$  family of halo orbits to the  $L_4$  and  $L_5$  families of axials orbits does not appear in the  $L_1$  halo stability chart [34]. The stability of the axial orbits is plotted as a function of amplitude  $A_z$ . Clearly, the axial orbits are hyperbolic for all families, that is,  $n_C = 2$  for each of these orbits.

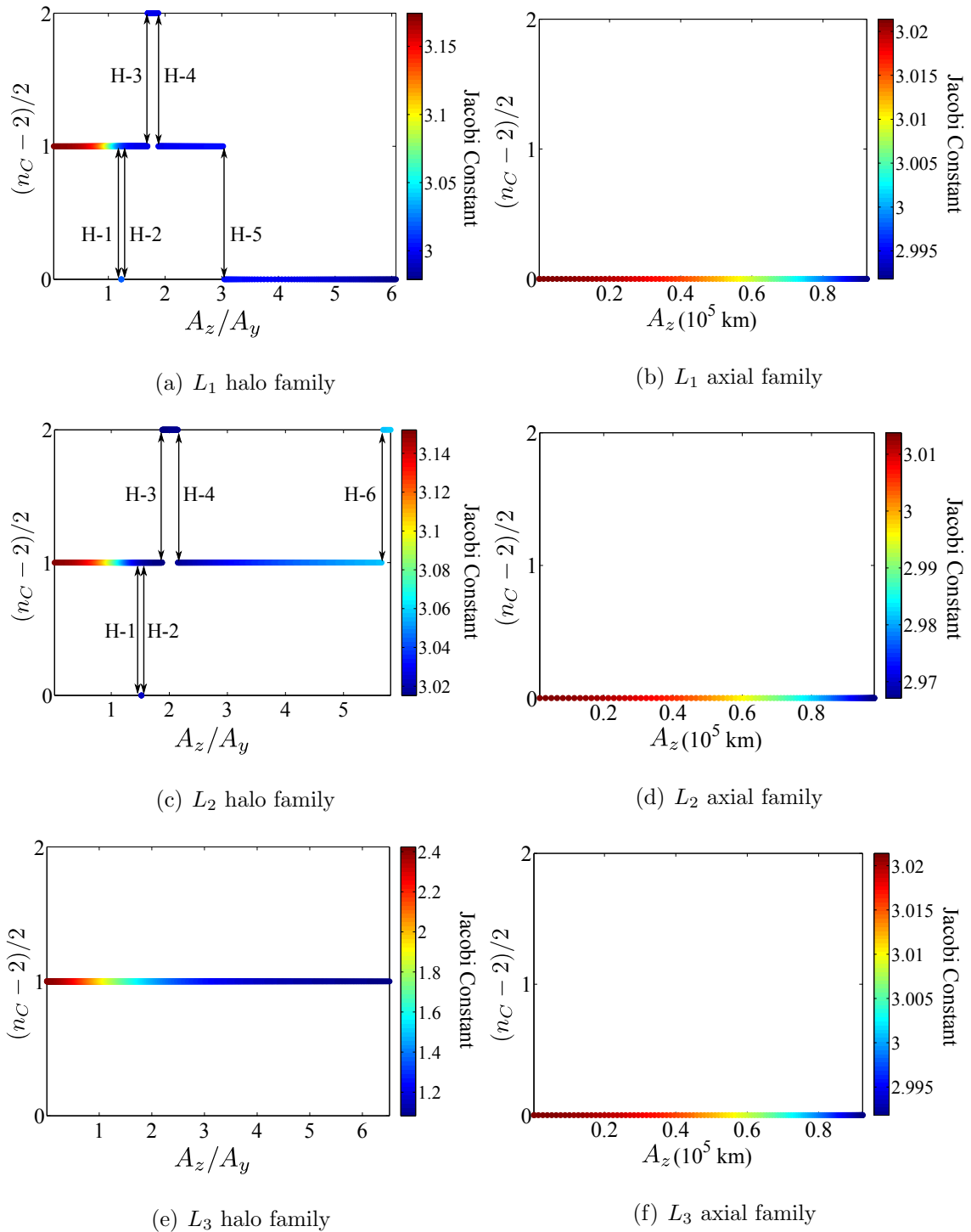


Figure 3.10. Stability information for halo and axial orbits in the Earth-Moon system

## Quasi-Periodic Orbits

Quasi-periodic orbits are solutions that exist within the center manifold of a nearby periodic orbit. These orbits are bounded, and close only as  $t \rightarrow \infty$ , that is, they are periodic solutions with an infinite period. The path traced by a quasi-periodic orbit lies on the surface of an invariant torus of dimension two or greater. Thus, a quasi-periodic orbit is defined by two or more frequencies, in contrast to the single frequency associated with a periodic orbit. Quasi-periodic orbits have been computed previously by various researchers [41–43]. In this investigation, the tori are computed directly via the methodology demonstrated by Olikara and Scheeres [44]. Note that a similar strategy is demonstrated by Castellá and Jorba [41] and employed by Gómez and Mondelo [24].

The path traced by a quasi-periodic orbit lies on the surface of an invariant torus of dimension two or greater. Thus, a quasi-periodic orbit is defined by two or more frequencies, in contrast to the single frequency associated with a periodic orbit. Assume that the function  $\bar{\psi}(\theta_0, \theta_1)$  describes a two-dimensional torus on which a quasi-periodic orbit lies with associated frequencies  $\omega_0 = \dot{\theta}_0$ ,  $\omega_1 = \dot{\theta}_1$ . Then, the dimension may be reduced to one by selecting an initial value of  $\theta_0$  so that an invariant circle,  $\bar{u}(\theta_1)$ , along the torus is defined. Integrating some initial state  $\bar{u}(\theta_1 = \theta_{1,0})$  along this circle for time  $T_q = \frac{2\pi}{\omega_0}$  yields the final state on the circle  $\bar{u}(\theta_{1,0} + \rho_q)$ , where  $\rho_q = \omega_1 \cdot T_q$ . A map,  $G$ , is defined based on the frequencies  $\omega_0$ ,  $\omega_1$  so that propagating discretized states along  $\bar{u}(\theta_1)$  for time  $T_q$  and removing the rotation by the angle  $\rho_q$  yields  $G(\bar{u}) = \bar{u}$ . To compute a torus, a differential corrections algorithm is employed to determine the values for  $T_q$ ,  $\rho_q$ , and the discretized states along  $\bar{u}(\theta_1)$  that satisfy  $G(\bar{u}) - \bar{u} = \bar{0}$ , while applying an additional constraint on the value of Jacobi constant. Once a torus is constructed, pseudo-arc length continuation is employed to locate additional tori in the family, assuming that additional phase constraints on  $\theta_0$  and  $\theta_1$  are incorporated. Gaps in a family of tori may occur due to resonance in the torus frequencies.

Pseudo-arclength continuation is successful to generate the complete family of tori as long as these resonance gaps are not too large. Given a periodic orbit, a family of tori is initialized by employing the associated stability information to locate a linear approximation for a nearby invariant circle. Let  $\lambda_C = e^{i\rho}$  be a complex eigenvalue and  $\bar{v}_C$  a corresponding eigenvector associated with the monodromy matrix computed from a fixed point  $\bar{x}^*$  along the periodic orbit. Then, the initial guess for an invariant curve centered on  $\bar{x}^*$  is of the form  $\bar{u}(\theta_1) = k \cdot (\cos(\theta_1)\text{Re}(\bar{v}_C) - \sin(\theta_1)\text{Im}(\bar{v}_C))$ , where  $k$  is a small value used to scale the circle. The period  $T$  and the argument  $\rho$  of the complex eigenvalue associated with the central periodic orbit serve as an initial guess for the values of  $T_q$  and  $\rho_q$  associated with a nearby torus. A truncated Fourier series is used to represent the invariant curve, and a Newton-Raphson method is employed to compute  $T_q$ ,  $\rho_q$ , and the discretized states along  $\bar{u}(\theta_1)$  that satisfy the constraints. Further details on the computation of tori are available in Olikara and Scheeres [44].

For periodic orbits with a nontrivial center manifold of dimension  $(n_C - 2)/2 \geq 1$ , quasi-periodic orbits associated with the central periodic orbit may be computed. For example, the halo orbits that exist before the bifurcations H-1 in the  $L_1$  and  $L_2$  halo families correspond to  $n_C = 4$ . Thus, in the vicinity of each these orbits there exists a family of quasi-periodic solutions called *quasi-halo* orbits. These solutions correspond to two-dimensional tori that do not self-intersect in the phase space but may appear to be self-intersecting when projected into configuration space. Selecting the  $L_1$  halo orbit corresponding to  $C = 3.15$ , sample members from the family of quasi-halo tori, each also corresponding to the Jacobi constant value  $C = 3.15$ , are computed and appear in Figure 3.11 as gray surfaces. Similarly, the vertical orbits that exist before the bifurcations V-1 in the families of  $L_1$ ,  $L_2$  and  $L_3$  vertical orbits correspond to  $n_C = 4$ . Thus, there exist families of quasi-periodic solutions, commonly denoted the *Lissajous* orbits, in the vicinity of the vertical orbits. These Lissajous orbits cover two-dimensional tori. Sample tori corresponding to the  $L_2$  vertical orbit that exists for  $C = 3.15$  appear in Figure 3.12.

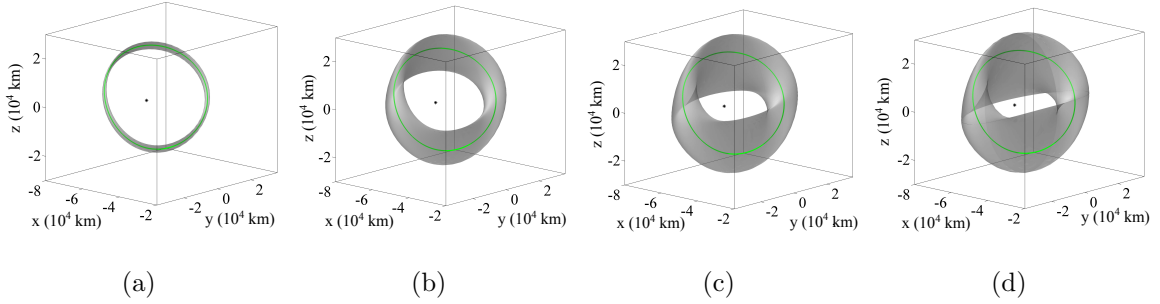


Figure 3.11. Quasi-periodic tori associated with an  $L_1$  halo orbit in the Earth-Moon system for  $C = 3.15$

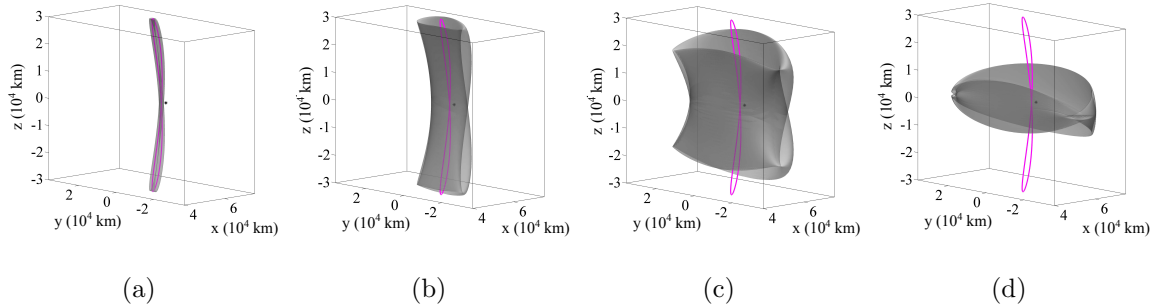


Figure 3.12. Quasi-periodic tori associated with an  $L_2$  vertical orbit in the Earth-Moon system for  $C = 3.15$

### 3.4.3 Hyperbolic Manifolds Asymptotic to the Global Center Manifold

Recall that, in the linear system, local hyperbolic manifolds asymptotic to libration point orbits are computed by combining initial conditions from the local center manifold and the stable or unstable manifold. In the nonlinear system, these manifolds also exist and are computed by exploiting stability information associated with orbits within the global center manifold.

For an unstable orbit  $\bar{x}(t)$  of period  $T$ , invariant manifold structures exist that provide transport toward and away from the orbit. A local stable/unstable manifold is computed by introducing a perturbation to some state,  $\bar{x}^* = \bar{x}(\tau)$ ,  $0 \leq \tau \leq T$ ,

that is located along the periodic orbit. This perturbation is along the direction of the stable/unstable eigenvector associated with the monodromy matrix,  $\Phi(\tau + T, \tau)$ , corresponding to  $\bar{x}^*$ . Assume that  $\lambda^S < 1$  and  $\lambda^U = 1/\lambda^S$  are the stable and unstable eigenvalues of the monodromy matrix associated with an unstable periodic orbit. Let  $\bar{v}^U$  and  $\bar{v}^S$  be their associated eigenvectors, each of unit length, and define  $\bar{v}^{U+}$ ,  $\bar{v}^{U-}$ ,  $\bar{v}^{S+}$ ,  $\bar{v}^{S-}$  as the two directions associated with each eigenvector. Define the stable eigenvector as  $\bar{v}_S^+ = [x_S \ y_S \ z_S \ \dot{x}_S \ \dot{y}_S \ \dot{z}_S]^T$ , where  $x_S > 0$ . The magnitude of the eigenvector is adjusted such that

$$\bar{w}_S^+ = \bar{v}_S^+ / \sqrt{x_S^2 + y_S^2 + z_S^2}. \quad (3.59)$$

Thus, the position components of the eigenvector  $\bar{w}_S^+$  are now of unit length and the step along the direction of the eigenvector may be computed as

$$\bar{x}^{S+} = \bar{x}^* + d \cdot \bar{w}_S^+, \quad (3.60)$$

$$\bar{x}^{S-} = \bar{x}^* - d \cdot \bar{w}_S^+, \quad (3.61)$$

where  $d$  represents a distance away from the fixed point. Likewise, the unstable eigenvector is defined as  $\bar{v}_U^+ = [x_U \ y_U \ z_U \ \dot{x}_U \ \dot{y}_U \ \dot{z}_U]^T$ , where  $x_U > 0$ . Then, the eigenvector employed to compute the unstable manifold direction is

$$\bar{w}_U^+ = \bar{v}_U^+ / \sqrt{x_U^2 + y_U^2 + z_U^2}, \quad (3.62)$$

and the step along the direction of the eigenvector is defined as

$$\bar{x}^{U+} = \bar{x}^* + d \cdot \bar{w}_U^+, \quad (3.63)$$

$$\bar{x}^{U-} = \bar{x}^* - d \cdot \bar{w}_U^+. \quad (3.64)$$

The result is an approximation for the local manifolds associated with the fixed point along the orbit. The local half-manifold,  $W_{\bar{x}^*, loc}^{U-}$  ( $W_{\bar{x}^*, loc}^{S-}$ ), is approximated by introducing a perturbation relative to  $\bar{x}^*$  along the directions  $\bar{w}^{U-}$  ( $\bar{w}^{S-}$ ). Likewise, perturbing  $\bar{x}^*$  in the direction  $\bar{w}^{U+}$  ( $\bar{w}^{S+}$ ) produces the local half-manifold  $W_{\bar{x}^*, loc}^{U+}$

$(W_{\bar{x}^*, loc}^{S+})$ . The magnitude of the step along the direction of the eigenvector is denoted  $d$ , and the value of  $d$  is critical because it determines the accuracy with which the local manifolds are approximated. Selecting  $d$  too small yields manifold trajectories that require long integration times before departure from the vicinity of the periodic orbit, leading to accumulation of numerical error. If  $d$  is too large, then the approximation to the local manifold is poor. In this investigation, the value of  $d$  is selected so that propagating the initial state along the manifold back toward the periodic orbit, i.e., propagating  $\bar{x}^{S-}, \bar{x}^{S+}$  in forward-time and  $\bar{x}^{U-}, \bar{x}^{U+}$  in reverse-time, yields a manifold trajectory that completes at least 2 revolutions of the periodic orbit. The local stable manifolds are globalized by propagating the states  $\bar{x}^{S+}$  and  $\bar{x}^{S-}$  in reverse-time in the nonlinear model. This process yields the numerical approximation for the global stable manifolds,  $W_{\bar{x}^*}^{S+}$  and  $W_{\bar{x}^*}^{S-}$ , and unstable manifolds,  $W_{\bar{x}^*}^{U+}$  and  $W_{\bar{x}^*}^{U-}$ , where  $-$  and  $+$  indicate the left and right sets of manifolds, respectively. The collection of all unstable manifolds forms the surfaces  $W^{U+}$  and  $W^{U-}$  that reflect asymptotic flow away from the periodic orbit. Likewise, the collection of all stable manifolds forms the surfaces  $W^{S+}$  and  $W^{S-}$  that reflect asymptotic flow toward the orbit. In Figure 3.13(a), a subset of trajectories on the unstable/stable manifold associated with an  $L_1$  northern halo/ $L_2$  vertical orbit in the Earth-Moon system are propagated for a fixed time interval, and are plotted in red/blue.

Several numerical schemes have been developed to locate the stable/unstable manifolds asymptotic to quasi-periodic orbits [23, 45, 46]. In this analysis, families of quasi-periodic tori and their associated manifolds are computed numerically using techniques demonstrated by Olikara and Scheeres [44]. Recall from Section 3.4.2 that the function  $\bar{\nu}(\theta_0, \theta_1)$  describes a two-dimensional torus on which a quasi-periodic orbit with associated frequencies  $\omega_0 = \dot{\theta}_0, \omega_1 = \dot{\theta}_1$  lies, then, the dimension of the torus may be reduced to one by selecting an initial value of  $\theta_0$  so that an invariant circle,  $\bar{u}(\theta_1)$ , along the torus is defined. A map,  $G$ , is defined based on the frequencies  $\omega_0, \omega_1$  so that propagating discretized states along  $\bar{u}(\theta_1)$  for time  $T_0 = \frac{2\pi}{\omega_0}$  and removing

the rotation by angle  $\rho = \omega_1 \cdot T_0$  due to frequency  $\omega_1$  yields  $G(\bar{u}) = \bar{u}$ . To compute a torus, a differential corrections algorithm is employed to locate  $\omega_0$ ,  $\omega_1$ , and discretized states along  $\bar{u}(\theta_1)$  that satisfy  $G(\bar{u}) - \bar{u} = 0$ , while applying an additional constraint on the value of Jacobi constant. Once a torus is located, pseudo-arclength continuation supplies a method to locate additional tori in a family, assuming that additional phase constraints on  $\theta_0$  and  $\theta_1$  are included. The families of tori corresponding to quasi-halo and Lissajous orbits are initialized from the periodic halo and vertical orbits by employing the associated stability information to locate a linear approximation to a nearby invariant circle. Recalling that a periodic orbit represents a fixed point under the stroboscopic map  $F(\bar{x})$  defined by time  $T$ , then stability information for the periodic orbit is recovered by examining the eigenvalues associated with the linearization of the map, i.e., the monodromy matrix  $\Phi(T, 0) = F_{\bar{x}}$ . Analogously, the invariant circle,  $\bar{u}(\theta_1)$ , represents a fixed point of the map  $G(\bar{u})$  defined by time  $T_0$  and frequency  $\omega_1$ . Thus, stability of the torus is determined by the eigenvalues of the matrix defined by the linearization of the map  $G$ , that is,  $G_{\bar{x}}$ . The eigenvectors corresponding to eigenvalues that lie off of the unit circle in the complex plane are tangent to the stable and unstable manifolds associated with each of the discretized states along  $\bar{u}(\theta_1)$  on the torus.

Examples of tori corresponding to quasi-halo (left) and Lissajous (right) orbits appear in Figure 3.13(b). For each torus, a single manifold trajectory is propagated for a fixed time interval; propagating the manifolds back toward the quasi-periodic orbits (i.e., in forward-time for the stable manifold and in reverse-time for the unstable manifold) for  $2 \cdot T_0$  yields two revolutions along the quasi-periodic orbits, plotted in black. Alternatively, numerical methods exist to compute quasi-periodic orbits over a finite time interval. Assuming that the orbit is *nearly* periodic over a particular revolution, i.e., that the initial and final states are sufficiently close, the period,  $T$ , necessary to compute the monodromy matrix for periodic orbits, may be approximated. For example,  $T$  may be defined as the time elapsed between the initial state along a

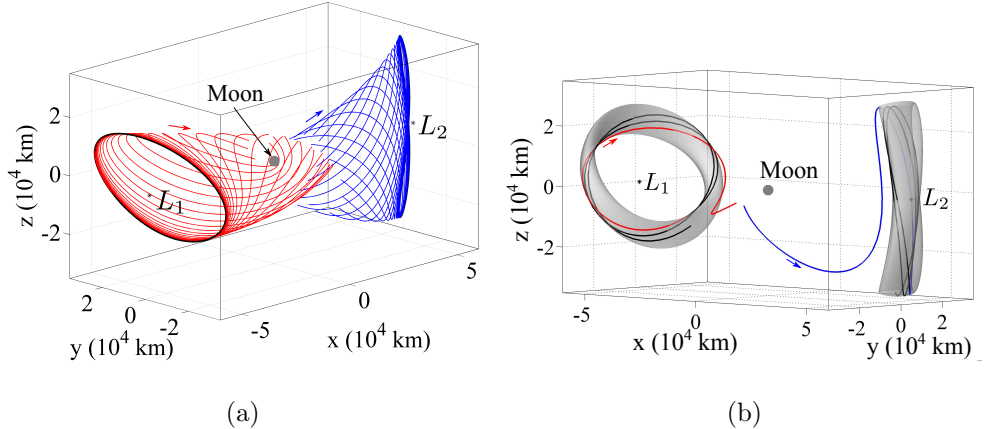


Figure 3.13. Sample stable (blue) and unstable (red) manifolds associated with periodic orbits and quasi-periodic tori with in the Earth-Moon system for  $C = 3.15$

particular revolution and the closest approach to that state within one revolution of the quasi-periodic orbit. With an approximation for the monodromy matrix computed (for one revolution of the quasi-periodic orbit), approximations to the global stable and unstable manifolds may be located using the same methodology as for periodic orbits. Employing this alternative strategy to compute the manifolds associated with quasi-periodic orbits yields qualitatively similar results when compared with the method defined by Olikara and Scheeres for all results in this study.

### 3.5 Invariant Manifolds as Separatrices and Transit

The notion of invariance has significant implications for the behaviors of solutions in the CR3BP. Recall the definition of invariance from Section 3.2: any solution which is initially in an invariant subspace remains in that subspace for all past and future times. Each of the Lagrange points is invariant, as are the periodic orbits that exist in the CR3BP. Additionally, the stable and unstable manifolds associated with the libration points, and with the periodic orbits, are invariant. Thus, by the

definition of invariance, no solution of the system defined by equation (4.1) can ever pass through a libration point, a periodic orbit, or an invariant manifold in the six-dimensional state space [33]. An examination of the regions near the libration points clarifies one impact of this invariance property, namely, the existence of transit and nontransit solutions. Transit trajectories are solutions that pass through a gateway of the zero-velocity curves in the vicinity of a collinear point. Thus, these solutions can pass between adjoining regions of the ZVCs. For example, trajectories that pass from the interior region, through the  $L_1$  gateway, and into the  $P_2$  region are transit trajectories. Conversely, trajectories that do not pass through the gateway are termed nontransit trajectories. Transit offers a means of transport throughout the space and is a phenomenon that is experienced by some Jupiter family comets, thus, techniques to construct and analyze transit solutions are of interest.

In the linear system, Conley [11], Wiggins et al. [33], Koon et al. [12], and Gómez et al. [13] demonstrate that the manifolds tubes asymptotic to the center manifold associated with a collinear libration point are separatrices that delineate two distinct trajectory behaviors, transit and nontransit. Then, the following behavior is implied: trajectories that lie inside these higher-dimensional stable or unstable manifold tubes may pass between adjoining regions of the ZVCs, while trajectories that lie outside of these manifold tubes cannot pass between the adjoining regions. While the analysis in is for the linear system, transit and nontransit solutions in the nonlinear system are also defined by their relationship to the invariant manifolds [12, 13]. Methods to locate and compute these solutions are demonstrated in following chapters.

## 4. POINCARÉ MAPS AND TRAJECTORY DESIGN

The Poincaré map is a valuable tool that offers insight into the complicated dynamics in the three-body problem. Defining a surface of section or hyperplane,  $\Sigma$ , a map is generated by propagating initial conditions and then recording and displaying crossings of the resulting trajectories with  $\Sigma$ . Combining the use of a Poincaré section with a constraint on the value of Jacobi constant reduces the dimension of the system by two. In the planar problem, the state space is, therefore, entirely represented by the projection onto a plane. In the spatial problem, these reductions yield a four-dimensional Poincaré map, i.e., a map that exists in  $\mathbb{R}^4$ . Thus, crossings of  $\Sigma$  are no longer fully represented in two dimensions and techniques to visualize the higher-dimensional Poincaré map are required.

### 4.1 Poincaré Maps

The first-return map, or Poincaré map, was introduced in 1881, by Henri Poincaré as a strategy to explore the stability of periodic orbits [9, 32]. Today, Poincaré maps are a relatively common tool in the analysis and visualization of the behavior of a dynamical system as it evolves. Consider an autonomous  $n$ -dimensional continuous-time system

$$\dot{\bar{x}} = \bar{f}(\bar{x}), \quad (4.1)$$

and recall that the flow,  $\phi_t$ , as the differential equation evolves, is defined by  $\bar{f}$  so that  $\phi_t(\bar{x}) = \phi(\bar{x}, t)$  is smooth and  $\frac{d}{dt}(\phi(\bar{x}, t))|_{t=\tau} = \bar{f}(\phi(\bar{x}, \tau))$ . Define  $\Sigma_1 \subset \mathbb{R}^n$  and  $\Sigma_2 \subset \mathbb{R}^n$  as  $(n - 1)$ -dimensional hypersurfaces, or surfaces of section, that represent cross sections of the dynamical flow,  $\phi_t$ . While  $\Sigma_1$  and  $\Sigma_2$  are not planar, in general, they should be transversal to  $\phi_t$ , that is, some component of the flow must be perpendicular

to the hypersurface [31]. A Poincaré map,  $P$ , is a mapping of  $\phi_t$  from one surface of section,  $\Sigma_1$ , to the next,  $\Sigma_2$ , that is,  $P : \Sigma_1 \rightarrow \Sigma_2$  [47]. The surfaces of section are often selected such that  $\Sigma_1 = \Sigma_2$ , in which case, the Poincaré map is a mapping of subsequent intersections with a single hypersurface.

For one hypersurface,  $\Sigma$ , there are three definitions that yield three distinct Poincaré maps. Define  $\Sigma^+$  as the hypersurface for which all intersections with the hyperplane occur such that the component of the flow normal to the surface of section changes from negative to positive. Then,  $\Sigma^-$  is the hypersurface that is defined by all intersections with the surface that are in the opposite direction. Finally, the hypersurface for which intersections may occur in either direction is denoted  $\Sigma^\pm$  or, simply,  $\Sigma$ . Hypersurfaces  $\Sigma^+$  and  $\Sigma^-$  are one-sided surfaces of section, while  $\Sigma$  is a two-sided surface of section [37]. A schematic of three trajectories intersecting a one-sided surface of section,  $\Sigma^+$ , is depicted in Figure 4.1.

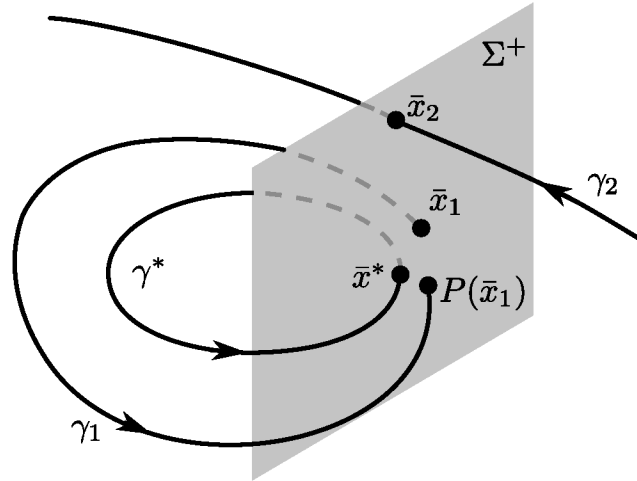


Figure 4.1. Schematic of a one-sided Poincaré map

A Poincaré map is often useful to locate regions of distinct behavior in the solution space. Define  $\gamma^*$  as a periodic solution of minimum period  $T$  that possesses a state  $\bar{x}^*$  along the trajectory. Then,  $\phi_t(\bar{x}^*) = \phi_{t+T}(\bar{x}^*)$  and  $\bar{x}^*(t_0) = \bar{x}^*(t_0+T)$ . The trajectory labeled  $\gamma^*$  in Figure 4.1 represents a periodic orbit that always intersects  $\Sigma$  in the

same location,  $\bar{x}^*$ . The point  $\bar{x}^*$  is defined as a fixed point, that is,  $\bar{x}^* = P(\bar{x}^*)$  [37]. The representative periodic solution,  $\gamma^*$ , intersects  $\Sigma$  in one fixed point, however, in general, a periodic solution may possess multiple fixed points that coincide with the surface of section. As an example, a two-sided surface of section that bisects  $\gamma^*$  contains two fixed points. Starting with the initial condition  $\bar{x}_1$  near  $\bar{x}^*$  on  $\Sigma^+$ , the trajectory labeled  $\gamma_1$  represents a solution that remains in the vicinity of  $\gamma^*$ , with a second crossing of  $\Sigma$  that lies nearby  $\bar{x}^*$ . The third trajectory,  $\gamma_2$ , possesses an initial state,  $\bar{x}_2$ , that represents the only intersection of  $\gamma_2$  with the map. This trajectory escapes the vicinity of  $\Sigma^+$  in both forward- and reverse-time. Traditional surfaces of section are sometimes represented as planes in configuration space, such as  $\Sigma = \{\bar{x} \mid x = 1 - \mu\}$ , or  $\Sigma = \{\bar{x} \mid y = 0\}$ . However,  $\Sigma$  may be any surface and a physical surface is not required. Nevertheless, to visualize the flow for a surface of section that is defined in terms of position coordinates, the Poincaré map is often projected onto a plane in a mixed position-velocity space.

#### 4.1.1 Identification of Structures within Poincaré Maps

Poincaré maps can be used as a tool to identify distinct qualitative behaviors within a system. An illustrative example of a Poincaré map is demonstrated in Figure 4.2. This map is generated in the PCR3BP, so that the map, defined by constraining the Jacobi constant value and employing a Poincaré section, is two-dimensional. In his “Numerical exploration of the restricted three-body problem” and subsequent papers, Michel Hénon examines the behavior of solutions based on their intersections with the Poincaré map [48–50]. Three types of behavior are readily identifiable from the map: periodic orbits, quasi-periodic motion, and chaotic trajectories. At least two stable periodic solutions are represented on the map in Figure 4.2. One such orbit, labeled “periodic orbit a”, corresponds to a single fixed point near the center of the map, indicated by a red asterisk. A second stable orbit, “periodic orbit b”, exists

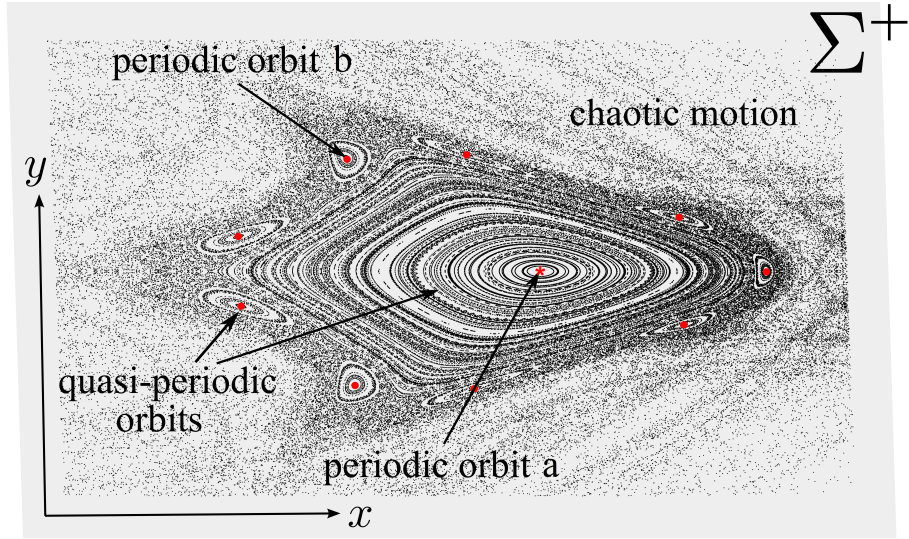


Figure 4.2. Illustrative Poincaré map

and possesses a total of nine fixed points on the map, depicted as red dots. The orbit does not close after a single revolution and, thus, this path includes multiple fixed points on the map. Because these orbits are stable, quasi-periodic orbits exist within their center subspaces. A quasi-periodic trajectory does not repeat in finite time, but is bounded within some vicinity of the associated periodic solution, thus, it does not intersect  $\Sigma$  in a single fixed point. Instead, the intersections of quasi-periodic orbits remain bounded with respect to the central fixed point of the associated periodic solution, such as  $\gamma_1$  in Figure 4.1. The concentric contours surrounding the fixed points in Figure 4.2 are the intersections formed by quasi-periodic solutions in the vicinity of the periodic orbits. Two distinct regions of quasi-periodic motion are visible, corresponding to the two distinct periodic orbits. A large region of quasi-periodic motion is readily identifiable around the central fixed point on the map. Additionally, a chain of nine *islands* of quasi-periodic motion encompass the nine fixed points belonging to the other periodic solution. These islands are identified as *ergodic* regions by Hénon because they fill only a portion of the space and cannot be connected

by a simple curve [50]. Because the quasi-periodic solutions are elements of the center subspace of the periodic orbit, they are invariant solutions and can never cross one another. Thus, each concentric contour belongs to a distinct quasi-periodic orbit. A notable feature of these stable periodic and associated quasi-periodic orbits is their “robustness,” that is, given a small perturbation in the initial state of a solution in this regime, the resulting orbit is, generally, only slightly perturbed from the original solution. Finally, a large region of chaotic motion is evident that surrounds the local zones of periodic and quasi-periodic motion. The seemingly random intersections in the chaotic region reflect trajectories for which small perturbations in the initial state propagate to large perturbations in the final state. Crossings of unstable periodic orbits may lie within the chaotic zones, but are, generally, not readily distinguishable. Unstable periodic orbits may possess a nontrivial center manifold and, therefore, may be associated with nearby quasi-periodic solutions. However, when propagating random initial conditions nearby a fixed point associated with an unstable periodic orbit, the unstable/stable manifold will dominate and the behavior will, generally, appear chaotic. Thus, subsequent crossings of the map exist in chaotic regions. While there is no apparent structure within the chaotic regions, the trajectories in this regime share the common trait that they escape the regions of periodic and quasi-periodic motion, similar to  $\gamma_2$  in Figure 4.1, rather than remaining bounded to these regions.

#### 4.1.2 Dimensionality of Poincaré Maps

Poincaré maps representing crossings of manifold structures with  $\Sigma$  are employed throughout this investigation, thus, it is useful to define the dimensionality of the structures (libration point orbits and their associated invariant manifolds) in the vicinity of the collinear libration points. Details on the dimension of structures in the vicinity of the collinear points are additionally provided by Gómez et al. [13].

The collinear points possess a topological structure of type saddle  $\times$  center  $\times$  center. Then, there exists a four-dimensional center manifold (topologically, an invariant 4-sphere) in the vicinity of these libration points that may be reduced to a 3-sphere via a constraint on the Jacobi constant value. The center manifold is comprised of a combination of one-dimensional periodic orbits (e.g., Lyapunov, vertical, halo, and axial orbits) and two-dimensional tori corresponding to families of quasi-periodic solutions associated with the periodic orbits. The stable and unstable manifolds form four-dimensional ‘tubes’ asymptotic to the 3-sphere of the center manifold. The stable/unstable manifold asymptotic to a particular periodic orbit is two-dimensional, that is, any point on the surface is defined by two parameters, (1) the departure location on the one-dimensional orbit, and (2) the time-of-flight along the manifold. A manifold asymptotic to a particular quasi-periodic orbit is three-dimensional and any point on the surface is defined by three parameters, (1)–(2) the departure location on the two-dimensional torus, and (3) the time-of-flight along the manifold. Thus, the collection of manifolds that are asymptotic to the three-dimensional center manifold is four-dimensional, and is parameterized by the three angles on the 3-sphere and a time-of-flight along the manifold. Then, a Poincaré map depicting crossings of the stable/unstable manifold in the spatial problem is three-dimensional in  $\mathbb{R}^4$ .

In the planar problem, the two-dimensional center manifold associated with a collinear point is composed solely of planar Lyapunov orbits. For a particular value of Jacobi constant, the center manifold consists of a single periodic orbit and is, therefore, one-dimensional. The manifolds asymptotic to the periodic orbit are two-dimensional, as in the spatial problem. Thus, a Poincaré map representing crossings of the stable or unstable manifold associated with a Lyapunov orbit is one-dimensional in  $\mathbb{R}^2$ , and the manifold crossings appear as closed contours on the map.

## 4.2 Existing Design Techniques Employing Poincaré Maps in the Planar Problem

Poincaré maps have been previously demonstrated as a useful tool for a variety of applications in the CR3BP. Early use of Poincaré maps included the analysis of periodic and quasi-periodic orbits as well as chaotic zones by Hénon [48, 50]. More recently, Koon et al. [12], Gómez et al. [23], Barrabés et al. [51, 52], and Parker et al. [53] employ a variety of types of Poincaré maps to locate heteroclinic connections, i.e., free transfers between periodic orbits employing invariant manifolds, linking planar orbits in the CR3BP. Koon et al. [12] additionally demonstrates the use of invariant manifolds and Poincaré maps to locate planar transit trajectories that bridge adjoining regions of the ZVCs. Villac and Scheeres [47] as well as Paskowitz and Scheeres [25] employ periapse maps to classify regions of immediate escape/capture in the Hill three-body problem. Haapala [14] employs periapse maps to demonstrate that the invariant manifolds provide the boundaries for these regions of escape from the smaller primary in the planar CR3BP. Haapala [54–56], Davis [15, 28, 56], and Howell [55, 56] also examine these regions of escape from the perspective of invariant manifolds.

Recall that, in the full spatial problem, the center manifold in the vicinity of the collinear libration points is a 4-sphere that may be reduced to a 3-sphere using a constraint on the Jacobi constant value. In the planar problem, however, only the periodic Lyapunov orbits exist within the two-dimensional center manifold. By constraining the value of the Jacobi constant, the center manifold is comprised of a single Lyapunov orbit and the manifold surface asymptotic to the Lyapunov orbit is two-dimensional. Because the system is three-dimensional for a particular value of Jacobi constant, these two-dimensional manifold tubes act as separatrices that distinguish two categories of behavior: transit solutions that can pass through adjoining regions of the ZVCs, and nontransit trajectories that are bounded to their region of origina-

tion [11–13, 33]. The crossings of the two-dimensional manifold on a Poincaré map generally form a closed contour in  $\mathbb{R}^2$ , and initial conditions within this contour correspond to transit trajectories. Poincaré maps are, therefore, useful to identify transit orbits that traverse adjoining regions defined by the ZVCs. Maps also prove valuable to locate transfer trajectories that provide connections between libration point orbits.

In the following example, strategies employing Poincaré maps to compute maneuver-free transfers and transit trajectories are demonstrated. By displaying crossings of stable and unstable invariant manifold structures associated with libration point orbits on a map, initial conditions corresponding to transit orbits may be located. Trajectories that exist within the intersection of stable and unstable manifold tubes correspond to maneuver-free (heteroclinic/homoclinic) transfers between libration point orbits. These trajectories possess crossings on the map that lie on the intersection of two distinct contours, one contour associated with a stable manifold and the other with an unstable manifold. To demonstrate the use of Poincaré maps to locate heteroclinic connections between planar libration point orbits, consider the map in Figure 4.3. The plot in 4.3(b) depicts a projection of the crossings of the stable manifold

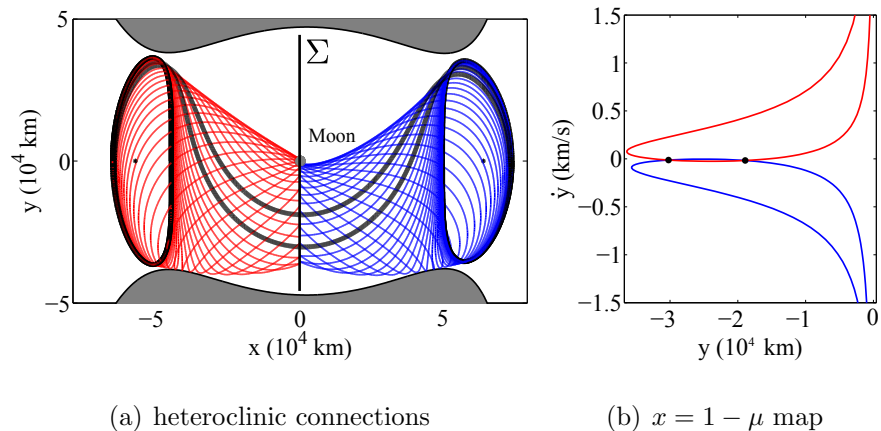


Figure 4.3. Heteroclinic connections are determined from the intersection of manifold contours on a Poincaré map for the planar problem; Earth-Moon system for  $C = 3.15$  (Moon-centered view)

asymptotic to an  $L_1$  Lyapunov orbit and the unstable manifold associated with an  $L_2$  Lyapunov orbit with the surface  $\Sigma$ , apparent in Figure 4.3(a), defined by  $x = 1 - \mu$  for  $C = 3.15$  in the Earth-Moon system; these intersections with  $\Sigma$  form contours in the  $y\text{-}\dot{y}$  phase space. The map is one-sided, that is, only crossings in one direction ( $\dot{x} > 0$  in this example) are included. For each point on the map,  $x = 1 - \mu$ ,  $y$  and  $\dot{y}$  are available from the map, and  $\dot{x}$  is computed from the specified value of Jacobi constant. Thus, an intersection of the two contours in the  $y\text{-}\dot{y}$  plane indicates a match in the full state space, and the existence of a heteroclinic connection between the  $L_1$  and  $L_2$  Lyapunov orbits. The contours in Figure 4.3(b) intersect in two locations, marked by black dots on the map, yielding two distinct heteroclinic transfers that are plotted in black in Figure 4.3(a). To compute a transit solution, initial conditions *within* one of the contours are selected. The green dot in Figure 4.4(b) represents an initial condition that is within both contours, thus, corresponds to transit in both

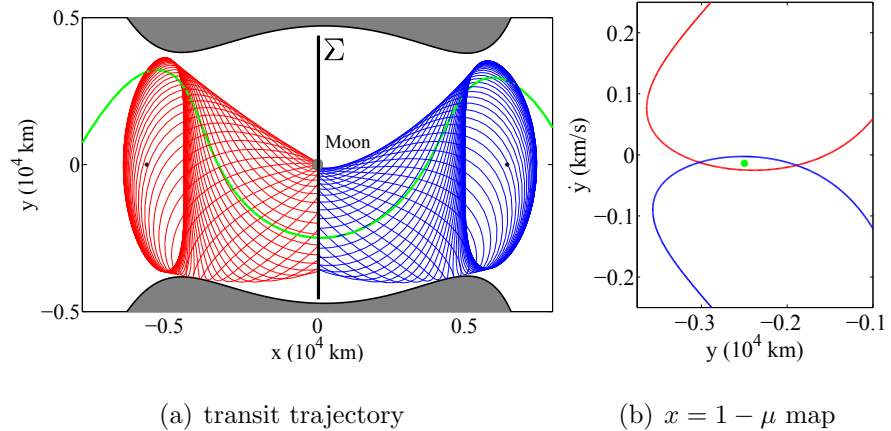


Figure 4.4. A transit solution is computed from initial conditions within the manifold contours on a Poincaré map for the planar problem; Earth-Moon system for  $C = 3.15$  (Moon-centered view)

reverse- and forward-time, through the  $L_1$  and  $L_2$  gateways, respectively. The map in the figure is the same map as in Figure 4.3(b), however, represents a close view of the region of overlap of the red and blue contours with different axis scaling. Propagating

this state yields the green transit trajectory in Figure 4.4(a) that enters the  $P_2$  region through the  $L_1$  gateway from the interior, and subsequently escapes to the exterior region through  $L_2$ .

### 4.3 Existing Design Techniques Employing Poincaré Maps in the Spatial Problem

While a Poincaré map associated with a particular value of Jacobi constant in the planar CR3BP is two-dimensional (i.e.,  $\in \mathbb{R}^2$ ), maps in the spatial problem are at least four-dimensional ( $\in \mathbb{R}^4$ ) and are difficult to display visually. Previous researchers employ a number of approaches to represent the information contained in higher-dimensional Poincaré maps. Generally, these methods either serve to reduce the dimension of the map, or to offer strategies for visually representing the higher-dimensional data set. As a third option, the map may be projected into a lower-dimensional space so that, while some information is lost, valuable insight might still be gained.

Early work with higher-dimensional maps generally includes orthographic projections to gain insight into the higher-dimensional space, e.g. Froeschlé [16,17], Martinet and Magnenat [18] as well as Contopoulos et al. [19]. Froeschlé [17] additionally considers “slices” of the three-dimensional projection of a map. Here, he plots numerous stereoscopic projections, each of which include only the crossings of the map within some tolerance of a prescribed value of one of the state variables. Later, Patsis and Zachilas employ rotation of a three-dimensional image so that all projections may be considered, and include color to represent the fourth dimension [20]. Geisel [21] applies this method to investigate structures within the CR3BP. While the strategies employed by Patsis, Zachilas, and Geisel serve to represent the full map, rotation of the view is required to consider all possible orthographic projections.

Alternatively to considering projections of a higher-dimensional map, the dimension of the map may be reduced by applying additional constraints. For example, to examine the behavior in the vicinity of the collinear libration points, Jorba and Masdemont [22] and Gómez et al. [23] obtain higher-order normal form expansions of the Hamiltonian in the vicinity of the equilibrium points to decouple the oscillatory and unstable motion. A change in variables allows for the removal of the unstable behavior via a reduction to the center manifold, and yields a system with two degrees of freedom. Thus, two-dimensional Poincaré maps associated with periodic and quasi-periodic orbits in the spatial problem for a particular energy level are represented using two nonphysical coordinates. Gómez et al. [13, 24] compute the stable/unstable manifold asymptotic to the center manifold associated with a collinear point for a particular energy level and employ a Poincaré map to reduce the problem to four dimensions. Constraints on the values of two additional variables are applied by considering only crossings of the map that exist within some tolerance of those values. Thus, a Poincaré map corresponding to constraints on 3 different variables is approximated. The resulting map is two-dimensional and may be represented by the projection onto a plane. Paskowitz and Scheeres [25] employ periapse maps to classify trajectory behavior in the spatial problem, and represent the full six-dimensional state associated with a periapse map crossing by plotting vectors instead of points. The basepoint of each vector represents the position components in three-dimensional configuration space, and the length and orientation of the vector indicate the velocity at periapsis. In the following example, strategies demonstrated by Gómez et al. [13, 24] to reduce the dimension of a Poincaré map in the spatial problem are further explored.

Recall that, in the spatial problem, both periodic and quasi-periodic orbits exist within the center manifold associated with a collinear libration point and that the hyperbolic invariant manifold tangent to this center manifold provides the separatrix that distinguishes transit from nontransit behavior in the spatial problem. Gómez

et al. [13, 24] exploit this information to locate transit trajectories in the spatial problem using Poincaré maps. These authors additionally employ maps to compute heteroclinic and homoclinic connections between libration point orbits in the spatial problem. Because a Poincaré map displaying crossings of the four-dimensional stable/unstable manifold is a three-dimensional surface that exists in  $\mathbb{R}^4$ , the map is reduced to a contour in  $\mathbb{R}^2$  by constraining two additional variables. To demonstrate the application of this method, consider an example in the Earth-Moon system for the Jacobi constant value  $C = 3.15$ . Sample libration point orbits within the center manifolds associated with  $L_1$  and  $L_2$  are computed, including the periodic halo and vertical orbits as well as subsets of the families of quasi-periodic tori that are generated via the method demonstrated by Olikara and Scheeres [44]. The stable and unstable manifolds associated with each of the periodic and quasi-periodic orbits are additionally computed as described by Olikara and Scheeres. While both northern and southern halo orbits exist, only the northern halo and associated quasi-halo orbits are actually computed numerically. The manifolds associated with the southern orbits are obtained via a reflection across the  $x$ - $y$  plane. A total of  $\sim 10^6$  manifold initial conditions are generated to approximate the hyperbolic invariant manifold asymptotic to the center subspace of each collinear point, i.e., asymptotic to the set of sample periodic and quasi-periodic orbits in the vicinity of the libration points.

To search for transfers connecting libration point orbits in the vicinity of  $L_1$  and  $L_2$ , the unstable manifold asymptotic to the  $L_1$  center manifold and the stable manifold associated with the center manifold of  $L_2$  are employed. The previously generated initial conditions corresponding to trajectories on these manifold surfaces are propagated, and crossings of the hyperplane  $\Sigma_{P_2}^+ = \{\bar{x}|x = 1 - \mu, \dot{x} > 0\}$  are recorded. The projection of the resulting map onto the  $y$ - $z$  plane appears as a pair of two-dimensional disks in Figure 4.5(a), where red and blue points correspond to the unstable and stable manifolds, respectively. Note that the surface of the Moon is also included as the gray sphere on the plot, and that a subset of the manifold arcs impact the Moon.

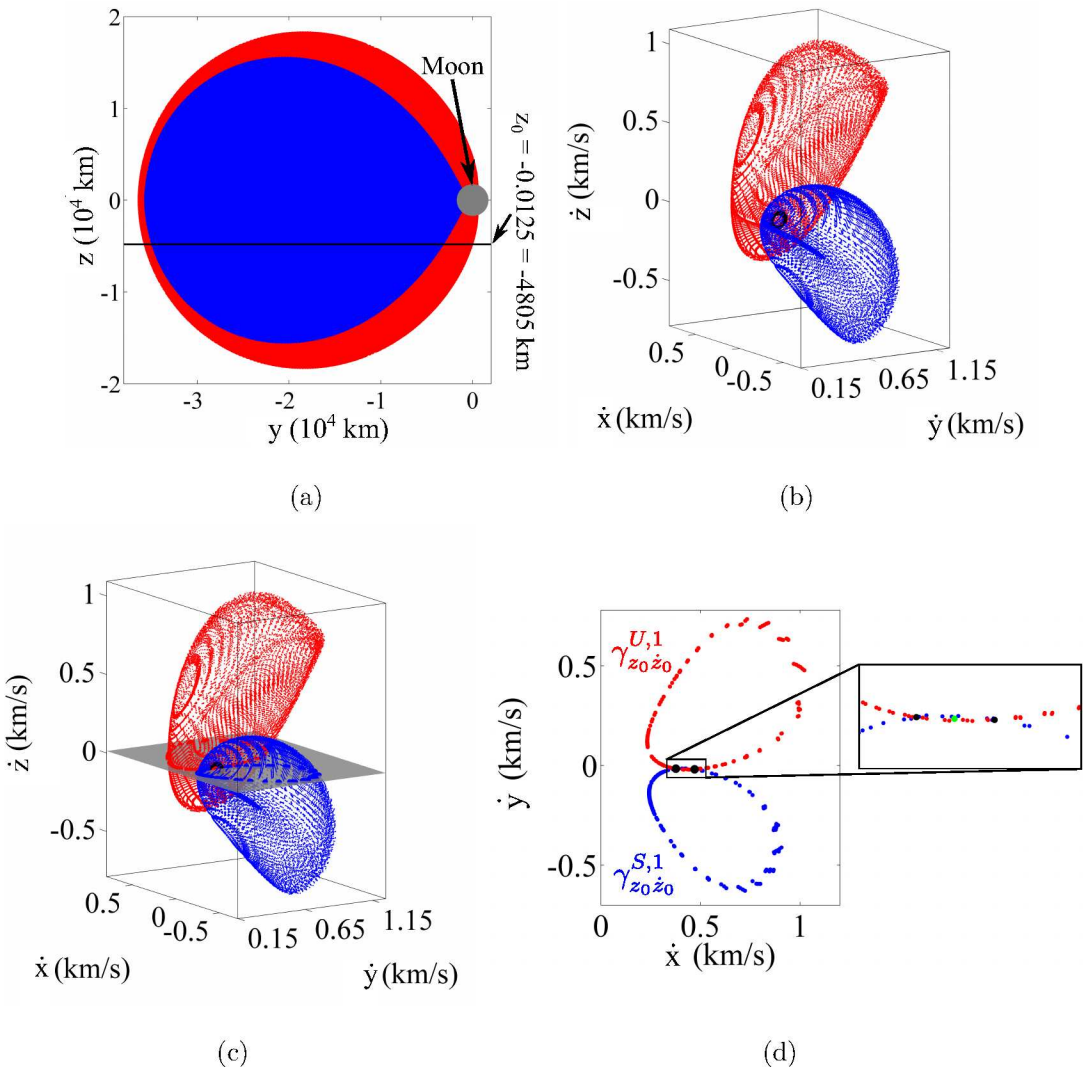


Figure 4.5. Reducing  $y = 0$  map of invariant manifolds to 1D contours in  $\mathbb{R}^2$  for  $C = 3.15$  in the Earth-Moon system, (a) projection of map onto  $y$ - $z$  plane, (b) reducing to 2D surfaces by selecting  $z = z_0$  reveals black contour defining intersection of manifolds, (c)  $\dot{z} = \dot{z}_0$  plane intersects surfaces to form contours, (d) maps reduced to 1D by constraining  $z \approx z_0$ ,  $\dot{z} \approx \dot{z}_0$

The projection of the map onto another plane in the phase space (excluding the  $x$ -coordinate), such as the  $\dot{y}$ - $\dot{z}$  velocity plane, also appears as two-dimensional disks. By constraining one additional variable, the Poincaré map associated with the sta-

ble/unstable manifold is reduced to a two-dimensional surface in  $\mathbb{R}^3$ . In this example, the constraint  $z = z_0 = -0.0125 = -4805$  km is selected and is represented by the black line in Figure 4.5(a). Because a finite number of trajectories sampled from each manifold surface are integrated, all points within the range  $(z_0 - \delta) \leq z \leq (z_0 + \delta)$  are included, where  $\delta \sim 200$  km for this example. Now, projecting the map into velocity space yields the two-dimensional surfaces that appear in Figure 4.5(b). The red and blue surfaces intersect with one another forming a contour, plotted in black, that represents heteroclinic connections between libration point orbits in the vicinity of  $L_1$  and  $L_2$ . Selecting a black point on the map and propagating the associated state in the CR3B model will yield a maneuver-free transfer that provides a connection between  $L_1$  and  $L_2$  orbits. By applying one additional constraint, the Poincaré map associated with each manifold is reduced to a one-dimensional contour in  $\mathbb{R}^2$ . Arbitrarily selecting a value of  $\dot{z} = \dot{z}_0 = 13.2$  m/s ( $\delta \sim 1$  m/s), represented by the gray plane in Figure 4.5(c), yields the contours plotted in Figure 4.5(d). These contours are labeled  $\gamma_{z_0\dot{z}_0}^{U,1}$  and  $\gamma_{z_0\dot{z}_0}^{S,1}$  using the notation defined by Gómez et al. Here,  $U$  or  $S$  denotes the contour as belonging to the unstable or stable manifold, the number 1 indicates that these contours correspond to the first crossings of the manifolds with the map, and the subscripts  $z_0\dot{z}_0$  indicate that the map crossings are defined for constrained values of  $z = z_0$  and  $\dot{z} = \dot{z}_0$ .

The contours on the map in Figure 4.5(d) intersect in two locations, indicated by the two black points. The states associated with these points represent the two heteroclinic connections that lie on the intersection of the black contour and the gray plane in Figure 4.5(c). Analogously to the planar problem, choosing any point within the narrow region of overlap of the red and blue contours yields a transit trajectory that passes through the  $L_1$  and  $L_2$  gateways. The heteroclinic connections and a sample transit orbit appear in Figure 4.6. Because the green initial condition is in close proximity to the stable and unstable manifolds, the transit trajectory retains some oscillatory behavior within the gateways, completing about one half of a revolution

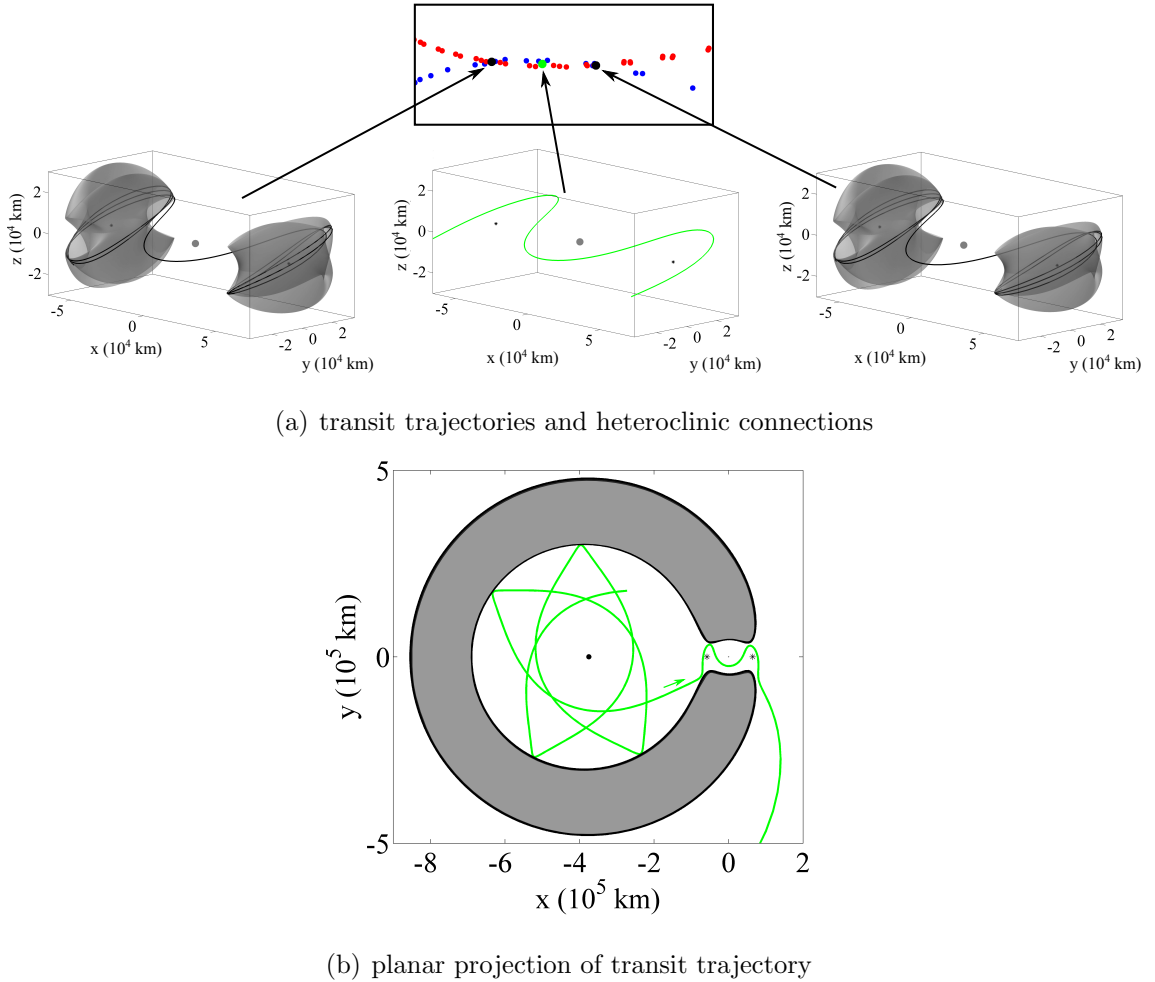
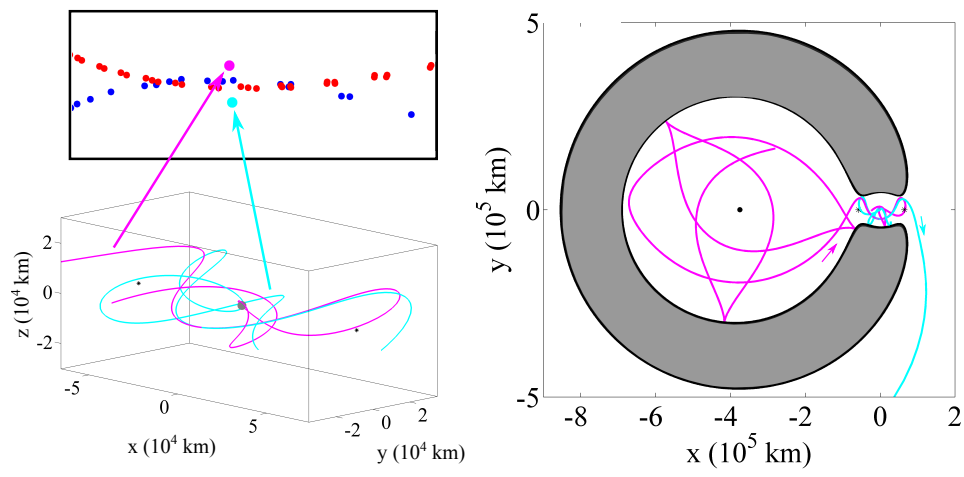


Figure 4.6. Heteroclinic connections and a transit trajectory located using maps in the Earth-Moon system (Moon-centered views)

about  $L_1$  during entry to the lunar region and about  $L_2$  during escape. Selecting any point within the red contour and outside of the blue contour yields a trajectory that enters through the  $L_1$  gateway but that does not immediately escape, such as the magenta arc in Figure 4.7. The cyan arc in Figure 4.7 corresponds to an initial condition selected within the blue contour, but outside of the red boundary. This trajectory immediately escapes through the  $L_2$  gateway, but does not immediately enter from the  $L_1$  gateway when propagated in reverse-time.



(a) locating trajectories that transit in one direction

(b) planar projection of trajectories

Figure 4.7. Trajectories with map crossings outside of the intersection of the manifold contours do not transit both gateways (Moon-centered views)

## 5. NEW APPLICATIONS FOR EXISITNG DESIGN TECHNIQUES

In the previous chapter, several of the existing techniques for trajectory design in the CR3BP are discussed. These techniques, outlined in Section 4.3, are demonstrated for the computation of transit trajectories and maneuver-free transfers between libration point orbits in the spatial problem. In the following sections, new applications for these methods are explored. In this investigation, strategies to design transit trajectories in the spatial problem are applied to examine the relationship between the behavior of comets that experience temporary capture by Jupiter and the invariant manifold structures associated with the collinear points in the Sun-Jupiter system. Additional applications, outside of the computation and analysis of transit trajectories or heteroclinic/homoclinic connections, include the search for periodic orbits in the spatial problem. By exploiting known symmetry properties, Poincaré maps prove useful to search for symmetric periodic orbits.

### 5.1 Analysis of the Temporary Capture of Jupiter-Family Comets

The application of Poincaré maps for the analysis of temporary satellite capture phenomena yields insight into the dynamics associated with the capture and transit events experienced by several Jupiter-family comets. Temporary satellite capture (TSC) about Jupiter is defined for this investigation when the osculating orbital elements associated with the satellite relative to Jupiter become elliptical for some period of time during encounter with Jupiter [57]. A number of Jupiter-family comets experience TSC, including 39P/Oterma, 147P/Kushida-Muramatsu, 82P/Gehrels 3, and 111P/Helin-Roman-Crockett [12, 55, 58–61]. To enter and exit the Jupiter region

during a TSC event, these comets must transit through the  $L_1$  and/or  $L_2$  gateways. In the CR3BP, transit phenomena are explained via the stable/unstable invariant manifolds associated with libration point orbits. Thus, in this investigation, strategies to employ Poincaré maps for the study of transit in the CR3BP are applied to gain insight into the naturally occurring temporary capture of Jupiter-family comets.

### 5.1.1 Comet 39P/Oterma

Between 1910 and 1990, comet 39P/Oterma (OTR) experienced two distinct TSC events. The first temporary capture occurred between 1935 and 1939, during which time OTR entered from the exterior region and passed directly through the Jupiter region and into an interior orbit. A single revolution about the Sun in the rotating frame occurs in the interior region, followed by a second encounter with Jupiter. The second TSC event took place from 1962 to 1964, during which time the comet passed directly through the Jupiter region and returned to an exterior orbit. The path of comet OTR between 1910 and 1990 appears in Figure 5.1 for the Sun-Jupiter rotating frame.

The transition of OTR between the exterior/interior regions and the Jupiter region through the  $L_2/L_1$  gateways may be examined by applying the techniques demonstrated by Gómez et al. [13, 24] Poincaré maps have been previously applied to study the motion of Jupiter-family comets (e.g., Koon et al. [12], Haapala and Howell [55]. To explore the relationship between the trajectory of OTR and the invariant manifolds asymptotic to the center manifold of  $L_1$  or  $L_2$ , Poincaré maps associated with the surfaces  $\Sigma_{P_2}^- = \{\bar{x}|x = 1 - \mu, \dot{x} < 0\}$ ,  $\Sigma_{P_2}^+ = \{\bar{x}|x = 1 - \mu, \dot{x} > 0\}$  are employed. The crossings of OTR with  $\Sigma_{P_2}$  are observed relative to the crossings of the stable and unstable invariant manifolds. To compute the map, a value of  $C = 3.02$  (near the osculating Jacobi constant value for OTR) is assumed, and a sample set of periodic and quasi-periodic orbits within the center manifold associated with  $L_1$  and  $L_2$  are

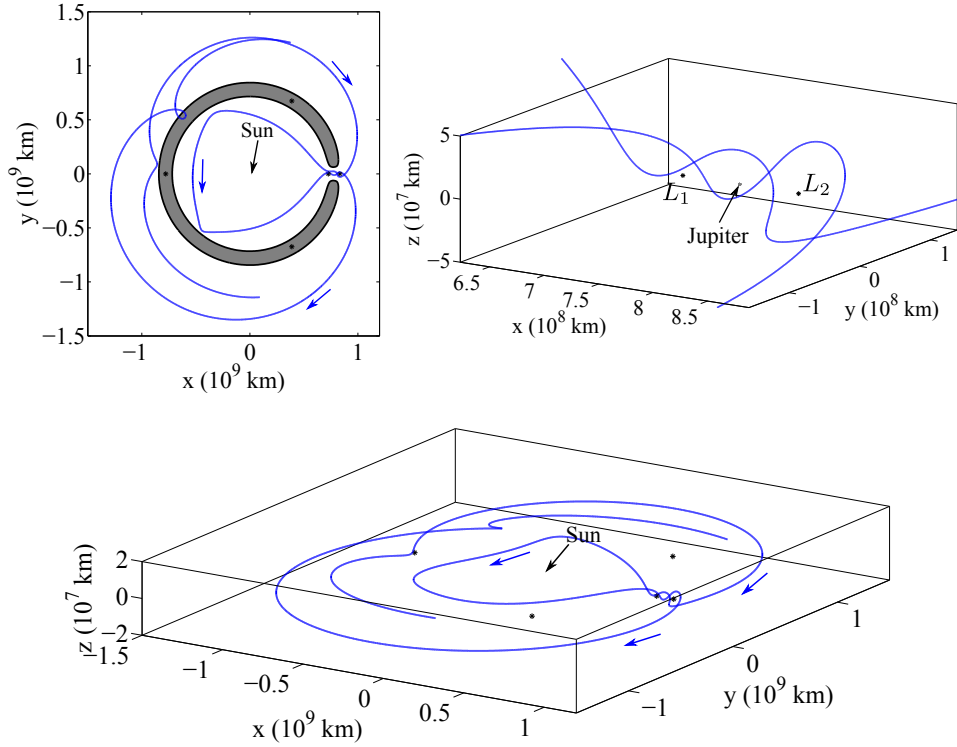


Figure 5.1. Ephemeris path of comet OTR as viewed in the Jupiter-centered Sun-Jupiter rotating frame

computed. Approximately  $1 \times 10^6$  initial conditions are computed for the unstable manifold associated with the  $L_1$  and  $L_2$  libration point orbits and are integrated in the CR3B model. The stable manifolds are determined, using symmetry properties, by the transformation  $t \rightarrow -t$ ,  $y \rightarrow -y$ ,  $\dot{x} \rightarrow -\dot{x}$ ,  $\dot{z} \rightarrow -\dot{z}$ .

In the CR3BP, trajectories that enter through the  $L_2$  gateway from the exterior lie within the unstable manifold that departs the center manifold of  $L_2$ , considering the manifold half-tubes that are propagated into the  $P_2$  region  $W_{L_2}^{U-}$ . Similarly, trajectories that escape through  $L_2$  exist within the stable manifold tube  $W_{L_2}^{S-}$ . Likewise, trajectories that escape through the  $L_1$  gateway to the interior lie within the stable manifold  $W_{L_1}^{S+}$ , and trajectories that enter through  $L_1$  from the interior exist within the unstable manifold  $W_{L_1}^{U+}$  asymptotic to the center manifold of  $L_1$ . Noting that

OTR crosses  $\Sigma_{P_2}$  once as it passes through the  $P_2$  region for each TSC event, it is expected that the first crossing of OTR after entry from the exterior region lies within the first crossing of  $W_{L_2}^{U-}$  and within the first crossing of  $W_{L_1}^{S+}$ . Define  $(y_1, z_1)$  as the  $(y, z)$  location at the crossing of the path of OTR with  $\Sigma_{P_2}^-$  after entry from the exterior. To locate this first crossing of the comet path relative to the manifolds  $W_{L_2}^{U-}$  and  $W_{L_1}^{S+}$ , the contours  $\gamma_{y_1 z_1}^{U,1}$  and  $\gamma_{y_1 z_1}^{S,1}$  are computed. The velocity  $(\dot{y}_1, \dot{z}_1)$  associated with the crossing of OTR is expected to lie within both contours  $\gamma_{y_1 z_1}^{U,1}$  and  $\gamma_{y_1 z_1}^{S,1}$ . Recall from the previous discussion that the contours  $\gamma_{y_1 z_1}^{U,1}$  and  $\gamma_{y_1 z_1}^{S,1}$  are obtained by considering only those crossings of the manifold within some tolerance of the locations  $y = y_1$  and  $z = z_1$ . An examination of the map in Figure 5.2(a) reveals that the

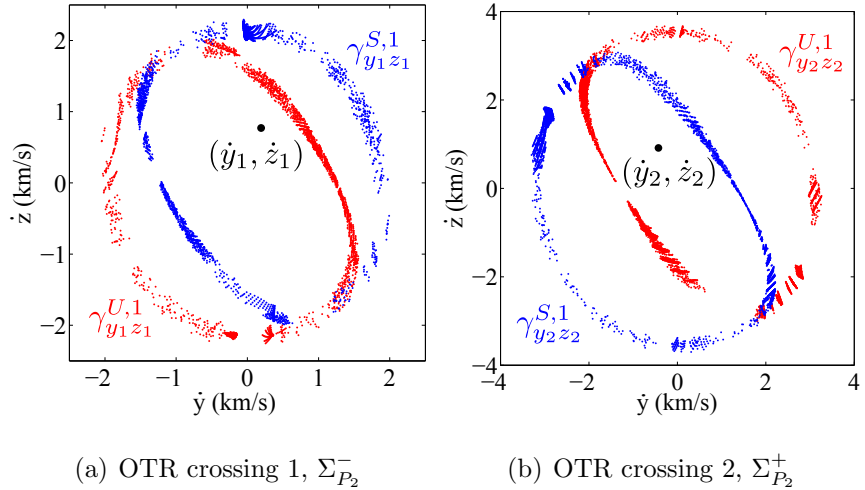


Figure 5.2. Location of OTR state relative to invariant manifolds at  $\Sigma_{P_2}$  for  $C = 3.02$

crossing of the path of OTR indeed lies within these contours formed by the invariant manifolds. During the second TSC event, OTR crosses  $\Sigma_{P_2}^+$  once as it passes through the  $P_2$  region after entry from the interior. The location of this crossing is defined as  $(y_2, z_2)$ , and the associated velocity states in the  $y$  and  $z$  directions are  $\dot{y}_2$  and  $\dot{z}_2$ . It is expected that the crossing of OTR with  $\Sigma_{P_2}^+$  lies within the first crossing of  $W_{L_1}^{U+}$  and within the first crossing of  $W_{L_2}^{S-}$ . The map crossing of the comet path is located

relative to these manifolds by considering the contours  $\gamma_{y_2 z_2}^{U,1}$  and  $\gamma_{y_2 z_2}^{S,1}$  on the map, and the velocity  $(\dot{y}_2, \dot{z}_2)$  is expected to be within both contours. The map in Figure 5.2(b) indicates that the path of OTR during the second TSC event is also within the expected invariant manifold tubes. Thus, the behavior of OTR during TSC appears to be governed by the invariant manifold tubes asymptotic to the center manifolds of  $L_1$  and  $L_2$ . Both the type of transit (exterior-to-interior and interior-to-exterior) and duration of the TSC event (direct pass through the  $P_2$  region) are determined by these manifolds.

### 5.1.2 Comet 111P/Helin-Roman-Crockett

Shortly after the discovery of comet 111P/Helin-Roman-Crockett (HRC) in 1989, it was determined that the comet had experienced a close approach to Jupiter. [59,61] Transitioning from an interior orbit to the Jupiter region in 1967, the comet was temporarily captured for until 1985, at which time HRC returned to the interior region. Unlike the relatively brief TSC events experienced by the comet 39P/Oterma, HRC remained captured about Jupiter for 18.5 years. The path of HRC in the vicinity of Jupiter during TSC appears in Figure 5.3 in the Sun-Jupiter rotating frame. As

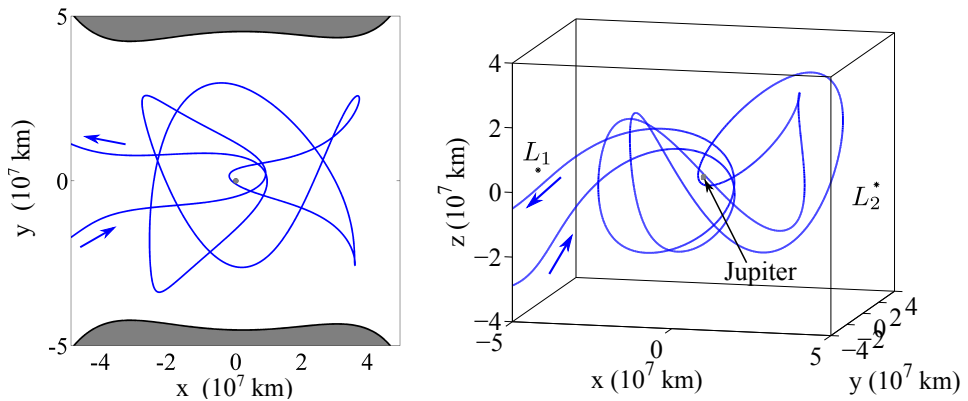


Figure 5.3. Ephemeris path of comet HRC as viewed in the Jupiter-centered Sun-Jupiter rotating frame; Jupiter 10 $\times$  actual size

with the analysis of the behavior of comet 39P/Oterma in the previous section, to examine the relationship between the trajectory of HRC and the invariant manifolds associated with the center subspace in the vicinity of  $L_1$ , Poincaré maps are employed. The four crossings of HRC with the surface  $\Sigma_{P_2}^- = \{\bar{x}|x = 1 - \mu, \dot{x} < 0\}$  are observed relative to the crossings of the stable and unstable invariant manifolds. A value of  $C = 3.029$  (near the osculating value for HRC) is assumed, and a sample set of periodic and quasi-periodic orbits within the center manifold of  $L_1$  are computed for this Jacobi constant value. The unstable manifold associated with the set of  $L_1$  libration point orbits is approximated via  $\sim 10^6$  initial conditions which are numerically integrated in the CR3B model. The stable manifold is, again, determined via symmetry properties.

Recall that, in the CR3BP, trajectories that enter through the  $L_1$  gateway from the interior lie within the unstable manifold  $W_{L_1}^{U+}$ , and trajectories that escape to the interior through this gateway exist within the stable manifold  $W_{L_1}^{S+}$  asymptotic to the center manifold of  $L_1$ . Then, it is expected that the first crossing of HRC with  $\Sigma_{P_2}^-$  after entry from the interior lies within the first crossing of  $W_{L_1}^{U+}$ , and that the last crossing before escape from the Jupiter region is within the first crossing of  $W_{L_1}^{S+}$ . Define  $(y_i, z_i)$  as the  $(y, z)$  location at the  $i^{th}$ ,  $i = 1-4$ , crossing of the path of HRC with  $\Sigma_{P_2}^-$  after entry from the interior. To locate the state along the comet path at the  $i^{th}$  map crossing relative to the unstable manifold, the contour  $\gamma_{y_i z_i}^{U,1}$  is computed for each value of  $i$  by considering only those crossings of the manifold within some tolerance of the locations  $y = y_i$  and  $z = z_i$ . To check for escape back to the interior, the contour  $\gamma_{y_i z_i}^{S,1}$  is also located. Each of the velocities  $(\dot{y}_i, \dot{z}_i)$  associated with the map crossings of HRC are expected to lie within the corresponding contour  $\gamma_{y_i z_i}^{U,i}$ . If  $(\dot{y}_i, \dot{z}_i)$  also lies within  $\gamma_{y_i z_i}^{S,1}$ , then HRC is expected to immediately escape and transition back to the interior region.

For  $i = 1-4$ , the contours  $\gamma_{y_i z_i}^{U,i}$  and  $\gamma_{y_i z_i}^{S,1}$  appear in Figures 5.4(a)–5.4(d) in red and blue, respectively. The states  $(\dot{y}_i, \dot{z}_i)$  along the path of HRC are also included and are plotted in black. As the manifolds evolve and  $i$  increases, the individual manifold arcs

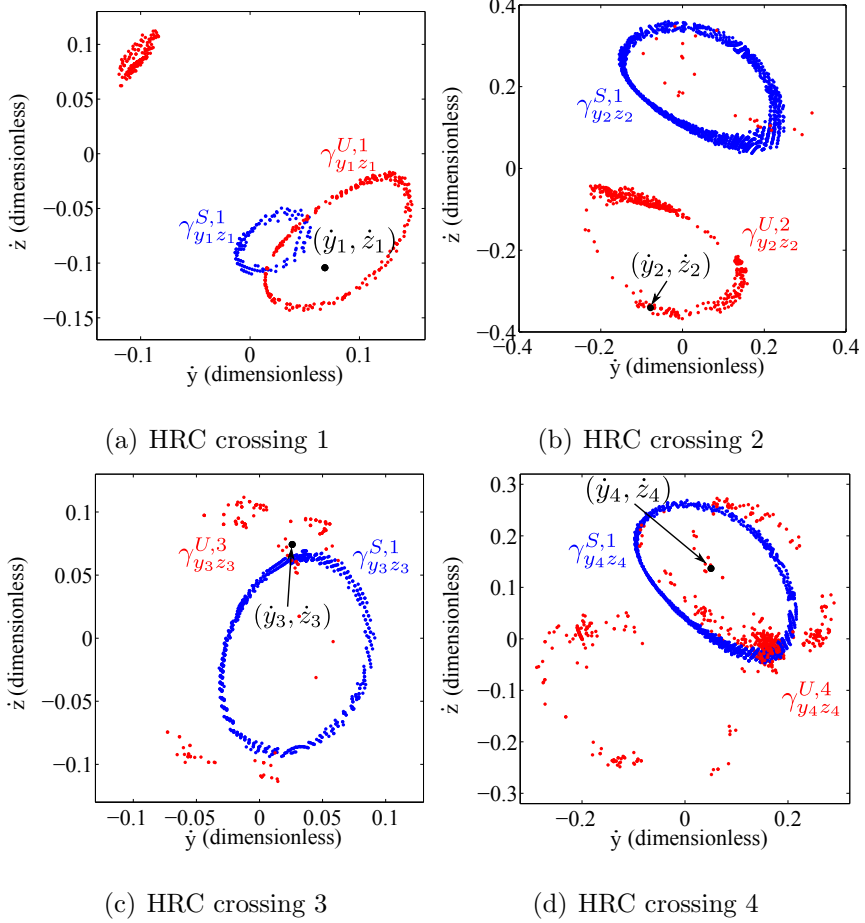


Figure 5.4. Location of HRC transit relative to invariant manifolds for  $C = 3.029$

tend to disperse. The crossings associated with  $\gamma_{y_i z_i}^{U,i}$  become diffuse and the manifold structures no longer appear as contours on the map. From the map in Figure 5.4(a), it is clear that the trajectory of HRC lies within the unstable manifold tube associated with the center manifold of  $L_1$ . This crossing of HRC *does not* lie within the first cut of the stable manifold, however, and therefore cannot yet transition back to the interior region. Indeed,  $(\dot{y}_i, \dot{z}_i)$  lies outside of  $\gamma_{y_i z_i}^{S,1}$  for  $i = 1, 2, 3$ , and the comet remains temporarily captured in the vicinity of Jupiter. For  $i = 4$ , however,  $(\dot{y}_i, \dot{z}_i)$  does fall within  $\gamma_{y_i z_i}^{S,1}$ , as evident from Figure 5.4(d), resulting in immediate escape through the  $L_1$  gateway back to the interior region.

The maps in Figure 5.4, computed from strategies introduced by Gómez et al. (2001, 2004), prove useful to gain insight into the behavior of the path of comet HRC during temporary capture. [13, 24] However, it is notable that the manifold structures on the map become diffuse as the manifolds evolve (such as for  $\gamma_{y_2 z_2}^{U;2} - \gamma_{y_4 z_4}^{U;4}$  in Figures 5.4(c)–5.4(d)). The resulting lack of structure on the map presents difficulties when attempting to locate initial conditions ‘inside’ the manifold tubes. Additionally, the computation required to locate a sufficient number of sample members from the families of quasi-periodic orbits that comprise the center manifold associated with a libration point is nontrivial, and a large number of manifold arcs must be numerically integrated to obtain the Poincaré maps. Thus, alternative methods to locate trajectories with specified behaviors are useful.

## 5.2 Locating Periodic Orbits in the Spatial Problem

Poincaré maps prove useful to reveal structures that indicate the existence of nearby periodic orbits. In the planar problem, quasi-periodic orbit structures in the vicinity of a stable periodic orbit form concentric rings on a map and the existence of a central stable periodic orbit may be inferred when such structures appear [48, 50]. Quasi-periodic orbits in the spatial problem are higher-dimensional, however; thus, the structures formed by crossings of quasi-periodic tori with a surface of section are also higher-dimensional. In this section, Poincaré maps are employed in the spatial problem to search for symmetric, stable periodic lunar orbits. To begin the discussion, it is useful to first consider the problem of locating periodic orbits in the planar problem. Periapse maps have been employed previously for this problem and prove useful for this discussion.

### 5.2.1 Periapse Maps

The use of periapse maps displaying crossings of invariant manifolds asymptotic to planar Lyapunov orbits, as well as crossings resulting from numerical integration of a grid of periapse initial conditions in the  $P_2$ -region, has been demonstrated to locate regions of quasi-periodic nontransit solutions and their central periodic orbits by Haapala [14], as well as Davis and Howell [27, 28]. Previous work employing periapse maps includes the classification of regions of immediate escape/capture by Villac and Scheeres [47] and by Paskowitz and Scheeres [25] in the Hill three-body problem. The periapse map, defined for passages of perilune in the Earth-Moon system, is computed by recording crossings of the surface of section  $\Sigma_r = \{\bar{x}|\dot{r} = ((x - 1 + \mu)^2 + y^2 + z^2)^{\frac{1}{2}}, \dot{r} = 0, \ddot{r} \geq 0\}$ , where  $r$  is the radial distance between  $P_2$  and  $P_3$ . Recall that, in the planar problem, the manifolds asymptotic to the planar Lyapunov orbits bound transit trajectories that connect adjoining regions of the ZVCs. Crossings of the invariant manifolds with the Poincaré map yield contours that yield boundaries for regions on the map that are associated with transit trajectories. For example, consider the periapse map representing crossings of the unstable manifold associated with an  $L_1$  Lyapunov orbit for  $C = 3.172$ , as depicted in Figure 5.5(a). Manifold periapses over a 2.5-year simulation are plotted in black; the first three periapses along  $L_1$  entry trajectories are plotted in orange, cyan, and magenta, respectively. An analogous map of periapses along the  $L_2$  Lyapunov unstable manifold, and  $L_2$  entry trajectories appears in Figure 5.5(b). Here, orange, cyan, and magenta points correspond to the first, second, and third passages of perilune after entry through  $L_2$ . Note that the  $L_2$  gateway is very narrow, indicating that temporary capture through  $L_2$  is less probable, thus, the colored regions on the map are considerably smaller when compared with the  $L_1$  transit regions. The dotted lines on the maps supply a boundary between periapses and apoapses (i.e.,  $\ddot{r} = 0$ ). These maps prove useful for the location of long-term capture trajectories. Because trajectories that lie within the

manifold asymptotic to a Lyapunov orbit necessarily transit to an adjoining region of the ZVCs, it is possible to identify regions on the map that are not visited by the manifold and that correspond to regions of long-term capture. Gridding the region within the ZVCs with initial conditions and integrating in reverse-time, a background map is generated. For initial conditions that lead to (reverse-time) escape through either the  $L_1$  or  $L_2$  gateways, all subsequent crossings of the map are colored in magenta in Figure 5.5(c). Periapses along trajectories that remain captured for the 2.5-year simulation are plotted in cyan. Map crossings along the unstable manifolds associated with both the  $L_1$  and  $L_2$  Lyapunov orbits are also included in black. Vacant regions, not visited by the unstable manifolds, are visible and correspond to regions of periapses associated with long-term capture trajectories. These vacant regions are filled by the cyan capture orbit periapses on the map in Figure 5.5(c). Concentric contours in the cyan regions of long-term capture periapses are centered on a nearby periodic orbit. Initial conditions within the innermost contour are useful to seed a differential corrections algorithm to locate the periodic solution. Two sample periodic orbits are computed using initial guesses from the map and appear in Figure 5.6 with passages of perilune plotted as red points.

Increasing the energy level, the maps from Figure 5.5 are reproduced for  $C = 3.15$  and appear in Figure 5.7. Clearly, the  $L_2$  gateway has expanded and the periapses along  $L_2$  transits fill larger regions on the map. Sample transit trajectories are computed by selecting a periapsis within the magenta regions on the maps in Figures 5.7(a)–5.7(b) and integrating in reverse-time; the resulting paths are overplotted in blue with black periapses. Producing a background map, as in Figure 5.7(c), it is apparent that the region of periapses corresponding to long-term capture is reduced by increasing the energy level. For  $C = 3.15$ , all of the planar long-term capture orbits impact the Moon. It should be noted that, while these long-term capture periapses correspond to orbits that remain in the vicinity of the Moon for the 2.5-year

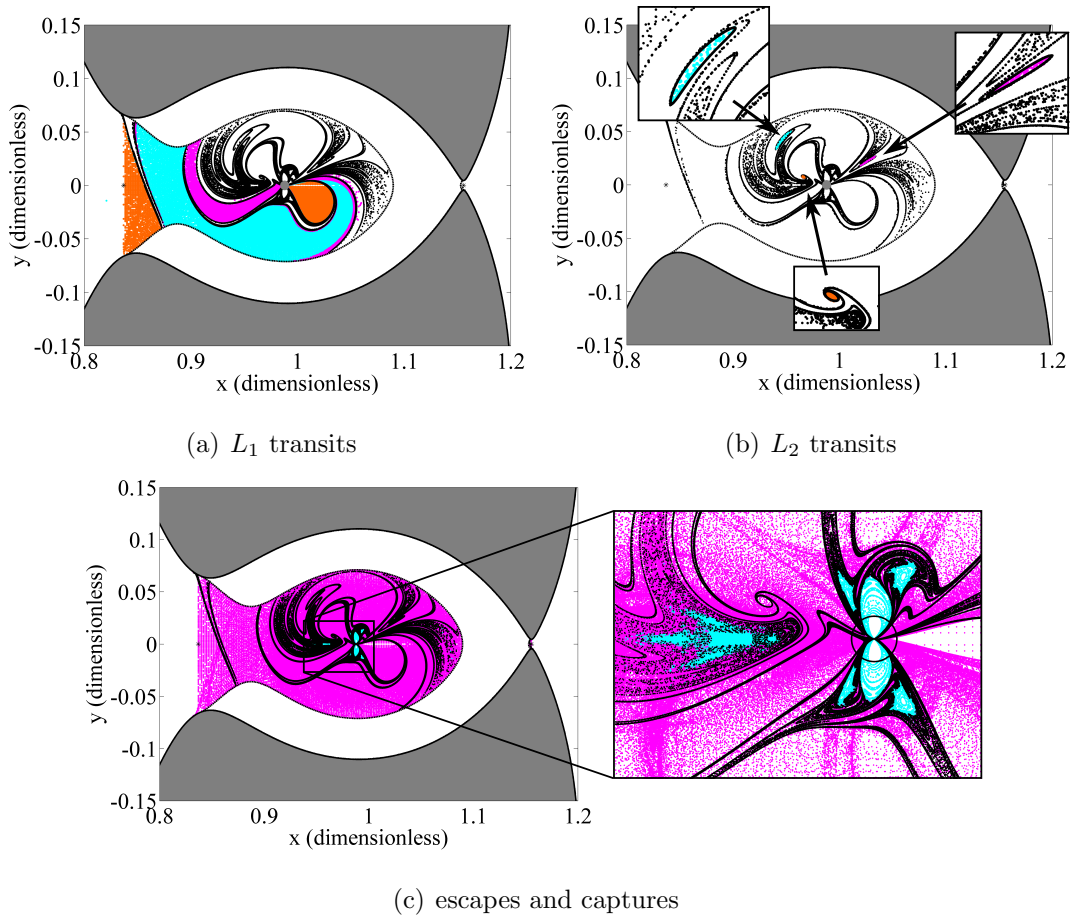


Figure 5.5. Planar periapse map for  $C = 3.172$  in the Earth-Moon system, (a) first, second, and third periapses along  $L_1$  temporary capture trajectories plotted in orange, cyan, magenta, and periapses along  $L_1$  unstable manifold plotted in black, (b) first, second, and third periapses along  $L_2$  temporary capture trajectories plotted in orange, cyan, magenta, and periapses along  $L_2$  unstable manifold plotted in black, (c) periapses along transit (magenta) and nontransit (cyan) trajectories

reverse-time simulation, many of these trajectories may escape if integrated over a longer time interval.

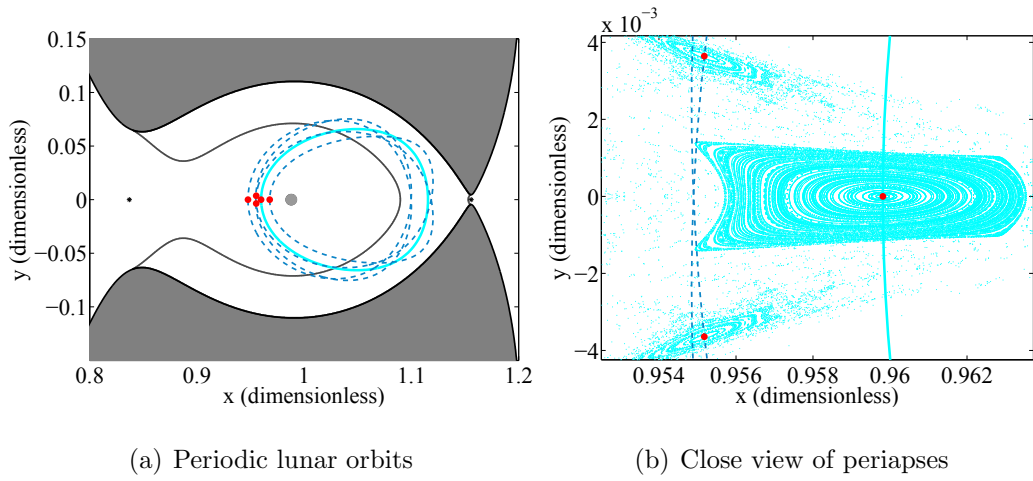


Figure 5.6. A pair of sample periodic orbits is computed via an initial guess from the cyan region of the periapse map for  $C = 3.172$  in the Earth-Moon system

### 5.2.2 Perpendicular Crossing Maps

While periapse maps are useful for the location of periodic orbits in the planar problem, the task of locating periodic orbits using Poincaré maps in the spatial problem is nontrivial. In the planar problem, a two-dimensional torus associated with a quasi-periodic orbit can delineate the three-dimensional space defined for a particular value of Jacobi constant. The crossings of these tori on the map form concentric contours, and delineate regions of stability from regions of chaos. However, because a three-dimensional torus cannot delineate the five-dimensional space in the spatial problem defined for a particular energy level, regions of stability on a higher-dimensional Poincaré map may be intermingled with crossings from chaotic trajectories. Thus, the clear structures (periodic orbits, regions of stability, chaotic zones) that are often visible in planar Poincaré maps may not be as readily distinguishable in the spatial problem. Higher-dimensional Poincaré maps may still prove useful in the search for periodic orbits in the spatial problem, however (e.g., Patsis and Zachilas [20]). This search may be simplified by exploiting the mirror theorem, which

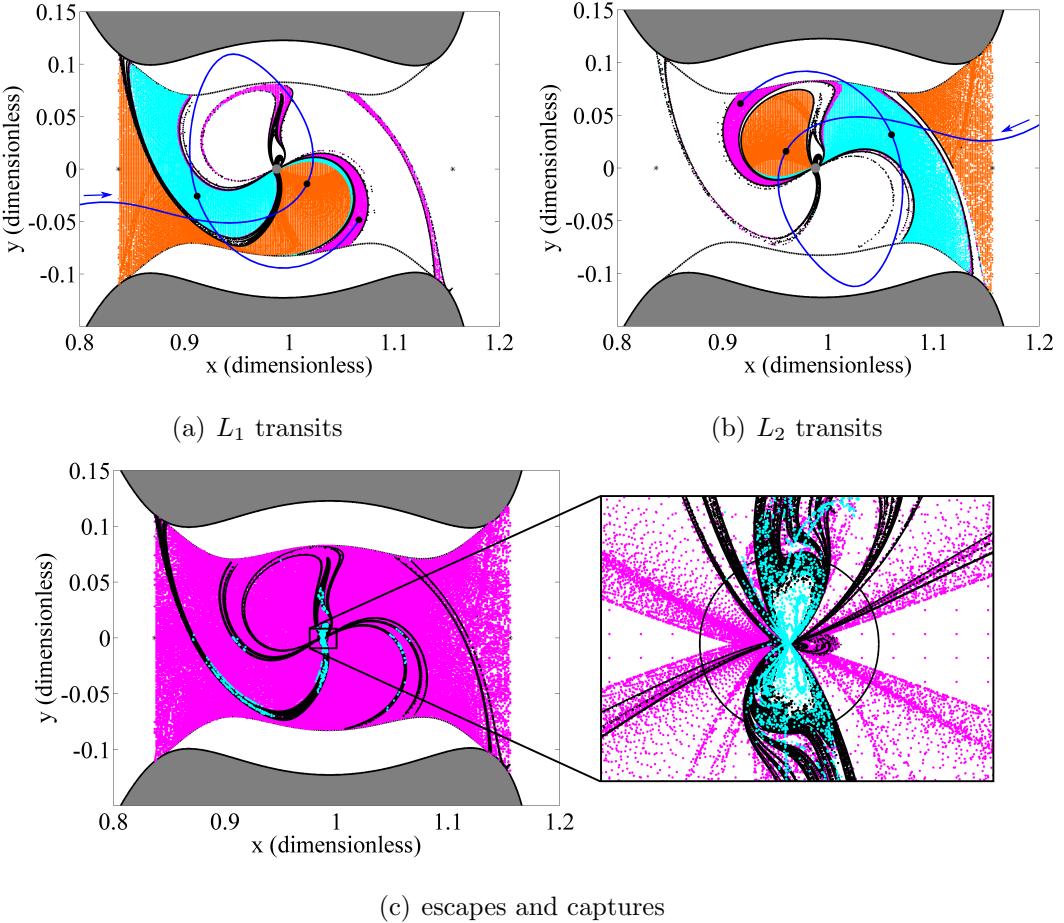


Figure 5.7. Planar periapse map for  $C = 3.15$  in the Earth-Moon system, (a) first, second, and third periapses along  $L_1$  temporary capture trajectories plotted in orange, cyan, magenta, and periapses along  $L_1$  unstable manifold plotted in black, (b) first, second, and third periapses along  $L_2$  temporary capture trajectories plotted in orange, cyan, magenta, and periapses along  $L_2$  unstable manifold plotted in black, (c) periapses along transit (magenta) and nontransit (cyan) trajectories

stipulates that any trajectory possessing perpendicular crossings of the  $x$ - $z$  plane at two distinct times is necessarily periodic [29]. To locate solutions that possess more than one perpendicular  $x$ - $z$  plane crossing, a grid of initial conditions on the  $x$ - $z$  plane is generated such that  $y = \dot{x} = \dot{z} = 0$ , and  $\dot{y}$  is selected to satisfy a particular value of

Jacobi constant. (Note that each of these grid points is, necessarily, an apse.) Each state on the grid is propagated for  $t = 210 \approx 2.5$  years. Returns to the  $x$ - $z$  plane are recorded, and map crossings for which  $|\dot{x}| > \delta$  and  $|\dot{z}| > \delta$  are removed from the set of returns. The resulting map is an approximation for the map defined by crossings of the surface  $\Sigma_{\perp} = \{\bar{x}|y = 0, \dot{x} = 0, \dot{z} = 0\}$ , and appears in Figure 5.8(a). Here,  $\delta = 2 \times 10^{-3} \approx 2.049$  m/s is selected for orbits that remain captured during the integration time, and  $\delta = 1 \times 10^{-2} \approx 10.25$  m/s for those trajectories that escape. While a single *quasi-periodic* trajectory in the vicinity of a stable orbit cannot cross  $\Sigma_{\perp}$  more than once in a finite time interval, a large number of quasi-periodic solutions may cross the surface once in the vicinity of the periodic orbit, forming visible structures of regions of increased density on the map. Even unstable periodic orbits with small unstable eigenvalues may possess a large number of neighboring trajectories that cross the map nearby the periodic solution before escaping. To search for periodic orbits, initial conditions within the dense regions of returns on the map in Figure 5.8(a) are selected and are numerically integrated. Trajectories that are nearly closed after a selected propagation time are employed as the initial guess for a corrections algorithm that enforces periodicity. Perpendicular crossings along a sample set of periodic orbits computed using this technique are plotted in Figure 5.8(b), where red points correspond to unstable and blue points represent linearly stable orbits. Note that several of the unstable orbits possess a maximal eigenvalue very near magnitude one. The map crossings along the periodic orbits are sorted and displayed in Figure 5.8(c) so that each color corresponds to a particular orbit geometry. Open circles and squares correspond to orbits whose crossing of  $\Sigma_{\perp}$  nearest to the Moon is on the lunar far side; solid circles and squares represent crossings along orbits for which the nearest crossing lies to the left of the Moon on the map. For a particular color of crossing, the solid squares represent crossings along the orbit that is the reflection of the trajectory associated with the solid circles across the  $x$ - $y$  plane. Likewise, open squares and circles represent crossings along two distinct orbits that are the reflection

of one another across the  $x$ - $y$  plane. To explore the relationship between the periodic orbits and invariant manifolds asymptotic to the center subspaces of  $L_1$  and  $L_2$ , a map displaying the crossings of each with  $\Sigma_\perp$  appears in Figure 5.8(d). Crossings along the unstable manifold associated with  $L_1$  and  $L_2$  appear in black; initial conditions from a background grid that, when propagated in reverse-time, yield transit/nontransit trajectories are plotted in magenta/cyan. From this representation, it is clear that all of the computed linearly stable periodic orbits (blue points) exist within the cyan region corresponding to nontransit solutions. Several of the blue points lie within the cyan region, but just outside the boundary formed by the manifolds. Additionally, several of the unstable periodic orbits possess crossings that lie within the cyan region corresponding to long-term capture. It should be noted, however, that each of these unstable periodic orbits possess a small maximal eigenvalue (the largest being  $\max |Re(\bar{\lambda})| = 2.6781$ , where  $\bar{\lambda}$  is the vector containing all eigenvalues of the monodromy matrix for a periodic orbit) indicating that trajectories in the vicinity of the periodic orbit escape over long time scales. In fact, integrating the periodic orbits that lie within the cyan region of the map for  $t = 5000 = 59.45$  years in both forward- and reverse-time, they all remain bounded in the vicinity of the Moon.

To help clarify the structures formed by the invariant manifolds on the map in Figure 5.8(d), it is useful to consider the relationship between the surfaces of section  $\Sigma_\perp$  and  $\Sigma_r$ . By the definition of a periapsis, the surface  $\Sigma_\perp$  is contained within the surface  $\Sigma_r$ , i.e., points for which  $y = \dot{x} = \dot{z} = 0$  correspond to periapses. Thus, each crossing of the maps in Figure 5.8 corresponds (approximately, considering the tolerance  $\delta$ ) to a passage of perilune. Where the perilune map intersects the  $x$ - $z$  plane, the condition that  $(x - 1 + \mu)\dot{x} + z\dot{z} = 0$  must be met for each point on the map. Periapse map crossings on the  $x$ - $z$  plane must be perpendicular to this plane when  $x \neq 0$  and  $z \neq 0$ , unless  $(x - 1 + \mu)\dot{x} = -z\dot{z} \neq 0$ . A batch of  $L_1$  and  $L_2$  three-dimensional transit trajectories is computed, and the first passage of perilune is recorded after entry to the  $P_2$  (Moon) region. A projection of the first crossings

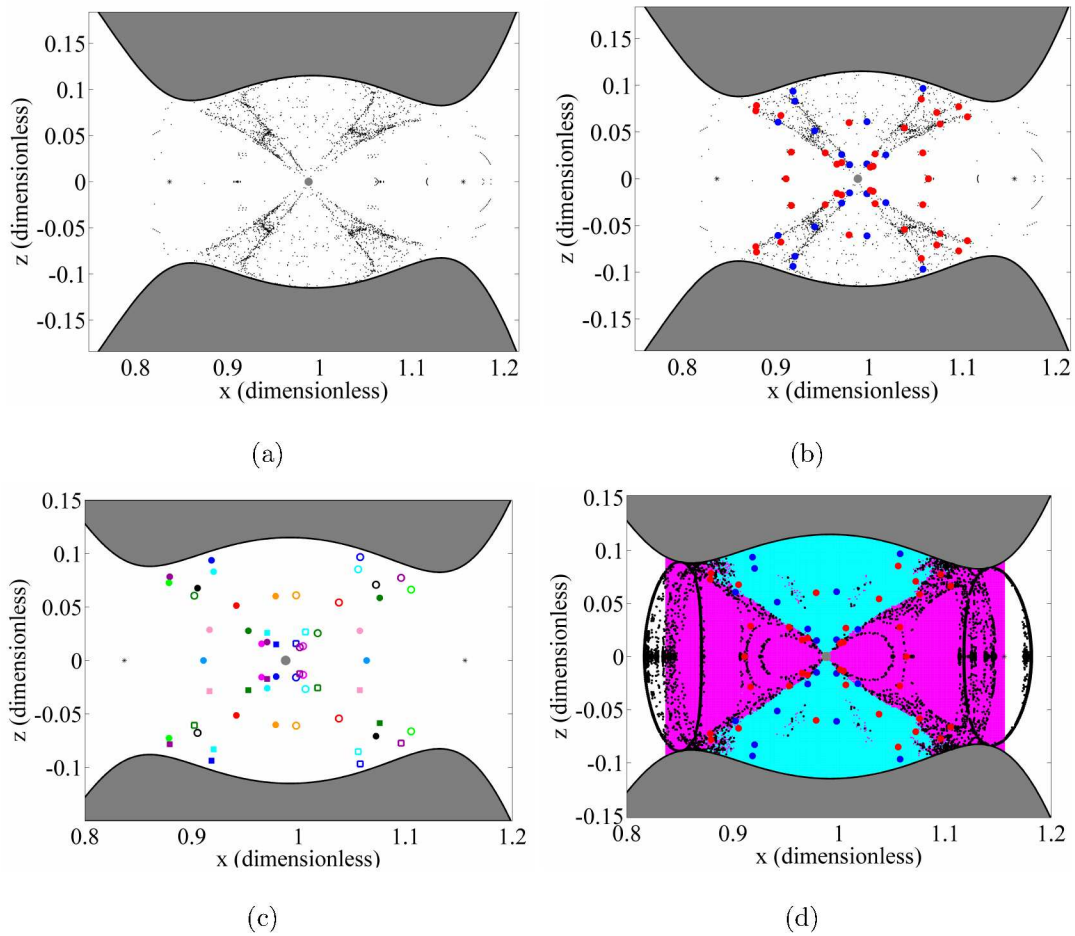


Figure 5.8. Maps representing perpendicular crossings associated with periodic orbits in the Earth-Moon system, (a) returns to  $y = 0$  surface with  $|\dot{x}|, |\dot{z}| < \delta$ , (b) returns to map with periodic orbit crossings over-plotted and colored consistent with linear stability (c) sorted crossings of sample periodic orbits, (d) crossings, colored consistent with linear stability, displayed with crossings of invariant manifolds in black; initial conditions corresponding to transit (cyan) and long-term capture (magenta) also displayed

of  $L_1$  and  $L_2$  entry trajectories into the  $x$ - $y$  plane appears in Figures 5.9(a)–5.9(b). Note that the projection into the  $x$ - $y$  plane of the first periapses along transits in the spatial problem closely matches the first periapses along planar transit trajectories, plotted in Figures 5.7(a)–5.7(b). In Figures 5.9(c)–5.9(d), the intersection between

the periapse map and the  $x$ - $z$  plane is visible along the gray plane. The manifold crossings of the surface  $\Sigma_{\perp}$  are included in black, and indeed appear to bound the transit trajectories.

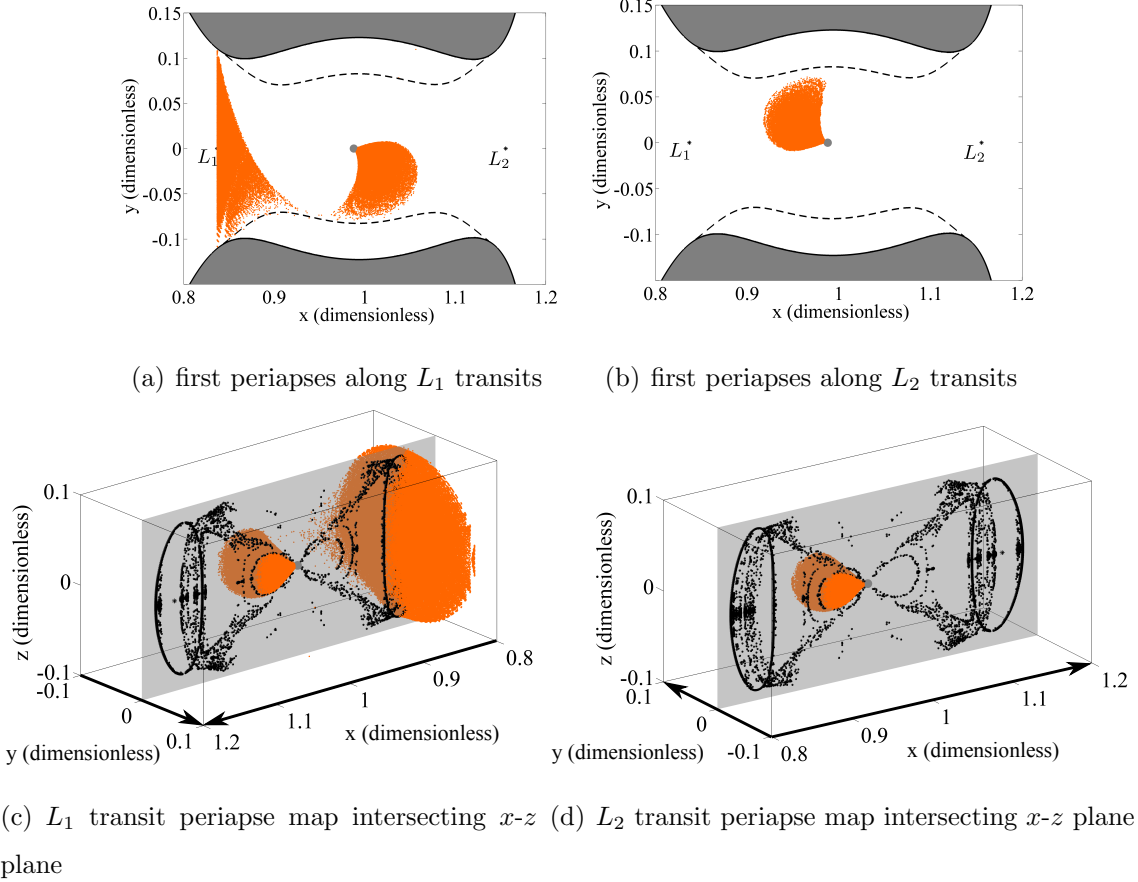


Figure 5.9. Maps corresponding to surfaces  $\Sigma_{\perp}$  and  $\Sigma_r$  in the Earth-Moon system

Projections of sample orbits, colored consistent with the map in Figure 5.8(c), onto the  $x$ - $y$  and  $x$ - $z$  planes are displayed in Figures 5.10 and 5.11. These orbits correspond to the solid circles or squares on the map in Figure 5.8(c). The orbits associated with the open circles or squares on the map appear essentially as the reflections of the orbits in Figures 5.10 and 5.11 across the  $y$ - $z$  plane, so that the nearest crossing of  $\Sigma_{\perp}$  is on the lunar far side. The plots in Figure 5.10 span  $1.225 \times 10^5$  km (the distance between  $L_1$  and  $L_2$ ) and  $6.535 \times 10^4$  km along the  $x$ - and  $y$ -axes, respectively. The

plots in Figure 5.11 span  $1.225 \times 10^5$  km and  $7.457 \times 10^4$  km along the  $x$ - and  $z$ -axes. The maximum real part of the eigenvalues,  $\max|Re(\bar{\lambda})|$ , associated with each periodic orbit appears in Table 5.1, in addition to the orbital period. The ‘Orbit Label’ in

Table 5.1 Properties of Periodic Orbits

Orbit Label	$\max Re(\bar{\lambda}) $	$T$ (days)
a	1.1534	21.6943
b	1	23.3841
c	1.7027	23.5697
d	17.1942	21.0535
e	2.8059	20.3035
f	3.0344	44.2226
g	5.5439	26.9540
h	1	25.4193

the table corresponds to the subfigure labels in Figures 5.10 and 5.11. Orbits of similar geometry to the orbit in Figures 5.10(d) and 5.11(d) are demonstrated in Michalodimitrakis [62] as well as Lara and Russell [63], who compute these orbits by identifying bifurcating orbits within families of planar solutions.

By exploiting existing techniques to reduce the dimension of a Poincaré map, new trajectory design applications can be explored. Here, strategies to compute transit trajectories in the spatial problem prove useful to examine the relationship between the behavior of comets that experience temporary capture by Jupiter and the invariant manifold structures associated with the collinear points in the Sun-Jupiter system. By additionally exploiting known symmetry properties of the CR3BP, Poincaré maps also prove useful to search for symmetric periodic orbits in the vicinity of the Moon.

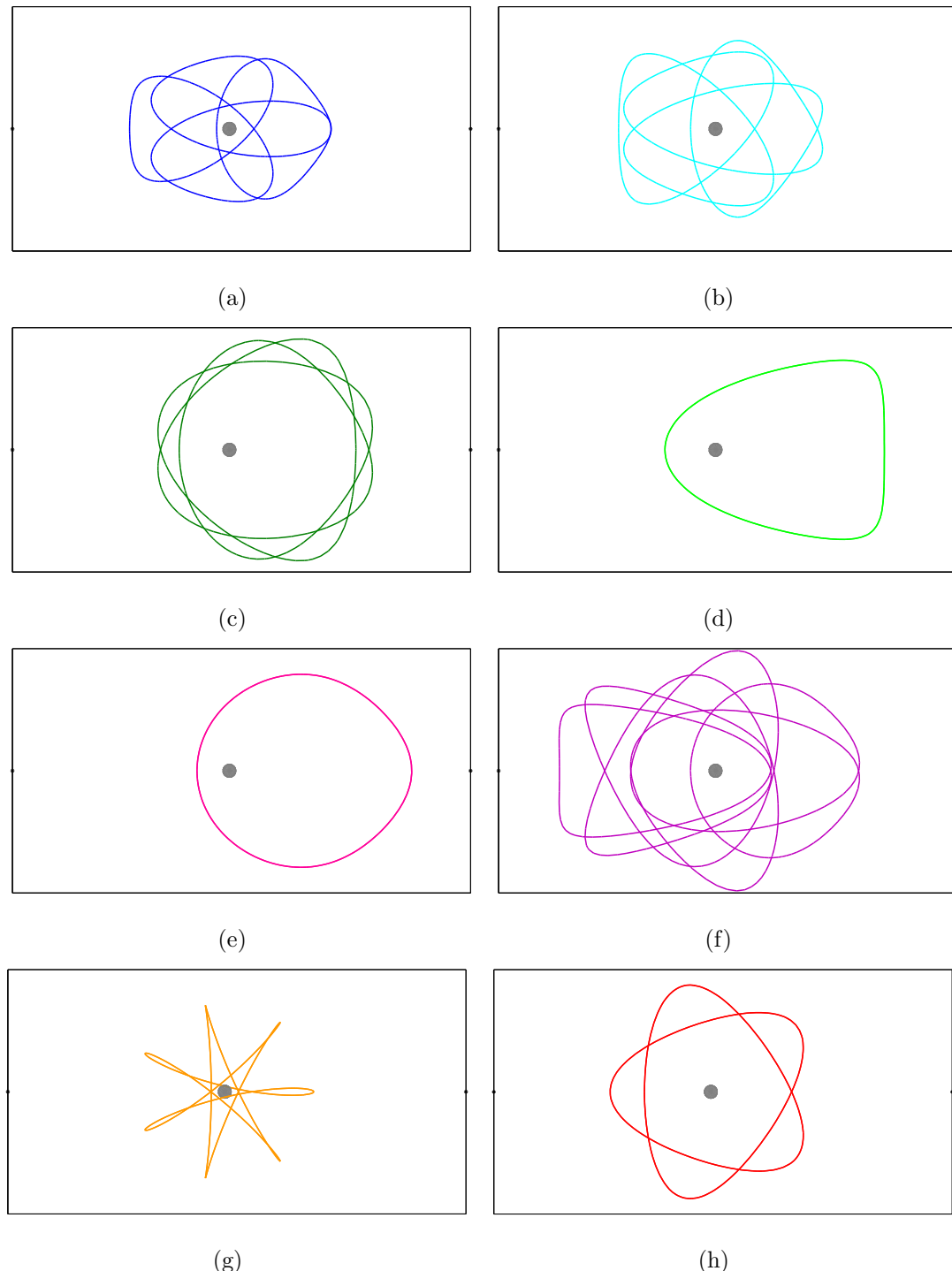


Figure 5.10. Projection of sample periodic orbits onto the  $x$ - $y$  plane in the Earth-Moon system

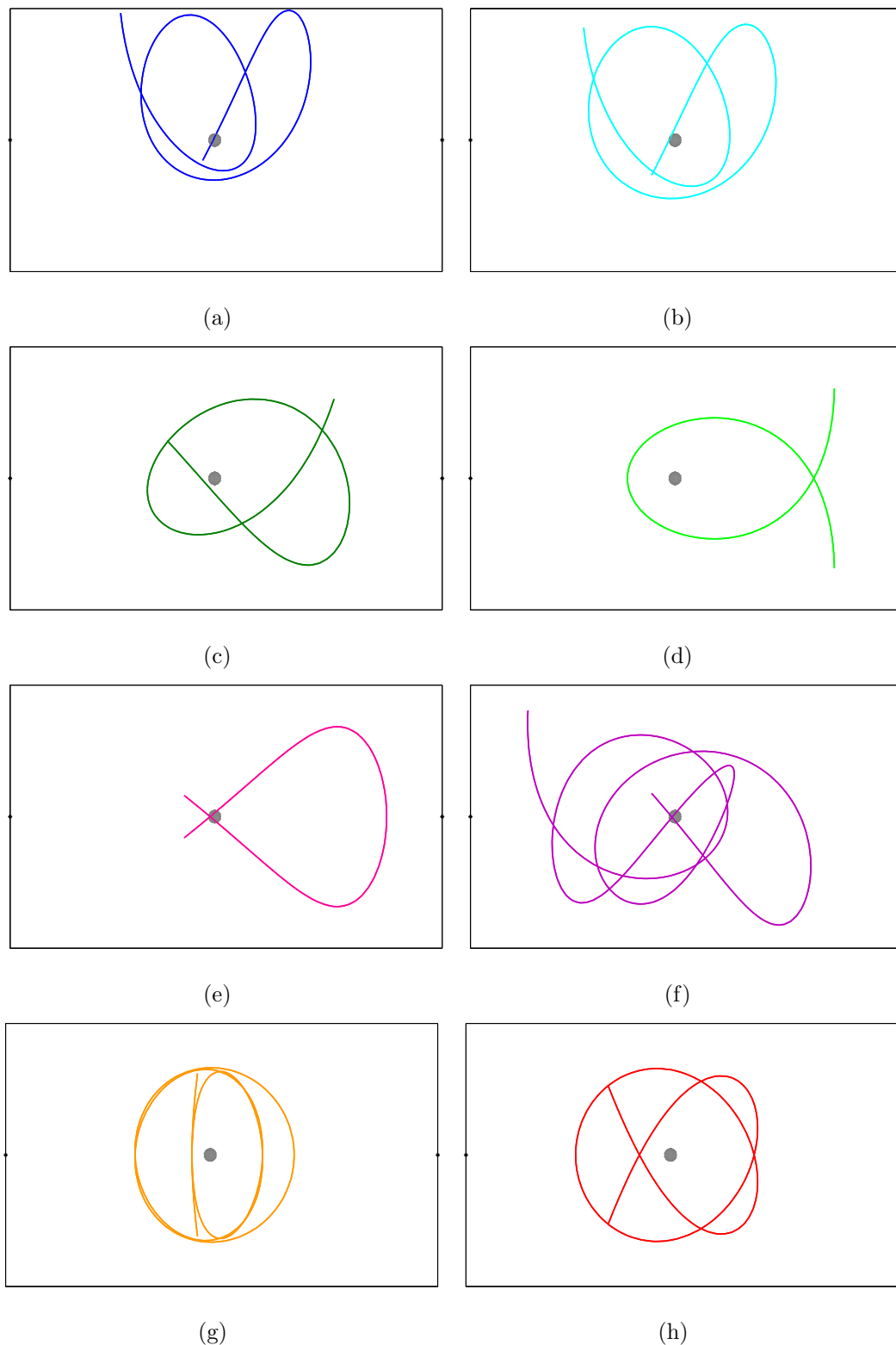


Figure 5.11. Projection of sample periodic orbits onto the  $x$ - $z$  plane in the Earth-Moon system

## 6. REPRESENTING HIGHER-DIMENSIONAL POINCARÉ MAPS

The graphical representation of multivariate data sets is examined extensively in the field of data visualization. Strategies to represent complicated and interconnected information facilitate the exploration of higher-dimensional data sets by exploiting the human ability to perceive and recognize patterns in data. While search algorithms may be employed for data analysis, the development of such algorithms often requires a priori knowledge concerning the solutions of interest. Exploiting the capability of human pattern recognition allows for the potential to reveal new or unexpected solutions. From a trajectory design perspective, a visual representation of the data allows the designer to both develop intuition about the available solution space as well as to remember trends and conclusions, and is useful in an interactive environment.

### 6.1 Data Display Techniques from Multidimensional Data Visualization

Many techniques exist to aid the visualization of higher-dimensional data sets. Parallel coordinates [64], and scatterplot matrices/trellis displays [65] are examples of modifications to the conventional two-axis plot that enable visual inspection of multivariate data. For example, a parallel coordinates plot of an  $n$ -dimensional data point includes a single  $x$ -axis and  $n$  parallel  $y$ -axes distributed with equal spacing along the  $x$ -axis. The data is often normalized or scaled, and the value of the  $i^{th}$  variable is plotted along the  $i^{th}$   $y$ -axis. The values on each vertical axis corresponding to one particular data point are connected so that the final representation for that data point is a series of jointed segments. While this technique does serve to represent multivariate data, the plots can become unwieldy for large data sets. Alternatively,

a scatterplot matrix consists of panels, organized in rows and columns, in which the data are plotted with different combinations of the data variables represented on the axes in each panel. Thus, the relationships between the different variables of interest may be displayed simultaneously. This type of strategy has been previously applied by Howell and Kakoi [66] to design transfers in the patched CR3B problem. These authors simultaneously view various projections of a Poincaré map to locate an intersection between stable and unstable invariant manifolds asymptotic to libration point orbits in different systems, specifically, the Sun-Earth and Earth-Moon systems. By locating such an intersection, transfers between libration point orbits in the two systems are designed.

An alternative approach to represent multidimensional data is via the use of glyphs. In data visualization, a glyph is a graphical entity whose physical characteristics are determined by one or more variables from the data set. An infinite number of unique graphical objects may be defined to represent a data point. A catalog of glyphs employed by previous authors for a variety of applications is presented by Ward [67]. Some examples include metroglyphs and stars [68, 69], Chernoff faces [70], and stick-figures [71]. The use of glyphs proves effective to enable visual inspection of the data, aiding the viewer with the identification of trends or anomalies in a data set. To illustrate their function for pattern recognition, the star, face, and stick-figure glyphs are employed in Figure 6.1 to represent data associated with various Chevrolet vehicles manufactured between 1970 and 1982. The variables represented include the (1) engine horsepower, (2) number of engine cylinders, (3)  $1/(vehicle\ acceleration)$  (acceleration measured in seconds to accelerate from 0 to 60 miles/hour), (4) weight (pounds), and (5) engine displacement (cubic inches). To display this information using stars, the data is scaled and shifted so that the values for each variable are mapped to the interval  $[0.1, 1]$ . The  $i^{th}$  variable is represented via the length of the  $i^{th}$  spoke of the glyph, where  $i = 1$  corresponds to the spoke oriented at  $0^\circ$  from the center. Using the Chernoff faces, the data are again mapped to the interval  $[0.1, 1]$

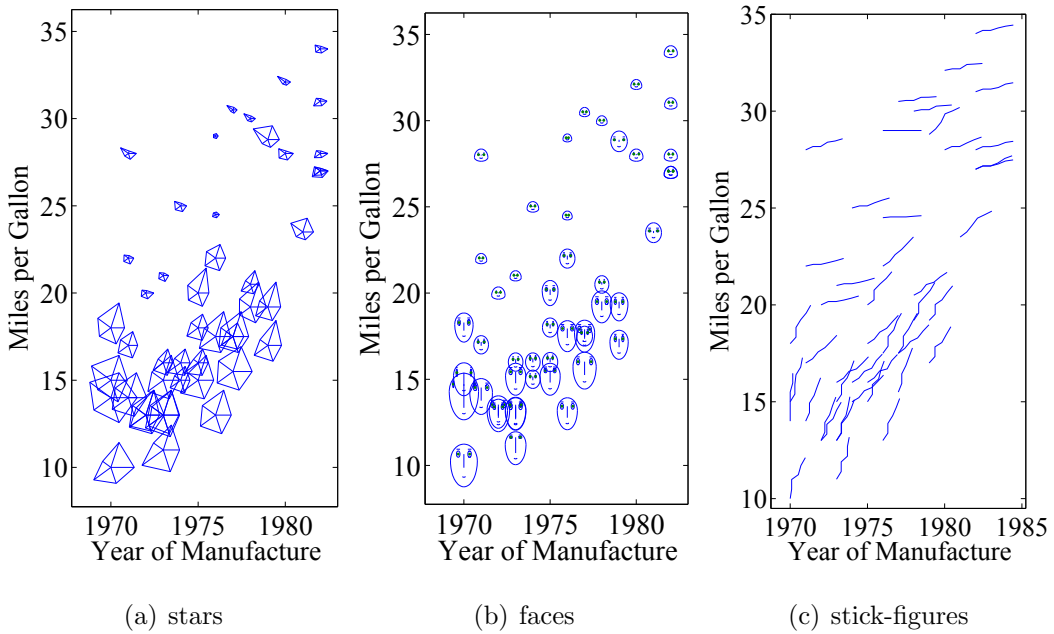


Figure 6.1. Star, face, and stick-figure representations for sample Chevrolet vehicle data

and values for each of the 5 variables are indicated via the ( $i = 1$ ) face size, (2) jaw shape, (3) width between the eyes, (4) vertical position of the eyes, and (5) length of the nose. To represent each data point using stick-figures, each variable of the data is normalized to the interval  $[0, 1]$ . A glyph composed of 5 connected segments is defined such that the orientation (between  $0^\circ$  and  $90^\circ$ ) of the  $i^{th}$  segment is determined by the  $i^{th}$  variable. The center of the star and face glyphs, and the base point location of the first segment in the stick-figure glyph additionally represents the year of manufacture, and the miles-per-gallon (MPG) associated with each vehicle via the  $x$ - and  $y$ -axes of the plot. Note that, defining  $a$  as the vehicle acceleration, the value  $1/a$  is what is represented for the data set so that larger values of  $1/a$  indicate faster acceleration. By representing  $1/a$  instead of  $a$ , each of the variables (1)–(5) is, generally, inversely related to the vehicle MPG.

From the glyph representations in Figure 6.1, several trends and anomalies in the data become visually apparent. Clearly, the vehicle MPG increases with the year of manufacture. Additionally, a region of lower MPG vehicles (represented by the stars with nearly equal spoke lengths, large faces with longer jaws and noses, and nearly vertical stick-figures) emerges that is distinct from the region of higher MPG vehicles, described by the smaller and more spear-shaped stars, smaller and rounder faces, and nearly horizontal stick-figures. Examining the individual glyphs reveals that the lower MPG vehicles are generally associated with greater horsepower, more engine cylinders, shorter acceleration times, greater weight, and larger engine displacement, all of which are intuitive observations. One glyph definition may be better suited for a particular application than others, and the choice of glyph will be problem dependent. In this example, the star and face glyphs may provide the more obvious distinction between the lower and higher MPG regions. An atypical or anomalous data point is also visually apparent from the set. Observing the graphs in Figures 6.1, the glyphs located at the year 1979 and 28.8 MPG within the region of higher MPG vehicles appear distinctive when compared to the surrounding data. The glyph representing this vehicle is similar to the glyphs associated with the lower MPG vehicles — the star glyph has a more equilateral shape, the face glyph is larger with a longer jaw, and the stick-figure is more nearly vertical — however, it lies within the region of higher MPG automobiles and may therefore be of interest for further investigation. Indeed, this glyph represents the 1979 Chevrolet Citation which was among the first front wheel drive compact cars produced by General Motors. This vehicle has a six cylinder engine, while most of the other vehicles in the high MPG group have four cylinders. However, the roughly 800 pounds of weight reduction gained by switching from rear wheel to front wheel drive allowed this car to have increased horsepower and reduced acceleration times, while still maintaining relatively high MPG. In 1980, the Chevrolet Citation was named Motor Trend magazine's Car of the Year. Of the seven vehicles evaluated, the Citation ranked within the top 3 for

all of the testing categories, except for time to complete a 1/4 mile track, and ranked first for vehicle MPG, shortest braking distance from 60 miles/hour, and greatest value for the money [72]. The decision to name the Citation the Car of the Year was later criticized due to poor production quality and low reliability [73].

Clearly, graphical representations, such as glyphs, enable visual inspection of higher-dimensional data and are useful to identify trends and anomalies, as well as regions of interest. In the following discussion, the use of glyphs to represent higher-dimensional Poincaré maps is explored for trajectory design applications.

## 6.2 Visual Representations for Higher-Dimensional Poincaré Maps

Maps in the spatial CR3BP must depict at least four state variables to fully represent crossings of a hyperplane for a given energy level,  $C$ . Thus, a potential application for the use of glyphs in trajectory design is apparent. Representing the crossings of a higher-dimensional Poincaré map using glyphs offers insight into the available solutions and facilitates user-interaction within the design process. While any of the glyph definitions discussed in Section 6.1 may be applied to represent the crossings of a map, a simple glyph that offers an intuitive representation for trajectory design applications is most useful.

The simplest glyph that represents a four-dimensional data point is, perhaps, a single segment. As defined by Pickett and Grinstein [71], the stick-figure glyph requires two segments to identify four variables associated with a particular data point. Two variables are represented by the location of the glyph along the  $x$ - and  $y$ -axes, and the orientation of each segment denotes the value associated with each additional variable. However, by varying both the length and orientation of each segment, four states are simultaneously represented. In this investigation, this alternative definition for the stick-figure glyph is adopted: two states are indicated by the coordinates of the segment basepoint, and two additional coordinates are represented by the length

and orientation of the segment. Then, the points used to represent crossings of a Poincaré map in the planar problem (e.g., Figure 4.3(b)) may be replaced with single segments, or vectors, in the spatial problem to represent four state variables while still employing a two-dimensional image for the visualization. One sample glyph definition appears in Figure 6.2, where  $q_i$ ,  $i = 1\text{--}4$  correspond to a set of selected state

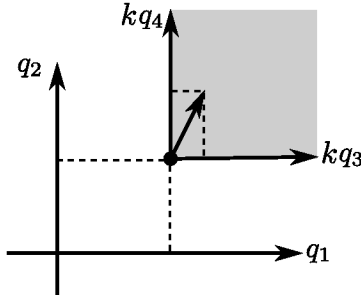


Figure 6.2. Glyph representation for a four-dimensional data point

variables and  $k$  is a scaling constant. For example, as one possible representation for crossings of  $\Sigma = \{\bar{x}|x = \text{constant}\}$  corresponding to a specified value of Jacobi constant, the state variables  $q_1 = y$ ,  $q_2 = z$ ,  $q_3 = \dot{y}$ ,  $q_4 = \dot{z}$  are displayed on the map. The basepoint of the vector indicates the position  $(y, z)$ , and supplies the origin for a second coordinate frame used to locate the velocity states  $k\dot{y}$  and  $k\dot{z}$ . The remaining state,  $\dot{x}$ , is then determined by the Jacobi constant value. If two crossings of a Poincaré map are represented by vectors for which the basepoints are nearly aligned, and the vector segments are of roughly the same length and orientation, then the states  $y$ ,  $z$ ,  $\dot{y}$ , and  $\dot{z}$  are assumed to be nearly the same for the pair of crossings. If those crossings are associated with the same value of Jacobi constant, then it is expected that the velocity  $\dot{x}$  is also similar in magnitude for these crossings. Note that, for general applications, different scaling constants can be applied to  $q_3$  and  $q_4$ .

Early use of vectors to represent information about a force field began with the study of electric and magnetic fields. To visualize magnetic forces, Michael Faraday introduced the idea of *lines of force* that permeate the space around a magnet. He

“imagined space around a magnet filled with a huge bundle of lines each of which, like a drawn arrow, had a definite direction, giving at any point the local direction of magnetic force [74].” Building on the work of Faraday, James Clerk Maxwell notes that, by displaying these lines of force, one would “obtain a geometrical model of the physical phenomena, which would tell us the *direction* of the force, but we should still require some method of indicating the *intensity* of the force at any point [75].” He proposes that a line of force curve be instead represented as a tube of variable section, where the cross-sectional area denotes intensity of the field along the curve [75]. Alternatively, variation of the magnitude and direction of the vectors, or the density of the lines of force drawn allow the intensity of the field to be represented [76]. In his investigation of behavior in the spatial CR3BP, Froeschlé [16] makes reference to the use of a glyph similar to that defined in Figure 6.2; however, he notes that this representation is difficult to interpret for background maps depicting crossings from a random initial conditions grid and does not employ this method for his results.

Glyphs are first employed to represent the crossings of a periapse map by Paskowitz and Scheeres [25]. The glyph employed by these authors is projected into three-dimensional configuration space to represent all six state variables. Alternatively, the glyph definition in Figure 6.2 may be viewed in a planar image, thus, a single projection of the map provides all of the information. This glyph representation is introduced for use with strategies to locate transfers between periodic orbits in the spatial problem by Haapala [77]. This definition is employed to compute a variety of maneuver-free and low-cost transfers between libration point orbits by Haapala and Howell [77, 78]. The definiton of this glyph is modified by Haapala and Howell [55] to represent six state variables, and is demonstrated to compute transit trajectories in the spatial problem. Vaquero [79] later adopts the strategy of employing glyphs to represent the crossings of a Poincaré map to compute transfers between resonant orbits in the spatial problem.

### 6.3 Employing Maps to Compute Libration Point Orbit Transfers

Poincaré maps may be applied to a variety of mission design scenarios. Employing glyphs to represent the crossings of higher-dimensional Poincaré maps, the maps can be utilized as an interactive trajectory design tool in the spatial problem. One design problem of interest is the computation of low-cost, short duration transfers between libration point orbits. For example, heteroclinic and homoclinic connections are free transfers that connect two distinct orbits, or an orbit back to itself, respectively, for zero  $\Delta v$ . Free transfers between quasi-periodic orbits are presented by Gómez et al. [13, 23] and Masdemont [80]. Masdemont [80] also computes connections between quasi-periodic and periodic orbits. Here, higher-dimensional Poincaré maps are demonstrated for the computation of low-cost and maneuver-free transfers between *periodic* libration point orbits. Stuart et al. [81] employ invariant manifolds in addition to low-thrust arcs to transfer between periodic libration point orbits in the CR3BP. In this investigation, only impulsive maneuvers are considered.

Orbits in the vicinity of the collinear libration points have been considered for storage depots for supplies or fueling stations for missions to Mars and the Moon. An exploration of the available transfers between libration point orbits is useful to assess the possibility of a network of storage orbits. Consider a sample design scenario in which a transfer from an  $L_1$  vertical to an  $L_2$  halo orbit is sought in the Earth-Moon system. The unstable manifold associated with the vertical orbit and the stable manifold asymptotic to the halo orbit are useful in the search for a transfer arc. An infinite number of transfers between members of the  $L_1$  vertical and  $L_2$  halo orbit families are possible, each defined by: (1) the initial vertical orbit within the family, (2) the ‘departure’ location along the vertical orbit, (3) the terminating halo orbit within the halo family, (4) the ‘insertion’ location along the halo orbit, and (5) the number of revolutions about the Moon that are incorporated (i.e., the time-of-flight). Employing manifolds to locate a transfer, the ‘departure’ and ‘insertion’ locations

along a particular orbit refer to the  $\tau$  value associated with a particular manifold arc, as defined in Chapter 3.4.3. For this example, an optimal transfer is desired such that the  $\Delta v$  required for the transfer is minimized while also maintaining a relatively low time-of-flight. The hyperplane  $\Sigma_{P_2}^+ = \{\bar{x} : x = 1 - \mu, \dot{x} > 0\}$  is selected for this example because it lies between the  $L_1$  and  $L_2$  points, although alternative hyperplanes could also be employed and may yield different solutions. To maintain a low time-of-flight, the manifolds are propagated only until their first crossing of  $\Sigma_{P_2}^+$ . A subset of arcs along the manifolds associated with vertical and halo orbits for  $C = 3.0555$  are displayed in Figure 6.3(a), in addition to the projection of  $\Sigma_{P_2}^+$  into configuration space as the gray plane. Numerical integration of the manifold arcs is terminated upon arrival at  $\Sigma_{P_2}^+$ , and the projection of the resulting Poincaré map into the  $y$ - $z$  plane appears in Figure 6.3(b). Note that  $x = 1 - \mu$  corresponds

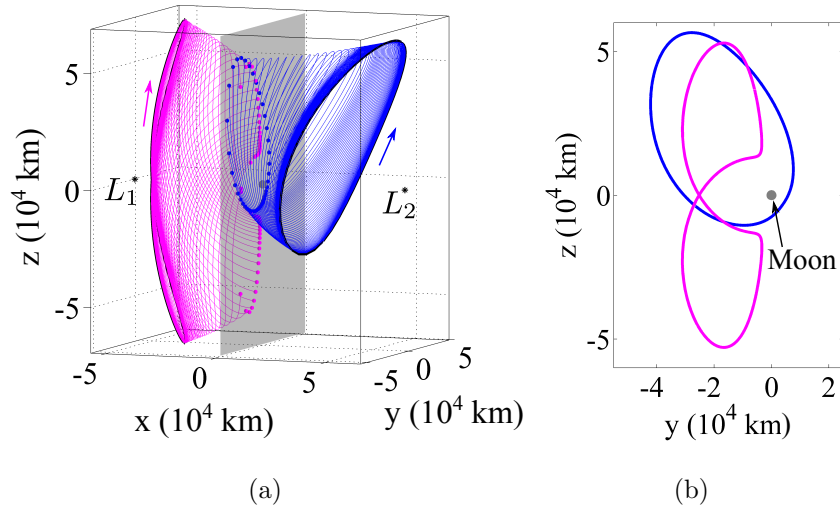


Figure 6.3. Manifolds are employed to search for a transfer between  $L_1$  vertical and  $L_2$  northern halo orbits in the Earth-Moon system,  $C = 3.0555$

to  $x = 0$  in Moon-centered coordinates. Inspection of the map reveals four feasible transfer opportunities that exist, corresponding to locations on the map where the magenta and blue contours intersect. However, no velocity information is available

from this projection of the map, making it difficult to select the transfer that requires minimal  $\Delta v$ . Thus, the interest in strategies to display both the position states and the associated velocity data is apparent.

The computation of a transfer between periodic orbits in the vicinity of  $L_1$  and  $L_2$  begins with the selection of the desired orbits within the orbit families. It is intuitive to initiate the search by selecting the vertical and halo orbits near the ‘beginning’ of their respective families. The  $L_1$  vertical orbits emanate from the  $L_1$  point, and therefore can be computed for  $C \leq 3.188$ . The  $L_2$  halo family originates with the bifurcating member of the Lyapunov family, which corresponds to a Jacobi constant value near  $C = 3.152$ . Because the  $L_2$  halo family does not exist for  $C > 3.152$ , the energy level  $C = 3.152$  offers an initial Jacobi constant value for the search. The Poincaré map corresponding to the manifolds associated with vertical and halo orbits for a nearby value,  $C = 3.14$ , appears in Figure 6.4(a). Each map crossing is now plotted using the glyph definition from Figure 6.2, such that  $(q_1, q_2) = (y, z)$  and  $(q_3, q_4) = (\dot{y}, \dot{z})$ . Thus, the basepoint of each segment represents the states  $y$  and  $z$ , and the segment length and orientation are determined by the states  $\dot{y}$  and  $\dot{z}$ . Here, the velocities have been scaled by a factor of  $k = 10000$  for clarity of the plot. All stable and unstable manifold crossings are plotted as vectors in gray on the map, while the stable/unstable crossings nearest to the four intersections of the magenta and blue contours from Figure 6.3(b) are plotted in blue/magenta in Figure 6.4. The pairs of crossings nearest the intersection of the contours in the  $y$ - $z$  projection are additionally labeled 1–4. Clearly, large velocity discontinuities exist for all four transfer opportunities, indicating that the manifolds associated with the vertical and halo orbits for  $C = 3.14$  may not offer a globally optimal transfer. (Note that allowing longer times-of-flight, i.e., propagating the manifolds through multiple crossings of  $\Sigma_{P_2}^+$ , could yield additional transfer options with smaller velocity discontinuities.) Considering the values  $C = 3.10$  and  $3.06$ , the maps in Figures 6.4(b)–6.4(c) are computed. Observing the behavior represented in the maps in Figure 6.4, it is evident

that the cost associated with the transfer opportunity labeled 2 reduces with  $C$  for this range of Jacobi constant values. The  $\Delta v_i$  for each transfer opportunity  $i = 1\text{--}4$  is computed and the values are listed in Table 6.1. Each  $\Delta v_i$  corresponds to the

$C$	$\Delta v_1$ (m/s)	$\Delta v_2$ (m/s)	$\Delta v_3$ (m/s)	$\Delta v_4$ (m/s)
3.14	1182	630	906	872
3.10	649	296	924	453
3.06	265	77	885	231

Table 6.1 Approximate cost for transfers 1→4

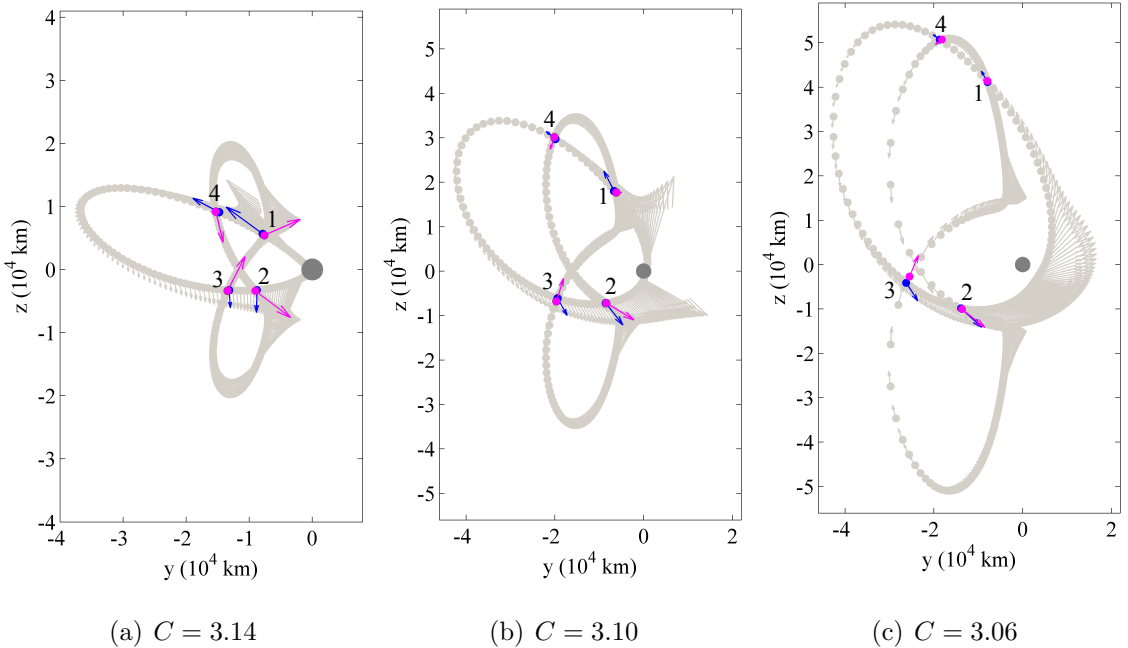


Figure 6.4. Searching for transfers between  $L_1$  vertical and  $L_2$  northern halo orbits in the Earth-Moon system

total  $\Delta v$  in all three velocity states, and not just the discontinuity between the  $y$ - and  $z$ -velocities as represented on the map. Note that position discontinuities also exist for each of the transfers in the table and that these discontinuities are in the

$y$ - and  $z$ -coordinates only. Selecting the manifolds corresponding to the pair of map crossings labeled 2 in Figure 6.4(c) yields an initial guess for a transfer between the vertical and halo orbits for  $C = 3.06$ . The velocity discontinuities for the initial guess are  $\Delta\dot{x} = 65.5$  m/s,  $\Delta\dot{y} = 39.0$  m/s, and  $\Delta\dot{z} = 10.2$  m/s. This initial guess supplies the seed for an optimization algorithm that searches for the vertical and halo orbits, as well as the associated manifolds, that deliver a local minimum in the required transfer  $\Delta v$ . The locally optimal solution appears in Figure 6.5 and requires a maneuver of  $\Delta v = 7.918$  m/s to connect the magenta and blue manifold arcs. Two

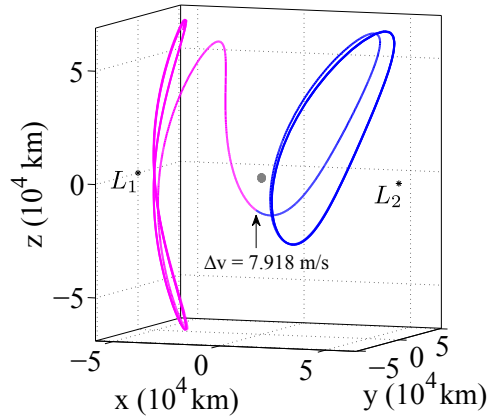


Figure 6.5. Locally optimal transfer in the Earth-Moon system,  $C_1 = 3.0571$ ,  $C_2 = 3.0468$ , TOF = 40.5559 days,  $\Delta v = 7.9048$  m/s

additional revolutions along the vertical/halo orbits are incorporated by integrating the initial/final state along the unstable/stable manifold for twice the period of the vertical/halo orbit in reverse-/forward-time. Note that, for this example,  $d_1 = 20$  km and  $d_2 = -20$  km so that the manifolds are propagated toward the Moon. Details on the optimization algorithm are provided in the upcoming sections. The vertical and halo orbits are allowed to vary within the family during the optimization routine, thus, there is a change in the Jacobi constant value between the unstable and stable arcs. The vertical and halo orbits in the locally optimal solution correspond to the

Jacobi constant values  $C = 3.0571$  and  $C = 3.0468$ , respectively, and the combined time-of-flight along the manifolds is 40.5559 days.

#### 6.4 Differential Corrections Algorithms to Compute Transfers between Periodic Libration Point Orbits

The trajectory arcs generated using Poincaré maps supply an initial guess for a low-cost or maneuver-free transfer between two periodic orbits; however, this guess is discontinuous and a differential corrections algorithm is required to enforce continuity, in addition to any other desired constraints. In this investigation, transfers between periodic libration point orbits are sought. Targeting algorithms have been previously employed to locate such transfers. Barrabés et al. [51] target homoclinic connections in the planar Earth-Moon CR3BP, and implement numerical continuation to expand a single solution into a family of homoclinic transfers. Haapala and Howell [54] demonstrate the use of targeting and continuation schemes to locate a family of heteroclinic connections between  $L_1$  and  $L_2$  Lyapunov orbits in the Sun-Saturn system. Senent et al. [82] and Stuart et al. [81] incorporate manifold arcs into low-thrust transfer trajectories, and Stuart et al. compute families of low-thrust connections between libration point orbits.

In this investigation, both free ( $\Delta v = 0$  m/s) and low-cost ( $\Delta v \leq 20$  m/s) transfers are computed between periodic libration point orbits. Free transfers between libration point orbits are termed heteroclinic/homoclinic connections and represent manifold arcs that are shared by the stable and unstable manifolds of two, not necessarily distinct, orbits. Define orbit 1 as the departure orbit, and orbit 2 as the arrival orbit. For the example in Section 6.3 of this chapter, periodic orbit 1 represents an  $L_1$  vertical orbit, while orbit 2 corresponds to an  $L_2$  halo orbit. To define a transfer that connects orbits 1 and 2 via the unstable and stable invariant manifolds, consider the schematic in Figure 6.6. Several points along an initial guess for a transfer trajectory from

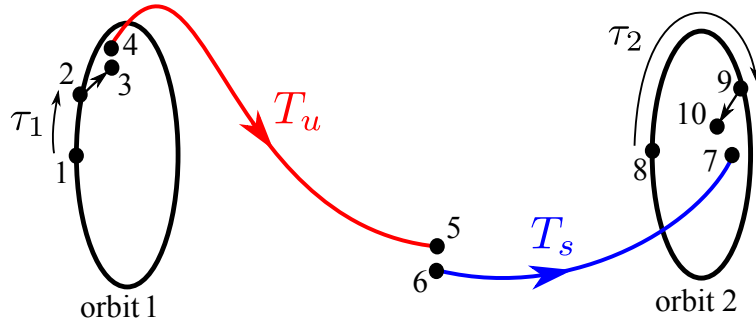


Figure 6.6. Defining the variables employed in targeting algorithms for transfers between periodic orbits

orbit 1 to orbit 2 are identified and numbered. Note that the numbers associated with each point do not necessarily correspond to their sequence in time. Let the point numbered 1 represent the initial state  $\bar{x}_1(t_{10})$  along periodic orbit 1, where  $T_1 = t_{1f} - t_{10} > 0$  is the orbital period. Point 2 represents the location  $\bar{x}_1(t_{10} + \tau_1)$  along the orbit after a coast time of  $\tau_1$ . Departure onto the unstable manifold occurs at this location by stepping along the unstable eigenvector direction  $\bar{w}^{U+}$ , as defined in equation (3.62), associated with the fixed point  $\bar{x}_1(t_{10} + \tau_1)$ . Point 3 represents this step and is computed as  $\bar{x}_{m1} = \bar{x}_1(t_{10} + \tau_1) + d_1 \cdot \bar{w}^{U+}$ , where  $d_1$  may be positive or negative. The ‘initial’ state,  $\bar{x}_u(t_{u0})$ , along the unstable manifold arc is represented as point 5, and point 4 corresponds to the ‘final’ state,  $\bar{x}_u(t_{uf})$ , after a propagation time of  $T_u = t_{uf} - t_{u0} < 0$ . Note that the ‘initial’ state along the unstable manifold arc is numerically integrated for a negative time interval. Similarly, point 6 represents the initial state,  $\bar{x}_s(t_{s0})$ , along the stable manifold. This state is numerically integrated in forward-time for  $T_s = t_{sf} - t_{s0} > 0$  to obtain point 7, i.e., the final state  $\bar{x}_s(t_{sf})$  along the stable manifold arc. Orbit 2 is defined by the initial state  $\bar{x}_2(t_{20})$  at point 8, and  $T_2 = t_{2f} - t_{20} > 0$  is the orbit period. Finally, point 9 represents the arrival location  $\bar{x}_2(t_{20} + \tau_2)$  along the orbit defined by the coast time  $\tau_2$  from the initial state  $\bar{x}_2(t_{20})$ . The step from point 9 onto the stable manifold,  $\bar{x}_{m2} = \bar{x}_2(t_{20} + \tau_2) + d_2 \cdot \bar{w}^{S+}$ , is labeled

point 10. Here,  $\bar{w}^{S+}$  corresponds to the stable eigenvector direction associated with the fixed point  $\bar{x}_2(t_{20} + \tau_2)$ . Again,  $d_2$  may be positive or negative.

As demonstrated by the example in Section 6.3, Poincaré maps prove useful to locate the periodic orbits and associated invariant manifolds corresponding to a low-cost transfer. The manifold initial conditions, i.e., points 5 and 6, are selected from the Poincaré map to generate the initial guess for the transfer and the associated values of  $\tau_1$  and  $\tau_2$  are recorded. Once the discontinuous baseline solution is generated, several quantities are allowed to vary to locate a nearby solution that is continuous in position. The quantities that define the unstable manifold ‘departure’ and stable manifold ‘insertion’ locations along orbits 1 and 2, i.e.,  $\tau_1$  and  $\tau_2$ , are varied, in addition to the times-of-flight,  $T_u$  and  $T_s$ , along the unstable and stable manifold arcs. The periodic orbits are permitted to vary within the respective families. That is,  $\bar{x}_{10}$  and  $\bar{x}_{20}$  are allowed to vary, with the constraint that each is associated with a periodic orbit. A discontinuity exists between the departure/insertion orbit state  $\bar{x}_i(\tau_i)$  and the manifold state  $\bar{x}_{mi} = \bar{x}_i(\tau_i) + d_i \bar{w}^i$ , where  $i = 1$  (unstable manifold) or  $2$  (stable manifold), and  $\bar{w}^1 = \bar{w}^{U+}$  and  $\bar{w}^2 = \bar{w}^{S+}$  represent the stable/unstable eigenvectors associated with the fixed points  $\bar{x}_i(\tau_i)$ ; however, the value of  $d_i$  is selected such that propagating  $\bar{x}_{mi}$  for  $2 \cdot T_i$  in reverse-time for  $i = 1$  or forward-time for  $i = 2$  yields a trajectory that remains in the vicinity of the periodic orbit for two revolutions. For the Earth-Moon system,  $|d_i| = 20$  km is selected to satisfy this requirement, assuming  $\bar{w}^i$  is normalized as defined in equations (3.59)–(3.62). Continuity in position is enforced where the stable and unstable manifolds connect to ensure a feasible transfer. By additionally applying constraints to satisfy continuity in velocity between the manifold arcs, a homoclinic (orbit 1 = orbit 2) or heteroclinic (orbit 1  $\neq$  orbit 2) connection is obtained. For cases where the transfer cannot be accomplished for  $\Delta v = 0$ , the velocity discontinuity is minimized via an optimization algorithm employing an SQP routine.

The libration point orbits and associated invariant manifolds are highly sensitive to perturbations. To reduce the integration times and improve convergence of the algorithms, patch points are distributed along the periodic orbits and manifold arcs, and multiple shooting is employed. Full state continuity is enforced between the segments defining each periodic orbit, as well as between the segments that comprise both the unstable and stable manifold arcs. Because the periodic orbits are not propagated as one continuous arc, the identity  $\Phi(t_f, t_0) = \Phi(t_f, t_n)\Phi(t_n, t_{n-1})\dots\Phi(t_1, t_0)$ , where  $t_0 < t_1 < \dots < t_n < t_f$ , is employed to approximate the monodromy matrix over one orbit during the differential corrections process. The eigenvectors of the approximated monodromy matrix are employed to define  $x_{mi}$ . Alternatively, Barrabés et al. [51] include the eigenvalues  $\lambda_i$  and eigenvectors  $\bar{w}^i$  associated with  $\Phi(t_f, t_0)$  as variables and enforce the additional constraint that  $\Phi(t_f, t_0)\bar{w}^i = \lambda_i\bar{w}^i$ , where  $\lambda_1 = \lambda_U$  and  $\lambda_2 = \lambda_S$ .

In this investigation, two differential corrections procedures are employed to compute either maneuver-free or low-cost transfers between periodic orbits. These procedures may be applied to compute transfers in both the planar and spatial problems. The details of these algorithms are provided in the following sections. In all algorithms, an  $n$ -vector of free variables,  $\bar{X}$ , and an  $m$ -vector of constraints,  $\bar{F}(\bar{X})$ , is defined so that where  $\bar{F}(\bar{X}^*) = \bar{0}$  when the constraints are satisfied. The feasible transfer is then defined by the variables contained in  $\bar{X}^*$ . Considering a first-order Taylor expansion about an initial guess  $\bar{X}_0$  nearby the desired feasible solution  $\bar{X}^*$  yields

$$\bar{F}(\bar{X}^*) = \bar{F}(\bar{X}_0) + D\bar{F}(\bar{X})|_{\bar{X}_0}(\bar{X}^* - \bar{X}_0), \quad (6.1)$$

where  $D\bar{F}(\bar{X})_{\bar{X}_0}$  is the Jacobian matrix of partial derivatives of the elements of  $\bar{F}$  with respect to the variables in  $\bar{X}$  evaluated at  $\bar{X}_0$ . Rearranging this expression yields

$$\bar{X}^* = \bar{X}_0 - (D\bar{F}(\bar{X})|_{\bar{X}_0})^{-1}\bar{F}(\bar{X}_0), \quad (6.2)$$

assuming that  $n = m$  and a unique solution exists. Note that  $\bar{F}(\bar{X}^*) = \bar{0}$  is eliminated from equation (6.1). In general,  $n > m$  and an infinite number of solutions are available. In this case, the minimum-norm pseudo-inverse is employed to locate  $\bar{X}^*$  nearest the initial guess  $\bar{X}_0$ . The minimum-norm solution is given as

$$\bar{X}^* = \bar{X}_0 - D\bar{F}(\bar{X})|_{\bar{X}_0}^T (D\bar{F}(\bar{X})|_{\bar{X}_0} D\bar{F}(\bar{X})|_{\bar{X}_0}^T)^{-1} \bar{F}(\bar{X}_0), \quad (6.3)$$

where a superscript  $T$  indicates that the matrix is transposed. For a nonlinear problem, the first-order Taylor expansion is an approximation and the system must be solved iteratively. In this case, the solution is written as

$$\bar{X}_{j+1} = \bar{X}_j - D\bar{F}(\bar{X})|_{\bar{X}_j}^T (D\bar{F}(\bar{X})|_{\bar{X}_j} D\bar{F}(\bar{X})|_{\bar{X}_j}^T)^{-1} \bar{F}(\bar{X}_j), \quad (6.4)$$

where  $\bar{X}_j$  contains the current values for the design variables, and  $\bar{X}_{j+1}$  contains the updated values. For an initial guess near  $\bar{X}^*$ , iteration of equation (6.4) generally converges quadratically to a feasible solution.

#### 6.4.1 Free Transfers Between Periodic Orbits

To compute heteroclinic and homoclinic connections, the following procedure is employed. Define the quantities contained in  $\bar{X}$  as free variables, and let  $\bar{F}$  represent the vector composed of the desired constraints to be applied within the corrections

process, where  $\bar{F} = \bar{0}$  when the constraints are satisfied. For maneuver-free transfers, these quantities are written as

$$\bar{X}_f = \begin{bmatrix} \bar{x}_1(t_{10}) \\ T_1 \\ \bar{x}_2(t_{20}) \\ T_2 \\ \tau_1 \\ \tau_2 \\ \bar{x}_u(t_{uf}) \\ T_u \\ \bar{x}_s(t_{s0}) \\ T_s \\ \beta_1 \\ \beta_2 \end{bmatrix}, \quad \bar{F}_f = \begin{bmatrix} x_1(t_{1f}) - x_1(t_{10}) \\ y_1(t_{1f}) - y_1(t_{10}) \\ z_1(t_{1f}) - z_1(t_{10}) \\ \dot{x}_1(t_{1f}) - \dot{x}_1(t_{10}) \\ \dot{y}_1(t_{1f}) - \text{sign}(\dot{y}_1(t_{10})) \cdot \beta_1^2 \\ \dot{z}_1(t_{1f}) - \dot{z}_1(t_{10}) \\ y_1(t_{10}) - 0 \\ x_2(t_{2f}) - x_2(t_{20}) \\ y_2(t_{2f}) - y_2(t_{20}) \\ z_2(t_{2f}) - z_2(t_{20}) \\ \dot{x}_2(t_{2f}) - \dot{x}_2(t_{20}) \\ \dot{y}_2(t_{2f}) - \text{sign}(\dot{y}_2(t_{20})) \cdot \beta_2^2 \\ \dot{z}_2(t_{2f}) - \dot{z}_2(t_{20}) \\ y_2(t_{20}) - 0 \\ \bar{x}_s(t_{s0}) - \bar{x}_u(t_{uf}) \\ \bar{x}_u(t_{u0}) - \bar{x}_{m1} \\ \bar{x}_s(t_{sf}) - \bar{x}_{m2} \end{bmatrix}.$$

The system is solved employing equation (6.4). Here, the terms  $x_i(t_{if}) - x_i(t_{i0})$ ,  $y_i(t_{if}) - y_i(t_{i0})$ ,  $z_i(t_{if}) - z_i(t_{i0})$ ,  $\dot{x}_i(t_{if}) - \dot{x}_i(t_{i0})$ ,  $\dot{z}_i(t_{if}) - \dot{z}_i(t_{i0})$ ,  $i = 1, 2$ , are included to enforce that orbits 1 and 2 are periodic. Because the value of  $C$  is constant along any arc, the remaining coordinate  $\dot{y}$  is, necessarily, equal in magnitude for the initial and final states along a periodic orbit; the term  $\dot{y}_i(t_{if}) - \text{sign}(\dot{y}_i(t_{i0})) \cdot \beta_i^2$  is included to additionally enforce that the direction of the velocity  $\dot{y}$  is consistent between the initial and final states along the orbit. The terms  $\beta_i$  are slack variable that are incorporated to apply the inequality constraints. Note that the initial state along each periodic orbit is defined to be an  $x$ -axis crossing such that  $\dot{y} \neq 0$ . The additional

constraints  $y_i(t_{i0}) - 0$  enforce that the initial condition remain on the  $x$ -axis. The term  $\bar{x}_s(t_{s0}) - \bar{x}_u(t_{uf})$  is included to enforce full-state continuity between the unstable and stable manifolds. Finally, the terms  $\bar{x}_u(t_{u0}) - \bar{x}_{m1}$ ,  $\bar{x}_s(t_{sf}) - \bar{x}_{m2}$  are employed to constrain the trajectories  $\bar{x}_u(t)$  and  $\bar{x}_s(t)$  to the unstable and stable manifold surfaces associated with orbits 1 and 2, respectively. Solutions that satisfy the equation  $\bar{F} = \bar{0}$  represent a fully continuous transfer arc between two periodic orbits, to within the specified tolerance. Again, a discontinuity exists between the manifold state  $\bar{x}_{mi}$  and orbit state  $\bar{x}_i(t_{i0} + \tau_i)$  ( $i = 1$  or  $2$ ), however, the value of  $d_i$  is selected such that propagating  $\bar{x}_{mi}$  for  $2 \cdot T_i$  in reverse-time for  $i = 1$  or forward-time for  $i = 2$  yields a trajectory that remains in the vicinity of the periodic orbit.

#### 6.4.2 Low-Cost Transfers Between Periodic Orbits

For transfers that cannot be completed for zero  $\Delta v$ , a nonzero maneuver is allowed and the previously described targeting algorithm for maneuver-free transfers must be modified. In this investigation, a single maneuver is permitted where the unstable manifold of orbit 1 meets the stable manifold of orbit 2. Then, the constraint  $\bar{x}_s(t_{s0}) - \bar{x}_u(t_{uf})$  in  $\bar{F}$  is replaced with the scalar constraints  $x_s(t_{s0}) - x_u(t_{uf})$ ,  $y_s(t_{s0}) - y_u(t_{uf})$ ,  $z_s(t_{s0}) - z_u(t_{uf})$ , so that only position continuity is enforced between the manifold arcs. Two options are employed to locate low-cost transfers in this investigation: an upper bound is enforced on the magnitude of the  $\Delta v$ , or optimization is employed to minimize the  $\Delta v$ .

##### Enforcing an Upper Limit on the $\Delta v$

To formulate a differential corrections process imposing an upper bound is enforced on the magnitude of the  $\Delta v$ , the following system is considered. Again, define the

quantities contained in  $\bar{X}$  as free variables, and let  $\bar{F}$  represent the vector composed of the desired constraints. To enforce that  $\Delta v \leq \Delta v_{max}$ , let

$$\bar{X}_v = \begin{bmatrix} \bar{x}_1(t_{10}) \\ T_1 \\ \bar{x}_2(t_{20}) \\ T_2 \\ \tau_1 \\ \tau_2 \\ \bar{x}_u(t_{uf}) \\ T_u \\ \bar{x}_s(t_{s0}) \\ T_s \\ \beta_1 \\ \beta_2 \\ \beta_v \end{bmatrix}, \quad \bar{F}_v = \begin{bmatrix} x_1(t_{1f}) - x_1(t_{10}) \\ y_1(t_{1f}) - y_1(t_{10}) \\ z_1(t_{1f}) - z_1(t_{10}) \\ \dot{x}_1(t_{1f}) - \dot{x}_1(t_{10}) \\ \dot{y}_1(t_{1f}) - \text{sign}(\dot{y}_1(t_{10})) \cdot \beta_1^2 \\ \dot{z}_1(t_{1f}) - \dot{z}_1(t_{10}) \\ y_1(t_{10}) - 0 \\ x_2(t_{2f}) - x_2(t_{20}) \\ y_2(t_{2f}) - y_2(t_{20}) \\ z_2(t_{2f}) - z_2(t_{20}) \\ \dot{x}_2(t_{2f}) - \dot{x}_2(t_{20}) \\ \dot{y}_2(t_{2f}) - \text{sign}(\dot{y}_2(t_{20})) \cdot \beta_2^2 \\ \dot{z}_2(t_{2f}) - \dot{z}_2(t_{20}) \\ y_2(t_{20}) - 0 \\ x_s(t_{s0}) - x_u(t_{uf}) \\ y_s(t_{s0}) - y_u(t_{uf}) \\ z_s(t_{s0}) - z_u(t_{uf}) \\ \Delta v - \Delta v_{max} + \beta_v^2 \\ \bar{x}_u(t_{u0}) - \bar{x}_{m1} \\ \bar{x}_s(t_{sf}) - \bar{x}_{m2} \end{bmatrix},$$

where  $\Delta v = \sqrt{(\dot{x}_{u0} - \dot{x}_{s0})^2 + (\dot{y}_{u0} - \dot{y}_{s0})^2 + (\dot{z}_{u0} - \dot{z}_{s0})^2}$  and  $\beta_v$  is a slack variable. The corrections algorithm proceeds employing equation (6.4).

### Finding the Locally Minimal $\Delta v$

To locate a locally optimal transfer, the velocity discontinuity along the transfer path is minimized via an optimization algorithm employing an SQP routine and the MATLAB function fmincon. The free variables and constraint vector for the problem are written as

$$\bar{X}_o = \begin{bmatrix} \bar{x}_1(t_{10}) \\ T_1 \\ \bar{x}_2(t_{20}) \\ T_2 \\ \tau_1 \\ \tau_2 \\ \bar{x}_u(t_{uf}) \\ T_u \\ \bar{x}_s(t_{s0}) \\ T_s \\ \beta_1 \\ \beta_2 \end{bmatrix}, \quad \bar{F}_o = \begin{bmatrix} x_1(t_{1f}) - x_1(t_{10}) \\ y_1(t_{1f}) - y_1(t_{10}) \\ z_1(t_{1f}) - z_1(t_{10}) \\ \dot{x}_1(t_{1f}) - \dot{x}_1(t_{10}) \\ \dot{y}_1(t_{1f}) - \text{sign}(\dot{y}_1(t_{10})) \cdot \beta_1^2 \\ \dot{z}_1(t_{1f}) - \dot{z}_1(t_{10}) \\ y_1(t_{10}) - 0 \\ x_2(t_{2f}) - x_2(t_{20}) \\ y_2(t_{2f}) - y_2(t_{20}) \\ z_2(t_{2f}) - z_2(t_{20}) \\ \dot{x}_2(t_{2f}) - \dot{x}_2(t_{20}) \\ \dot{y}_2(t_{2f}) - \text{sign}(\dot{y}_2(t_{20})) \cdot \beta_2^2 \\ \dot{z}_2(t_{2f}) - \dot{z}_2(t_{20}) \\ y_2(t_{20}) - 0 \\ x_s(t_{s0}) - x_u(t_{uf}) \\ y_s(t_{s0}) - y_u(t_{uf}) \\ z_s(t_{s0}) - z_u(t_{uf}) \\ \bar{x}_u(t_{u0}) - \bar{x}_{m1} \\ \bar{x}_s(t_{sf}) - \bar{x}_{m2} \end{bmatrix},$$

and the optimal transfer is required to satisfy  $\bar{F}(\bar{X}_o) = \bar{0}$ . The cost function

$$J = \sqrt{(\dot{x}_s(t_{s0}) - \dot{x}_u(t_{uf}))^2 + (\dot{y}_s(t_{s0}) - \dot{y}_u(t_{uf}))^2 + (\dot{z}_s(t_{s0}) - \dot{z}_u(t_{uf}))^2}, \quad (6.5)$$

defines the magnitude of the  $\Delta v$  required to connect the unstable and stable manifold arcs in the transfer. Here, the the quantities in  $\bar{X}_o$  are adjusted so that the function  $J$  is minimized to yield a low-cost transfer between periodic orbits.

## 6.5 Transfers Between Libration Point Orbits in Different Systems

In the previous section, an example of how to employ glyphs to represent higher-dimensional Poincaré maps is demonstrated to construct a transfer between orbits in the vicinity of  $L_1$  and  $L_2$  in the Earth-Moon system. A second application for the use of higher-dimensional maps is the design of transfers between different systems. Transfers to the Moon that leverage solar perturbations generally require little  $\Delta v$  and have been employed for the Hiten [83], Genesis [84], and ARTEMIS [6] missions.

Transfers between libration point orbits in different three-body systems have been previously demonstrated using Poincaré maps by a number of authors. Work to develop transfers between libration point orbits in different systems generally proceeds with the assumption of a patched or coupled CR3B model. In this model, the periodic libration point orbits from the CR3BP are assumed to exist within each system of interest, and invariant manifolds are computed as described in Section 3.4.3. Koon et al. [85, 86] consider transfers between planar libration point orbits in the Sun-Earth and Earth-Moon systems by propagating invariant manifolds asymptotic to these orbits until their crossing with a surface of section defined by some angle relative to the  $x$ -axis and centered at the Earth in each system. The map crossings are transformed to a common frame, e.g., the Sun-Earth rotating frame. The resulting map is three-dimensional as the Jacobi integral is not maintained as a constant value for the transformed system. The Poincaré map is projected into the  $y\text{-}\dot{y}$  plane, and locations corresponding to feasible transfers are determined by the intersections of the contours formed by the manifolds on the map. A  $\Delta v$  is required to account for any difference in the  $\dot{x}$  velocity. Note that this velocity discontinuity is not represented

on the map, but can often be eliminated via optimization by appropriate selection of the departure and arrival orbits. Koon et al. [87] also apply this technique to design transfers between planar orbits in the Jupiter-Europa and Jupiter-Ganymede systems.

In the spatial problem, Gómez et al. [24] employ a coupled CR3B model to design a transfer between libration point orbits in the Jupiter-Ganymede and Jupiter-Europa systems. These authors consider the families of libration point orbits in the spatial problem, and map the invariant manifolds asymptotic to these orbits to the surface of section  $\Sigma = \{\bar{x}|y = 0\}$ . The map crossings are transformed to a common frame, e.g., the Jupiter-Europa rotating frame. Again, because the Jacobi integral is not maintained as a constant value for the transformed system, the resulting map is five-dimensional. Assuming coplanar orbits for Europa and Ganymede about Jupiter, additional constraints on the values of  $z$  and  $\dot{z}$  may be applied for crossings of  $\Sigma$  to reduce the dimension of the map to three. Finally, the map is projected into the  $x\text{-}\dot{x}$  plane to determine the locations corresponding to feasible transfers. A  $\Delta v$  is generally required in the  $y$ -direction to complete the transfer. While the magnitude of this cost is not represented on the map, the resulting  $\Delta v$  is considerably reduced compared to the expected cost of a Hohmann transfer. Parker and Lo [88] also employ invariant manifolds from the Sun-Earth and Earth-Moon systems to reduce the  $\Delta v$  required to transfer from LEO to an Earth-Moon  $L_2$  halo orbit. Howell and Kakoi [66] represent higher-dimensional Poincaré maps displaying crossings of invariant manifolds using multiple projections of the map. These authors estimate the magnitude of any required maneuver from the projections of the map, and adjust the lunar phasing angle to reduce the  $\Delta v$  to transfer between halo orbits in the Sun-Earth and Earth-Moon frames.

In the following example, a system-to-system transfer is accomplished using Poincaré maps and employing glyphs to represent the map crossings. To design such a transfer,

it is useful to first define the variables that are employed in the patched CR3B model.

Let

$$\bar{x}_{EM} = [x_{EM}, y_{EM}, z_{EM}, \dot{x}_{EM}, \dot{y}_{EM}, \dot{z}_{EM}]^T$$

represent a state associated with a trajectory in the Earth-Moon system, and

$$\bar{x}_{SE} = [x_{SE}, y_{SE}, z_{SE}, \dot{x}_{SE}, \dot{y}_{SE}, \dot{z}_{SE}]^T$$

be a state in the Sun-Earth system. Then, these states are numerically integrated assuming the Earth-Moon and Sun-Earth CR3B models, respectively. The rate of the Moon's orbit about the Earth is employed to define the relative motion of the Earth-Moon and Sun-Earth rotating frames. Recall that the characteristic quantities for each system are summarized in Table 2.1. The Earth-Moon mass parameter, characteristic length, and orbital period are given as  $\mu_{EM} = 1.21506 \times 10^{-2}$ ,  $\ell_{EM}^* = 3.85693 \times 10^5$  km, and  $2\pi t_{EM}^* = 27.42$  days. The quantities associated with the Sun-Earth system are  $\mu_{SE} = 3.00390 \times 10^{-6}$ ,  $\ell_{SE}^* = 1.49598 \times 10^8$  km, and  $2\pi t_{SE}^* = 1.00$  years. The rate of rotation of the Moon relative to the Sun-Earth  $x$ -axis is given as  $\omega_{syn} = 1/t_{EM}^* - 1/t_{SE}^*$ , which gives a synodic lunar period of  $\frac{2\pi}{\omega_{syn}} = 29.65$  days. Employing the synodic period, data from Earth-Moon frame is transformed to Sun-Earth rotating coordinates as follows:

1. the  $x$ -coordinate is shifted by  $\mu_{EM}$  so that the state is Earth-centered,
2. the time and state variables are scaled to be dimensional quantities using Earth-Moon characteristic quantities,
3. the state is rotated into the Earth-centered Sun-Earth frame,
4. the time and state are nondimensionalized using Sun-Earth characteristic quantities,
5. the state is shifted to barycenteric coordinates by subtracting  $(1 - \mu_{SE})$  from the  $x$ -coordinate.

The rotation matrix employed in step 3 is

$$C = \begin{bmatrix} C_1 & C_2 \\ C_3 & C_4 \end{bmatrix}, \quad (6.6)$$

where the submatrices,  $C_i$ , are defined as follows:

$$C_1 = \begin{bmatrix} \cos(\omega_{syn}t + \phi_0) & -\sin(\omega_{syn}t + \phi_0) & 0 \\ \sin(\omega_{syn}t + \phi_0) & \cos(\omega_{syn}t + \phi_0) & 0 \\ 0 & 0 & 1 \end{bmatrix}, \quad (6.7)$$

$C_2 = 0_{3 \times 3}$  is the  $3 \times 3$  submatrix of zeroes,  $C_3 = \frac{dC_1}{dt}$ , and  $C_4 = C_1$ . Here,  $\phi_0$  is the initial lunar angle relative to the Sun-Earth rotating  $x$ -axis in the Earth-centered frame. Thus, after steps 1–2 are performed, the Earth-Moon rotating state is rotated to the Sun-Earth frame as  $\bar{x}_{SE} = C\bar{x}_{EM}$ .

To locate a transfer between orbits in the Earth-Moon and Sun-Earth systems, Poincaré maps associated with the hyperplane defined by some angle from the  $x$ -axis centered at the Earth are employed. Two different angles are defined, one angle ( $\theta_1$ ) for the Earth-Moon system, and one angle ( $\theta_2$ ) for the Sun-Earth system. The surface of section employed to generate the Poincaré map corresponds to  $\Sigma_{\theta_1} = \{\bar{x}_{EM} | \theta_{EM} = \theta_1\}$  in the Earth-Moon system, and  $\Sigma_{\theta_2} = \{\bar{x}_{SE} | \theta_{SE} = \theta_2\}$  in the Sun-Earth system, where  $\Sigma_{\theta_1} \equiv \Sigma_{\theta_2}$  when transformed to a common reference frame. Thus, in the Earth-Moon system,  $\tan(\theta_{EM}) = \frac{x_{EM} + \mu_{EM}}{y_{EM}}$  so that  $\theta_{EM}$  represents the angle from the Earth-Moon  $x$ -axis centered at the Earth. For the angle in the Sun-Earth system,  $\tan(\theta_{SE}) = \frac{x_{SE} - 1 + \mu_{SE}}{y_{SE}}$  and  $\theta_{SE}$  represents the angle from the Sun-Earth  $x$ -axis centered at the Earth. The resulting surface of section is depicted in Figure 6.7. Here,  $\phi_m$  represents the lunar angle associated with a particular crossing of the map. Thus, the state corresponding to an intersection of a trajectory with the surface  $\Sigma_\theta$  corresponds to the lunar angle  $\phi_m = \theta_2 - \theta_1$  relative to the Sun-Earth  $x$ -axis. The lunar phasing angle for other points along a manifold arc are determined by the time-of-flight along the arc and  $\omega_{syn}$ .

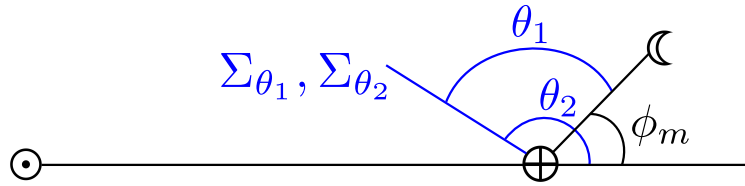


Figure 6.7. Defining the lunar angle from  $\Sigma_{\theta_1}$  and  $\Sigma_{\theta_2}$

Consider a transfer that departs from an  $L_2$  Lyapunov orbit in the Earth-Moon system, and connects to an  $L_1$  Lyapunov orbit in the Sun-Earth system. Three orbits are randomly selected from the family of Earth-Moon  $L_2$  Lyapunov orbits, corresponding to the following values of Jacobi constant and period ( $T$ ):  $C = 3.12653$ ,  $T = 15.2113$  days;  $C = 3.15011$ ,  $T = 14.9276$  days;  $C = 3.16442$ ,  $T = 14.7887$  days. For each orbit, 50 unstable manifold arcs, selected for even increments of  $\tau = \frac{i \cdot T}{50}$ ,  $i = 0, \dots, 49$ , are propagated for 35 days each. A subset of the resulting manifold arcs are plotted in magenta in Figure 6.8. Similarly, three sample orbits from the

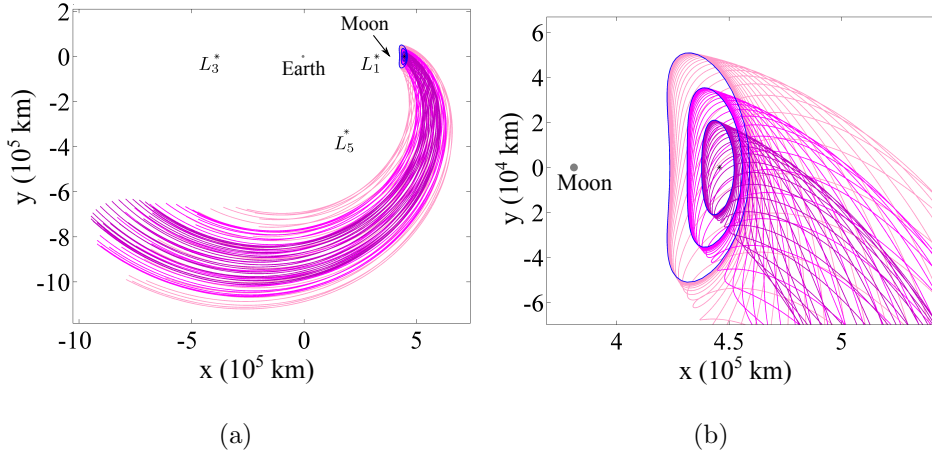


Figure 6.8. Unstable manifold arcs departing  $L_2$  Lyapunov orbits in the Earth-Moon system

Sun-Earth family of  $L_1$  Lyapunov orbits are selected, corresponding to the following values:  $C = 3.00089$ ,  $T = 175.081$  days;  $C = 3.00088$ ,  $T = 175.578$  days;  $C =$

$3.00084$ ,  $T = 177.069$  days. Stable manifold arcs associated with each orbit and corresponding to even increments of  $\tau = \frac{i \cdot T}{100}$ ,  $i = 0, \dots, 99$ , are propagated for 215 days each, and a subset of these trajectories appear in green in Figure 6.9. Values

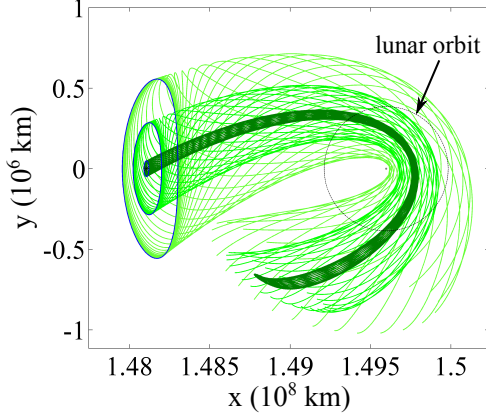


Figure 6.9. Stable manifold arcs approaching  $L_1$  Lyapunov orbits in the Sun-Earth system

for  $\theta_1$  and  $\theta_2$  are selected, and the invariant manifolds are propagated within the respective three-body systems. Crossings of  $\Sigma_{\theta_1}$  are recorded for all Earth-Moon trajectories, and intersections with  $\Sigma_{\theta_2}$  are captured for Sun-Earth arcs. To view the resulting three-dimensional Poincaré map, the states associated with crossings of the map are transformed into a common frame. For this example, the Earth-Moon data is transformed into the Sun-Earth rotating frame. Many projections can be considered to view the map. Here, polar coordinates are considered and the projection of the map into the  $r\dot{r}$  plane is selected, where  $r = \sqrt{(x_{SE} - 1 + \mu_{SE})^2 + y_{SE}^2}$  and  $\dot{r} = \left( [x_{SE} - 1 + \mu_{SE}, y_{SE}]^T [\dot{x}_{SE}, \dot{y}_{SE}] \right) / r$ . Because the magnitudes of  $r$  and  $\dot{r}$  may be disparate, the value of  $\dot{r}$  is scaled by a constant factor  $k_1$ . To display the third coordinate, a modification of the glyph in Figure 6.2 is considered. For the three-dimensional map, a vector is still employed as the glyph representing crossings of the Poincaré map. However, now both the length and orientation of the vector represent the remaining coordinate as pictured in Figure 6.10. The value of  $\dot{\theta}$  is represented via

the length of the vector as scaled by the parameter  $k_2$ . This velocity is additionally mapped to an angle,  $\gamma$ , that defines the orientation of the glyph within the range  $[0, \pi]$ . Thus,  $\gamma = \pi \left( \frac{\dot{\theta} - \dot{\theta}_{min}}{\dot{\theta}_{max} - \dot{\theta}_{min}} \right)$ , where  $\dot{\theta}_{min}$  and  $\dot{\theta}_{max}$  are the minimum and maximum values of  $\dot{\theta}$  of all states on the map. Adjusting the surfaces of section to reduce the

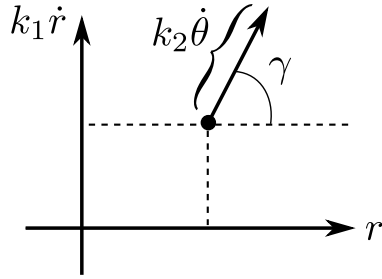


Figure 6.10. Glyph representation for a three-dimensional data point

position and velocity discontinuities, the values  $\theta_1 = 316^\circ$  and  $\theta_2 = 147^\circ$  are selected and the resulting map appears in Figure 6.11. For this example,  $k_1 = 0.01$  and

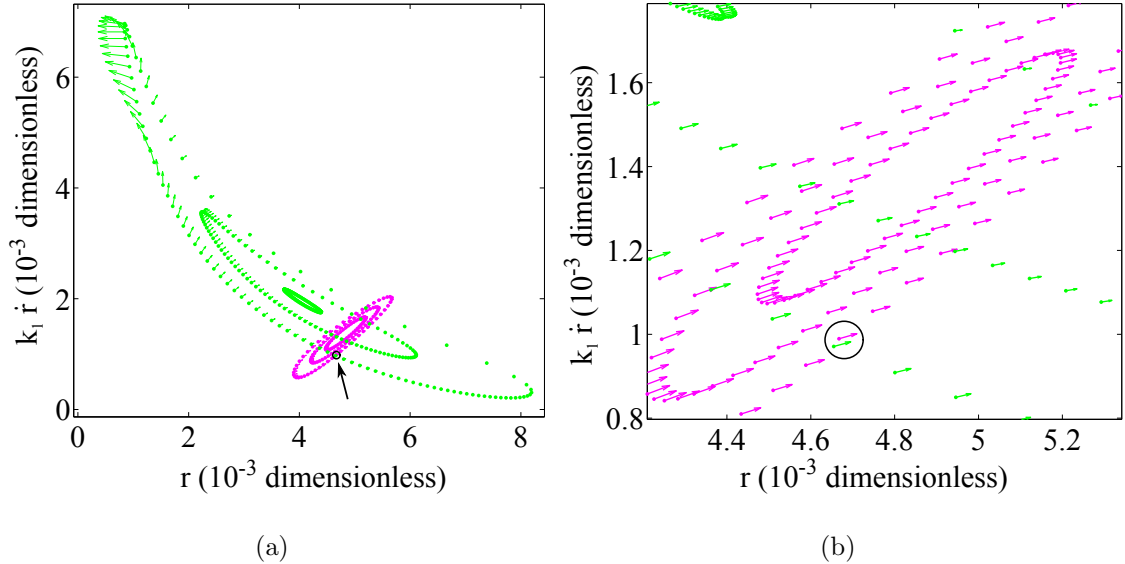


Figure 6.11. Employing a Poincaré map to locate a low-cost transfer between libration point orbits in the Earth-Moon and Sun-Earth systems

$k_2 = 1 \times 10^{-5}$ . By connecting the basepoints of the vectors representing the crossings of a particular invariant manifold on the map, a contour in the  $r\dot{r}$  plane is formed. Thus, the stable manifolds approaching the Sun-Earth Lyapunov orbits correspond to the three green contours on the map, and the Earth-Moon Lyapunov unstable manifolds are associated with the three magenta contours. As in the example from the previous section, a feasible transfer requiring zero  $\Delta v$  is located by identifying map crossings along the stable and unstable manifolds for which the basepoints of the crossings overlap, and the length and orientation of the vectors is identical. From the maps in Figure 6.11 it is apparent that each of the three green contours intersect each of the three magenta contours in the  $r$ -coordinate, indicating that a feasible transfer exists between any of the Sun-Earth and Earth-Moon orbits for the lunar angle defined by  $\theta_1 = 316^\circ$  and  $\theta_2 = 147^\circ$ . A portion of the velocity discontinuity is indicated by the difference in  $\dot{r}$  between a green and a magenta crossing for equal values of  $r$ . The zoomed in view of the map in Figure 6.11(b) provides additional information about the discontinuity in  $\dot{\theta}$ . The  $\dot{\theta}$ -discontinuity is apparently reduced by considering intersections between the outermost green and magenta contours, corresponding to the orbits associated with the lowest values of  $C$  in each system. The crossings nearest the intersection of these contours for which the  $r$ -discontinuity is minimal on the map are selected and are circled in black in Figure 6.11(b). Propagating the circled states within their respective systems yields the manifold arcs in Figure 6.12(a) that provide an initial guess for the transfer between the libration point orbits. A discontinuity of 312.97 km and 32.1 m/s exists where the magenta and green arcs join. Four revolutions along both the Earth-Moon  $L_1$  and Sun-Earth  $L_2$  Lyapunov orbits are incorporated into the design and the discontinuous transfer is plotted in the Sun-Earth system in Figure 6.12(b), and in the Earth-Moon system in Figures 6.12(c)–6.12(d). Note that two phasing segments are also included: one arc to connect the final state  $\bar{x}_1(T_1) = \bar{x}_1(0)$  at the  $x$ -axis crossing along the Earth-Moon departure orbit to the initial state  $\bar{x}_{u0}(0)$  along the unstable manifold, which is associated with

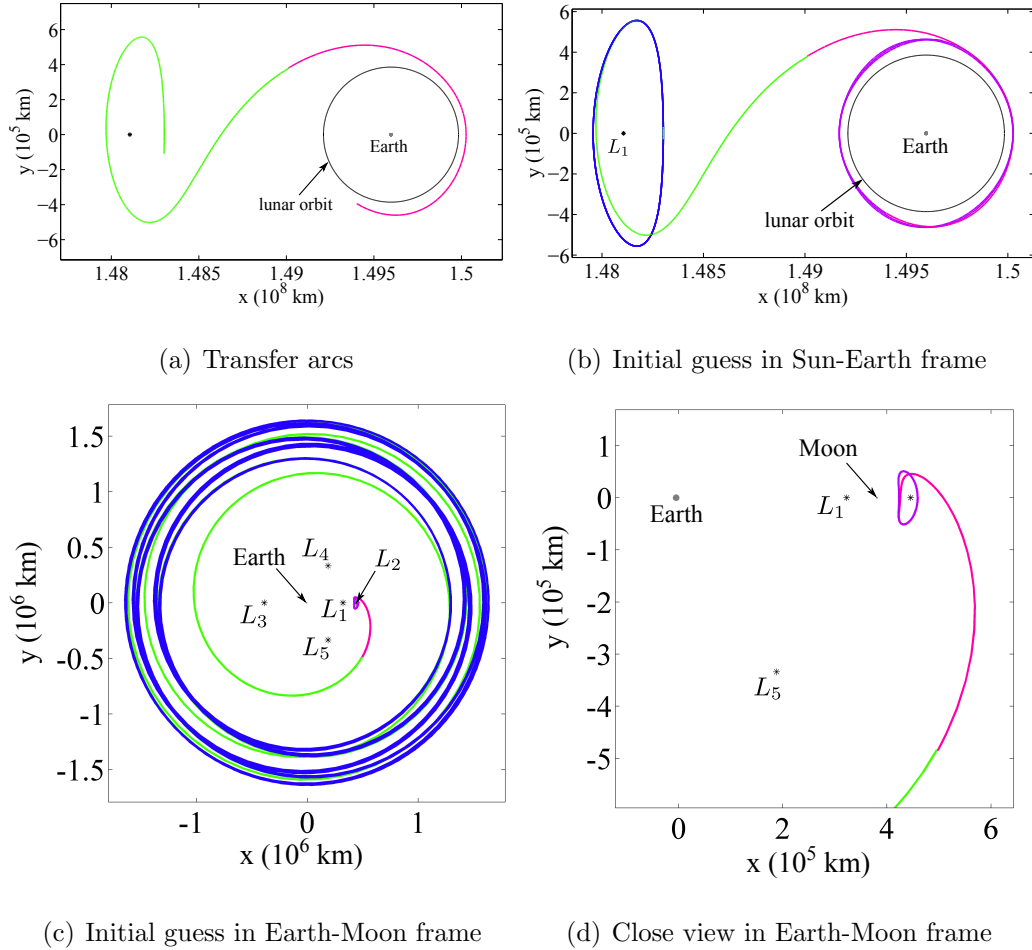


Figure 6.12. Constructing an initial guess for the system-to-system transfer

the departure location  $\bar{x}_1(\tau_1)$ ; and one segment to bridge the discontinuity between the final state  $\bar{x}_s(t_s)$  along the Sun-Earth orbit stable manifold and the initial state  $\bar{x}_2(0)$  at the  $x$ -axis crossing along the Sun-Earth arrival orbit.

To validate the solution obtained from the Poincaré map, the initial guess is differentially corrected within a Sun-Earth-Moon ephemeris model. First, the solution in the Sun-Earth rotating frame is discretized for multiple shooting, and the states associated with each node are transformed to the Earth-centered inertial frame. The resulting states are numerically integrated using the  $N$ -body equations of mo-

tion, and full state continuity is enforced within a corrections process. The initial lunar phasing angle is computed by considering the lunar angle  $\phi_m$  at the epoch associated with the final state along the unstable manifold. Assuming  $m$  arcs are included prior to the unstable manifold arc in the design, the initial angle is given as  $\phi_0 = \phi_m - 2\pi\omega_{syn}(|T_u| + \sum_{i=1}^m |T_i|)$ , where  $T_u$  is the elapsed time along the unstable manifold arc, and  $T_i$  is the time-of-flight along the  $i$ -th arc prior to the unstable manifold arc. Thus,  $\phi_0$  provides the lunar angle at the beginning of the transfer arcs in Figures 6.12(b)–6.12(d). The initial epoch is selected consistent with this lunar phasing angle and is employed to define the orientation of the bodies in the  $N$ -body system. Numerical integration of these nodes in the ephemeris model proceeds via the relative 4-body equations of motion as expressed in Earth-centered J2000 inertial coordinates. The second-order equations of motion are written as

$$\bar{R}_{13}'' = -G(m_3 + m_1)\frac{\bar{R}_{13}}{R_{13}^3} + \sum_{i=2,4} Gm_i \left( \frac{\bar{R}_{3i}}{R_{3i}^3} - \frac{\bar{R}_{1i}}{R_{1i}^3} \right), \quad (6.8)$$

where  $m_1$ ,  $m_2$ , and  $m_4$  represent the masses of the Earth, Moon, and Sun, respectively. The vector  $\bar{R}_{13}$  locates the spacecraft relative to the Earth, and  $\bar{R}_{ij} = \bar{R}_j - \bar{R}_i$  locates the  $i^{th}$  body relative to the  $j^{th}$  body. The respective distances are obtained via the planetary and lunar ephemeris file DE 421 [89]. The continuous solution, computed via the differential corrections process, appears in the Sun-Earth and Earth-Moon rotating frames in Figure 6.13. For details on differential corrections within the ephemeris model, see Pavlak [90]. Note that the distance between the primary bodies varies with time in the ephemeris model. The pulsation in the rotating frame is removed by normalizing the positions at each time instant using the instantaneous  $P_1$ - $P_2$  distance and multiplying by the characteristic length associated with the appropriate system.

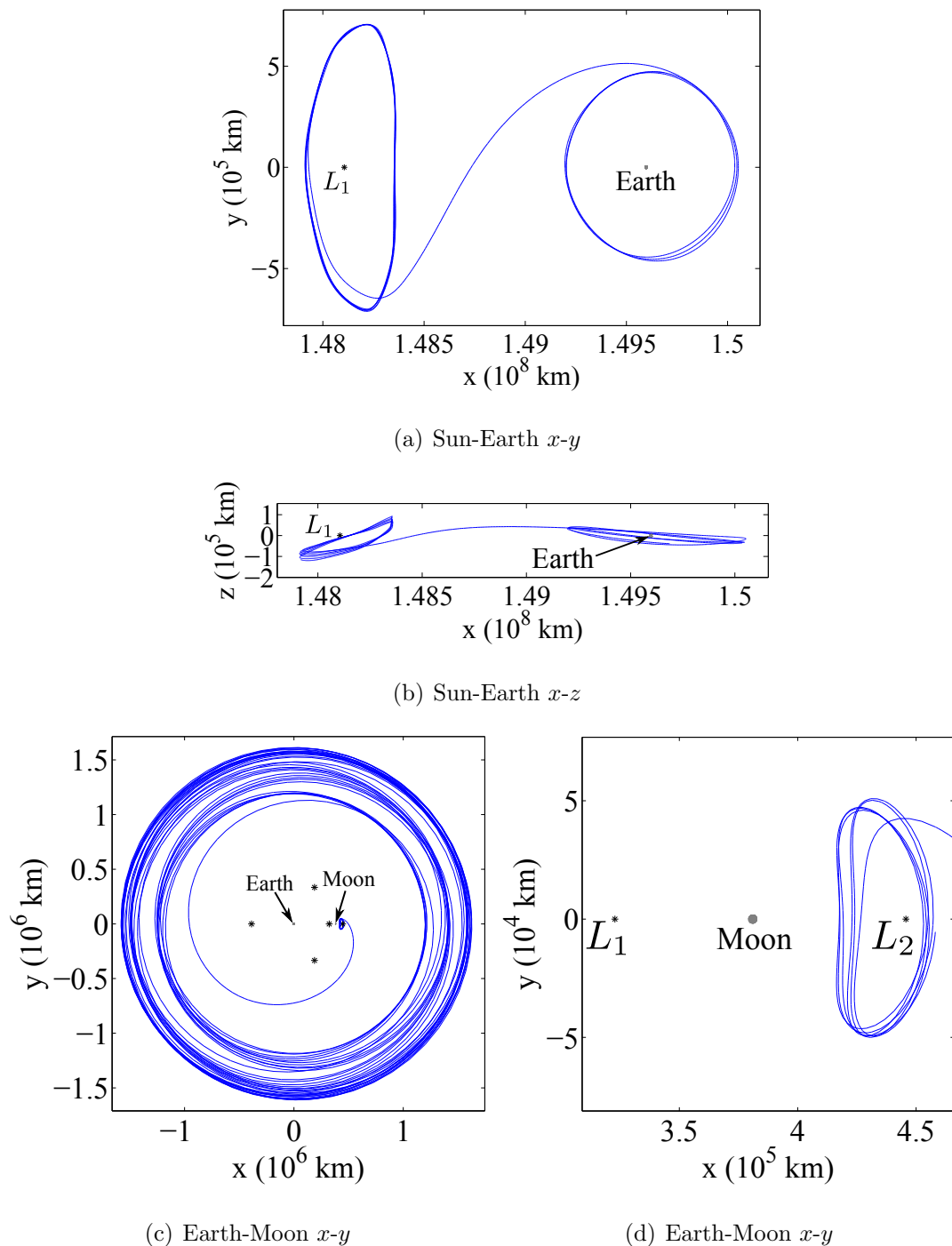


Figure 6.13. Converged transfer in the Sun-Earth-Moon ephemeris model with  $\Delta v = 0$

## 7. EXPLORING THE ROLE OF POINCARÉ MAPS IN AN INTERACTIVE TRAJECTORY DESIGN ENVIRONMENT

As mission requirements become increasingly complex, trajectory design tools that take advantage of the available natural dynamics are essential. An interactive design environment offers many advantages from the perspective of mission design. Many commonly used trajectory design tools employ an ephemeris model, in which only point solutions associated with a particular epoch can be considered. Working in an autonomous model, such as the CR3BP, enables an examination of the global solution space and facilitates user interaction within the design process. Tools such as point-and-click arc selection and real time computation and propagation of solutions allow the designer to explore the space while gaining intuition about the available solutions. Different design options can be considered simultaneously, allowing the user to adapt solutions based on the insight gained and to select a design that best meets the mission requirements.

Several tools exist that exploit dynamical systems theory for mission design, including Generator [91, 92] and LTool [93]. A tool to interactively compute libration point orbits and their associated manifolds is demonstrated by Mondelo et al. [94]. The AUTO software enables the computation of periodic orbits and numerical continuation of orbit families, as well as bifurcation detection and analysis [95]. An interactive design approach based in visual analytics has been previously demonstrated by Schlei [96] for a variety of mission design applications in multi-body regimes. Haa-pala et al. [97] demonstrate an Adaptive Trajectory Design<sup>©</sup> strategy that provides interactive access to a variety of multi-body solutions for rapid design and analysis

of trajectory options. A dynamic reference catalog, introduced by Folta et al. [98] as well as Guzzetti et al. [99], offers an interactive environment for orbit comparison and selection .

The focus in this chapter is on the design of transfers between libration point orbits employing Poincaré maps within an interactive design environment. Within this environment, the user can select a three-body system and specify the desired departure and arrival orbit types. By selecting a Jacobi constant value, the particular departure and arrival orbits from within the families are computed and the associated invariant manifolds may be propagated. To search for a transfer between the selected departure and arrival orbits, a Poincaré map is employed using the techniques demonstrated in the previous chapter. The characteristics associated with the Poincaré surface of section are specified by the user within the design environment. For the design of transfers in the planar problem, the user is able to specify the axes into which the two-dimensional map is projected. In the spatial problem, the attributes associated with the glyphs employed to represent crossings of the higher-dimensional map are defined. Finally, the number of arcs used to discretize the stable/unstable manifold is prescribed, in addition to the manifold propagation time, and the resulting arcs are numerically integrated while crossings of the surface of section are recorded. The Poincaré map is, then, displayed as designated by the user and crossings of the map are interactively selected to view the associated manifold arcs. Once an appropriate initial guess for the transfer is located, the solution is differentially corrected as described in Chapter 6.4. To enable the functions described, two Graphical User Interface (GUI) environments are developed in MATLAB including a Transfer Design Environment, and a Differential Corrections Environment. The implementation of the design process within these environments is described in detail in the upcoming sections.

### 7.0.1 Transfer Design Environment

The first step in the transfer design procedure is the location of a suitable initial guess for a transfer between libration point orbits. Once a guess is constructed, it is differentially corrected to generate a feasible solution. Here, an interactive design environment employing Poincaré maps is demonstrated to search for the initial guess. As an alternative, the guess can be located using an automated search algorithm. An automated strategy is considered in an upcoming section of Chapter 8.

The GUI developed to implement an interactive transfer design environment is depicted in Figure 7.1. Two blank plots appear and are employed to view the Poincaré

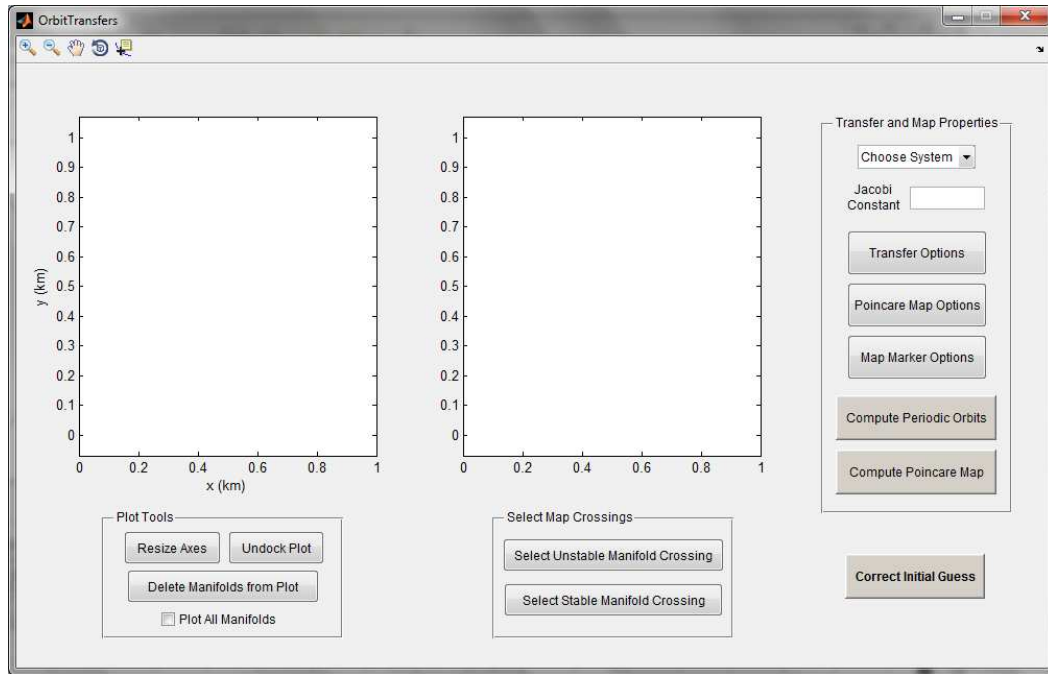


Figure 7.1. Transfer Design Environment

map and the libration point orbit transfer. The plots are populated as the user follows the design process. To the right of the plot windows, a panel labeled “Transfer and Map Properties” is included that allows the user to specify the desired three-body system and energy level, as well as the transfer and Poincaré map properties. Be-

neath the left plot appears a second panel titled “Plot Tools” that contains various plot options. A third panel labeled “Select Map Crossings” lies beneath the right plot window and includes the functions that enable the user to interactively select manifold arcs of interest from the Poincaré map. Finally, a button labeled “Correct Initial Guess” is included in the lower right corner of the GUI. Once an initial guess is located within the design environment, this button launches the Differential Corrections Environment in which the user can construct a feasible transfer.

To demonstrate the design procedure, consider the following example in which a maneuver-free transfer connecting northern and southern  $L_1$  halo orbits in the Earth-Moon system is sought. To begin, the Earth-Moon system is selected from within the drop-down menu in the “Transfer and Map Properties” panel. The other three-body system options include the Sun-Earth system and Hill 3BP, although it is straightforward to incorporate any additional systems of interest. Once the desired system is designated, an appropriate energy level is identified by entering a value within the “Jacobi Constant” text box. For this example, a value of  $C = 3.05$  is arbitrarily selected. Next, pressing the button labeled “Transfer Options,” the pop-up window depicted in Figure 7.2(a) appears. Within this window, two panels allow the user to specify characteristics associated with the departure and arrival orbits. Here, the user is able to designate the departure and arrival orbit types, as well as the number of manifold arcs that are employed to represent the unstable and stable manifold associated with these orbits. The desired propagation times for the manifold arcs is entered, and the drop-down menus labeled “Propagation Direction” allow the user to stipulate either the left or right half-manifolds for the propagation. For this example, the  $L_1$  northern halo family is selected as the departure orbit type, and 100 manifold arcs are designated to be propagated for 35 days each. Similarly, the southern halo family in the vicinity of  $L_1$  is defined as the arrival orbit type, and 100 manifold arcs are specified to be integrated for 35 days. The positive direction is selected for  $\bar{w}^U$ , indicating that the right half-manifolds will be employed to construct

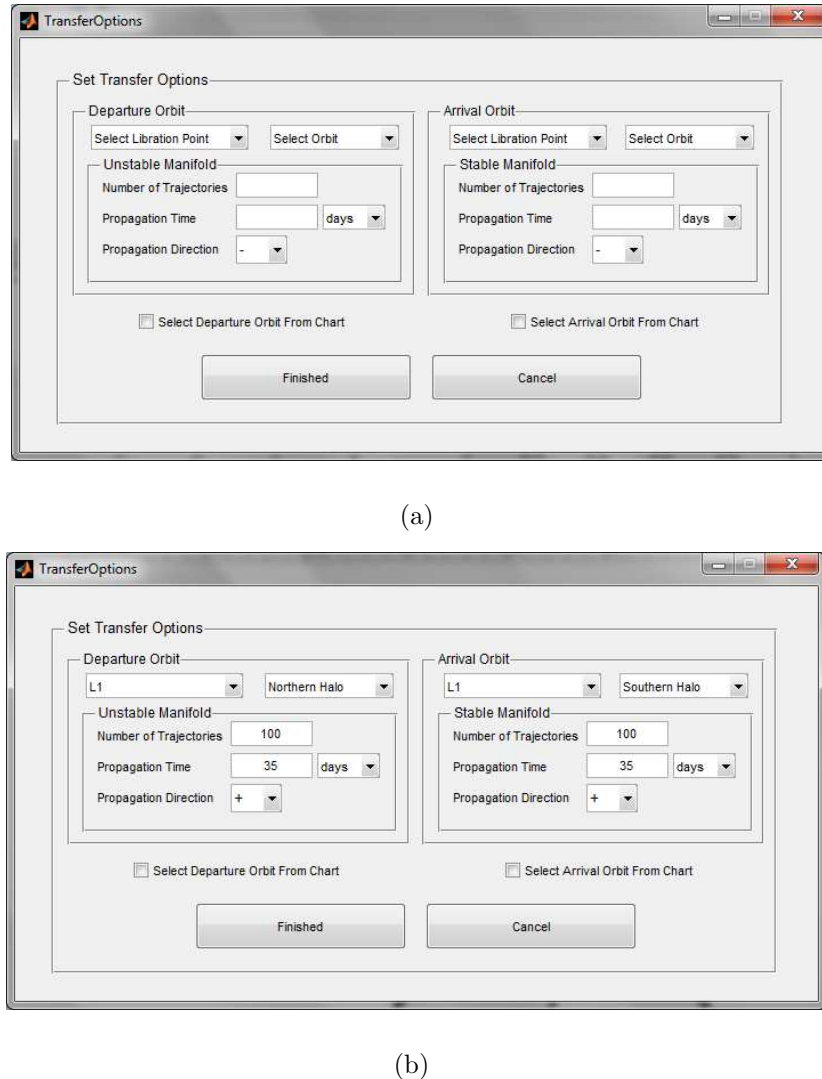


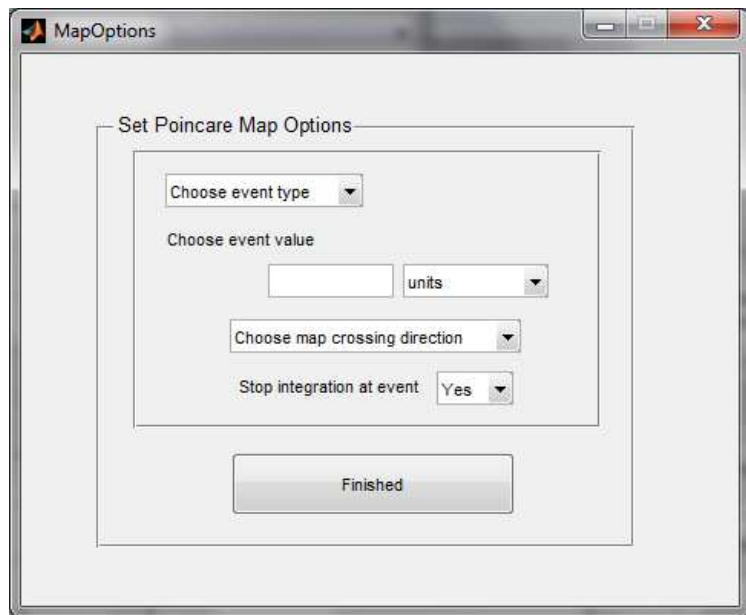
Figure 7.2. Transfer properties are selected

the transfer. These selections are populated in the window in Figure 7.2(b). Once the transfer orbit and manifold properties are identified, pressing the “Finished” button returns these properties to the Transfer Design Environment.

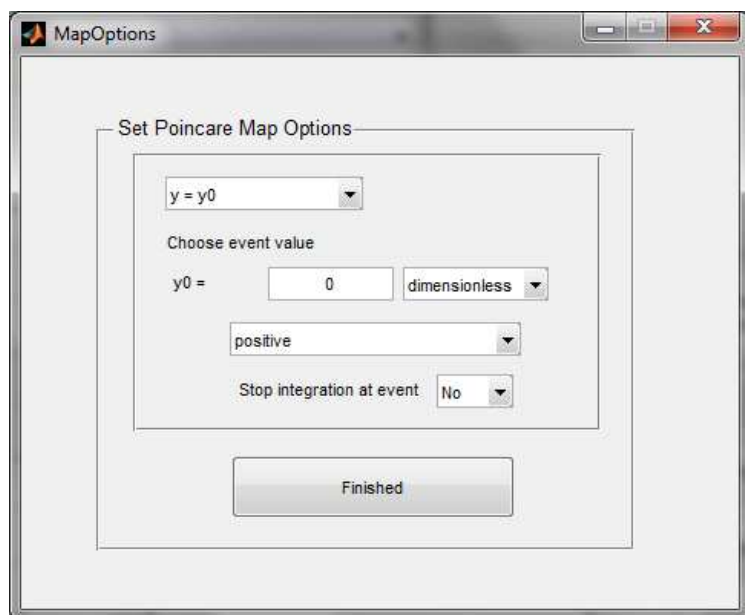
At this stage in the design procedure, the three-body system, energy level, orbit characteristics, and invariant manifold properties are identified. Now, the Poincaré surface of section is selected and the method of viewing the map is specified by press-

ing the “Poincaré Map Options” button. The pop-up window in Figure 7.3(a) appears where the surface of section is defined in addition to the direction of crossings considered. The stopping condition is also designated to determine if the manifolds are numerically integrated through the full specified propagation time, or if the integration is terminated upon intersection of the trajectory with the map. In this example, the event type selected is  $y = y_0$ , the event value  $y_0$  is set to zero, and the map crossing is set to “positive,” indicating that the surface of section to be employed is  $\Sigma^+ = \{\bar{x}|y = 0, \dot{y} > 0\}$ . The stopping condition is removed so that all crossings of  $\Sigma^+$  are included on the map. The user-selected options appear in Figure 7.3(b). By pressing “Finished,” the Poincaré map definitions are returned to the main Transfer Design Environment.

The remaining step before viewing the Poincaré map is the construction of the glyph that is employed to represent crossings of  $\Sigma^+$ . Pressing the “Map Marker Options” button, the pop-up window depicted in Figure 7.4(a) appears. Two buttons at the top of the window identify the type of glyph to be employed. The button on the left allows the map to be viewed as a puncture plot, whereas the button on the right specifies that map crossings are plotted using the vector glyph definition from Figure 6.2. For this example, the right button is selected and map crossings will be displayed as vectors. The basepoint of the vector corresponds to the variables selected in the lower left panel labeled “Basepoint 1,” which are set to the  $x$ - and  $z$ -coordinates. Note that the variables will be displayed in dimensional coordinates on the map. Two constants,  $k_1$  and  $k_2$ , are included so that the variables defining the basepoint can be scaled, if necessary. These constants are set equal to one, as the basepoint coordinates are similar in magnitude for this example. Thus,  $q_1 = x$  and  $q_2 = z$  for the glyph definition from Figure 6.2. By specifying “Basepoint 2,” each vector on the map is defined as the line segment connecting the coordinates from basepoint 1 and basepoint 2. That is, identifying the coordinates for basepoint 2 as  $\dot{x}$  and  $\dot{z}$ , each vector on the map is defined by the segment  $(x, z) \rightarrow (x + k_3\dot{x}, z + k_4\dot{z})$ .



(a)

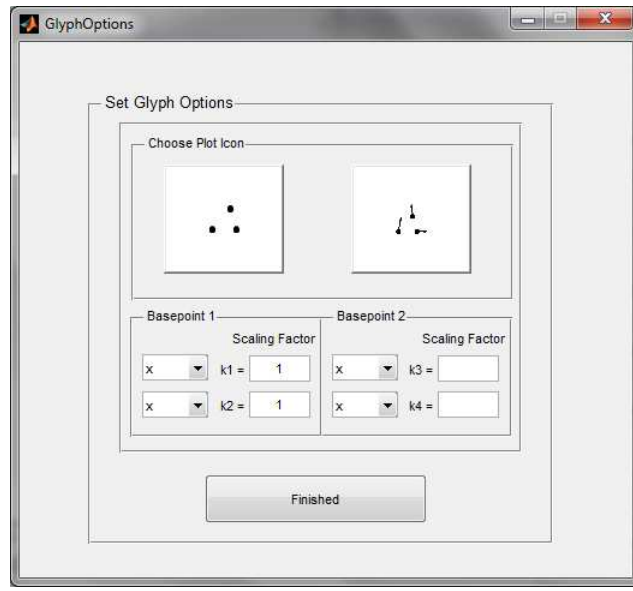


(b)

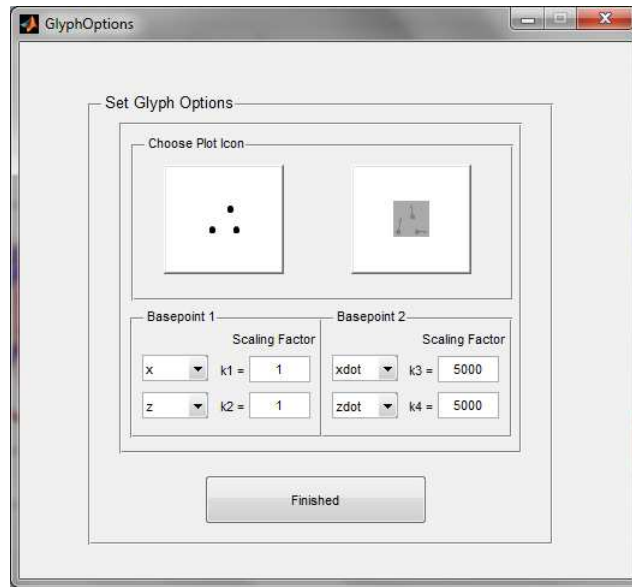
Figure 7.3. Poincaré map properties are defined

The associated scaling constants are set to  $k_3 = 5000$  and  $k_4 = 5000$  to account for the difference in magnitude between the position and velocity coordinates. The selected glyph definition is returned to the main design GUI by pressing the “Finished” button.

Now that all transfer and map properties are defined, the manifold arcs and associated Poincaré map may be computed. By pressing the “Compute Periodic Orbits” button, a differential corrections process is employed to target the desired orbits within the specified departure and arrival orbit families and associated with the Jacobi constant value set by the user. For this example, the resulting northern and southern  $L_1$  halo orbits appear in the plot on the left within the GUI in Figure 7.5. Pressing the “Compute Poincaré Map” button, initial conditions along the invariant manifold arcs computed and are propagated. Crossings of  $\Sigma^+$  are recorded and the resulting Poincaré map is displayed in the plot axes on the right in the GUI. Unstable manifold crossings are plotted in red, and the stable manifold is represented in blue. The zoom and pan tools, displayed as buttons in the upper left portion of the GUI, allow the user to inspect different regions of the map to search for an initial guess for a transfer. The map is plotted again in Figure 7.6 with three zoomed views included that depict the structures in various regions of the map. The zoomed view labeled 3 reveals a pair of crossings, circled in black, for which  $x$  is on the far side of the Moon,  $z \approx 0$ , and  $\dot{x} \approx 0$ . These crossings are selected within the design environment to reveal the corresponding manifold arcs. By pressing either of the buttons with in the “Select Map Crossings” panel, a pair of crosshairs appears. Navigating these crosshairs within the Poincaré map, the user is able to point-and-click on the map to identify the manifold arcs to be employed for the transfer. Using this method, the crossings circled in Figure 7.6 are selected and the resulting initial guess for a transfer between the northern and southern  $L_1$  halo orbits is represented in the plot window on the left in the GUI in Figure 7.7(a). If this transfer is satisfactory, it is passed to the Differential Corrections Environment to compute a feasible transfer. Otherwise,



(a)



(b)

Figure 7.4. Poincaré map display properties are specified

if further exploration is desired, the Jacobi constant value can be modified to examine the effect on the resulting on the Poincaré map. Adjusting the value of Jacobi

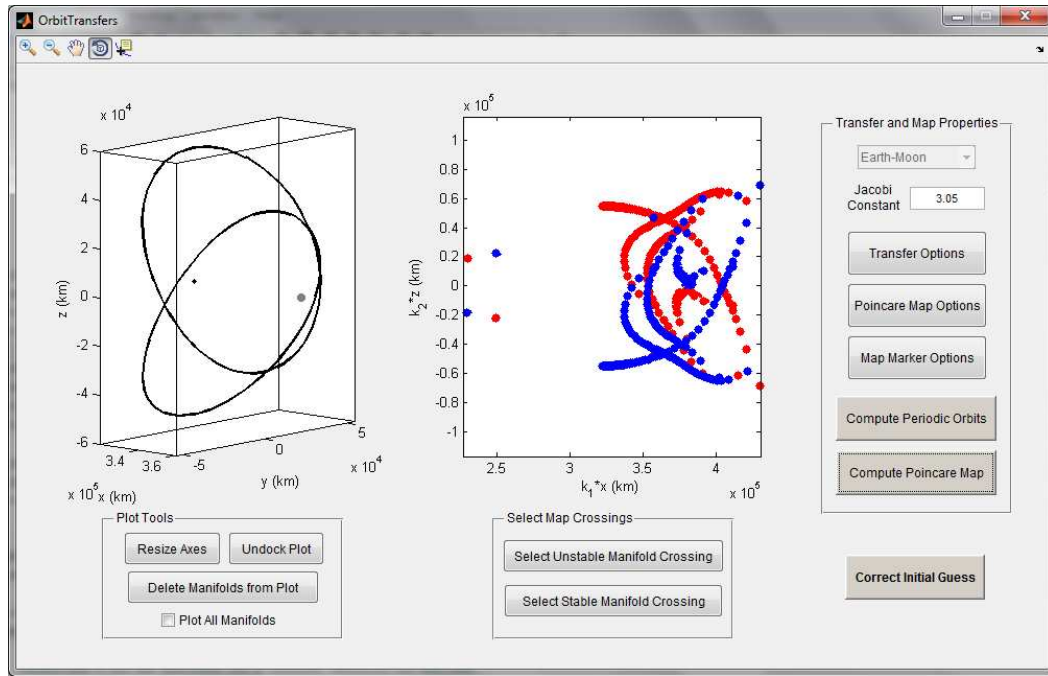


Figure 7.5. Transfer orbits are computed and manifold crossings of the Poincaré map are displayed

constant and pressing “Compute Periodic Orbits,” new halo orbits corresponding to the updated value of Jacobi constant are computed. Pressing “Compute Poincaré Map” reveals the map for the manifold arcs asymptotic to the halo orbits for the new value of Jacobi constant. For example, the map associated with  $C = 3.07$  is depicted in Figure 7.7(b). The crossings nearest  $z = \dot{x} = 0$  are selected within the equivalent region 3 on the new map, and the associated manifold arcs are plotted in the left plot window in Figure 7.7(b). Once a satisfactory initial guess for the transfer is located, it is passed to the Differential Corrections Environment by pressing the “Correct Initial Guess” button in the lower right of the design GUI. This environment is discussed in the following section.

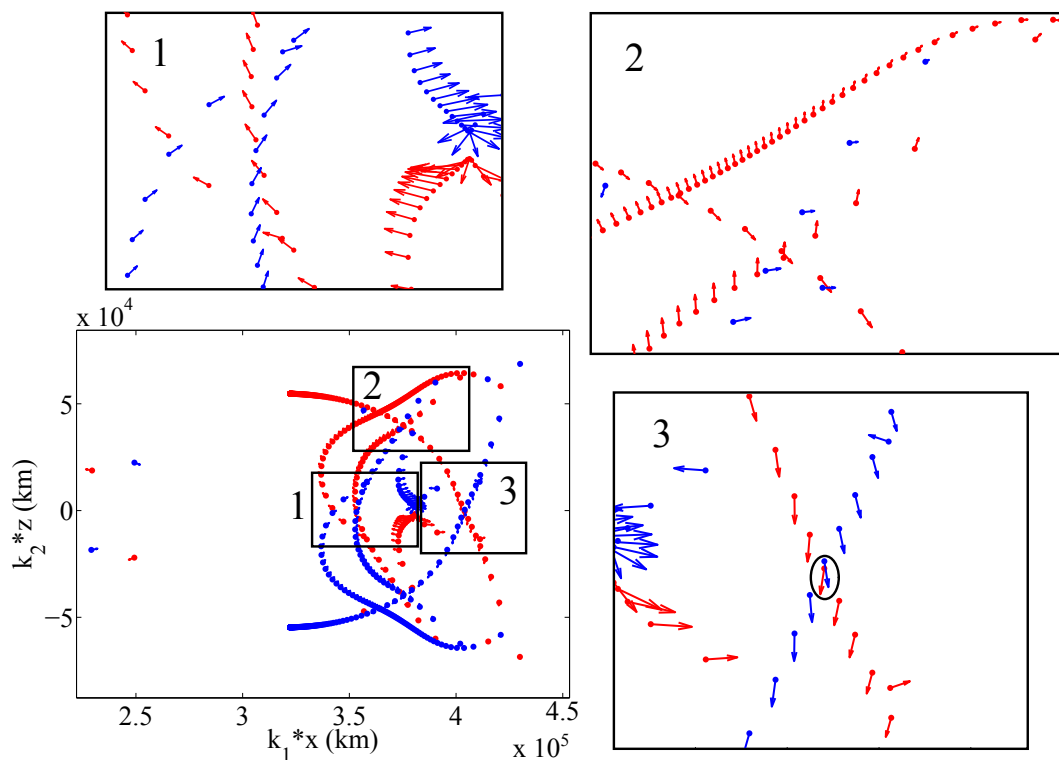


Figure 7.6. The Poincaré map is explored for transfer opportunities

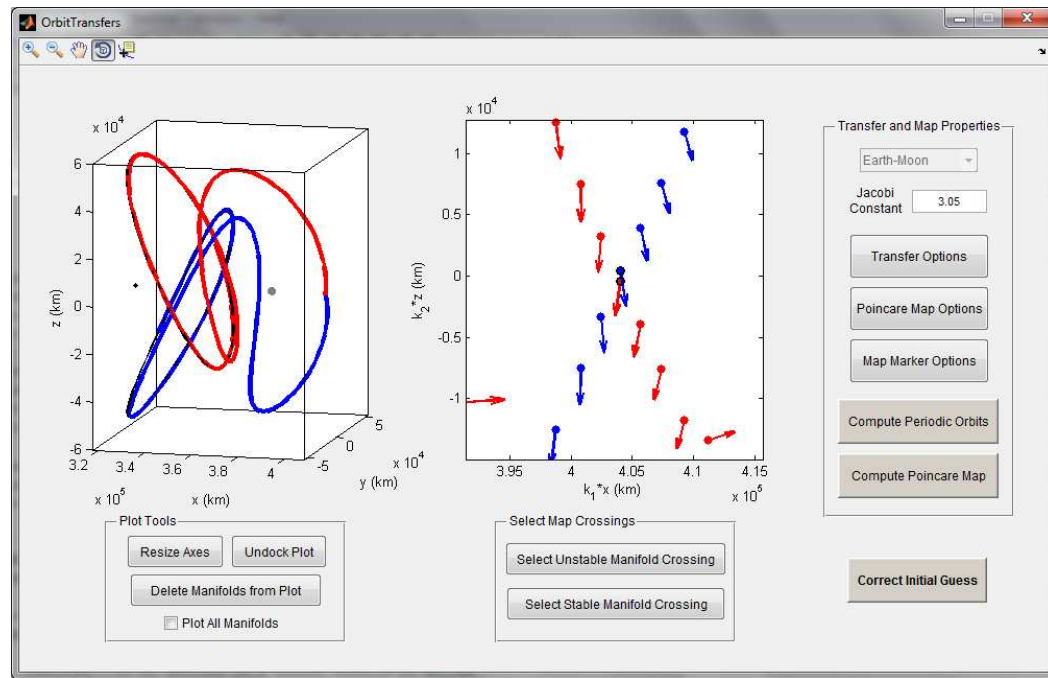
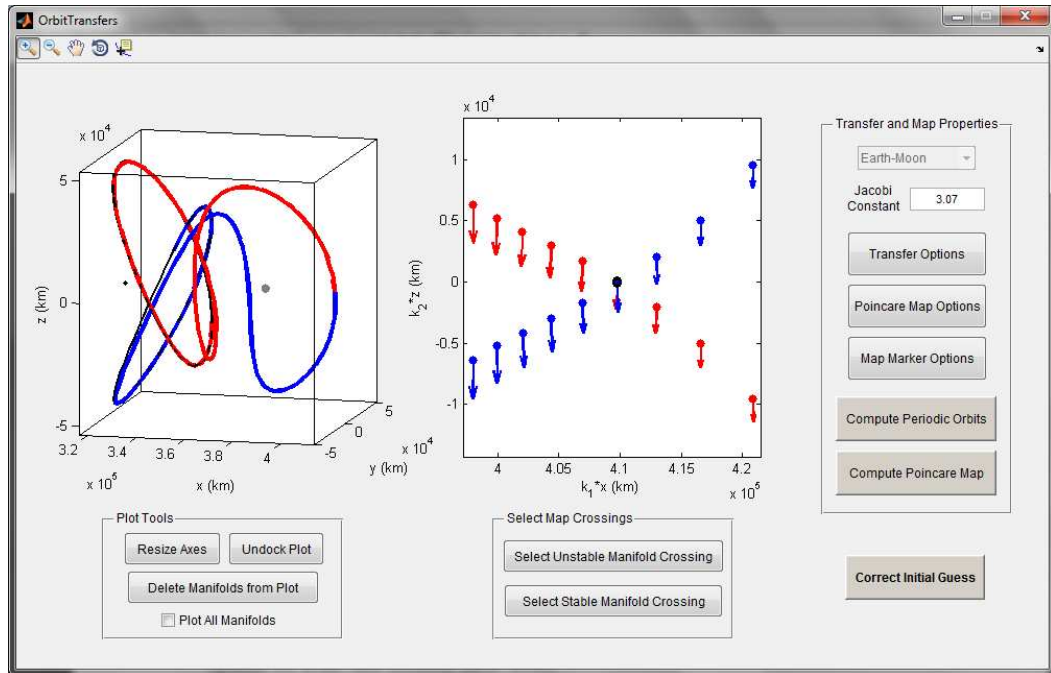
(a)  $C = 3.05$ (b)  $C = 3.07$ 

Figure 7.7. Transfer arcs are interactively selected from the Poincaré map

### 7.0.2 Differential Corrections Environment

Within the Transfer Design Environment, the user can explore and interact with the design options to search for an initial guess for a transfer between the departure and arrival orbits of interest. This guess is discontinuous, in general, and must be differentially corrected to locate a feasible transfer. Several variables are determined within the design environment that define the initial guess. These variables are discussed in Chapter 6.4 and include the following:

- $\bar{x}_{10}$ : the initial state along the departure orbit
- $T_1$ : the period of the departure orbit
- $\bar{x}_{20}$ : the initial state along the arrival orbit
- $T_2$ : the period of the arrival orbit
- $\bar{x}_{u0}$ : the final state along the unstable manifold arc at the intersection with the surface of section
- $T_u$ : the propagation time along the unstable manifold
- $\tau_1$ : the time that defines the location along the departure orbit from which the unstable manifold arc is computed
- $\bar{x}_{s0}$ : the initial state along the stable manifold arc at the intersection with the surface of section
- $T_s$ : the propagation time along the stable manifold
- $\tau_2$ : the time that defines the location along the arrival orbit from which the stable manifold arc is computed

When the “Correct Initial Guess” button is pressed within the Transfer Design Environment, these variables are passed to the Differential Corrections Environment where the algorithms described in Chapter 6.4 are employed to locate a feasible transfer.

The Differential Corrections Environment is depicted in Figure 7.8. The initial guess designed within the Transfer Design Environment appears in the plot window, and the list of variables on the left in the “Transfer Design Parameters” panel is

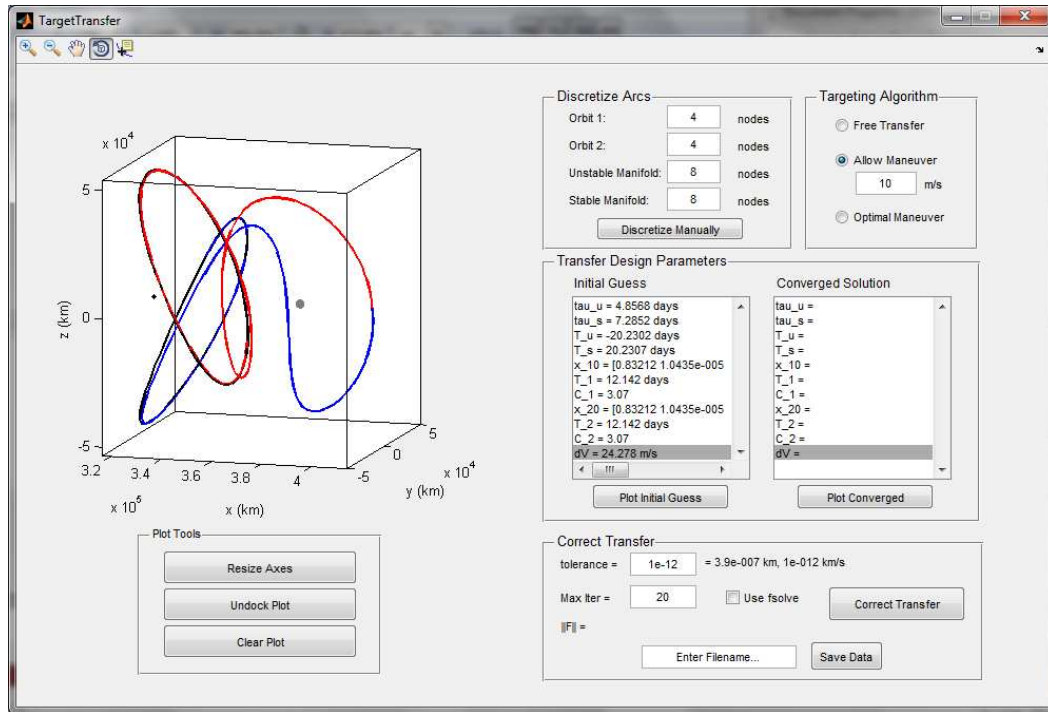


Figure 7.8. The initial guess for the transfer is displayed in the Differential Corrections Environment

populated with the corresponding values. Note that  $\tau_u$  and  $\tau_s$  in the list are equivalent to  $\tau_1$  and  $\tau_2$ , respectively. The discontinuity in the velocity, located where the red and blue manifold arcs join, is included at the bottom of the list; the current value is 24.278 m/s. To begin the differential corrections process, several parameters must be specified. At the top left of the GUI is a panel labeled “Discretize Arcs” containing four text boxes into which integer values are entered. These values specify the number of nodes that are employed to discretize the periodic orbits and the unstable and stable manifold arcs. This discretization enables a multiple-shooting scheme that reduces numerical sensitivities during the corrections process. For this example, four nodes are employed to discretize each halo orbit, and eight nodes are distributed along each manifold arc. By entering these values into the text boxes, the algorithm discretizes each arc into equal time segments. If more control over the node distribution process is

desired, the “Discretize Manually” button is employed. In addition to discretizing the initial guess, the user selects the targeting algorithm to be employed by choosing from the options in the “Targeting Algorithm” panel. Recall that a maneuver-free transfer is sought for this example. Thus, the goal is to reduce the  $\Delta v$  to zero employing differential corrections. In general, it may not be possible to remove the entire  $\Delta v$  in one step. That is, it is generally useful to reduce the  $\Delta v$  incrementally using a continuation process. Thus, to begin, the second option labeled “Allow Maneuver” is selected and a value of 10 m/s is input into the corresponding text box. The algorithm described in the section “Enforcing an Upper Limit on the  $\Delta v$ ” of Chapter 6.4.2 is employed within the corrections process. Pressing the “Correct Transfer” button, the algorithm proceeds and the output appears in Figure 7.9(a). The solution converges

```
iteration: 0, |||F||| = 0.01397 (dimensionless), iteration time: 1.051 seconds
iteration: 1, |||F||| = 0.0069882 (dimensionless), iteration time: 0.69025 seconds
iteration: 2, |||F||| = 0.00021281 (dimensionless), iteration time: 0.72914 seconds
iteration: 3, |||F||| = 2.2854e-006 (dimensionless), iteration time: 0.71776 seconds
iteration: 4, |||F||| = 1.2032e-007 (dimensionless), iteration time: 0.69175 seconds
iteration: 5, |||F||| = 2.8387e-011 (dimensionless), iteration time: 0.68801 seconds
iteration: 6, |||F||| = 3.9013e-014 (dimensionless), iteration time: 0.011382 seconds
```

(a) Reducing  $\Delta v$  to 10 m/s

```
iteration: 0, |||F||| = 0.0097768 (dimensionless), iteration time: 1.1714 seconds
iteration: 1, |||F||| = 0.00032025 (dimensionless), iteration time: 0.73872 seconds
iteration: 2, |||F||| = 2.0603e-007 (dimensionless), iteration time: 0.74103 seconds
iteration: 3, |||F||| = 5.7629e-008 (dimensionless), iteration time: 0.6903 seconds
iteration: 4, |||F||| = 3.2356e-012 (dimensionless), iteration time: 0.69136 seconds
iteration: 5, |||F||| = 3.1915e-014 (dimensionless), iteration time: 0.011376 seconds
```

(b) Reducing  $\Delta v$  to 0

Figure 7.9. Output from the differential corrections algorithms

to a feasible transfer in 6 iterations, noting that the tolerance specified within the “Correct Transfer” panel is  $1 \times 10^{-12}$  (nd). The corresponding tolerance values in dimensional units are provided and are approximately  $3.9 \times 10^{-7}$  km and  $1 \times 10^{-12}$  km/s. For the corrected solution, a  $\Delta v$  of 10 m/s exists where the unstable and stable manifold arcs join. The list of variables on the right in the “Transfer Design

Parameters” panel is now populated with the values associated with the converged transfer. The ultimate goal is to reduce the  $\Delta v$  to zero, and this is accomplished by, next, selecting the “Free Transfer” option within the “Targeting Algorithm” panel and pressing the “Correct Transfer” button. Now, the algorithm described in Chapter 6.4.1 is employed to remove the  $\Delta v$ , and a maneuver-free transfer is computed. The output from the algorithm is displayed in Figure 7.9(b) and the converged solution appears in Figure 7.10. Comparing the values in the list boxes on the left and right in

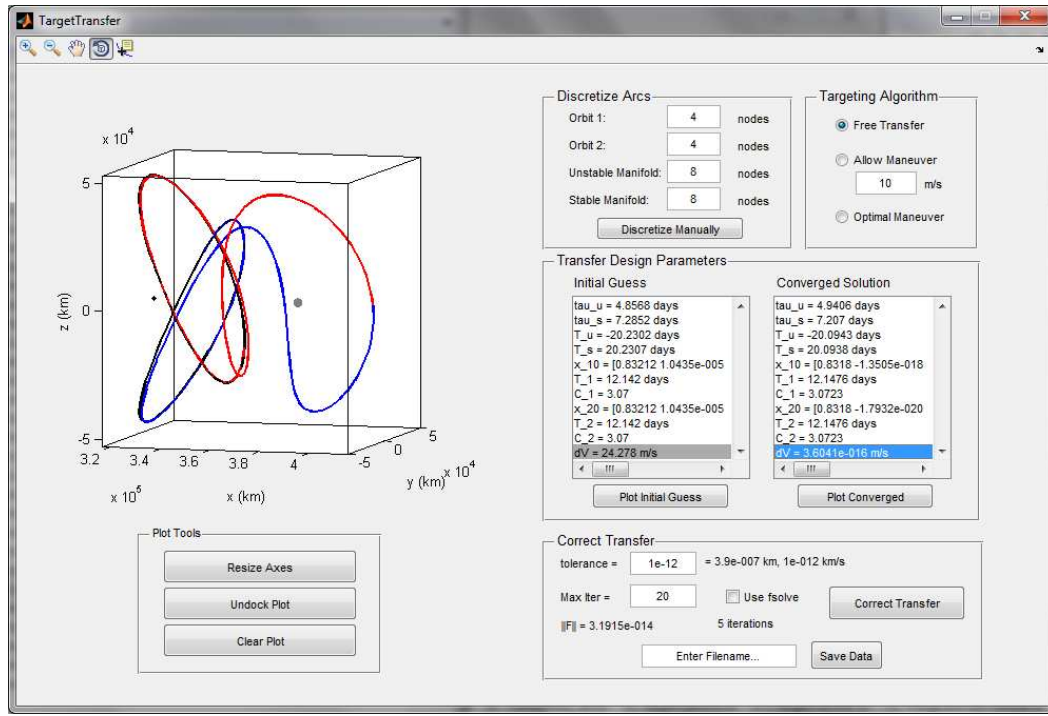


Figure 7.10. A transfer corresponding to  $\Delta v = 0$  is computed

the “Transfer Design Parameters” panel, changes in the manifold departure locations  $\tau$  are evident, in addition to an increase in the value of  $C$ , and a slight decrease in the time-of-flight TOF =  $|T_u| + T_s$  for the converged transfer. The values of the variables associated with the corrected solution are saved to a \*.mat file by entering a filename

into the text box at the bottom of the “Correct Transfer” panel and pressing the “Save Data” button.

The design process demonstrated here provides a method to incorporate Poincaré maps into the mission design process. Specifically, the search for maneuver-free and low-cost transfers is facilitated employing invariant manifolds associated with periodic libration point orbits. With interactive access to control variables such as the energy level and the desired libration point orbit types, the solutions space can be searched quickly and efficiently. An interactive differential corrections environment enables the user to apply differential corrections processes to locate feasible solutions and to incorporate any desired constraints on the allowed  $\Delta v$ . In this example, the design process is demonstrated and a novel heteroclinic connection between northern and southern  $L_1$  halo orbits is straightforward to locate.

## 8. CATALOG OF FREE AND LOW-COST TRANSFERS BETWEEN LIBRATION POINT ORBITS IN THE EARTH-MOON SYSTEM

The lunar libration points have been proposed as destinations in the next step of the development of the human presence in space [100]. Orbits in the vicinity of the Sun-Earth  $L_1$  and  $L_2$  points provide ideal locations for solar and cosmological observatories, and the role of human servicing of spacecraft in these orbits for future missions is an important consideration. Because transport between the Earth-Moon and Sun-Earth libration points requires relatively low  $\Delta v$ , such observatories could be transferred to Earth-Moon libration point orbits to enable human servicing missions [100]. The lunar libration points are also of interest for storage of fuel and supplies to service future missions to the Moon and Mars, and could serve as locations to build spacecraft to be delivered to Sun-Earth libration point orbits [100]. Thus, an understanding of the available transfers between the lunar libration point orbits is useful to assess transport options to, from, and between these orbits.

### 8.1 Catalog Taxonomy

The strategies demonstrated in the previous section prove useful to search for maneuver-free and low-cost, in terms of  $\Delta v$ , transfers between libration point orbits. In the following sections, transfers associated with periodic libration point orbits in the Earth-Moon system are computed and are presented in a catalog. The transfer types considered include the following:

- V1: Homoclinic connections associated with  $L_1$  vertical orbits

- V2: Homoclinic connections associated with  $L_2$  vertical orbits
- H1: Homoclinic connections associated with  $L_1$  halo orbits
- H2: Homoclinic connections associated with  $L_2$  halo orbits
- A1: Homoclinic connections associated with  $L_1$  axial orbits
- A2: Homoclinic connections associated with  $L_2$  axial orbits
- HH1: Heteroclinic connections connecting northern and southern  $L_1$  halo orbits
- HH2: Heteroclinic connections connecting northern and southern  $L_2$  halo orbits
- AA1: Heteroclinic connections connecting northern and southern  $L_1$  axial orbits
- AA2: Heteroclinic connections connecting northern and southern  $L_2$  axial orbits
- V1V2: Transfers between  $L_1$  and  $L_2$  vertical orbits
- H1H2: Transfers between  $L_1$  and  $L_2$  halo orbits
- A1A2: Transfers between  $L_1$  and  $L_2$  axial orbits
- V1H2: Transfers between  $L_1$  vertical orbits and  $L_2$  halo orbits
- H1V2: Transfers between  $L_1$  halo orbits and  $L_2$  vertical orbits

Because the solution space is infinite, boundaries are defined for the search and only those transfers that exist within the prescribed constraints are sought. These boundaries are defined so that the catalog contains transfers that:

1. exist within the  $P_2$  region of the ZVCs,
2. require a transfer time  $\leq 50$  days,
3. require no maneuver for transfer types V1, V2, H2, H2, HH1, HH2, AA1, AA2,
4. require a maneuver of  $\Delta v \leq 20$  m/s for transfer types V1V2, V1H2, H1V2, H1H2,
5. do not impact the Moon,
6. and exist for  $C \geq 3.03$ , with an exception for transfers of types A1, A2, AA1, AA2, and A1A2.

The lower limit on the value of  $C$  is selected based on the observation that crossings of the Poincaré maps grow sparse for  $C < 3.03$  and time-of-flight (TOF)  $\leq 50$  days; thus, very few transfers meeting the criteria in 1–4 are identified near this lower limit.

This value of  $C$  corresponds to  $L_1$  and  $L_2$  vertical orbits with maximum  $z$ -amplitudes around 76710 and 75280, respectively, and  $L_1$  and  $L_2$  halo orbits with maximum  $z$ -amplitudes near 60350 and 72480 km. It should be noted that the value of  $C$  along the halo family is not unique, and only those halo orbits that exist between the bifurcating orbit from the Lyapunov family and the first orbit for which  $C = 3.03$  are considered. Because the  $L_1$  and  $L_2$  axial families exist for a narrow range of Jacobi constant values ( $2.991 \leq C \leq 3.021$  and  $2.967 \leq C \leq 3.014$ , respectively) the transfers associated with these orbits are not subject to the  $C \geq 3.03$  constraint. During the search, some transfers with times-of-flight greater than 50 days are located and are included in the catalog up to TOF = 75 days. While a thorough search for transfers corresponding to  $\text{TOF} \leq 50$  days is completed, it is likely that some transfers corresponding to  $50 < \text{TOF} < 75$  days are not included.

Heteroclinic and homoclinic connections represent maneuver-free transfers between periodic orbits. For the transfer types V1, V2, H2, H2, HH1, HH2, A1, A2, AA1, and AA2, only free transfers are considered. However, no free transfers are found in the Earth-Moon system within the TOF constraints for transfers of type V1V2, H1H2, A1A2, V1H2, and H1V2. Thus, only those solutions that require a maneuver of  $\leq 20$  m/s are considered for these transfer types. In this catalog the locally optimal solutions are presented, however, there may exist a range of trajectories near the optimal solution within the  $0 \leq \Delta v \leq 20$  m/s and  $\text{TOF} \leq 50$  day boundaries. Any transfers that impact the Earth or Moon are, generally, discarded.

For all transfers computed in this catalog, associated transfer information is provided in a series of tables including a transfer label that includes the orbit type and the transfer number (e.g., V1-1 represents the first homoclinic connection associated with an  $L_1$  vertical orbit presented in the catalog), the Jacobi constant value associated with the transfer, the TOF along the transfer path, and the figure number in which the transfer is plotted. For low-cost transfers, two Jacobi constant values are listed and correspond to the values associated with the departure ( $C_1$ ) and arrival

( $C_2$ ) orbits. Additionally, the maneuver ( $\Delta v$ ) required to complete the transfer is provided and corresponds to the location in the figures where the red and blue manifold arcs join. All computed transfers that meet the defined search parameters are cataloged in the tables and figures as outlined in Table 8.1. Note that the plots of

Table 8.1 Catalog of Libration Point Orbit Transfers

Transfer Type	Table	Figures
V1	8.2	8.1 – 8.18
V2	8.2	8.19 – 8.36
H1	8.3	8.37 – 8.53
H2	8.3	8.54 – 8.67
A1	8.4	8.68 – 8.69
A2	8.4	8.70 – 8.71
HH1	8.5	8.72 – 8.82
HH2	8.5	8.83 – 8.88
AA1	8.5	8.89
AA2	8.5	8.90
V1V2	8.6	8.91 – 8.98
H1H2	8.6	8.99 – 8.104
A1A2	8.6	8.105
V1H2	8.6	8.106 – 8.108
H1V2	8.6	8.109 – 8.111

the transfers appear in Moon-centered coordinates.

As a result of the generation of this catalog, some observations are made about the transfers and their geometries. It is noted that homoclinic connections associated with  $L_1$  orbits are often accompanied by transfers of similar geometry associated with

an  $L_2$  orbit of the same orbit type. Likewise, for many of the heteroclinic connections computed between northern and southern  $L_1$  halo/ axial orbits, a connection of similar geometry is also located between northern and southern  $L_2$  halo/axial orbits. Thus, in this catalog, all free  $L_1$  and  $L_2$  orbit transfers are grouped as “partners” and are presented together in the tables. For clarity, define a pair of transfer partners as consisting of two solutions: (A) a transfer associated with an  $L_1$  orbit, and (B) a transfer associated with an  $L_2$  orbit of the same orbit type as the  $L_1$  orbit. That is, if (A) corresponds to an  $L_1$  vertical orbit, then (B) corresponds to an  $L_2$  vertical orbit. The  $L_1$  orbit transfers (A) are listed on the left side of the tables and their partner  $L_2$  orbit transfers (B) appear on the right. Partner transfers (A) and (B) are of similar geometry, that is, they appear roughly as reflections of one another across the  $y$ - $z$  plane at  $x = 1 - \mu$  (i.e.,  $x = 0$  in Moon-centered coordinates). The low-cost transfers between two distinct orbit types (V1H2 and H1V2) are also grouped according to geometry; however, low-cost transfers between the same orbit type (V1V2 and H1H2) are not grouped as partners because the  $L_1$  and  $L_2$  orbit types involved in the transfer are the same. If no partner transfer is located for an  $L_1$  ( $L_2$ ) orbit, the entries in the table for the  $L_2$  ( $L_1$ ) orbit transfer appear as dashes. The transfer cases for which no partner transfer is computed are discussed in further detail in the upcoming section on catalog observations and discussion. The transfer number is the same for two transfers of the same geometry, e.g., V1- $n$  and V2- $n$  represent homoclinic connections of the same geometry and associated with  $L_1$  and  $L_2$  vertical orbits, respectively. For partner transfers, the tables are organized according to descending values of  $C$  for the  $L_1$  orbit transfers. The  $L_2$  orbit transfers are then, generally, organized with the  $L_1$  orbit transfers according to matching geometry. The value of  $C$  does not necessarily decrease monotonically for these partner  $L_2$  orbit transfers within the tables, however, the figures in all sections are organized by descending Jacobi constant value. Recall that some transfers with times-of-flight greater than 50 days are included in the catalog up to TOF = 75 days. If a pair of partner transfers

is computed with one partner corresponding to  $\text{TOF} \leq 75$  days and one to  $\text{TOF} > 75$  days, both transfers are included in the catalog.

In the following sections, the computed transfers are cataloged as described. Discussion and observations are included in the final sections of this chapter.

## 8.2 Homoclinic Connections Associated with Vertical Orbits

Table 8.2 Vertical Orbit Homoclinic Connections

Label	$C$	TOF (days)	Figure No.	Label	$C$	TOF (days)	Figure No.
V1-1	3.1775	52.5825	8.1	V2-1	-	-	-
V1-2	3.1580	53.1241	8.2	V2-2	-	-	-
V1-3	3.1565	50.5069	8.3	V2-3	-	-	-
V1-4	-	-	-	V2-4	3.1450	72.2670	8.19
V1-5	3.1389	51.1528	8.4	V2-5	3.1288	62.5025	8.22
V1-6	-	-	-	V2-6	3.1361	61.8870	8.21
V1-7	3.1316	50.4070	8.5	V2-7	3.1416	59.5273	8.20
V1-8	3.1271	60.7297	8.6	V2-8	3.1198	63.4957	8.23
V1-9	3.1201	53.1732	8.7	V2-9	-	-	-
V1-10	3.1126	63.9845	8.8	V2-10	-	-	-
V1-11	-	-	-	V2-11	3.1093	58.1397	8.24
V1-12	3.1060	66.0469	8.9	V2-12	3.1054	76.3231	8.25
V1-13	3.1059	39.9676	8.10	V2-13	3.1053	46.9066	8.27
V1-14	3.1008	51.4635	8.11	V2-14	3.0999	58.4020	8.28
V1-15	3.0947	67.9682	8.12	V2-15	3.1045	70.6015	8.26
V1-16	3.0897	55.3035	8.13	V2-16	3.0876	60.1932	8.29
V1-17	3.0885	38.7444	8.14	V2-17	3.0852	45.2766	8.30
V1-18	3.0870	47.0461	8.15	V2-18	3.0827	52.7960	8.31
V1-19	3.0825	51.4976	8.16	V2-19	3.0697	59.1197	8.34
V1-20	3.0768	73.6204	8.17	V2-20	3.0798	79.5223	8.32
V1-21	3.0760	72.0903	8.18	V2-21	3.0618	79.4076	8.35
V1-22	-	-	-	V2-22	3.0707	71.3786	8.33
V1-23	-	-	-	V2-23	3.0315	69.6960	8.36

### $L_1$ Vertical Orbits

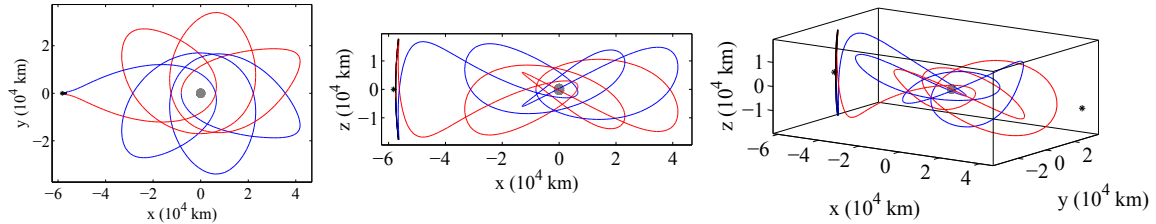


Figure 8.1. V1-1,  $C = 3.1775$ , TOF = 52.5825 days

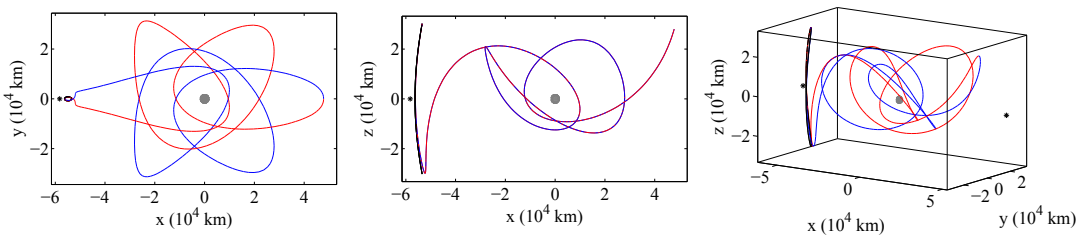


Figure 8.2. V1-2,  $C = 3.1580$ , TOF = 53.1241 days

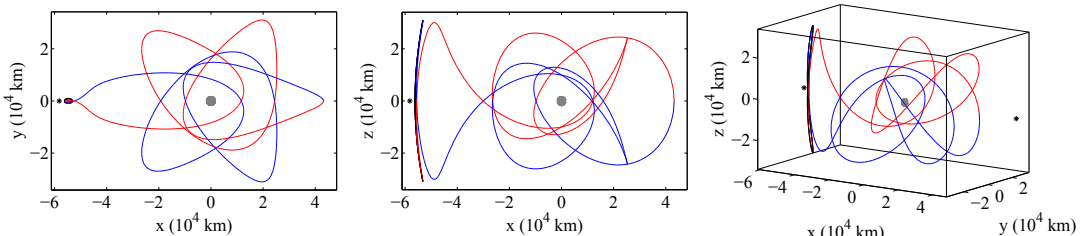


Figure 8.3. V1-3,  $C = 3.1565$ , TOF = 50.5069 days

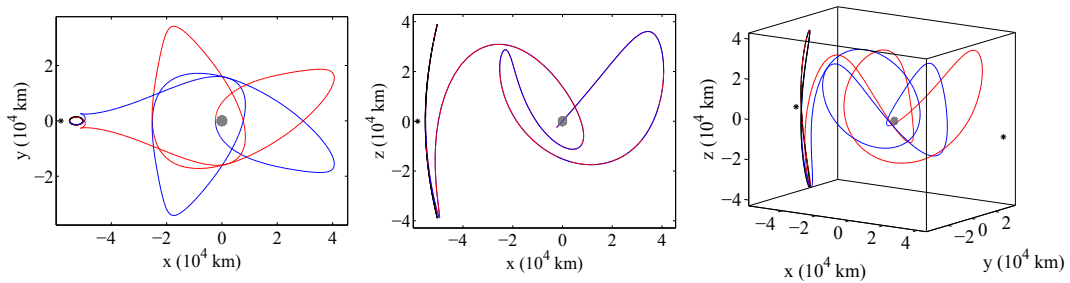


Figure 8.4. V1-5,  $C = 3.1389$ , TOF = 51.1528 days

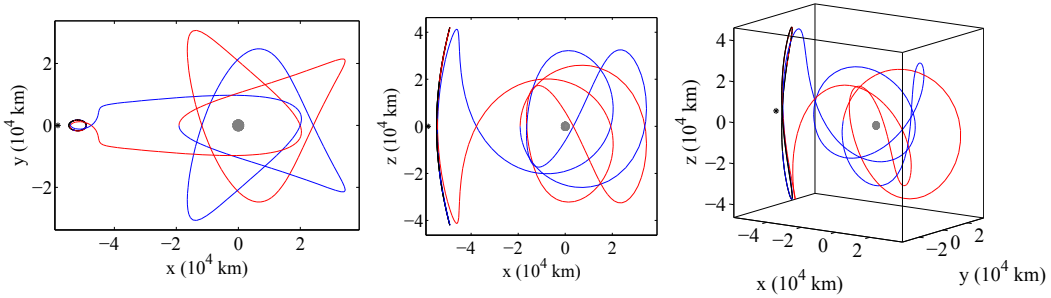


Figure 8.5. V1-7,  $C = 3.1316$ , TOF = 50.4070 days

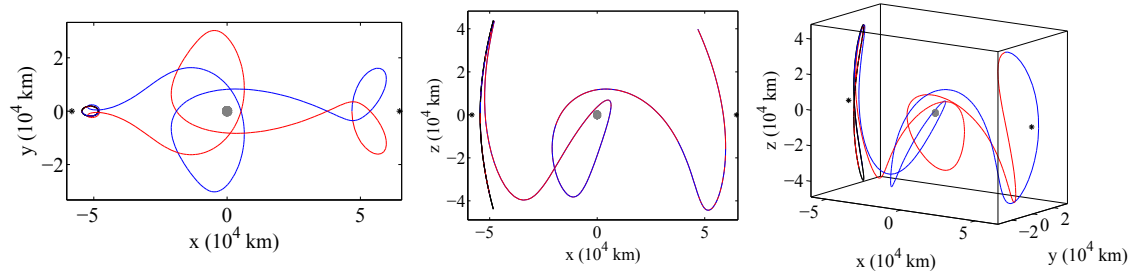


Figure 8.6. V1-8,  $C = 3.1271$ , TOF = 60.7297 days

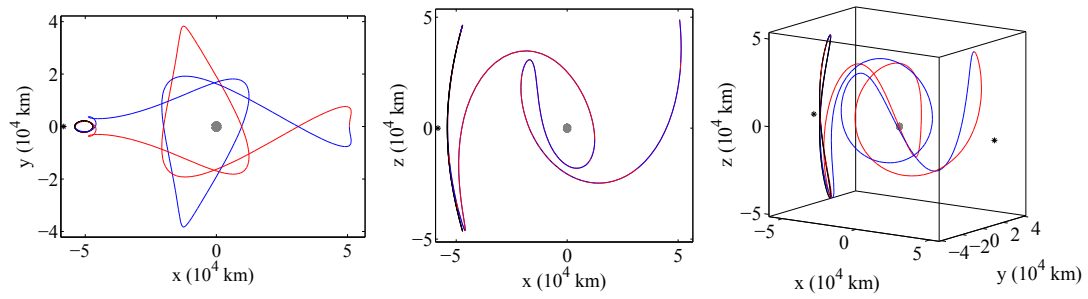


Figure 8.7. V1-9,  $C = 3.1201$ , TOF = 53.1732 days

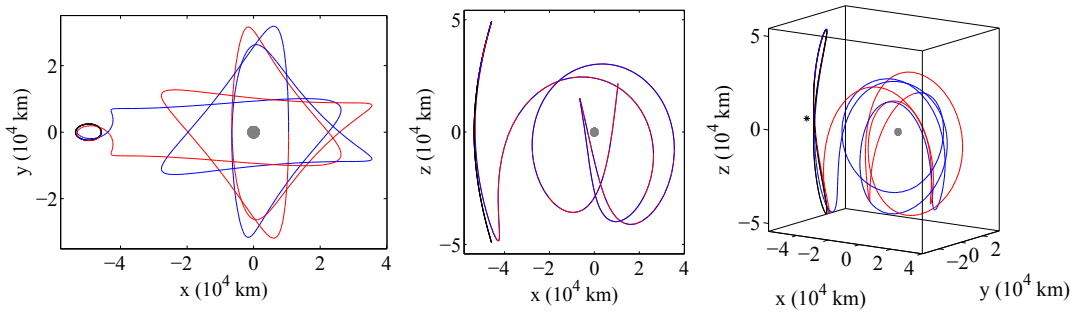


Figure 8.8. V1-10,  $C = 3.1126$ , TOF = 63.9845 days

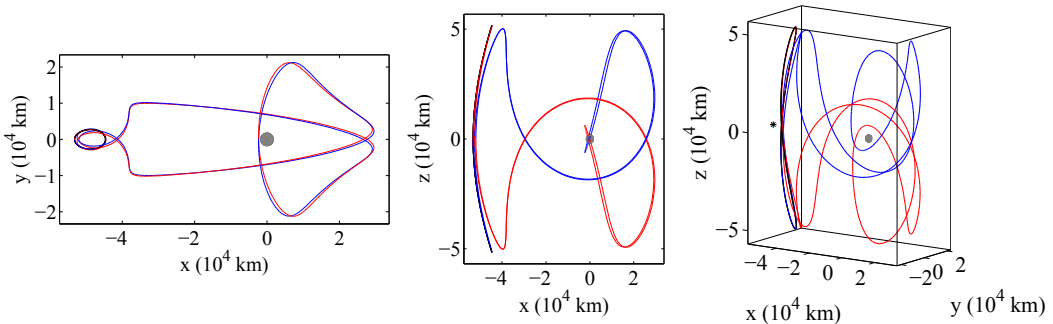
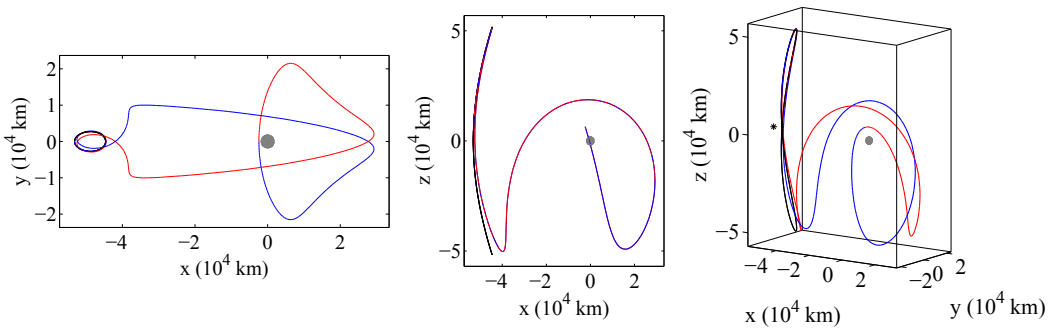
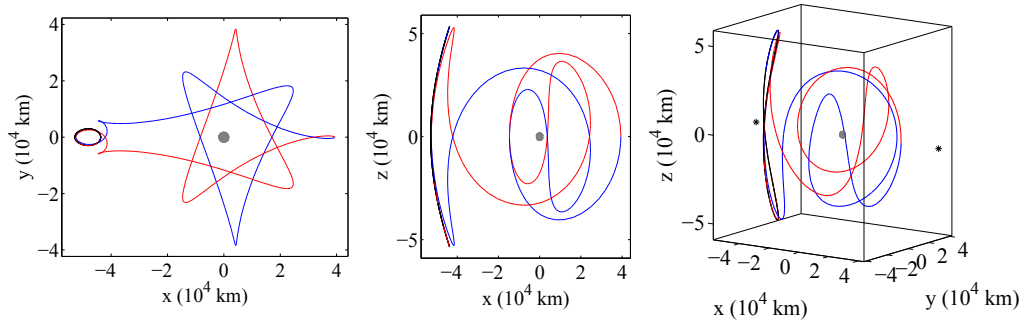
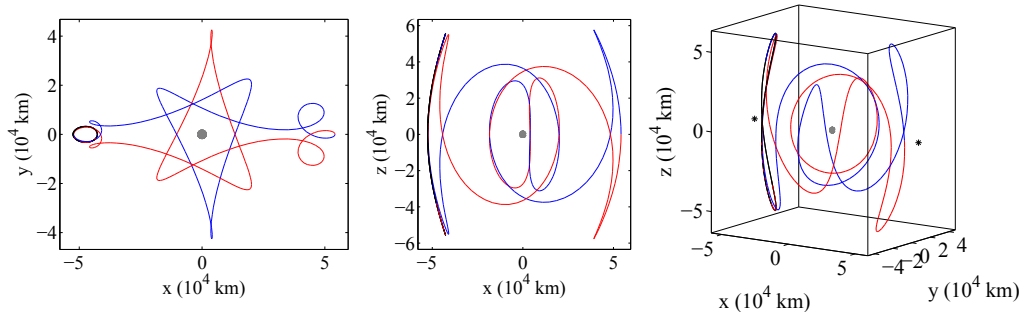


Figure 8.9. V1-12,  $C = 3.1060$ , TOF = 66.0469 days

Figure 8.10. V1-13,  $C = 3.1059$ , TOF = 39.9676 daysFigure 8.11. V1-14,  $C = 3.1008$ , TOF = 51.4635 daysFigure 8.12. V1-15,  $C = 3.0947$  TOF = 67.9682 days

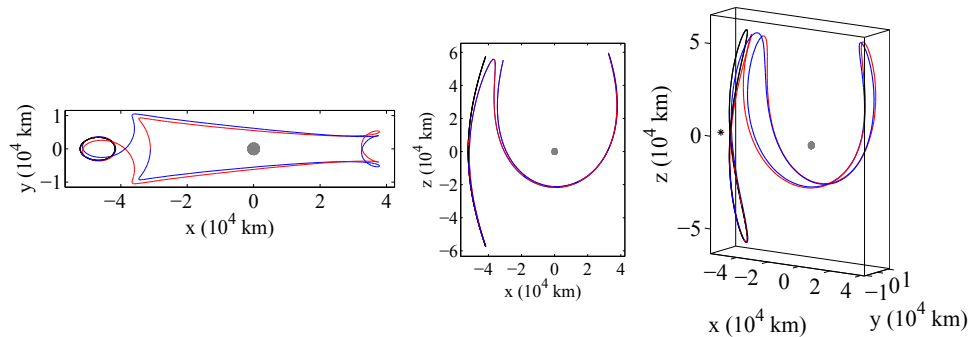


Figure 8.13. V1-16,  $C = 3.0897$ , TOF = 55.3035 days

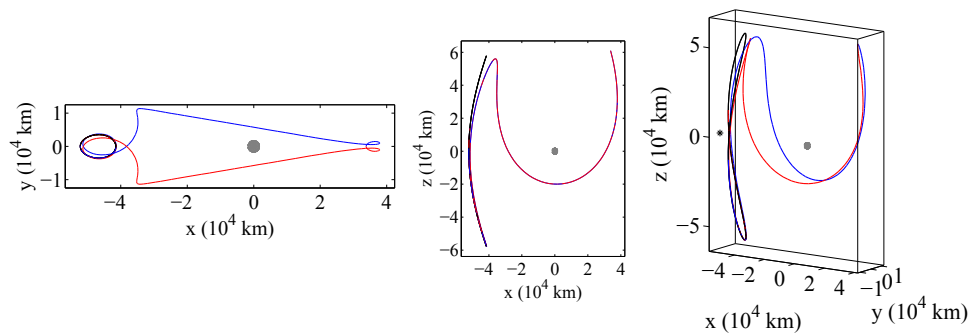


Figure 8.14. V1-17,  $C = 3.0885$ , TOF = 38.7444 days

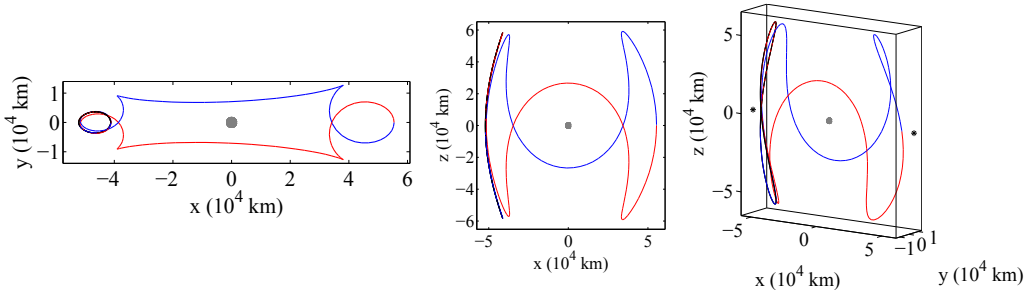


Figure 8.15. V1-18,  $C = 3.0870$ , TOF = 47.0461 days

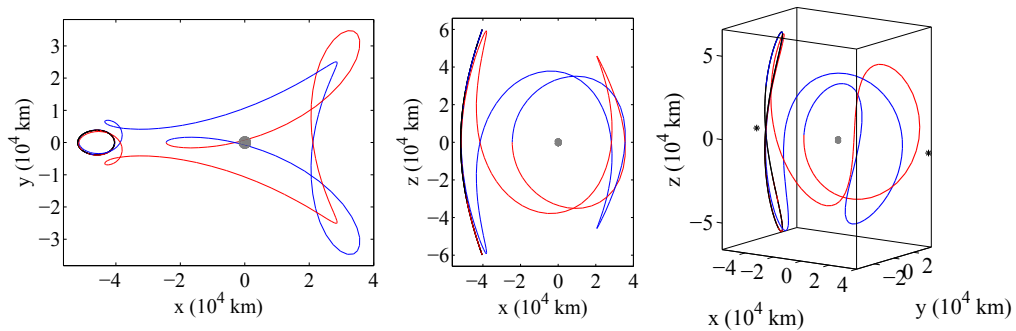


Figure 8.16. V1-19,  $C = 3.0825$ , TOF = 51.4976 days

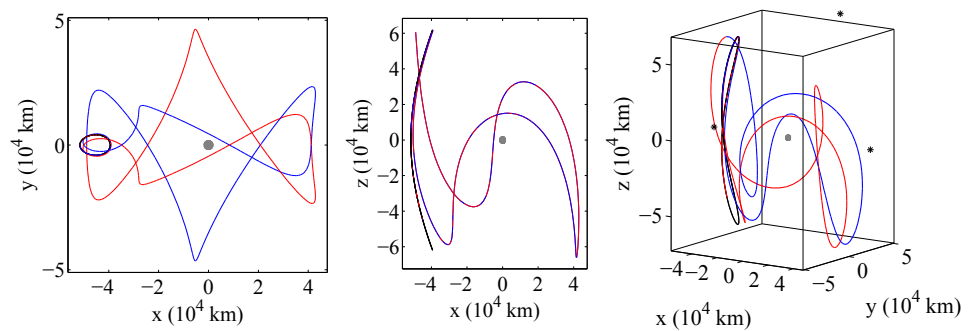


Figure 8.17. V1-20,  $C = 3.0768$ , TOF = 73.6204 days

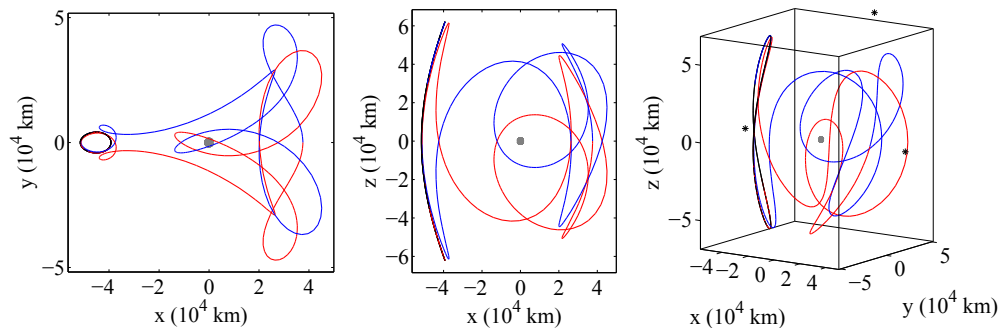


Figure 8.18. V1-21,  $C = 3.0760$ , TOF = 72.0903 days

## $L_2$ Vertical Orbits

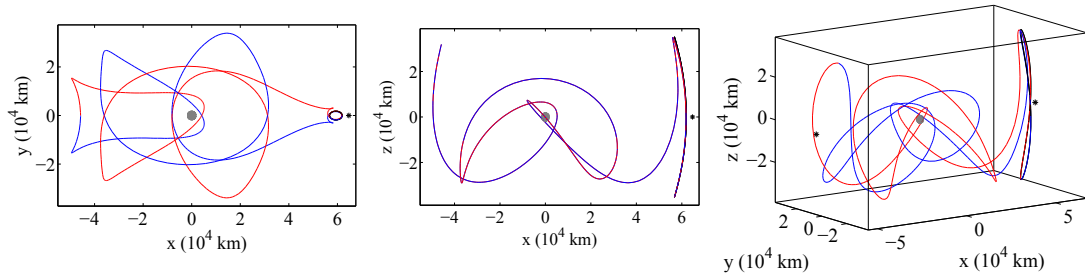


Figure 8.19. V2-4,  $C = 3.1450$ , TOF = 72.2670 days

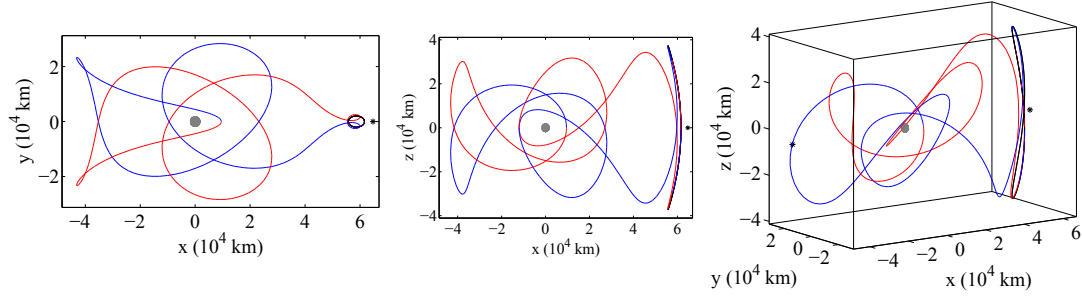


Figure 8.20. V2-7,  $C = 3.1416$ , TOF = 59.5273 days

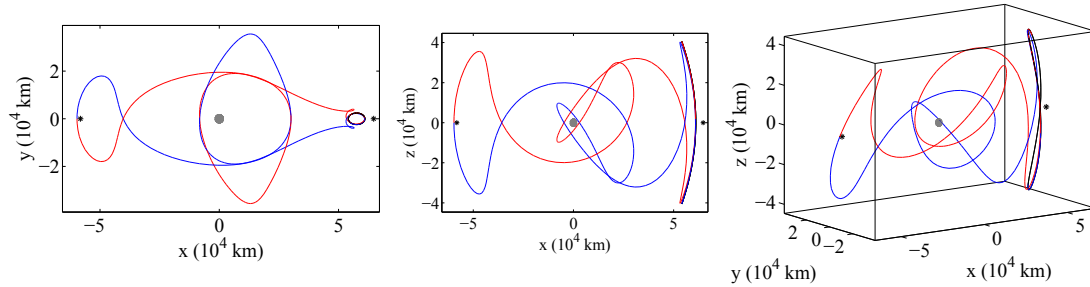


Figure 8.21. V2-6,  $C = 3.1361$ , TOF = 61.8870 days

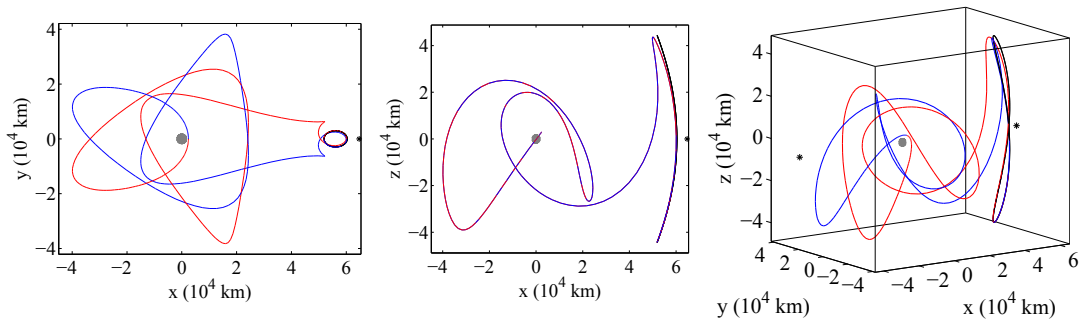


Figure 8.22. V2-5,  $C = 3.1288$ , TOF = 62.5025 days

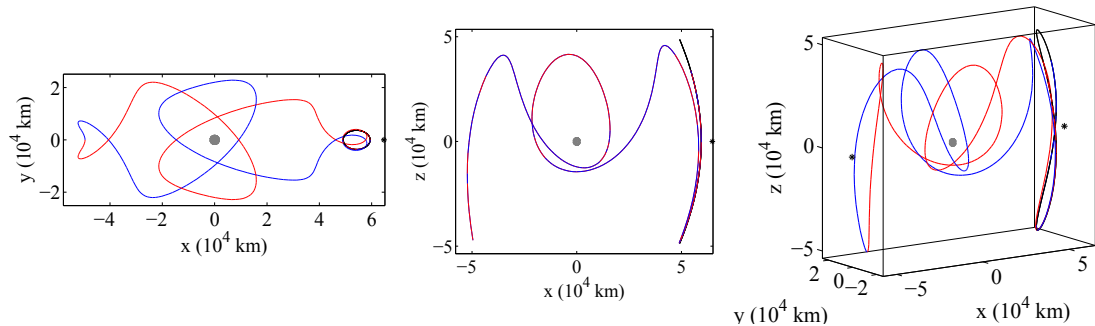


Figure 8.23. V2-8,  $C = 3.1198$ , TOF = 63.4957 days

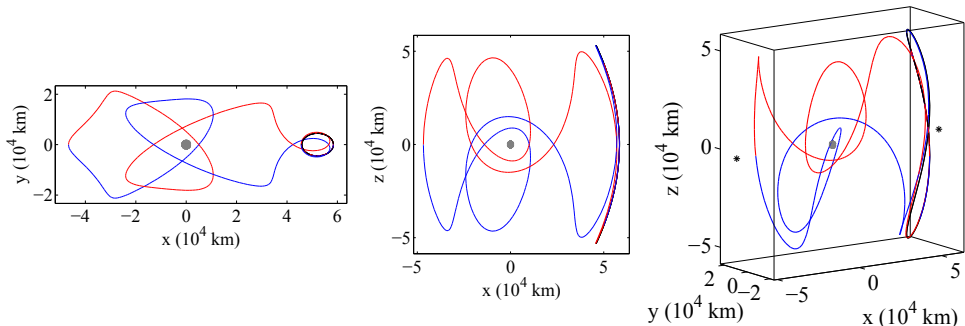


Figure 8.24. V2-11,  $C = 3.1093$ , TOF = 58.1397 days

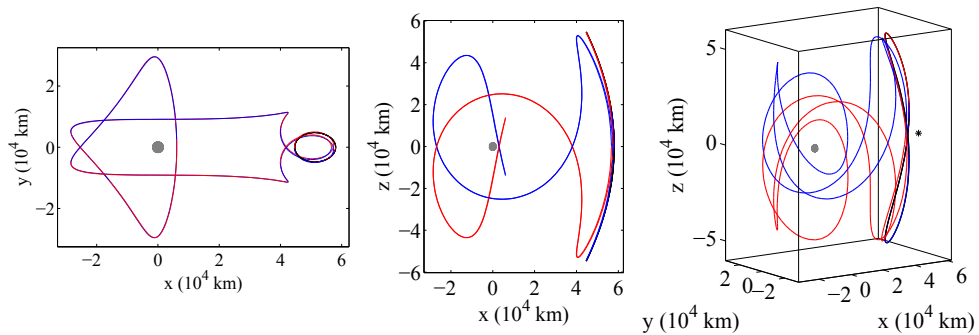


Figure 8.25. V2-12,  $C = 3.1054$ , TOF = 76.3231 days

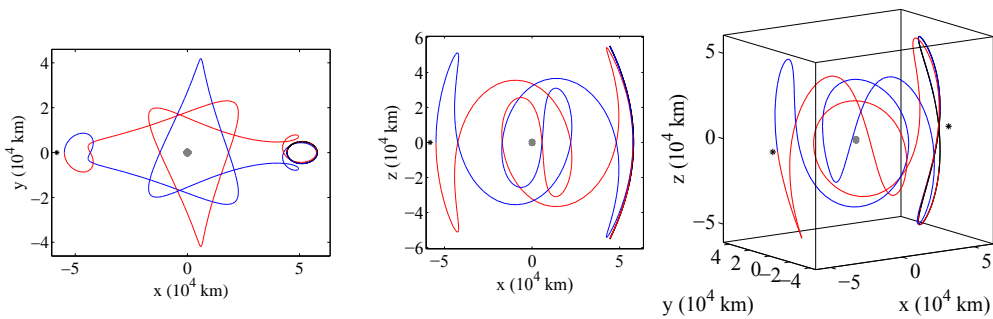


Figure 8.26. V2-15,  $C = 3.1045$ , TOF = 70.6015 days

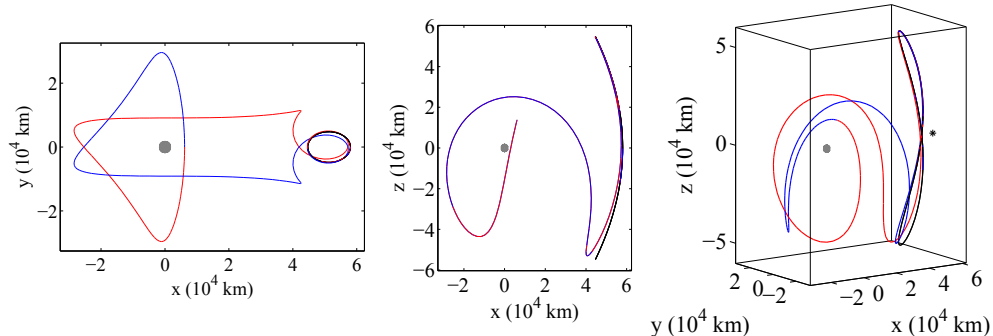


Figure 8.27. V2-13,  $C = 3.1053$ , TOF = 46.9066 days

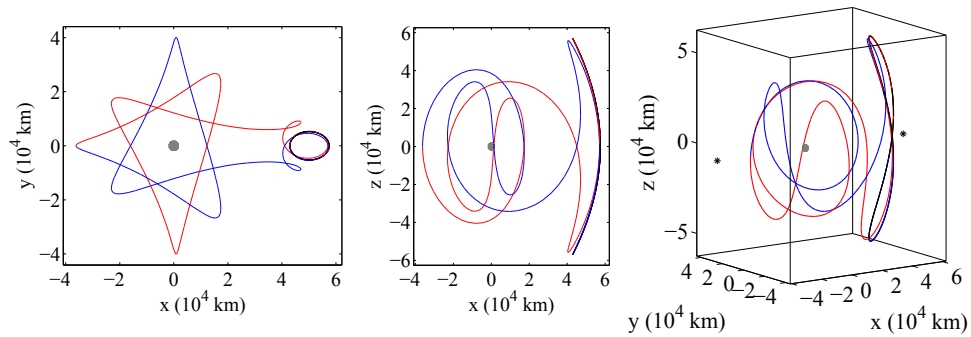


Figure 8.28. V2-14,  $C = 3.0999$ , TOF = 58.4020 days

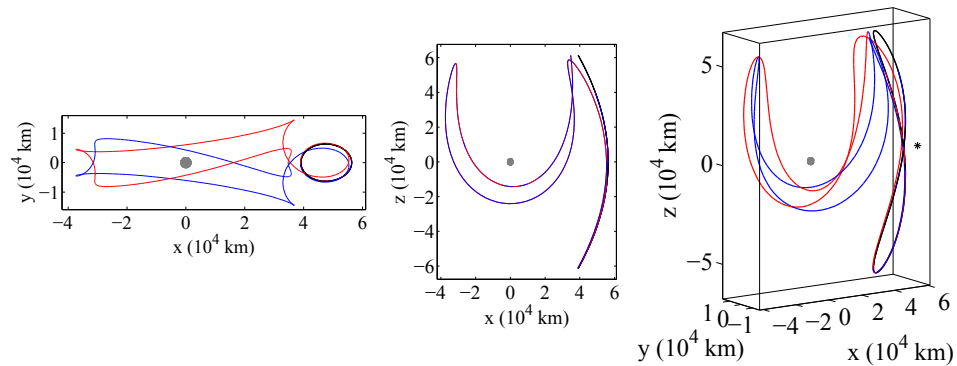


Figure 8.29. V2-16,  $C = 3.0876$ , TOF = 60.1932 days

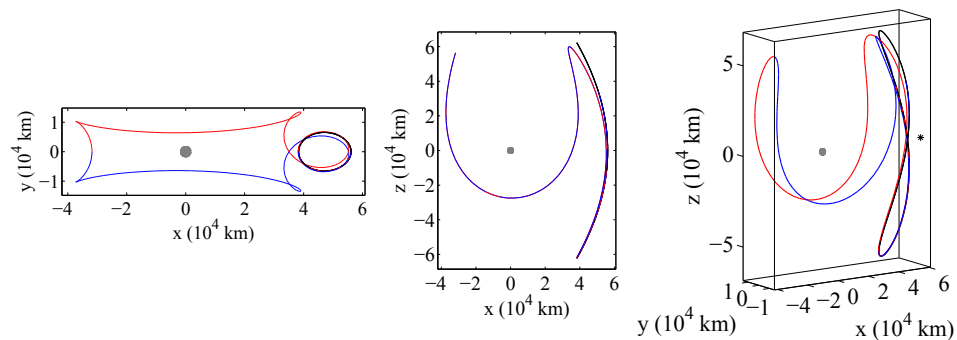


Figure 8.30. V2-17,  $C = 3.0852$ , TOF = 45.2766 days

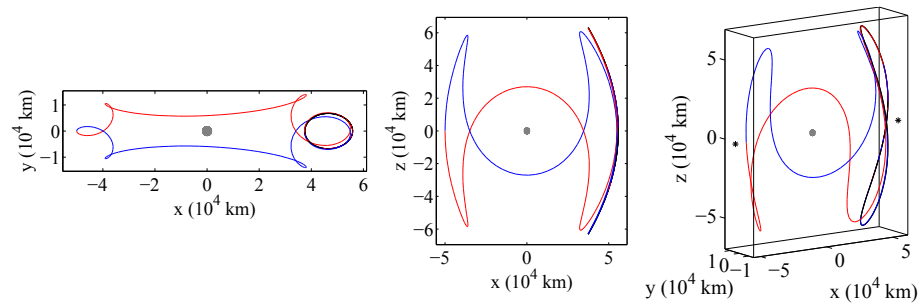


Figure 8.31. V2-18,  $C = 3.0827$ , TOF = 52.7960 days

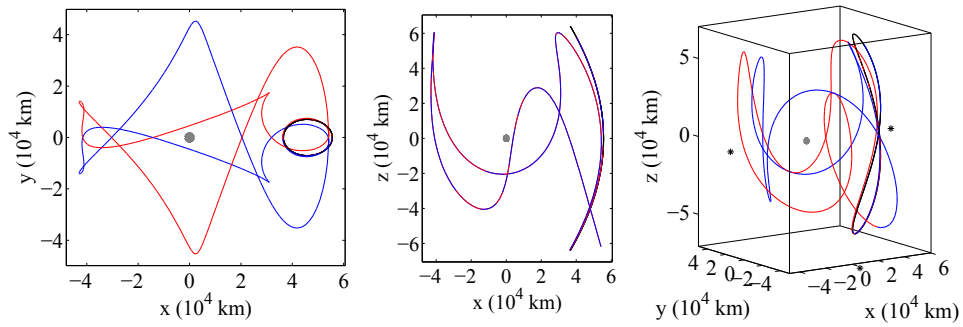


Figure 8.32. V2-20,  $C = 3.0798$  TOF = 79.5223 days

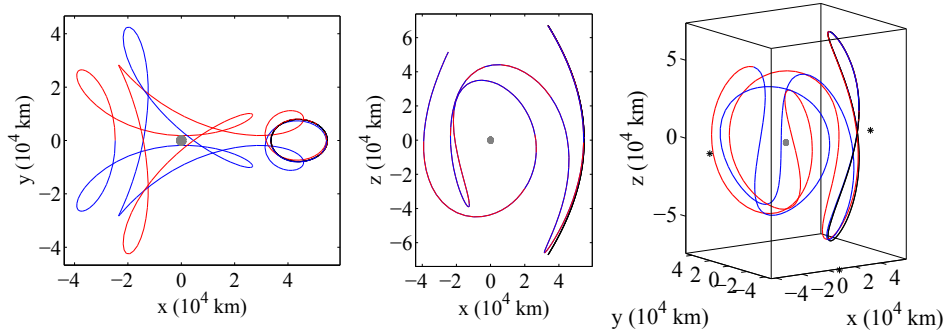


Figure 8.33. V2-22,  $C = 3.0707$ , TOF = 71.3786 days

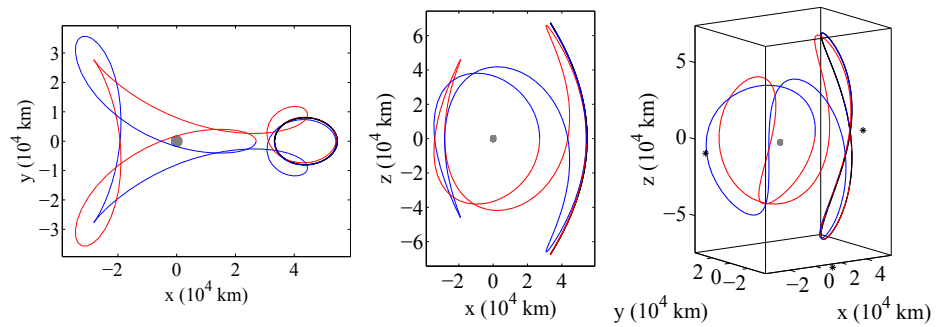


Figure 8.34. V2-19,  $C = 3.0697$ , TOF = 59.1197 days

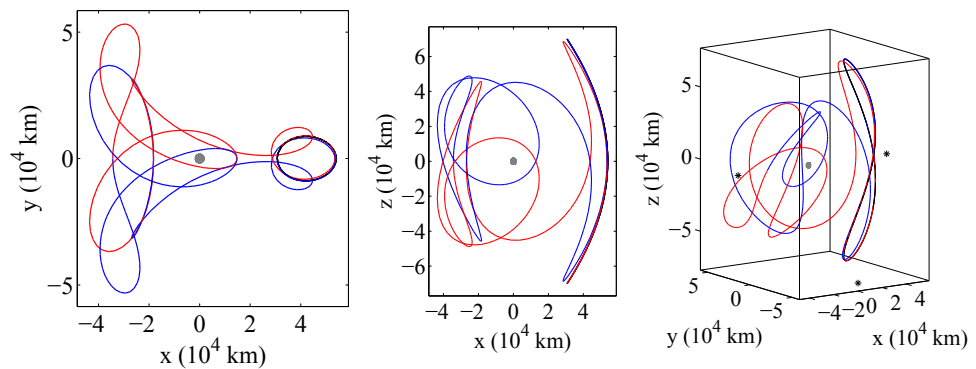


Figure 8.35. V2-21,  $C = 3.0618$ , TOF = 79.4076 days

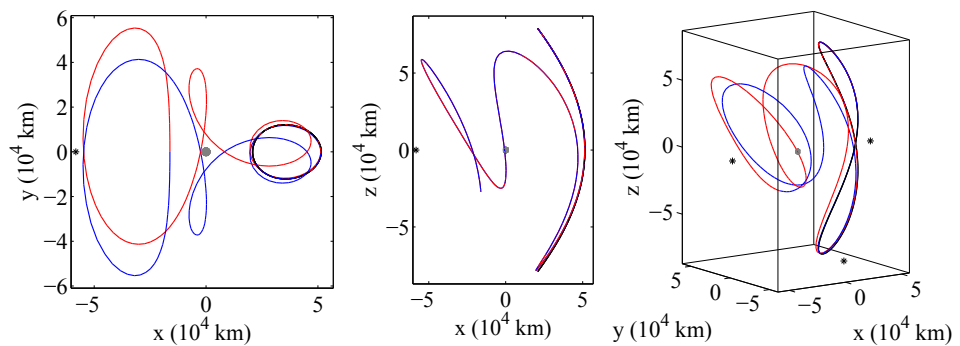


Figure 8.36. V2-23,  $C = 3.0315$ , TOF = 69.6960 days

### 8.3 Homoclinic Connections Associated with Halo Orbits

Table 8.3 Halo Orbit Homoclinic Connections

Label	$C$	TOF (days)	Figure No.	Label	$C$	TOF (days)	Figure No.
H1-1	3.1685	62.9075	8.37	H2-1	-	-	-
H1-2	-	-	-	H2-2	3.1517	45.0669	8.54
H1-3	3.1658	44.5716	8.38	H2-3	-	-	-
H1-4	3.1638	69.2250	8.39	H2-4	-	-	-
H1-5	-	-	-	H2-5	3.1510	57.1765	8.55
H1-6	3.1453	45.3983	8.40	H2-6	-	-	-
H1-7	3.1352	61.7935	8.41	H2-7	-	-	-
H1-8	3.1051	73.5694	8.42	H2-8	3.1013	78.4380	8.56
H1-9	3.0837	60.1211	8.43	H2-9	3.0892	65.4246	8.57
H1-10	3.0766	65.1147	8.44	H2-10	3.0746	72.0334	8.62
H1-11	3.0763	52.9703	8.45	H2-11	3.0820	58.3090	8.58
H1-12	3.0726	59.7869	8.46	H2-12	3.0775	64.9840	8.60
H1-13	3.0725	64.6227	8.47	H2-13	3.0618	78.4496	8.65
H1-14	3.0723	65.9529	8.48	H2-14	3.0687	75.1186	8.63
H1-15	3.0701	72.4875	8.49	H2-15	3.0790	74.7334	8.59
H1-16	3.0600	71.7162	8.50	H2-16	3.0764	73.6022	8.61
H1-17	3.0584	70.6021	8.51	H2-17	3.0663	75.1945	8.64
H1-18	3.0498	62.5695	8.52	H2-18	3.0616	66.4187	8.66
H1-19	3.0366	63.1381	8.53	H2-19	3.0485	65.5675	8.67

## $L_1$ Halo Orbits

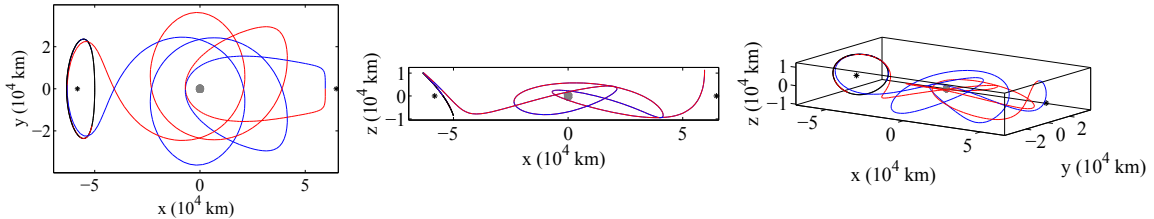


Figure 8.37. H1-1,  $C = 3.1685$ , TOF = 62.9075 days

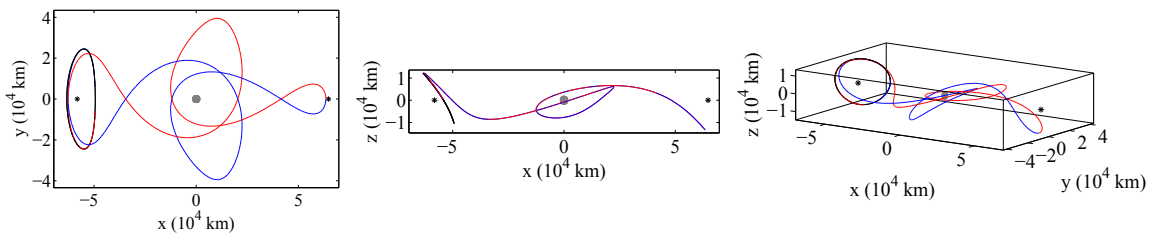


Figure 8.38. H1-3,  $C = 3.1658$ , TOF = 44.5716 days

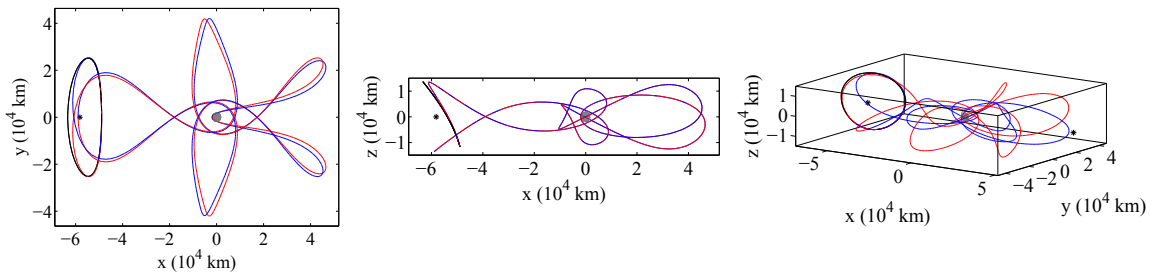


Figure 8.39. H1-4,  $C = 3.1638$ , TOF = 69.2250 days

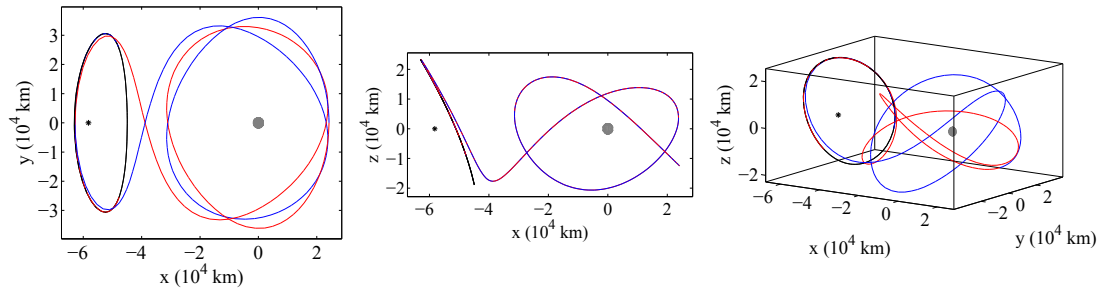


Figure 8.40. H1-6,  $C = 3.1453$ , TOF = 45.3983 days

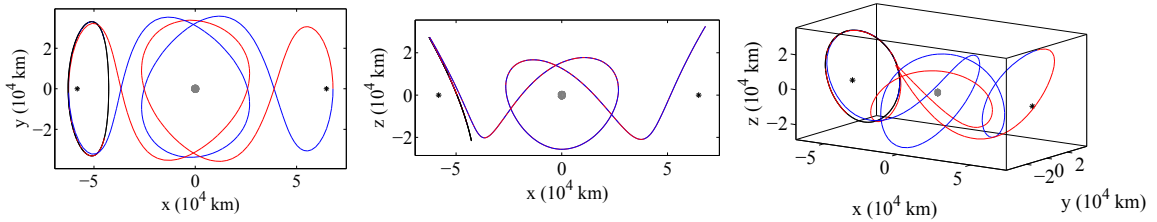


Figure 8.41. H1-7,  $C = 3.1352$ , TOF = 61.7935 days

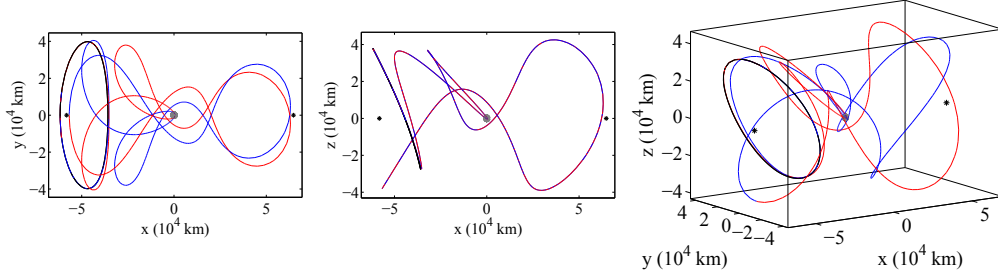


Figure 8.42. H1-8,  $C = 3.1051$  TOF = 73.5694 days; Note that this connection impacts the Moon

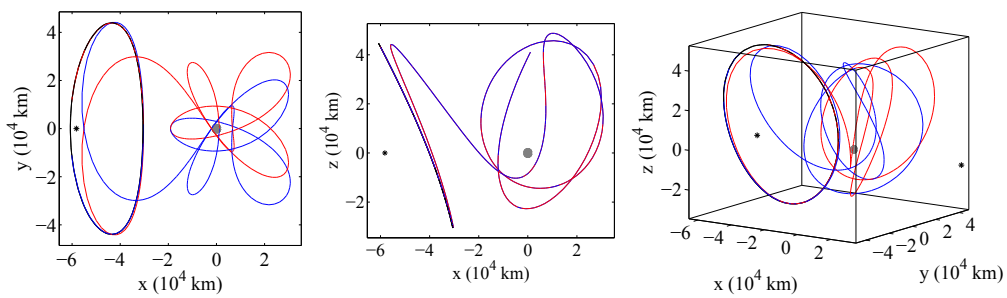


Figure 8.43. H1-9,  $C = 3.0837$ , TOF = 60.1211 days

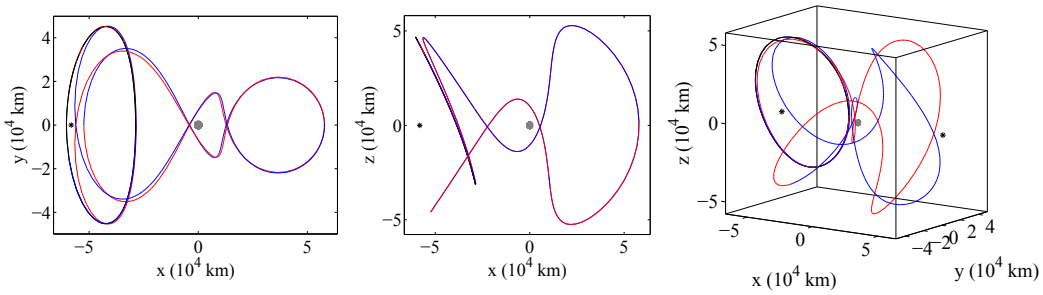


Figure 8.44. H1-10,  $C = 3.0766$ , TOF = 65.1147 days

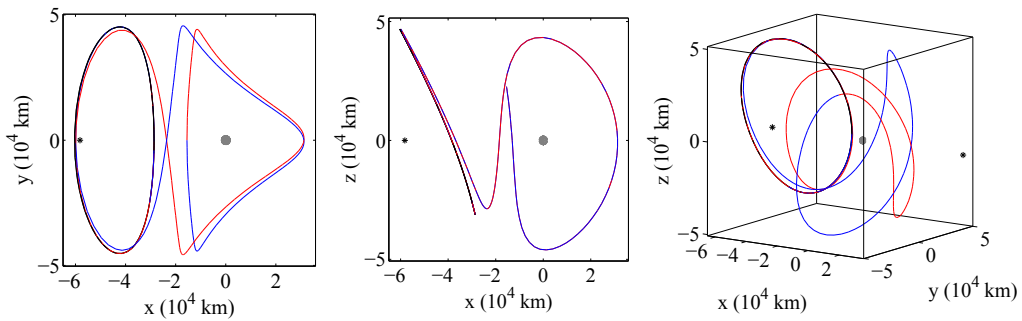


Figure 8.45. H1-11,  $C = 3.0763$ , TOF = 52.9703 days

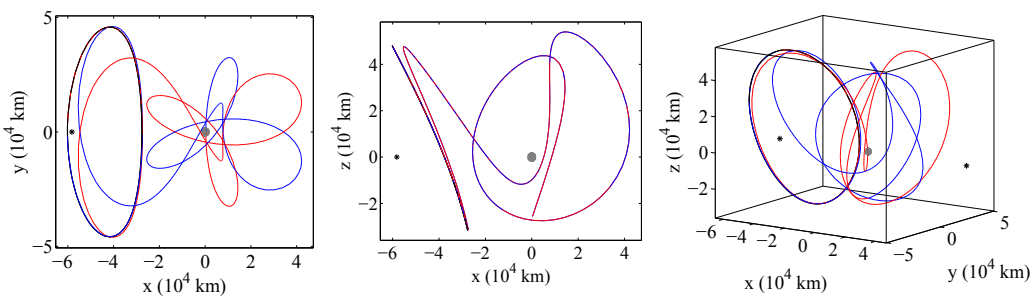


Figure 8.46. H1-12,  $C = 3.0726$ , TOF = 59.7869 days

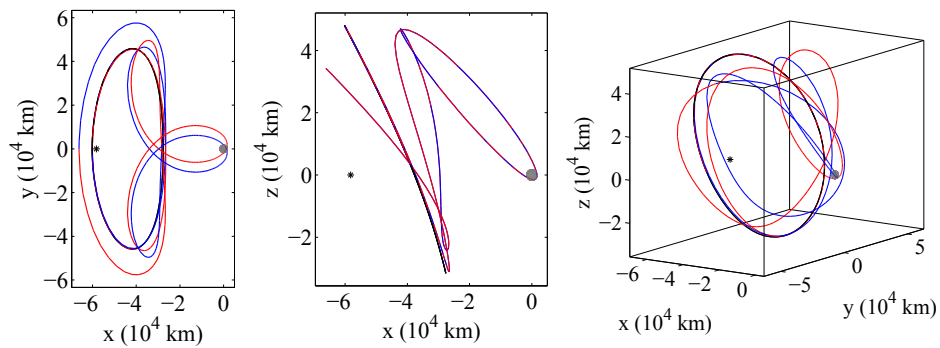


Figure 8.47. H1-13,  $C = 3.0725$ , TOF = 64.6227 days

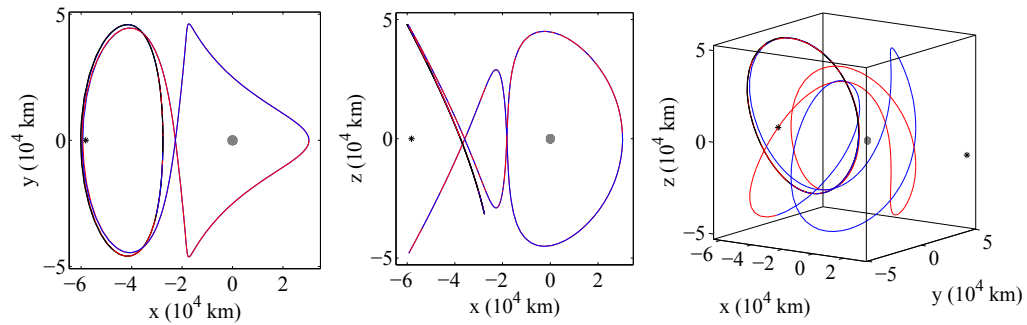


Figure 8.48. H1-14,  $C = 3.0723$ , TOF = 65.9529 days

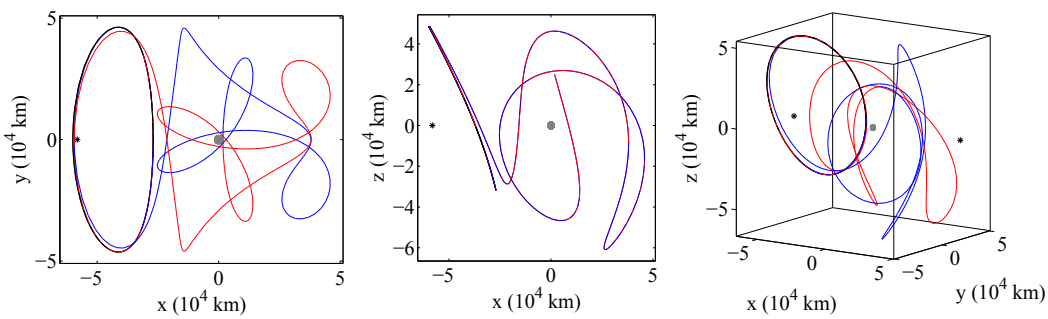


Figure 8.49. H1-15,  $C = 3.0701$ , TOF = 72.4875 days

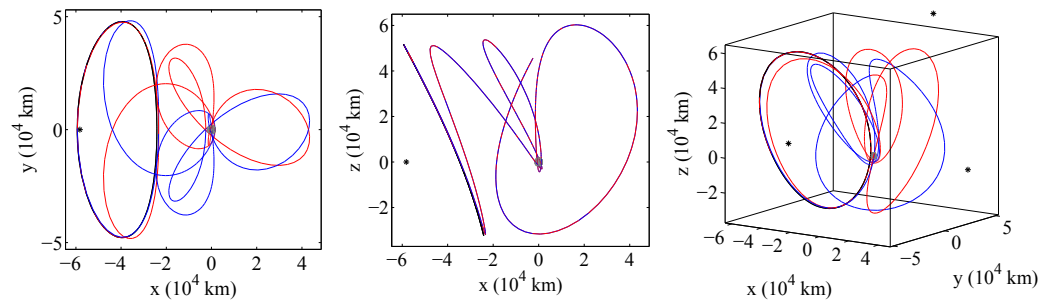


Figure 8.50. H1-16,  $C = 3.0600$ , TOF = 71.7162 days

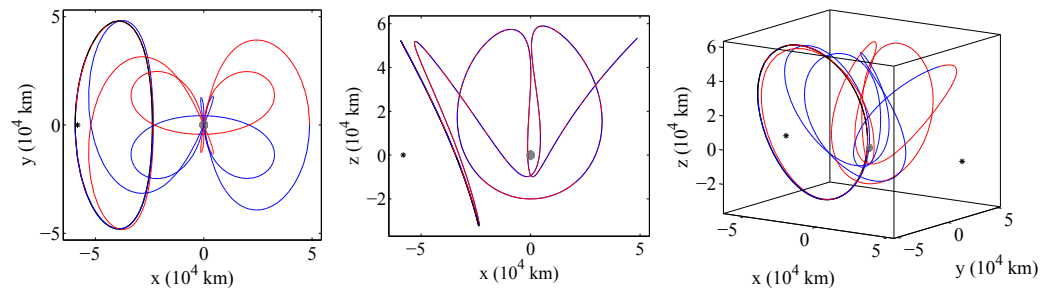


Figure 8.51. H1-17,  $C = 3.0584$ , TOF = 70.6021 days

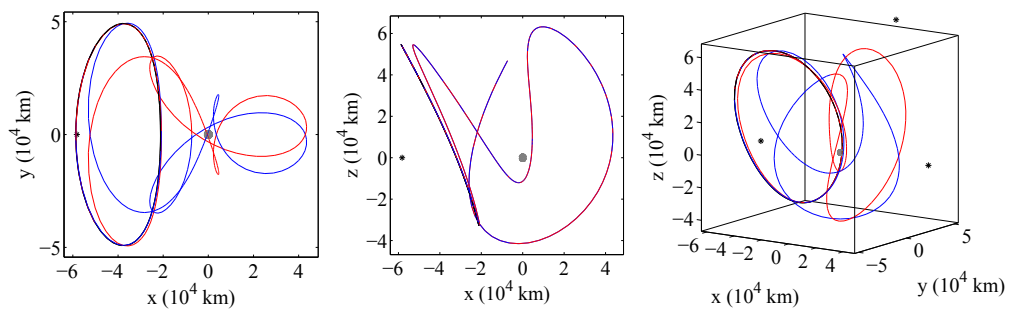


Figure 8.52. H1-18,  $C = 3.0498$ , TOF = 62.5695 days

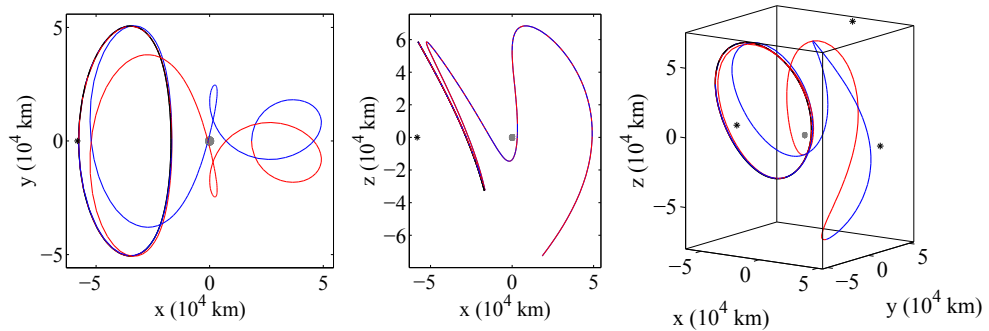


Figure 8.53. H1-19,  $C = 3.0366$ , TOF = 63.1381 days

## $L_2$ Halo Orbits

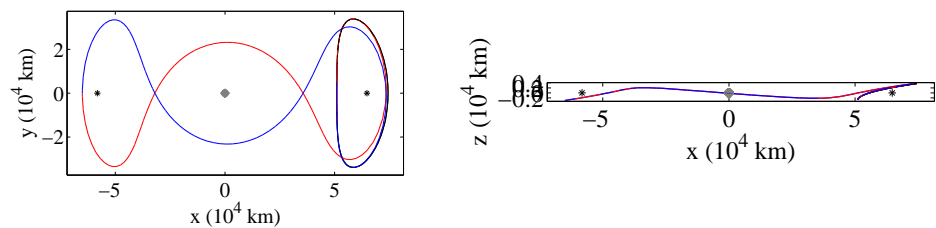


Figure 8.54. H2-2,  $C = 3.1517$ , TOF = 45.0669 days

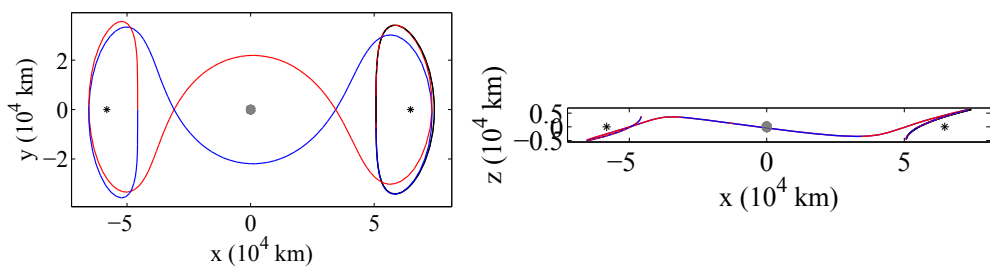


Figure 8.55. H2-5,  $C = 3.1510$ , TOF = 57.1765 days

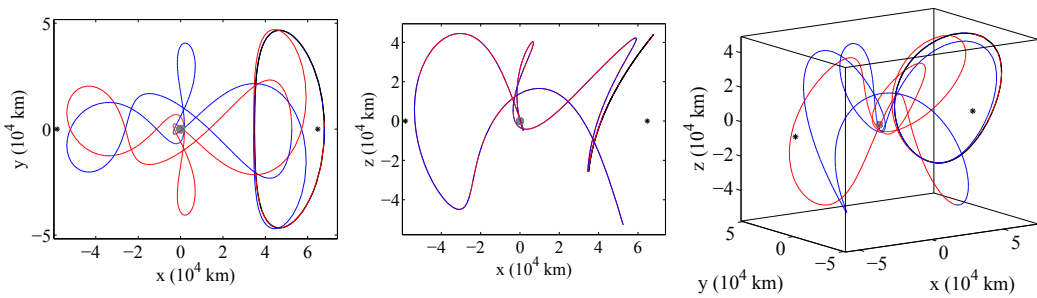


Figure 8.56. H2-8,  $C = 3.1013$ , TOF = 78.4380 days

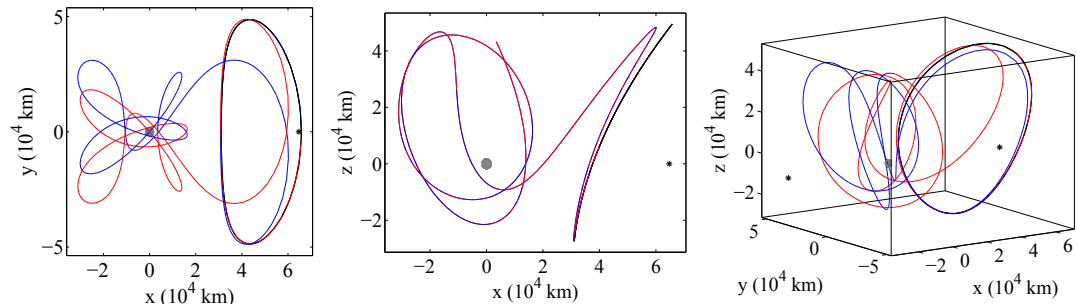


Figure 8.57. H2-9,  $C = 3.0892$ , TOF = 65.4246 days

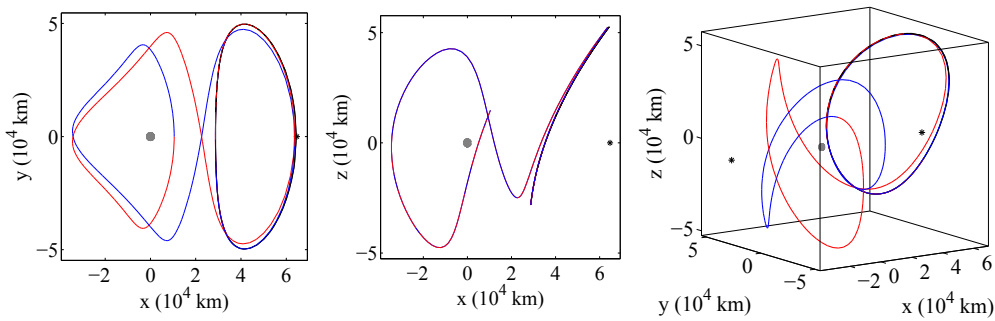


Figure 8.58. H2-11,  $C = 3.0820$ , TOF = 58.3090 days

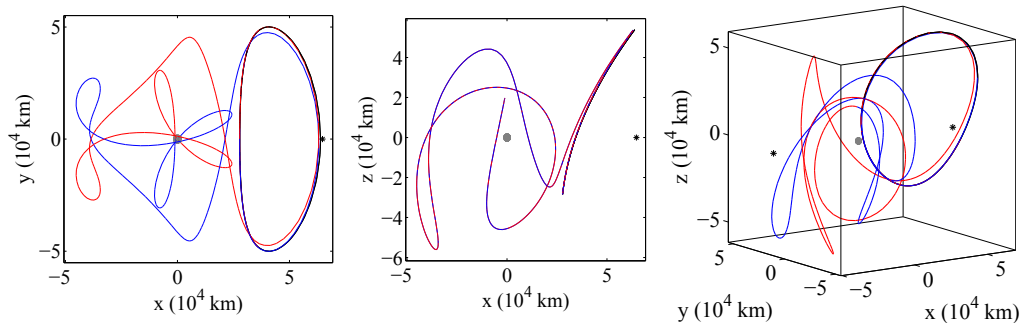


Figure 8.59. H2-15,  $C = 3.0790$ , TOF = 74.7334 days

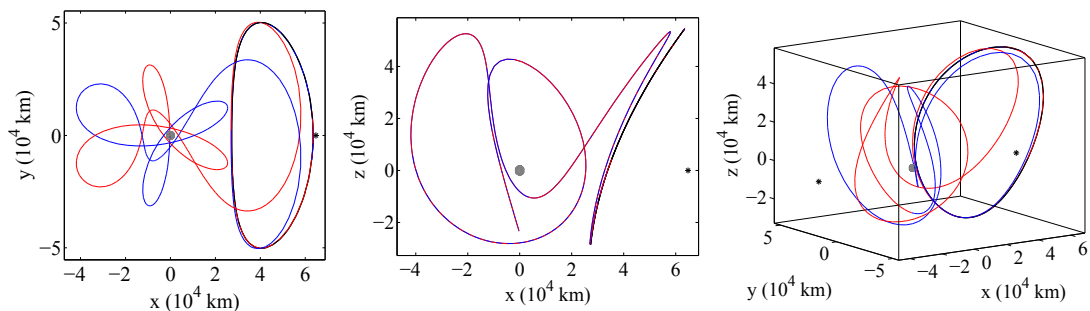
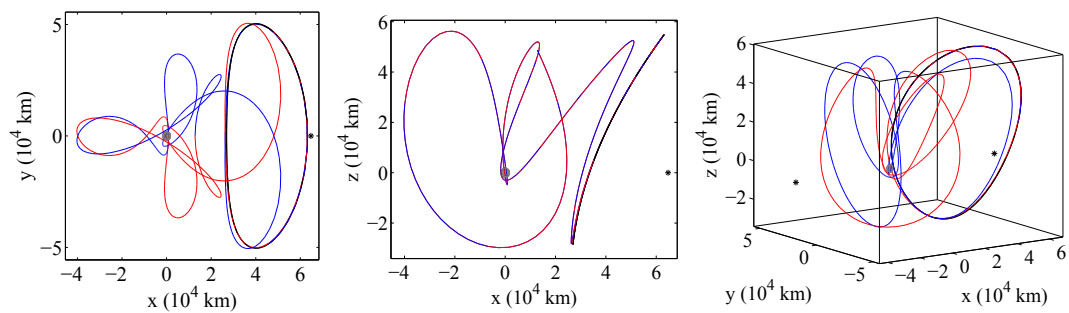
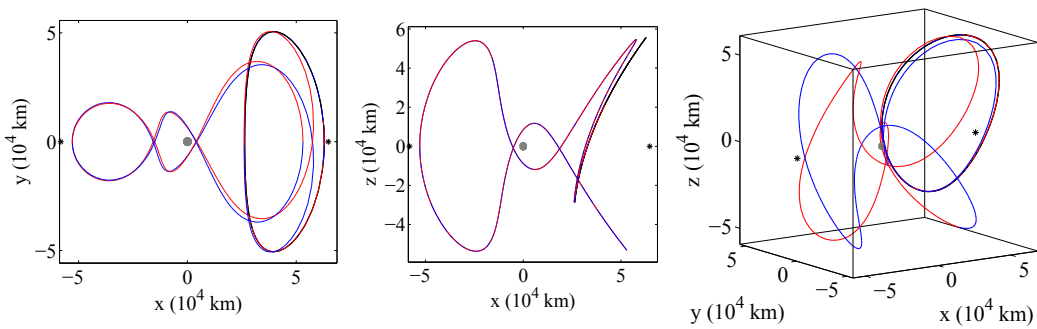
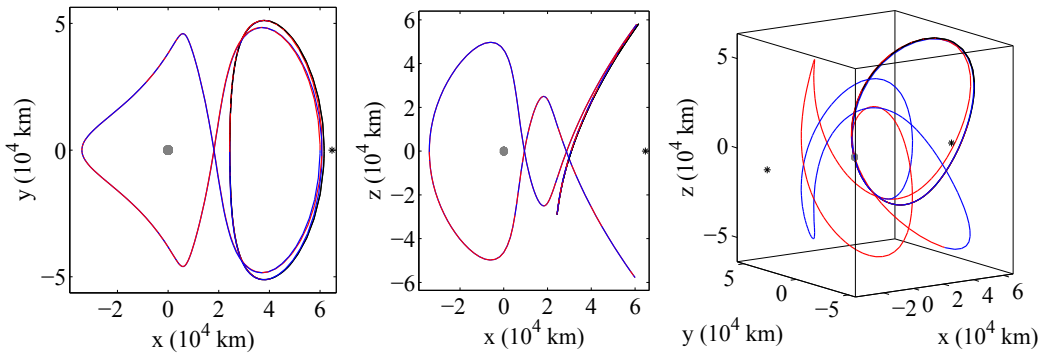


Figure 8.60. H2-12,  $C = 3.0775$ , TOF = 64.9840 days

Figure 8.61. H2-16,  $C = 3.0764$ , TOF = 73.6022 daysFigure 8.62. H2-10,  $C = 3.0746$ , TOF = 72.0334 daysFigure 8.63. H2-14,  $C = 3.0687$ , TOF = 75.1186 days

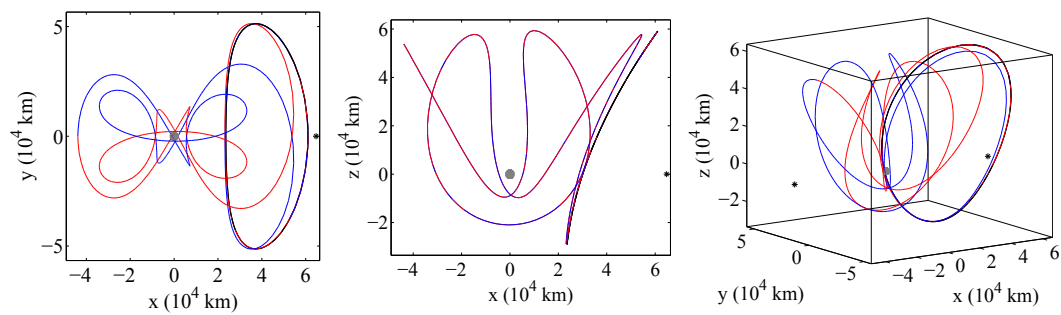


Figure 8.64. H2-17,  $C = 3.0663$ , TOF = 75.1945 days

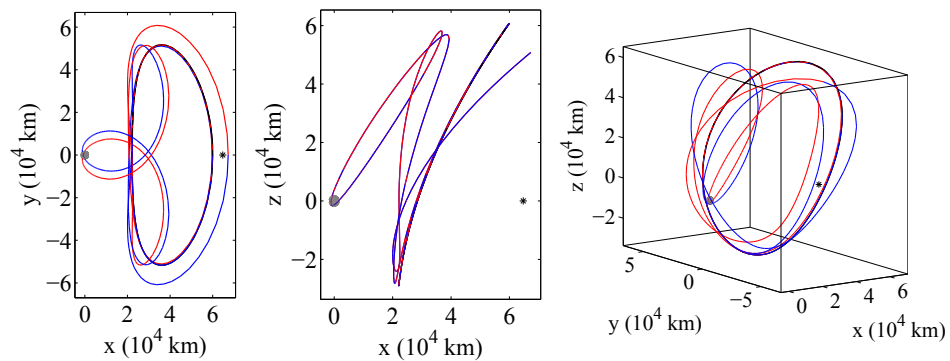


Figure 8.65. H2-13,  $C = 3.0618$ , TOF = 78.4496 days

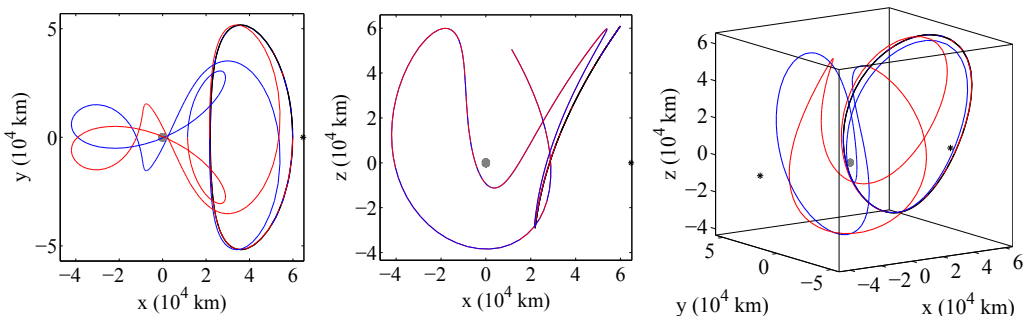


Figure 8.66. H2-18,  $C = 3.0616$ , TOF = 66.4187 days

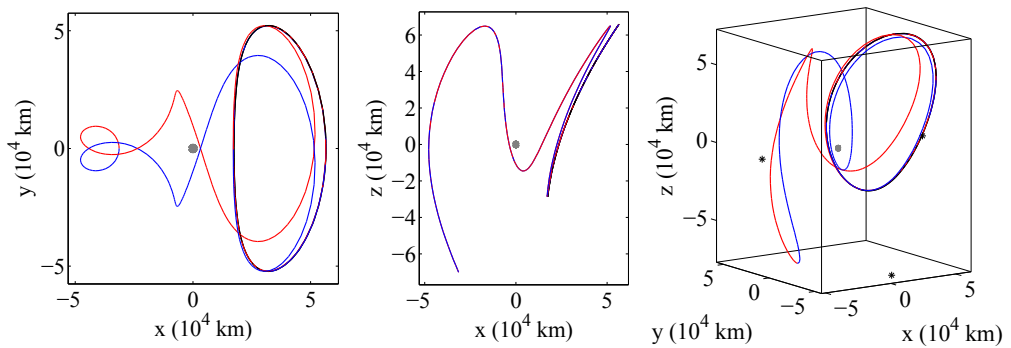


Figure 8.67. H2-19,  $C = 3.0485$ , TOF = 65.5675 days

## 8.4 Homoclinic Connections Associated with Axial Orbits

Table 8.4 Axial Orbit Homoclinic Connections

Label	$C$	TOF (days)	Figure No.	Label	$C$	TOF (days)	Figure No.
A1-1	3.0048	71.2748	8.68	A2-1	2.9862	83.8149	8.70
A1-2	3.0028	68.6406	8.69	A2-1	2.9818	79.6937	8.71

### $L_1$ Axial Orbits

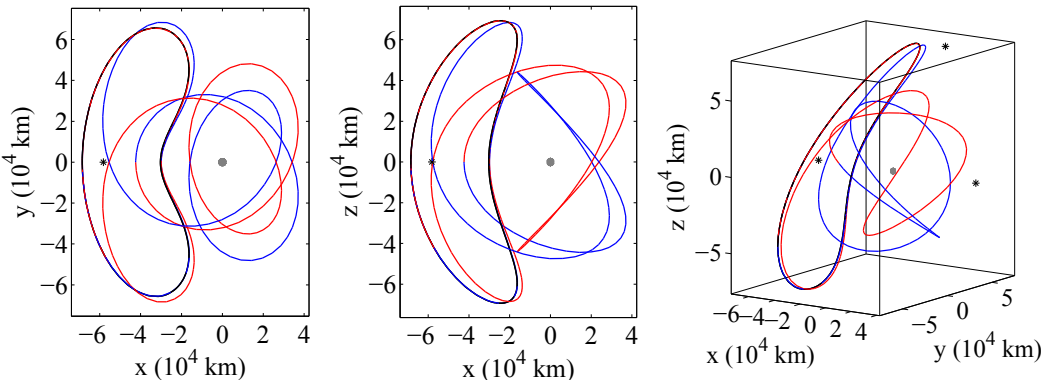


Figure 8.68. A1-1,  $C = 3.0048$ , TOF = 71.2748 days

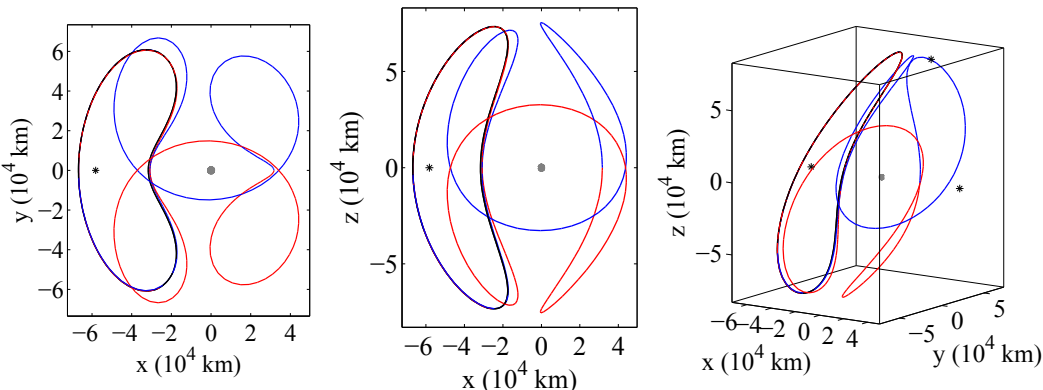


Figure 8.69. A1-2,  $C = 3.0028$  TOF = 68.6406 days

## $L_2$ Axial Orbits

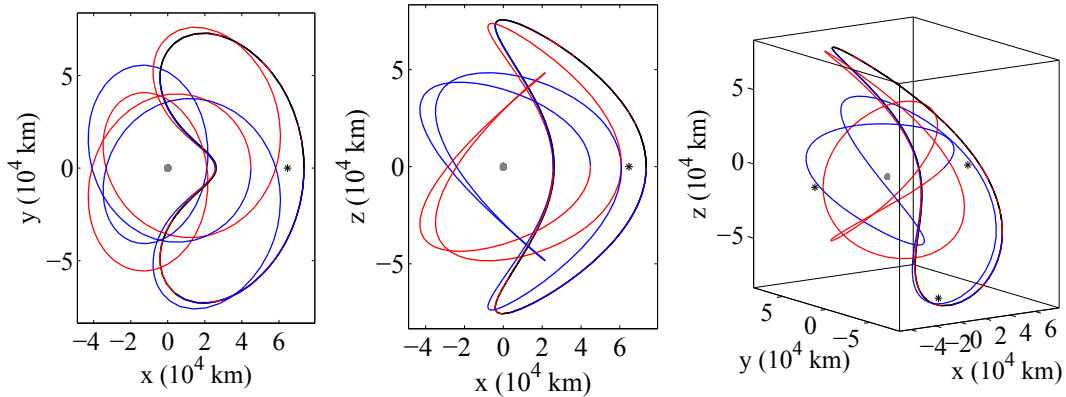


Figure 8.70. A2-1,  $C = 2.9862$  TOF = 83.8149 days

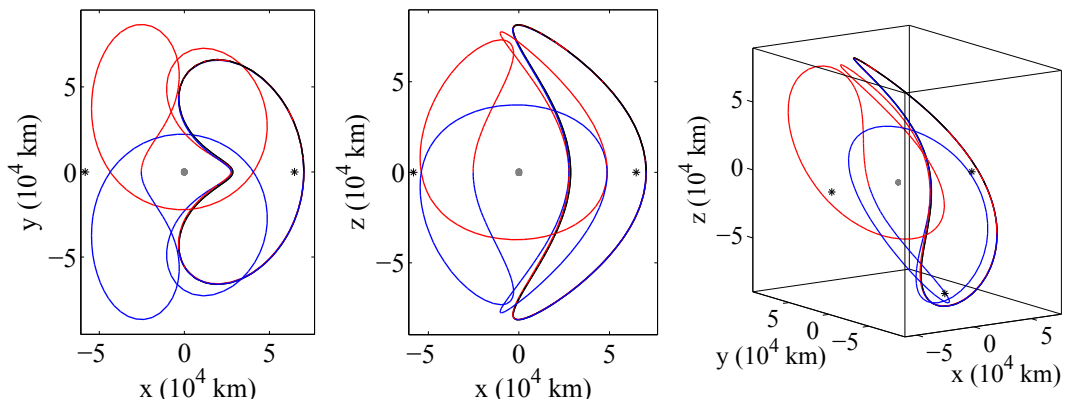


Figure 8.71. A2-2,  $C = 2.9818$  TOF = 79.6937 days

## 8.5 Heteroclinic Connections between Northern and Southern Halo/Axial Orbits

Table 8.5 Heteroclinic Connections between Northern and Southern Orbits

Label	$C$	TOF (days)	Figure No.	Label	$C$	TOF (days)	Figure No.
HH1-1	3.1694	74.7445	8.72	HH2-1	-	-	-
HH1-2	3.1635	42.3206	8.73	HH2-2	-	-	-
HH1-3	3.1625	51.6166	8.74	HH2-3	-	-	-
HH1-4	3.1589	54.2482	8.75	HH2-4	-	-	-
HH1-5	3.1580	57.1155	8.76	HH2-5	-	-	-
HH1-6	3.1422	41.5511	8.77	HH2-6	-	-	-
HH1-7	-	-	-	HH2-7	3.1395	65.6368	8.83
HH1-8	3.1189	41.1956	8.78	HH2-8	3.1267	46.5733	8.84
HH1-9	3.0779	65.9390	8.79	HH2-9	3.0850	70.6057	8.85
HH1-10	3.0768	43.9812	8.80	HH2-10	3.0742	50.6271	8.86
HH1-11	3.0723	40.1881	8.81	HH2-11	3.0686	47.7498	8.87
HH1-12	3.0497	61.8061	8.82	HH2-12	3.0551	66.4160	8.88
AA1-1	3.0037	56.2121	8.89	AA2-1	2.984	66.8773	8.90

### $L_1$ Halo Orbits

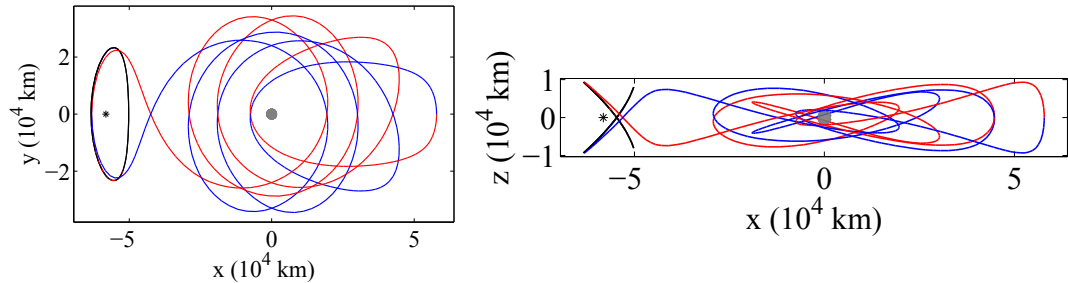


Figure 8.72. HH1-1,  $C = 3.1694$ , TOF = 74.7445 days

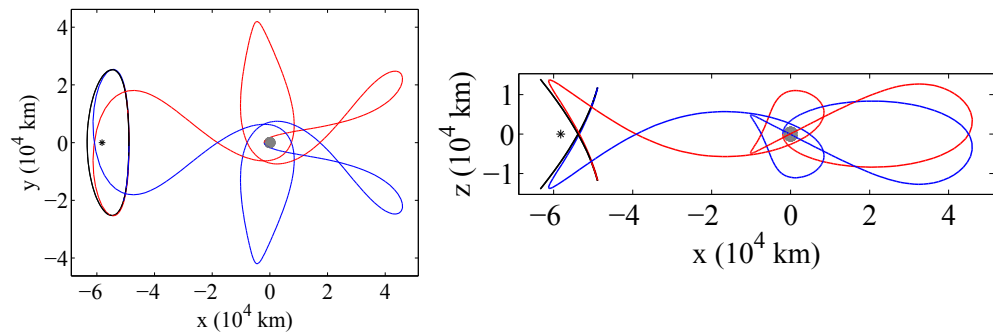


Figure 8.73. HH1-2,  $C = 3.1635$ , TOF = 42.3206 days

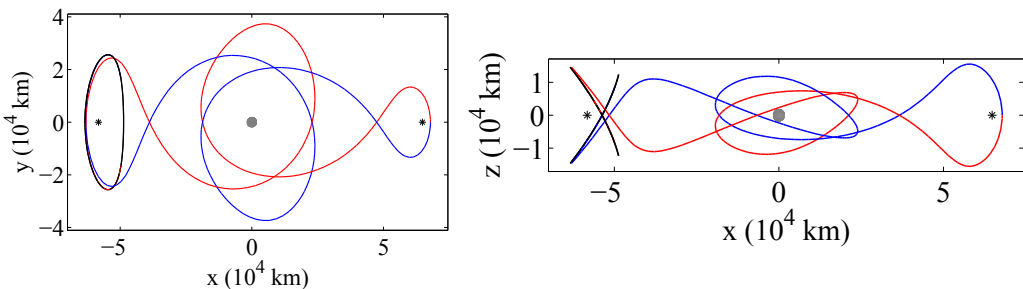
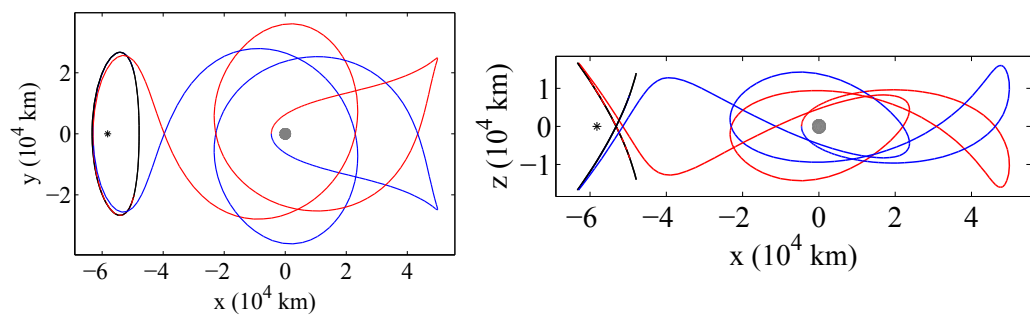
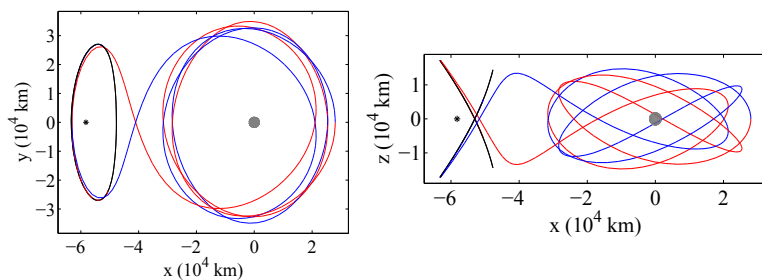
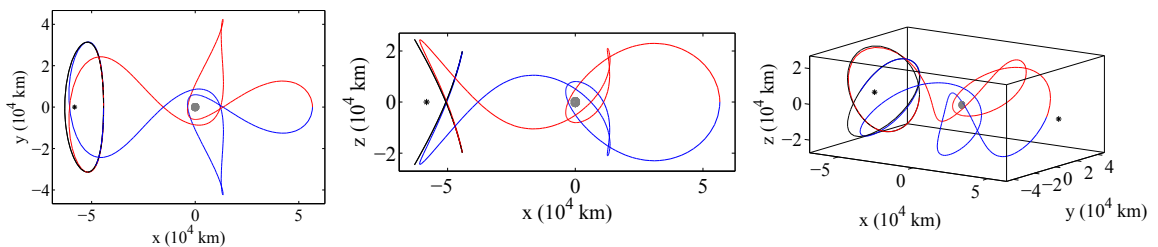


Figure 8.74. HH1-3,  $C = 3.1625$ , TOF = 51.6166 days

Figure 8.75. HH1-4,  $C = 3.1589$ , TOF = 54.2482 daysFigure 8.76. HH1-5,  $C = 3.1580$ , TOF = 57.1155 daysFigure 8.77. HH1-6,  $C = 3.1422$ , TOF = 41.5511 days

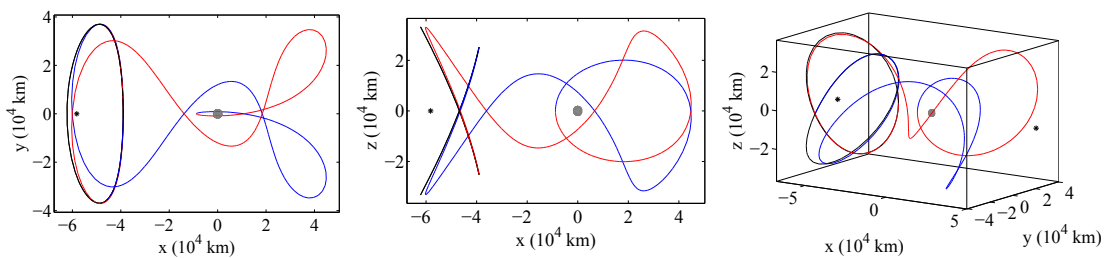


Figure 8.78. HH1-8,  $C = 3.1189$ , TOF = 41.1956 days

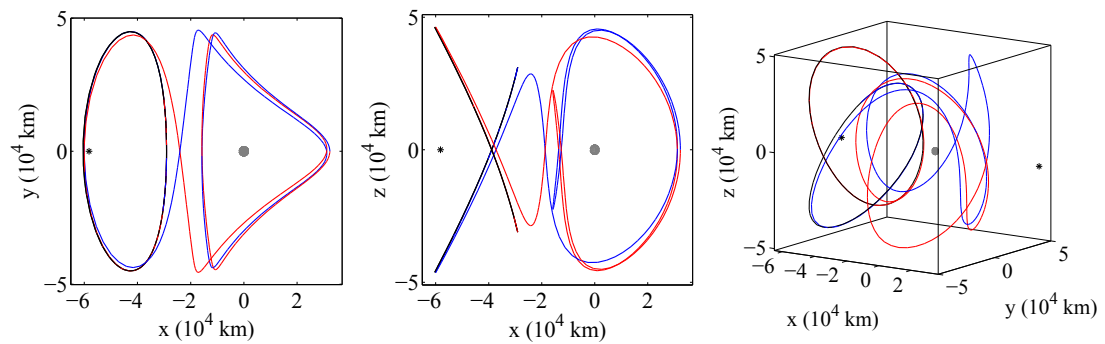


Figure 8.79. HH1-9,  $C = 3.0779$ , TOF = 65.9390 days

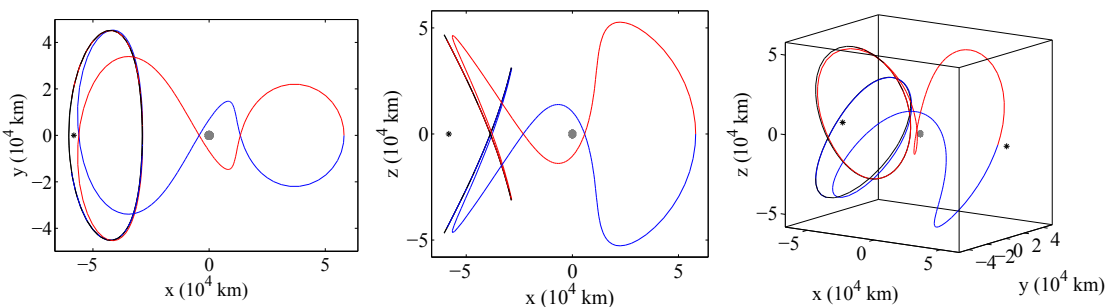


Figure 8.80. HH1-10,  $C = 3.0768$ , TOF = 43.9812 days

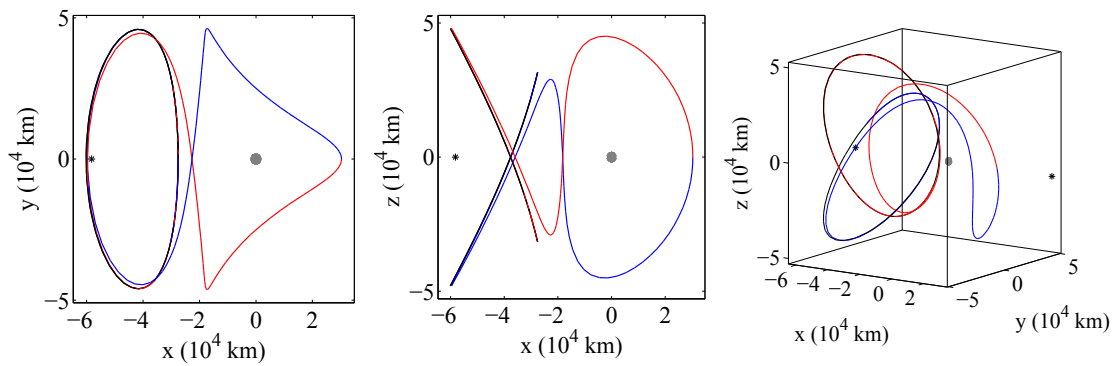


Figure 8.81. HH1-11,  $C = 3.0723$ , TOF = 40.1881 days

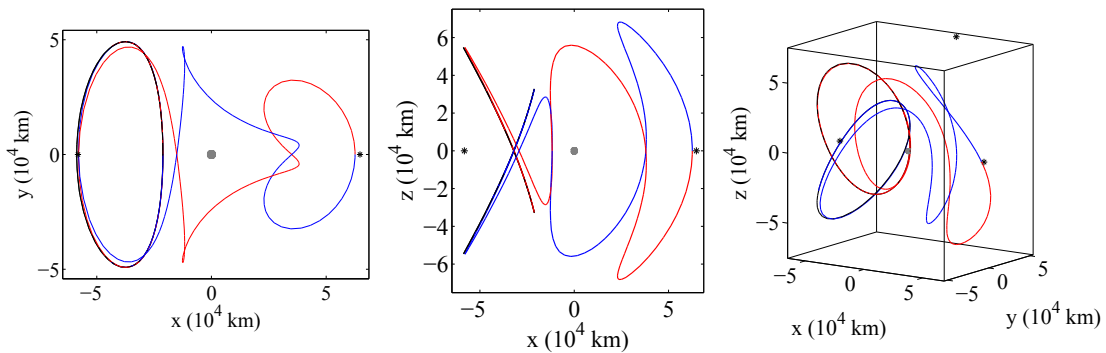


Figure 8.82. HH1-12,  $C = 3.0497$ , TOF = 61.8061 days

## $L_2$ Halo Orbits

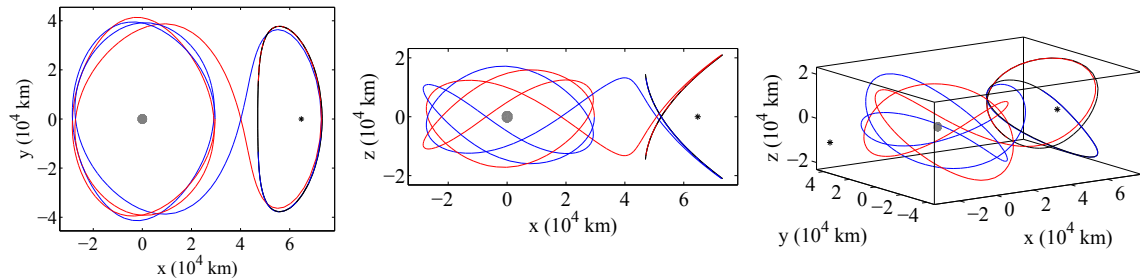


Figure 8.83. HH2-7,  $C = 3.1395$ , TOF = 65.6368 days

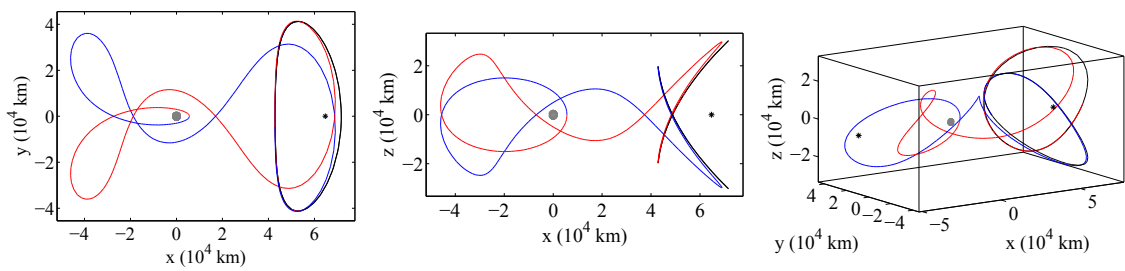


Figure 8.84. HH2-8,  $C = 3.1267$ , TOF = 46.5733 days

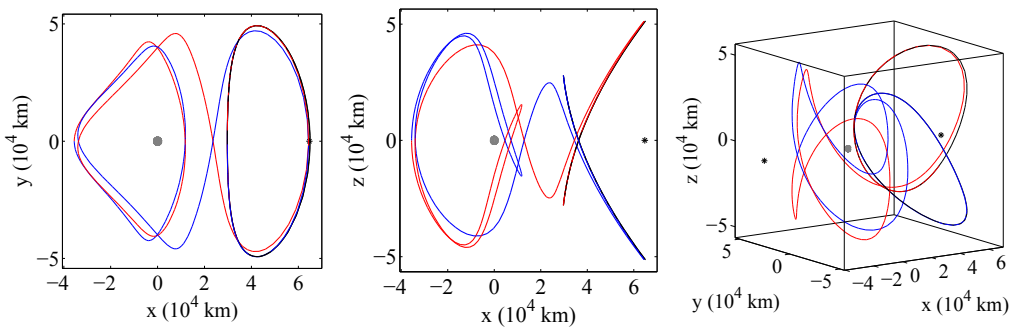


Figure 8.85. HH2-9,  $C = 3.0850$ , TOF = 70.6057 days

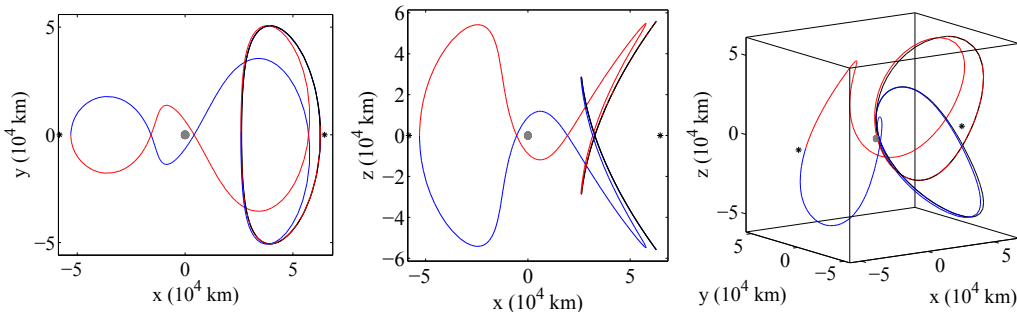


Figure 8.86. HH2-10,  $C = 3.0742$ , TOF = 50.6271 days

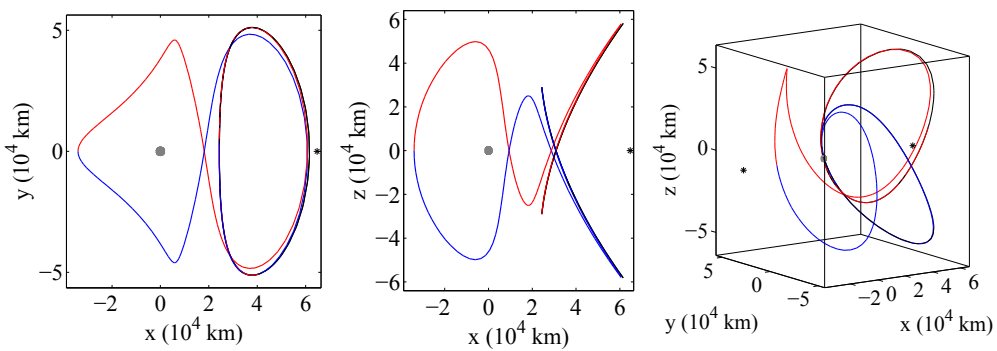


Figure 8.87. HH2-11,  $C = 3.0686$ , TOF = 47.7498 days

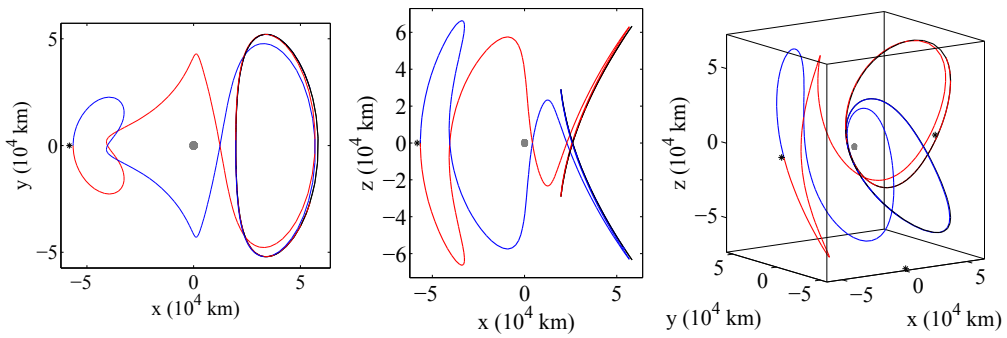


Figure 8.88. HH2-12,  $C = 3.0551$ , TOF = 66.4160 days

## Axial Orbits

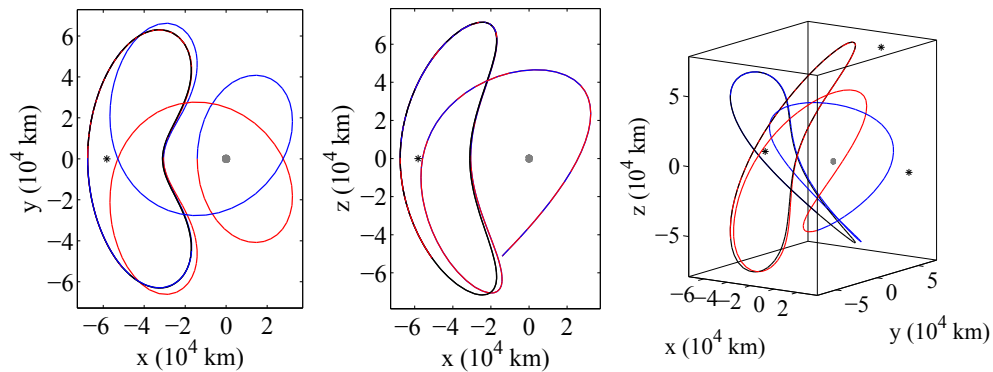


Figure 8.89. AA1-1,  $C = 3.0037$ , TOF = 56.2121 days

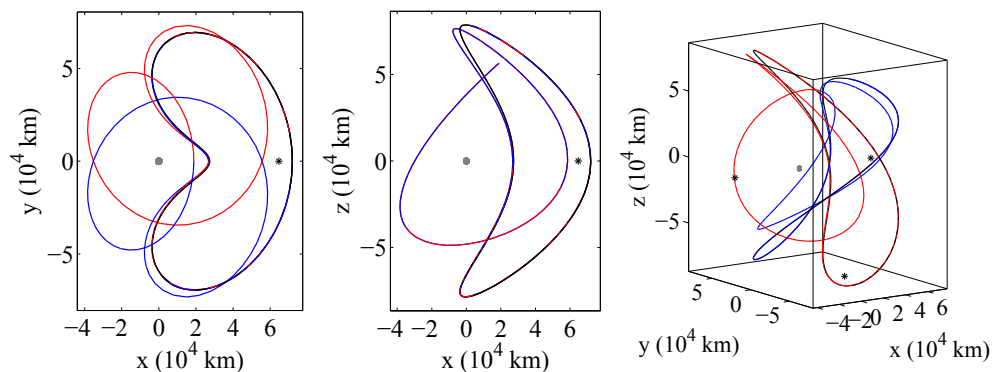


Figure 8.90. AA2-1,  $C = 2.984$ , TOF = 66.8773 days

## 8.6 Low-Cost Transfers

Table 8.6 Low-Cost Transfers

Label	$C_1$	$C_2$	TOF (days)	$\Delta v$ (m/s)	Figure No.
V1V2-1	3.1616	3.1536	40.1034	4.7099	8.91
V1V2-2	3.1564	3.1504	39.5552	16.0344	8.92
V1V2-3	3.1265	3.1147	35.9293	7.9431	8.93
V1V2-4	3.1139	3.1073	54.9474	5.733	8.94
V1V2-5	3.0986	3.0951	41.2976	9.854	8.95
V1V2-6	3.0949	3.1039	53.0685	19.5612	8.96
V1V2-7	3.0898	3.0875	49.5468	4.653	8.97
V1V2-8	3.0849	3.0884	33.1433	5.254	8.98
H1H2-1	3.1681	3.1468	43.003	7.9742	8.99
H1H2-2	3.1469	3.1317	28.9769	18.2642	8.100
H1H2-3	3.1269	3.1158	51.0004	13.915	8.101
H1H2-4	3.0930	3.0972	59.7738	3.5776	8.102
H1H2-5	3.0698	3.0717	62.1769	5.1442	8.103
H1H2-6	3.0537	3.0795	51.1918	11.8545	8.104
A1A2-1	3.0058	2.9835	52.0105	25.7533	8.105
V1H2-1	-	-	-	-	-
H1V2-1	3.1636	3.1666	40.529	4.5 - not optimal	8.109
V1H2-2	3.1604	3.1223	37.5423	17.8769	8.106
H1V2-2	3.1327	3.1517	36.7461	11.7682	8.110
V1H2-3	3.0571	3.0468	40.5559	7.9048	8.107
H1V2-3	3.0338	3.0538	41.1473	16.5722	8.111
V1H2-4	3.0542	3.0544	62.8311	0.28067	8.108
H1V2-4	-	-	-	-	-

### 8.6.1 Transfers between $L_1$ Vertical and $L_2$ Vertical Orbits

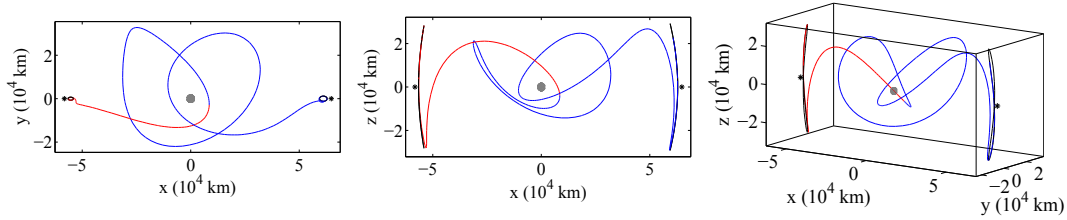


Figure 8.91. V1V2-1,  $C_1 = 3.1616$ ,  $C_2 = 3.1536$ , TOF = 40.1034 days,  $\Delta v = 4.7099$  m/s

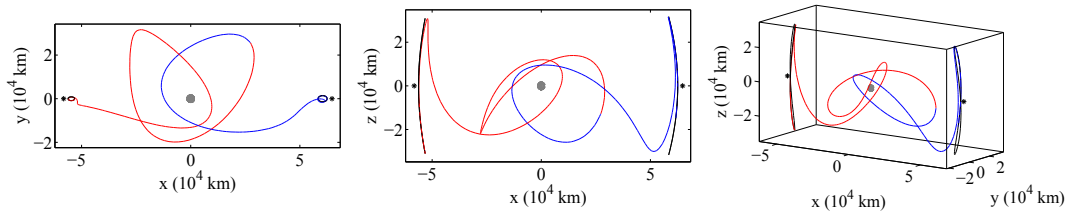


Figure 8.92. V1V2-2,  $C_1 = 3.1564$ ,  $C_2 = 3.1504$ , tof = 39.5552 days,  $\Delta v = 16.0344$  m/s

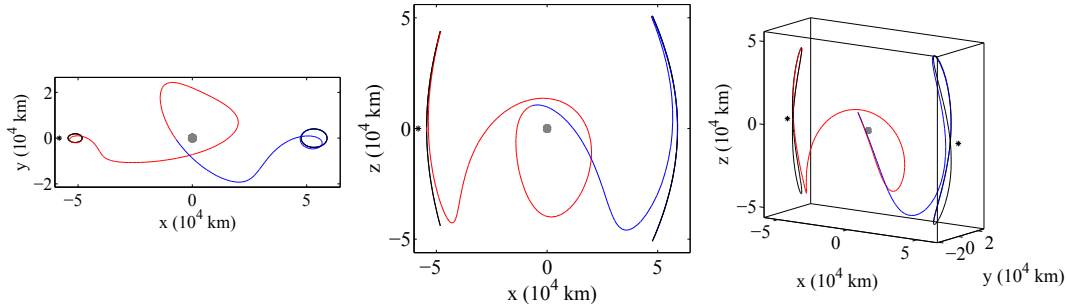


Figure 8.93. V1V2-3,  $C_1 = 3.1265$ ,  $C_2 = 3.1147$ , tof = 35.9293 days,  $\Delta v = 7.9431$  m/s

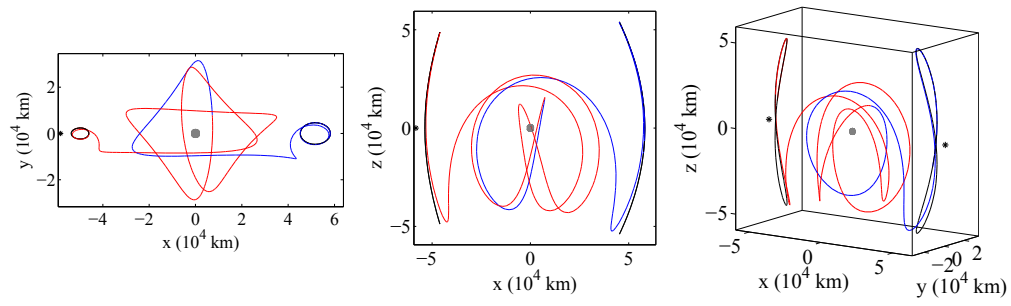


Figure 8.94. V1V2-4,  $C_1 = 3.1139$ ,  $C_2 = 3.1073$ , tof = 54.9474 days,  
 $\Delta v = 5.733 \text{ m/s}$

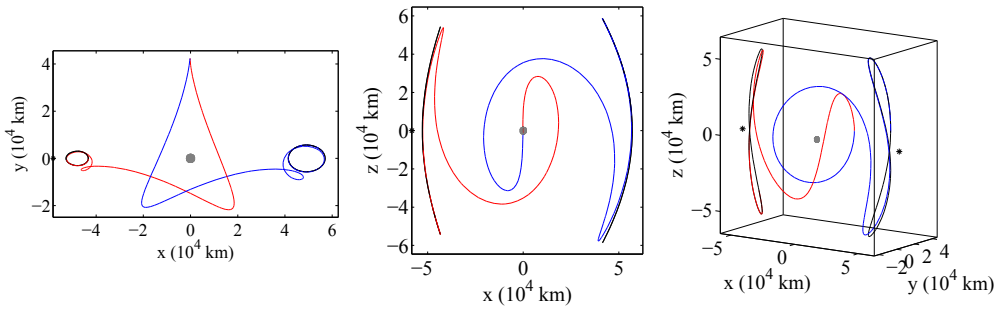


Figure 8.95. V1V2-5,  $C_1 = 3.0986$ ,  $C_2 = 3.0951$ , tof = 41.2976 days,  
 $\Delta v = 9.854 \text{ m/s}$

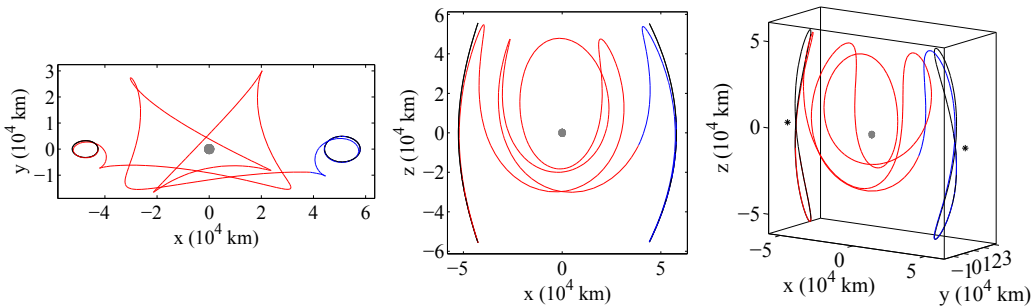


Figure 8.96. V1V2-6,  $C_1 = 3.0949$ ,  $C_2 = 3.1039$ , tof = 53.0685 days,  
 $\Delta v = 19.5612 \text{ m/s}$

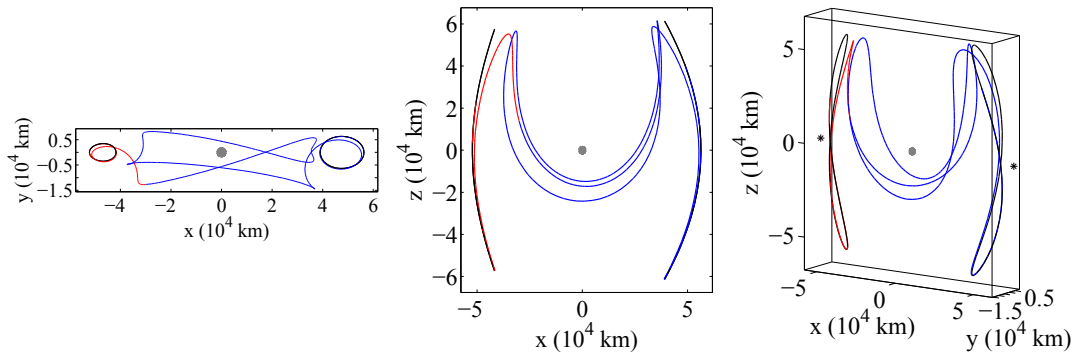


Figure 8.97. V1V2-7,  $C_1 = 3.0898$ ,  $C_2 = 3.0875$ , tof = 49.5468 days,  $\Delta v = 4.653$  m/s

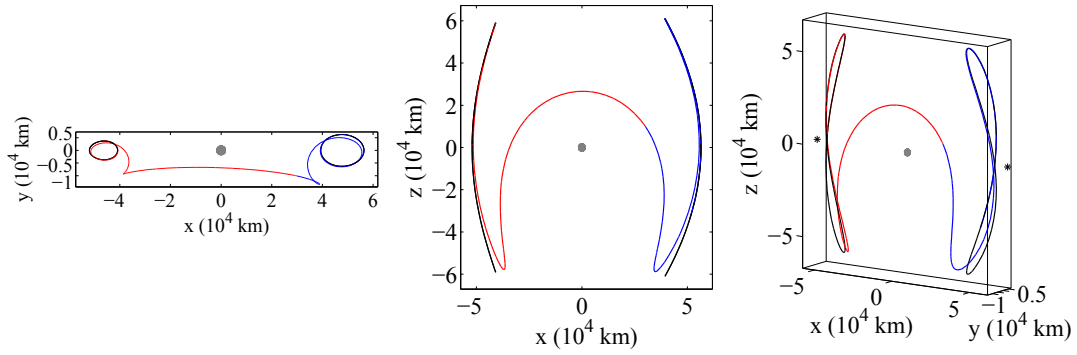


Figure 8.98. V1V2-8,  $C_1 = 3.0849$ ,  $C_2 = 3.0884$ , tof = 33.1433 days,  $\Delta v = 5.254$  m/s

### 8.6.2 Transfers between $L_1$ Halo and $L_2$ Halo Orbits

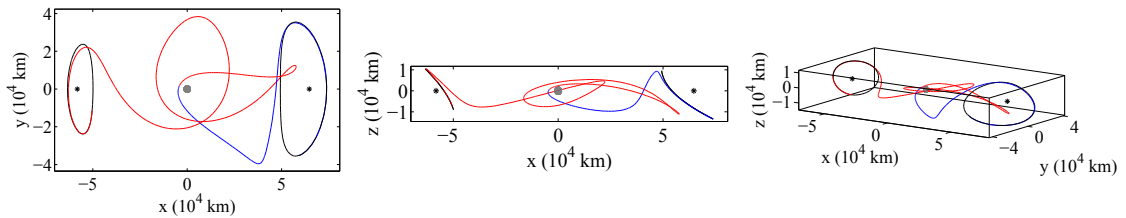


Figure 8.99. H1H2-1,  $C_1 = 3.1681$ ,  $C_2 = 3.1468$ , TOF = 43.003 days,  $\Delta v = 7.9742$  m/s

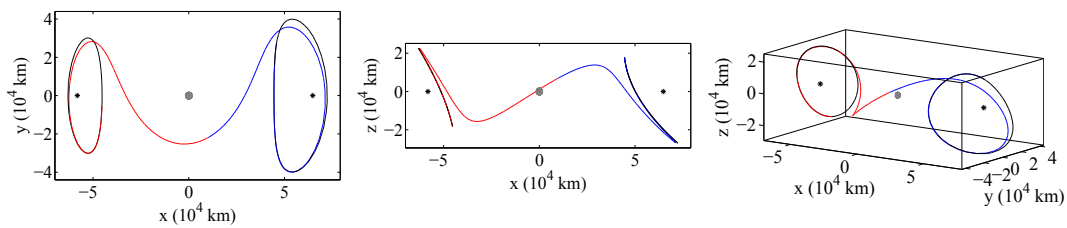


Figure 8.100. H1H2-2,  $C_1 = 3.1469$ ,  $C_2 = 3.1317$ , TOF = 28.9771 days,  $\Delta v = 18.2642$  m/s

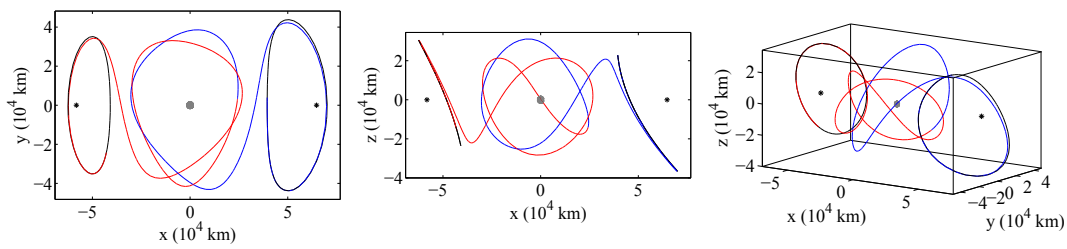


Figure 8.101. H1H2-3,  $C_1 = 3.1269$ ,  $C_2 = 3.1158$ , TOF = 51.0004 days,  $\Delta v = 13.915$  m/s

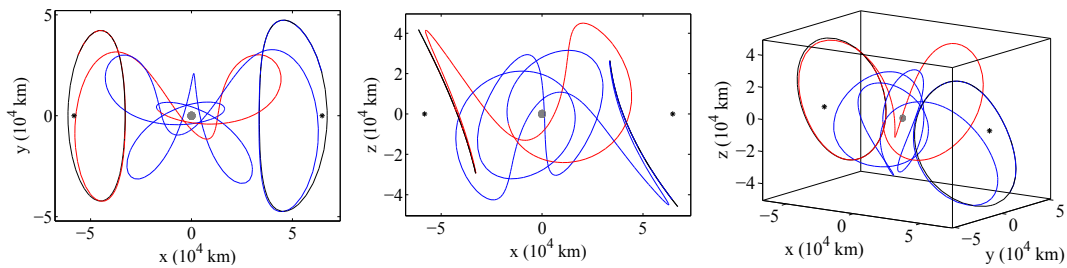


Figure 8.102. H1H2-4,  $C_1 = 3.0930$ ,  $C_2 = 3.0972$ , TOF = 59.7738 days,  $\Delta v = 3.5776$  m/s

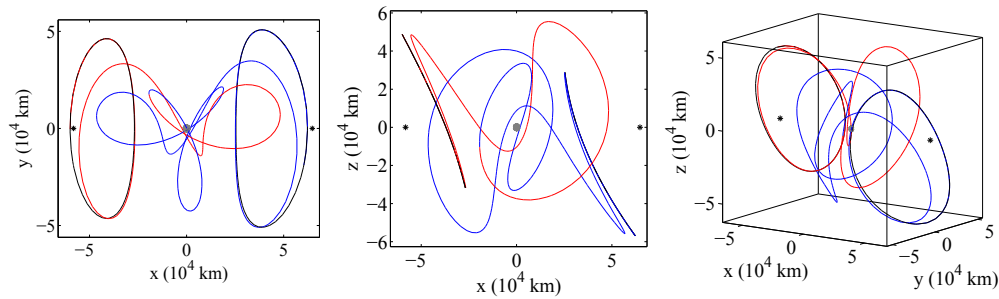


Figure 8.103. H1H2-5,  $C_1 = 3.0698$ ,  $C_2 = 3.0717$ , tof = 62.1769 days,  $\Delta v = 5.1442 \text{ m/s}$

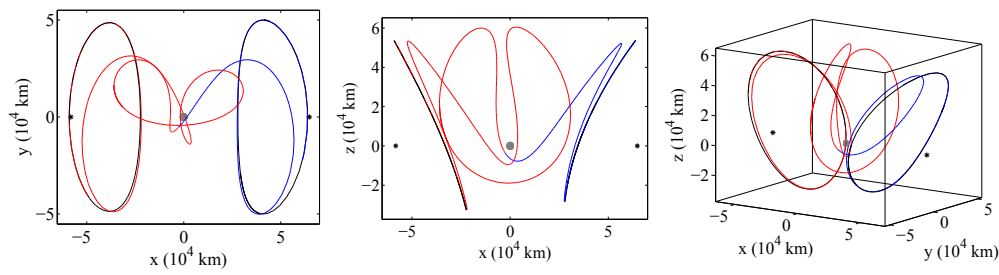


Figure 8.104. H1H2-6,  $C_1 = 3.0537$ ,  $C_2 = 3.0795$ , tof = 51.1918 days,  $\Delta v = 11.8545 \text{ m/s}$

### 8.6.3 Transfers between $L_1$ Axial and $L_2$ Axial Orbits

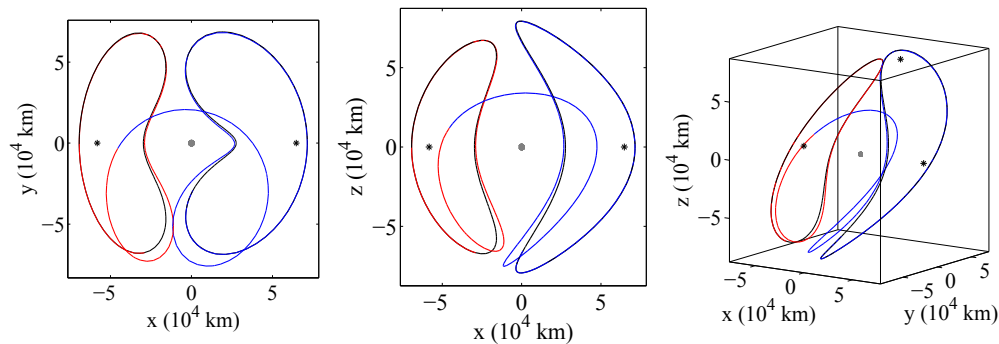


Figure 8.105. A1A2-1,  $C_1 = 3.0058$ ,  $C_2 = 2.9835$ , TOF = 52.0105 days,  $\Delta v = 25.7533 \text{ m/s}$

#### 8.6.4 Transfers between $L_1$ Vertical and $L_2$ Halo Orbits

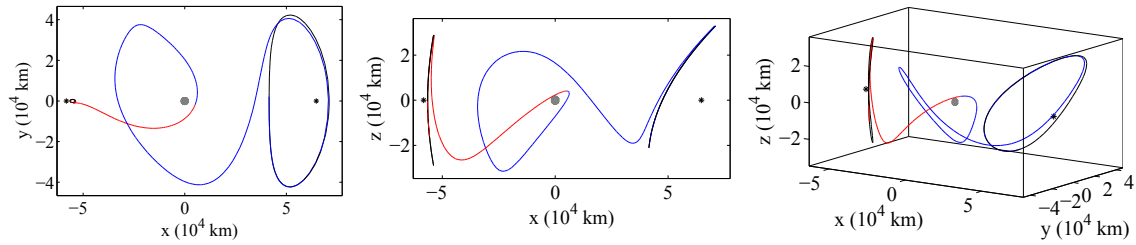


Figure 8.106. V1H2-2,  $C_1 = 3.1604$ ,  $C_2 = 3.1223$ , TOF = 37.5423 days,  $\Delta v = 17.8769$  m/s

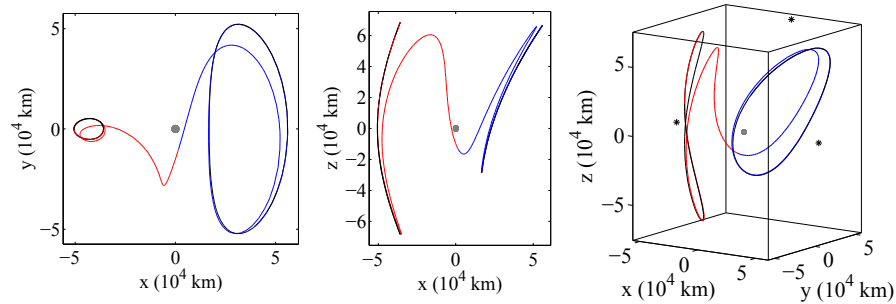


Figure 8.107. V1H2-3,  $C_1 = 3.0571$ ,  $C_2 = 3.0468$ , TOF = 40.5559 days,  $\Delta v = 7.9048$  m/s

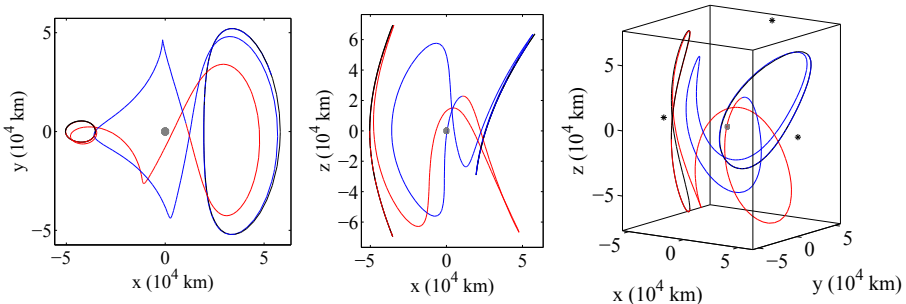


Figure 8.108. V1H2-4,  $C_1 = 3.0542$ ,  $C_2 = 3.0544$ , TOF = 62.8318 days,  $\Delta v = 0.24305$  m/s; Note that this solution is not optimal - the required  $\Delta v$  is reduced using fmincon but an optimal solution is not reached.

### 8.6.5 Transfers between $L_1$ Halo and $L_2$ Vertical Orbits

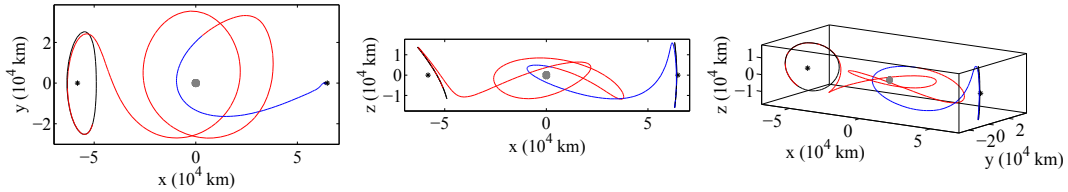


Figure 8.109. H1V2-1,  $C_1 = 3.1636$ ,  $C_2 = 3.1666$ , TOF = 40.529 days,  $\Delta v = 4.5 \text{ m/s}$ ; Note that this solution is not optimal - reducing the required  $\Delta v$  causes the halo orbit to approach the  $x - y$  plane, and the vertical orbit to approach the  $L_2$  point, thus, reducing the  $z$ -amplitude and approaching a transfer between an  $L_1$  Lyapunov orbit and the  $L_2$  libration point.

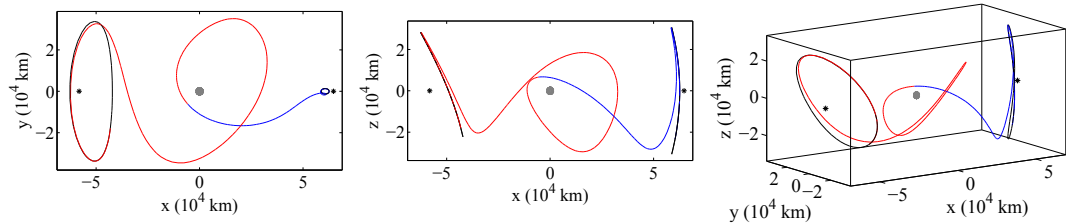


Figure 8.110. H1V2-2,  $C_1 = 3.1327$ ,  $C_2 = 3.1517$ , TOF = 36.7461 days,  $\Delta v = 11.7682 \text{ m/s}$

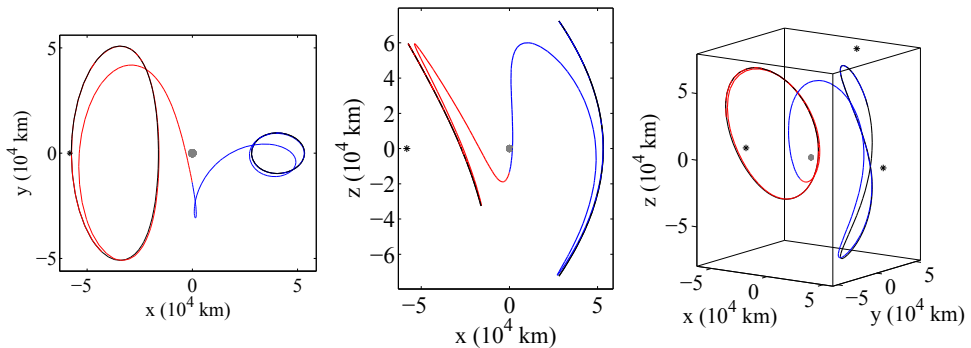


Figure 8.111. H1V2-3,  $C_1 = 3.0338$ ,  $C_2 = 3.0538$ , TOF = 41.1473 days,  $\Delta v = 16.5722 \text{ m/s}$

## 8.7 Catalog Observations and Discussion

An examination of the libration point orbit transfers computed for this catalog yields insight into the existence of these solutions. Some general observations and resulting implications are discussed in the following sections.

### 8.7.1 General Observations about Heteroclinic/Homoclinic Connections

As previously noted, connections associated with  $L_1$  orbits are often accompanied by transfers of similar geometry associated with an  $L_2$  orbit of the same orbit type, and most of the orbit transfers presented are grouped as “partners” in the tables. In Table 8.2, homoclinic connections associated with  $L_1$  and  $L_2$  vertical orbits are listed and are paired according to their geometry. Likewise, homoclinic connections associated with  $L_1$  and  $L_2$  halo orbits are recorded in Table 8.3, and are partnered by matching geometry. Finally, heteroclinic connections between northern and southern members of the halo/axial orbit families are paired into partners and are cataloged in Table 8.5. For the partner transfers corresponding to heteroclinic and homoclinic connections, the time-of-flight is longer for the  $L_2$  orbit transfer for all computed connections. In general, partner transfers appear to exist nearby one another in terms of the Jacobi constant value ( $\Delta C \approx 0.001\text{--}0.01$ ), although the associated values of  $C$  are quite different ( $\Delta C \approx 0.05$ ) for several of the pairs. For those transfers that do not possess a partner, the partner entries appear in dashes in each table. An examination of these tables indicates that the transfers appear with partners with greater prevalence as  $C$  decreases, i.e., as the energy level increases.

### 8.7.2 General Observations about Low-Cost Transfers

The low-cost transfers considered in this catalog are of the types V1V2, H1H2, A1A2, V1H2, and H1V2. These transfers are organized according to type in Table

8.6, where types V1H2 and H1V2 are associated with distinct departure and arrival orbits and are, therefore, grouped in partners. Two pairs of partner transfers (V1H2-2 + H1V2-2, and V1H2-3 + H1V2-3) are computed and correspond to times-of-flight within 1 day of each other. A direct transfer, i.e., a transfer that does not complete a full revolution about the Moon, is located for each transfer type:

- V1V2-5: TOF = 33.14 days,  $\Delta v = 5.25$  m/s, Figure 8.98
- H1H2-2: TOF = 28.98 days,  $\Delta v = 18.26$  m/s, Figure 8.100
- A1A2-1: TOF = 52.01 days,  $\Delta v = 25.75$  m/s, Figure 8.105
- V1H2-3: TOF = 40.56 days,  $\Delta v = 7.90$  m/s, Figure 8.107
- H1V2-3: TOF = 41.15 days,  $\Delta v = 16.57$  m/s, Figure 8.111

The transfers V1V2-5 and H1H2-2 also correspond to the minimum TOF for the transfers of their respective type, while V1H2-3 and H1V2-3 do not. Note that A1A2-1 does not meet the TOF or  $\Delta v$  boundaries for the catalog, but is included because it is the only transfer of this type that is identified near these boundaries.

The majority of the transfers of type H1H2 are between northern and southern members of the halo family; however, one transfer, H1H2-6, is identified that connects two members from the northern families. Again, only one solution is identified for the type A1A2 and requires 52.0105 days and  $\Delta v = 25.7533$  m/s to complete the transfer. This transfer is between two northern members of the axial families, where a northern member is defined such that the maximum  $z$ -excursion occurs for  $y > 0$ . Clearly, this solution violates the  $\Delta v$  limit defined for the low-cost transfers in this catalog and is included because it is the only transfer located near the defined limits. As a final note, for any locally optimal transfer associated with  $\text{TOF} > 50$  days and  $\Delta v < 20$  m/s, it is possible that other nearby solutions may exist for which the time-of-flight is  $\leq 50$  days while maintaining  $\Delta v \leq 20$  m/s.

### 8.7.3 Existence of Partner Transfers

The existence of partner transfers associated with  $L_1$  and  $L_2$  orbits of the same type and possessing similar geometry to one another is observed within the catalog. Recall that a pair of transfer partners consists of two solutions: (A) a transfer associated with an  $L_1$  orbit, and (B) a transfer associated with an  $L_2$  orbit of the same orbit type as the  $L_1$  orbit. Partner transfers (A) and (B) are of similar geometry, that is, they appear roughly as reflections of one another across the  $y$ - $z$  plane at  $x = 1 - \mu$  (i.e.,  $x = 0$  in Moon-centered coordinates). To explain why many of these transfers appear in pairs, it is useful to consider Hill's three body problem (H3BP), where the  $L_1$  and  $L_2$  families of orbits both exist for the same energy level range and are reflections of one another across the  $y$ -axis [10]. Details on the derivation of the equations of motion for the H3BP are available in Appendix D. Many of the transfers presented in the catalog appear to originate from the H3BP and persist for a range of values of  $\mu$ . Evolving the solution with the mass parameter, some transfers may become extinct at a critical value  $\mu_{cr}$ . It is also possible that some solutions may not exist for the Hill problem, but instead emerge as  $\mu$  evolves *away* from zero. In these cases, it is not necessarily expected that the transfers would appear in pairs associated with  $L_1$  and  $L_2$  orbits.

Consider the homoclinic connections associated with  $L_1$  and  $L_2$  vertical orbits paired according to their geometry and cataloged in Table 8.2. As an example, the transfers labeled V1-4 and V1-11 do not appear to exist for the Earth-Moon system, thus, the entries V2-4 and V2-11 do not possess a partner transfer in the Earth-Moon system. Computing transfers of similar geometry for a small value of  $\mu$  and using a numerical continuation scheme to increase the mass parameter, these solutions appear to die out at the critical values of  $\mu_{cr} = 8.953 \times 10^{-4}$  and  $\mu_{cr} = 3.623 \times 10^{-6}$ , respectively. Due to the nonlinearity of the problem, solutions with a particular

transfer geometry computed for  $0 < \mu \leq \mu_{cr}$ , where  $\mu_{cr} < \mu_{EM}$ , could re-emerge for  $\mu > \mu_{EM}$ .

For a homoclinic connection that does not exist as a *free* transfer in the Earth-Moon system, it may be possible to locate a *low-cost* transfer of the same geometry. While transfer V2-10 does not appear to exist in the Earth-Moon system, a transfer possessing similar structure to the homoclinic connection V1-10 is computed for the  $L_2$  vertical orbit near  $C = 3.1131$  and requires approximately  $\Delta v = 18$  m/s and 71.51 days time-of-flight. This transfer appears in Figure 8.112 (note that this connection is not an optimal solution). Similarly, the homoclinic connection V1-23 does not exist

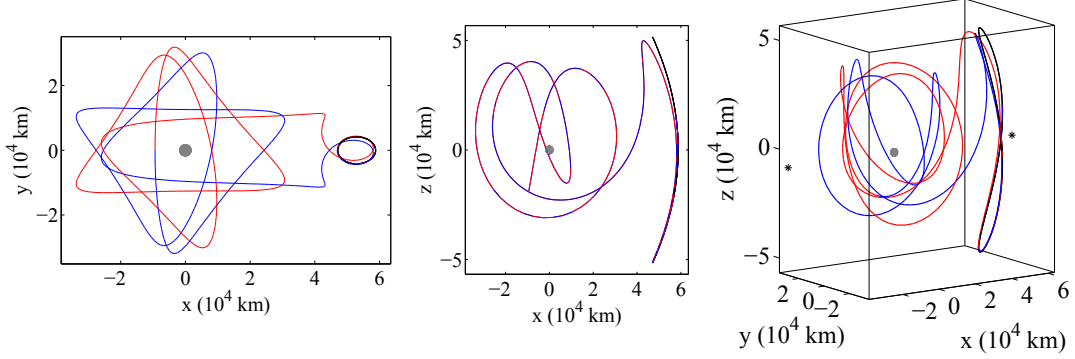


Figure 8.112. Low-cost transfer associated with an  $L_2$  vertical orbit possessing geometry similar to V1-10,  $C_1 = C_2 = 3.1131$ , TOF = 71.5102 days,  $\Delta v = 18.218$  m/s

for the Earth-Moon mass parameter, however, a locally optimal transfer possessing similar geometry to V2-23 and requiring 21.3 m/s is computed and appears in Figure 8.113. Allowing the time-of-flight to increase to  $TOF > 75$  days, a nearby homoclinic connection of similar geometry (but incorporating a second revolution in the vicinity of  $L_2$  when compared with the transfer in Figure 8.113) and associated with a nearby value of Jacobi constant is located and is plotted in Figure 8.114. Although the Jacobi constant values associated with the departure and arrival  $L_1$  vertical orbits

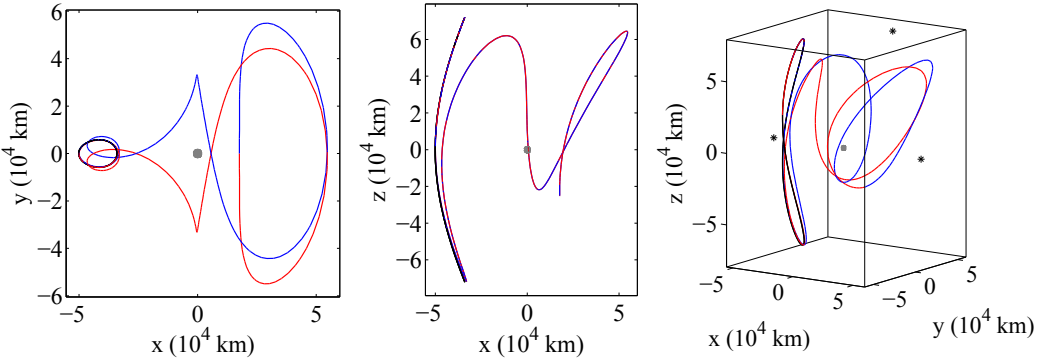


Figure 8.113. Locally optimal transfer of geometry similar to V2-23,  $C_1 = C_2 = 3.0469$ , tof = 65.2842 days,  $\Delta v = 21.3015$  m/s

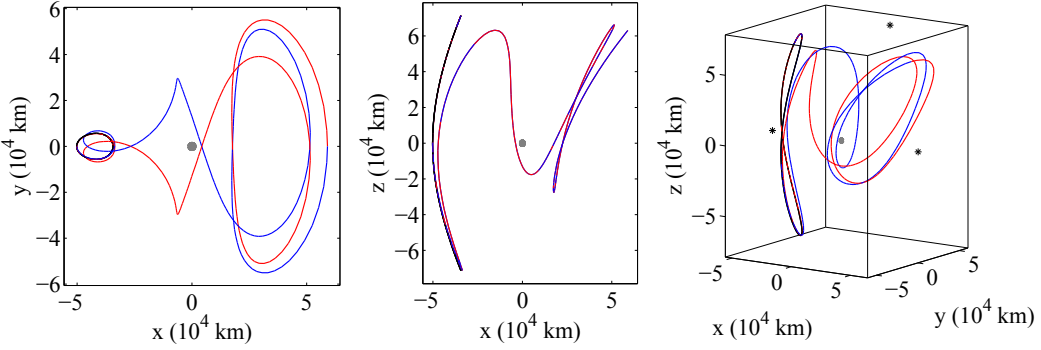


Figure 8.114. Homoclinic connection possessing geometry similar to V2-23 but incorporating an additional revolution about  $L_2$ ,  $C = 3.0492$ , TOF = 76.5048 days

are allowed to vary for the transfers in Figures 8.112 and 8.113, these values differ from one another on the order of  $10^{-6}$  and  $10^{-9}$ , respectively.

In some cases, a free transfer may exist in the planar problem, but may not exist in the spatial problem. Consider the homoclinic connections associated with  $L_1$  and  $L_2$  halo orbits, as cataloged in Table 8.3. The transfer H2-6 does not exist for the Earth-Moon mass parameter, however, a transfer requiring  $\Delta v = 20$  m/s and of the same geometry as H1-6 appears in Figure 8.115. This solution is not optimal; further decreasing the required  $\Delta v$  reduces the  $z$ -amplitude of the halo orbit such that the

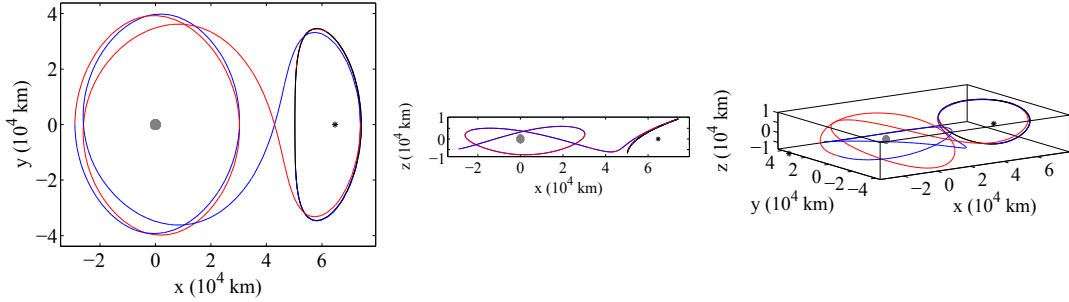


Figure 8.115. Low-cost transfer associated with an  $L_2$  halo orbit and of geometry similar to H1-6,  $C_1 = 3.1496$ ,  $C_2 = 3.1495$ , TOF = 53.52 days,  $\Delta v = 20$  m/s

free transfer is a planar connection associated with a Lyapunov orbit. To further demonstrate that the free transfer does not exist in the spatial problem, Poincaré maps for energy levels near the Jacobi constant values ( $C = 3.1495\text{--}3.1496$ ) associated with the transfer in Figure 8.115 appear in Figure 8.116. The map in Figure 8.116(a) is for a higher energy level (lower value of  $C$ ) than  $C = 3.1495$  and the map in Figure

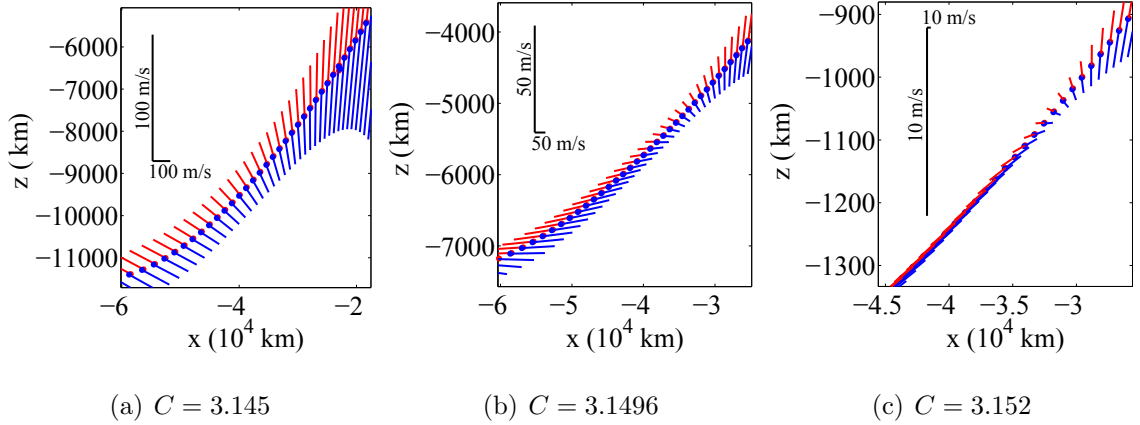


Figure 8.116. Poincaré maps at  $y = 0$  for various energy levels

8.116(c) is for an energy level slightly greater than that associated with the bifurcation to the planar Lyapunov family, i.e., the value for which the halo orbit collapses to the  $x$ - $y$  plane. The invariant manifolds associated with the northern halo orbit at

each energy level are computed, and crossings of the manifolds with the surface of section  $\Sigma^- = \{\bar{x}|y = 0, \dot{y} < 0\}$  are plotted as vectors, where the arrowheads are not included on the vectors for clarity of the plots. Red vectors indicate unstable manifold crossings, while blue segments represent the stable manifold. Here, the base point of each segment indicates the  $(x, z)$  coordinate of that crossing, and the components of the vector in the  $x$  and  $z$  directions represent the  $\dot{x}$  and  $\dot{z}$  values. That is, for the vector definition in Figure 6.2,  $(q_1, q_2) = (x, z)$ , and  $(q_3, q_4) = (\dot{x}, \dot{z})$ . The scaling constant  $k$  is set to 30000 for this example. It should be noted that, for clarity, the plot axes on the maps in Figure 8.116 are not scaled equally. These figures represent a close view of the contours, formed by the projection of the manifold crossings onto the  $x$ - $z$  plane, employed to construct the transfer in Figure 8.115. All crossings of the map that are not along these contours are removed from the plots. Because the axes are not scaled equally, two black lines are included to indicate the velocity magnitude scale in the  $x$  and  $z$  directions. Clearly, as the Jacobi constant value approaches the bifurcating halo orbit that lies within the  $x$ - $y$  plane, the magnitude of the minimum velocity difference between the stable and unstable manifold crossings decreases; however, the  $\Delta v$  is nonzero for all of the maps shown, indicating that the free transfer does not exist for any of these energy levels. Further increasing the Jacobi constant value, the halo orbit quickly collapses to the plane. Thus, the Poincaré maps in Figure 8.116 are useful to demonstrate that the homoclinic connection H2-6 does not exist in the Earth-Moon *spatial* CR3BP. A similar discussion holds for transfer H2-7, which also does not exist in the Earth-Moon system. Low-cost transfers of the same geometry as connection H1-7 may be computed for  $L_2$  halo orbits; a sample transfer is depicted in Figure 8.117. Again, reducing the magnitude of the  $\Delta v$  via differential corrections yields a *planar* free transfer. Thus, for H1-6 and H1-7, it appears that these solutions do not have partner transfers in the spatial problem. It is likely that the solutions H2-6 and H2-7 exist for other values of  $\mu$ , but have collapsed to the  $x$ - $y$  plane for the mass parameter associated with the Earth-Moon

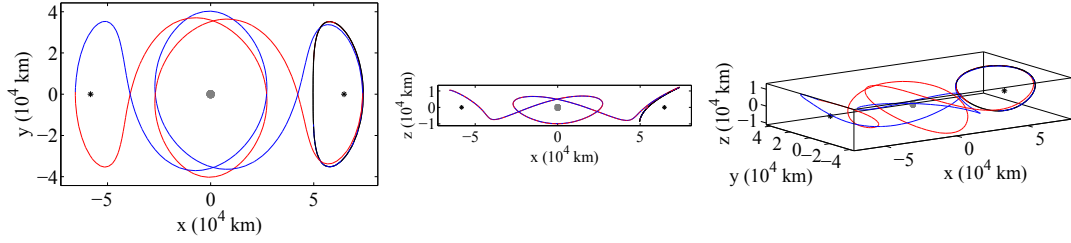


Figure 8.117. Low-cost transfer associated with an  $L_2$  halo orbit and of geometry similar to H1-7,  $C_1 = 3.1477$ ,  $C_2 = 3.1478$ , TOF = 65.6326 days,  $\Delta v = 20$  m/s

system. Indeed, a search for H2-6 in the Sun-Earth system yields the homoclinic connection for a value of  $C = 3.0007640$ . For the H3BP, the solution H2-6 exists at the energy level  $C = 3.6051$ . While connection H2-7 appears to have collapsed to the planar problem before the Sun-Earth value of mass parameter, this solution exists for the Hill problem at the energy level  $C = 3.7222$ .

As a final note, all transfers considered in this catalog are between periodic orbits. In the vicinity of many of these orbits, quasi-periodic solutions also exist and can be considered when computing transfers [101]. Thus, for transfers that do not exist between periodic orbits for the Earth-Moon mass parameter, a nearby free transfer between *quasi-periodic* orbits may be available.

#### 8.7.4 Computation of Vertical Homoclinic Transfers in the Hill Problem

To further explore the relationship between partner transfers and the Hill problem, solutions from the catalog of vertical orbit homoclinic connections are recomputed in the H3BP. The Jacobi constant values and nondimensional times-of-flight associated with these transfers are provided in Table 8.7. Here, the number  $n$  corresponds to the transfer label V1- $n$ /V2- $n$  from the Earth-Moon catalog. Due to the symmetry properties of the H3BP, the values for  $C$  and TOF listed in Table 8.7 are associated

Table 8.7 Vertical Orbit Homoclinic Connections in the Hill Problem

$n$	$C$	TOF (nd)	$n$	$C$	TOF (nd)
*1	4.2212	18.2771	13	2.9313	14.995
*2	3.8047	18.4065	14	2.792	17.6643
*3	-	-	15	2.746	21.0201
*4	3.9026	19.6142	16	2.5992	18.3837
5	3.4549	17.6615	17	2.5872	14.9856
*6	-	-	18	2.5313	16.8458
7	3.4223	17.1844	19	2.3794	18.0943
8	3.2489	18.8157	20	2.4241	22.8567
*9	2.7141	19.4363	21	2.2477	22.838
*10	3.0511	20.4187	*22	2.7141	19.4363
*11	3.2283	17.1679	*23	-	-
12	2.9328	21.3477			

with both V1- $n$  and V2- $n$ . While the transfers are organized according to descending Jacobi constant value for the Earth-Moon catalog, the Jacobi constant values do not decrease monotonically as  $n$  increases in the Hill problem.

Not all transfers from the Earth-Moon catalog exist in the H3BP. For those solutions that do not, the table entries are given as dashes. Starred entries in the table correspond to transfers from the Earth-Moon catalog that do not possess a partner. Several of the solutions that do not have partner transfers in the Earth-Moon system *do* exist within the Hill problem and, therefore, originate as a pair of partner transfers. It is likely that, as  $\mu$  is transitioned away from zero, the nonlinearities of the problem cause the  $L_1$  and  $L_2$  orbit manifolds to evolve such that the free connection becomes extinct for either the  $L_1$  or the  $L_2$  orbit family. It should additionally be noted that,

although a particular solution may exist in the H3BP and the Earth-Moon system, it may not exist for all  $0 < \mu < \mu_{EM}$ , where  $\mu_{EM}$  is the mass parameter for the Earth-Moon system.

While most of the solutions V1- $n$  and V2- $n$  appear to originate in the H3BP, several of these transfers exist for  $\mu = \mu_{EM}$  but become extinct as  $\mu \rightarrow 0$ . Specifically, V1- $n$  and V2- $n$  do not exist as free transfers in the H3BP for  $n = 3, 6$ , and 23. Because these solutions do not originate from the Hill problem in partners, but emerge as  $\mu$  is evolved away from zero, it is not expected that they should possess partner transfers for the Earth-Moon system. For  $n = 9$ , and 22, the entries in Table 8.7 are equivalent because both solutions appear to collapse to the same transfer in the Hill problem. Thus, while V1-9 and V2-22 do not appear to be (approximately) symmetric and are associated with significantly different Jacobi constant values, they seem to evolve from one pair of partner transfers in the Hill problem. The solution V1-9/V1-22 is plotted for the Hill problem in Figure 8.118, where a primary body of arbitrary size is included as the gray sphere. Note that the axis labels  $x, y, z$  in Figure 8.118 correspond to the coordinates  $\xi, \eta, \zeta$ , respectively, from the equations of motion (D.13)–(D.15).

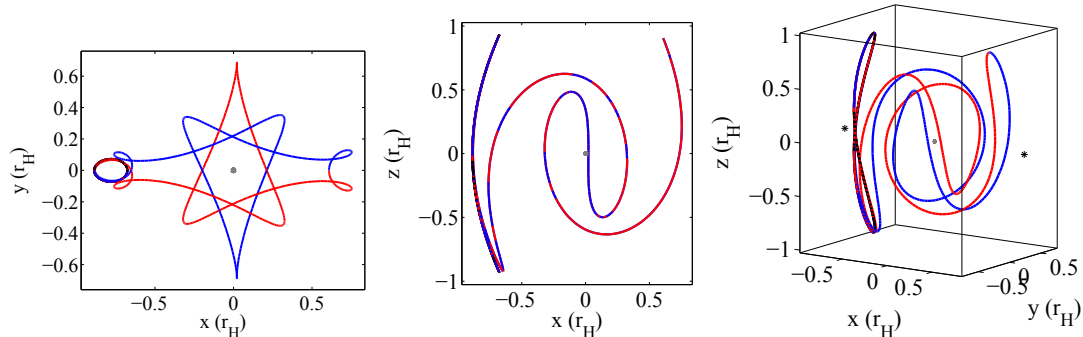


Figure 8.118. V1-9/V1-22 in the Hill problem,  $C = 2.7141$ , TOF = 19.4363 nd

### 8.7.5 Groupings of Transfers of Similar Geometry

Previous discussion has focused on the existence of  $L_1$  and  $L_2$  orbit partner transfers that possess similar geometry to one another. However, there also emerge groupings of  $L_1$  or  $L_2$  orbit transfers of similar structure that are associated with nearby values of Jacobi constant. Recall that, for the purposes of the catalog, transfer “partners” are defined to consist of two solutions: (A) a transfer associated with an  $L_1$  orbit, and (B) a transfer associated with an  $L_2$  orbit of the same orbit type as the  $L_1$  orbit, where (A) and (B) appear roughly as reflections of one another across the  $y$ - $z$  plane at  $x = 1 - \mu$ . Similarly, let a transfer “grouping” define a group of 2 or more solutions that may be associated with different orbit types and different libration points. For example, a grouping of transfers could include the types V1, H2, and V1H2. Different solutions within a grouping of transfers can have significantly different times-of-flight, but are notable because they tend to cluster around a particular range of Jacobi constant values and appear to exploit similar dynamics to affect the transfer. In many cases, a transfer grouping offers evidence of the existence of other nearby dynamical structures, as will be demonstrated in this discussion.

Transfer groupings appear throughout the catalog and include most of the transfer types. As an example, the transfers appearing in Figures 8.119–8.123 represent heteroclinic and homoclinic connections associated with  $L_1$  halo orbits within the range  $C = 3.0723\text{--}3.0787$ . Note that, because the transfer in Figure 8.123 corresponds to  $\text{TOF} > 75$ , it was not included in the catalog of homoclinic connections of type H1. Clearly, each of these solutions employs similar dynamics to complete the transfer, and the geometry of these transfers suggests the existence of other solutions of interest that may exist nearby. Specifically, these connections resemble the behavior of orbits within the family of double-period Distant Prograde Orbits (DPOs), previously presented in Section 5.2.2. For example, the connections in Figures 8.122–8.123 appear to complete a full revolution in the vicinity of a nearby DPO before continuing to

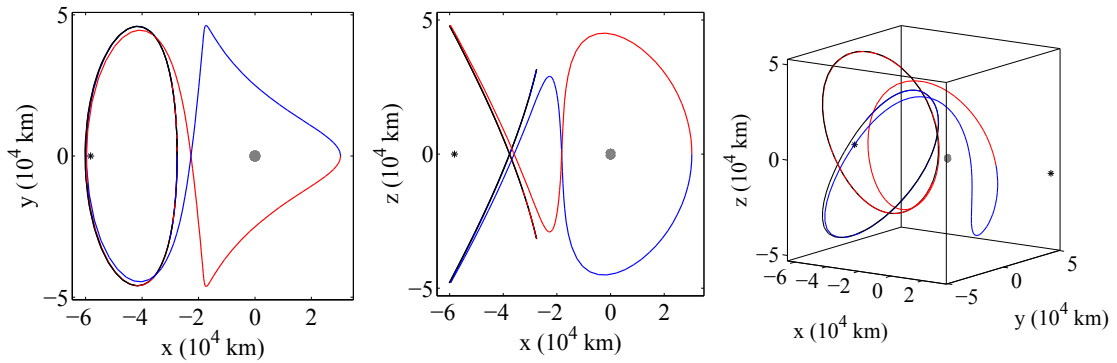


Figure 8.119. HH1-11,  $C = 3.0723$ , TOF = 40.1881 days

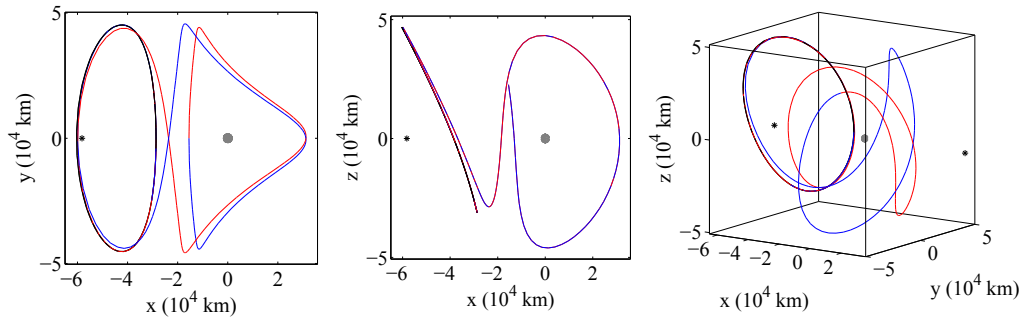


Figure 8.120. H1-11,  $C = 3.0763$ , TOF = 52.9703 days

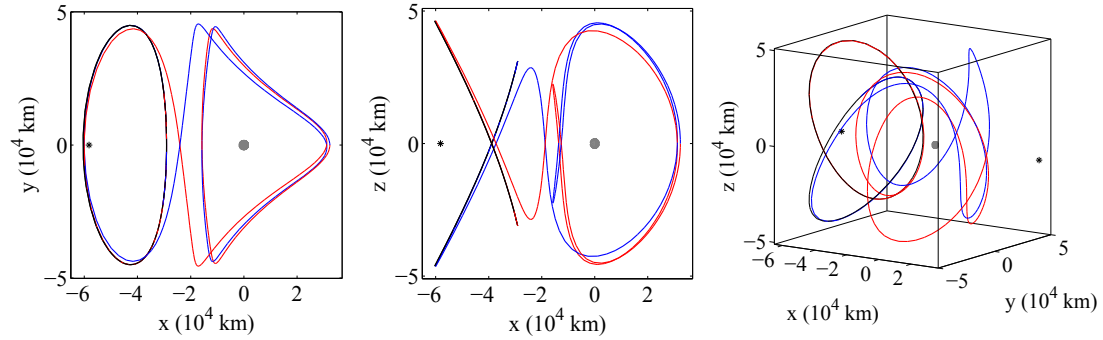


Figure 8.121. HH1-9,  $C = 3.0779$ , TOF = 65.9390 days

their respective arrival orbits. This grouping of transfers implies the existence of the nearby DPO, as well as the possible existence of a nearby low-cost transfer between

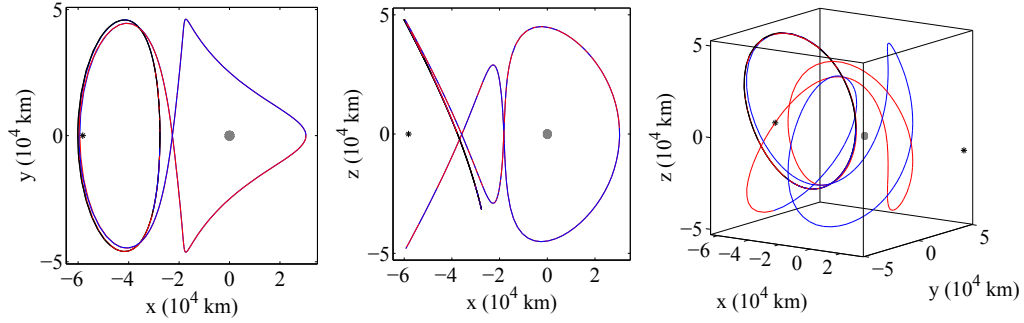


Figure 8.122. H1-14,  $C = 3.0723$ , TOF = 65.9529 days

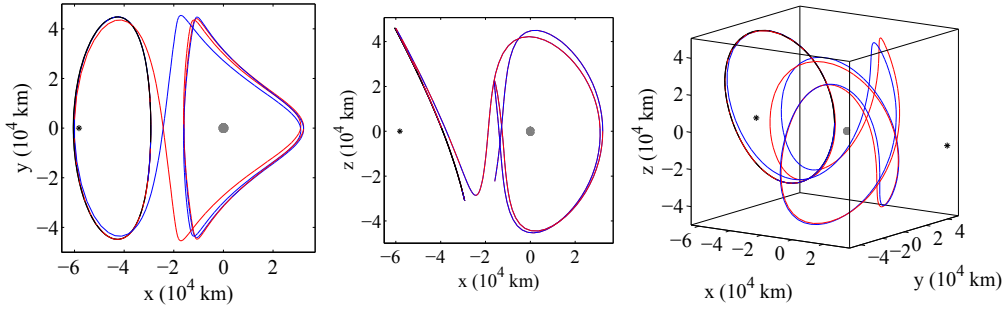


Figure 8.123. Homoclinic connection associated with an  $L_1$  halo orbit in the Earth-Moon system,  $C = 3.0787$ , TOF = 79.0007 days

an  $L_1$  halo orbit and a member of the family of DPOs. Searching for such a transfer reveals the locally optimal connection between an  $L_1$  halo and a DPO presented in Figure 8.124. This transfer requires a  $\Delta v$  of only 6.6609 m/s, corresponds to arrival and departure orbit energy levels near that of the homoclinic connection in Figure 8.123, and has a time-of-flight that is roughly half of this homoclinic connection, as the transfer back to the halo orbit is no longer included.

A second grouping, consisting of the partners to the transfers appearing in Figures 8.119–8.123, also exists. The transfer grouping in Figures 8.125–8.129 represents heteroclinic and homoclinic connections associated with  $L_2$  halo orbits within the range  $C = 3.0686$ – $3.0865$ . The transfer in Figure 8.129 corresponds to  $\text{TOF} > 75$  and

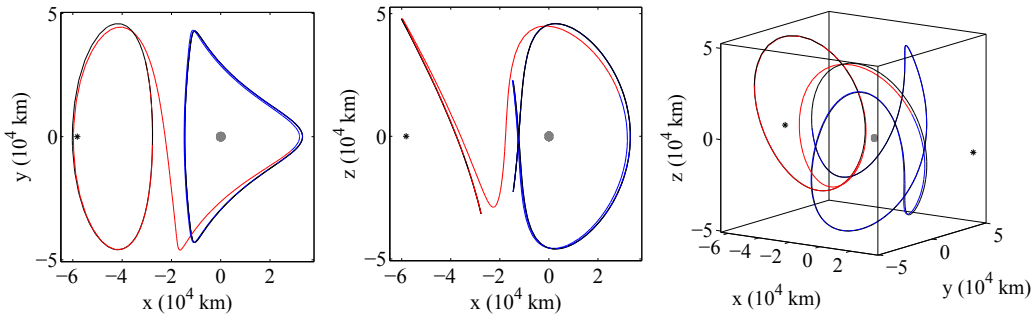


Figure 8.124. Transfer from an  $L_1$  halo orbit to a distant prograde orbit in the Earth-Moon system,  $C_1 = 3.0727$ ,  $C_2 = 3.0776$ , TOF = 41.5601 days,  $\Delta v = 6.6609$  m/s

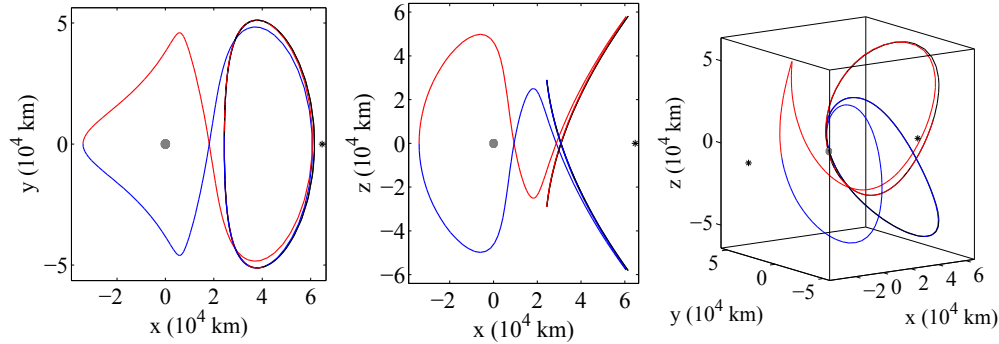


Figure 8.125. HH2-11,  $C = 3.0686$ , TOF = 47.7498 days

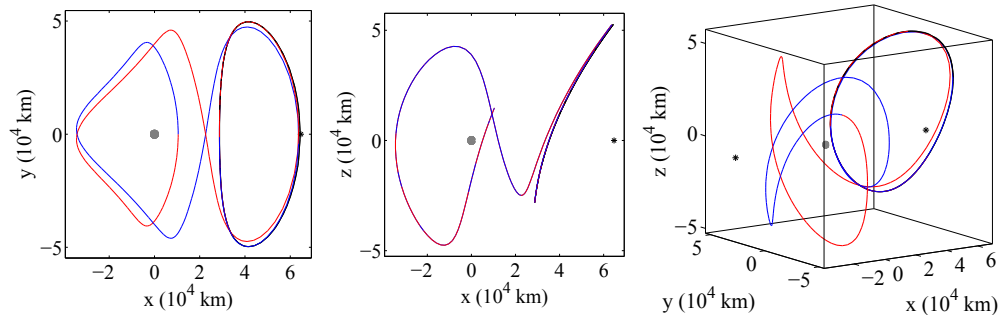


Figure 8.126. H2-11,  $C = 3.0820$ , TOF = 58.3090 days

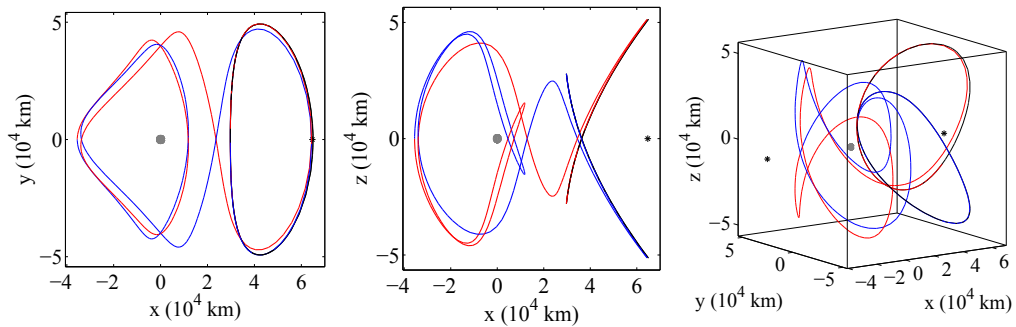


Figure 8.127. HH2-9,  $C = 3.0850$ , TOF = 70.6057 days

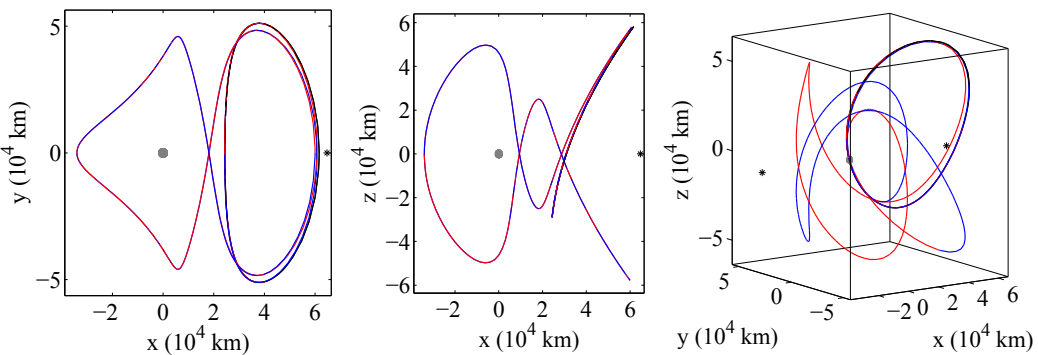


Figure 8.128. H2-14,  $C = 3.0687$ , TOF = 75.1186 days

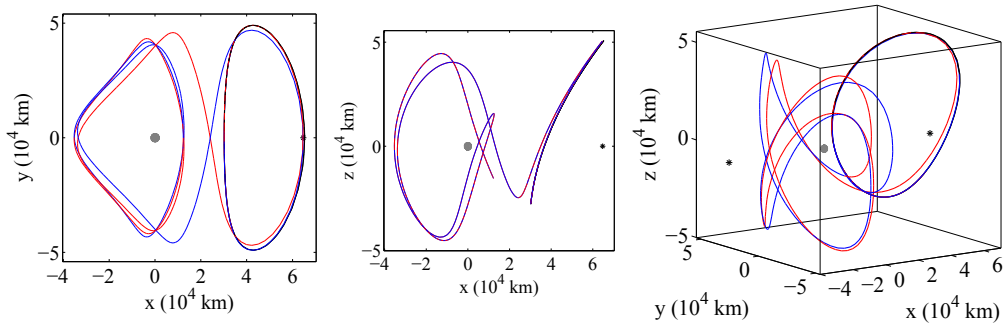


Figure 8.129. Homoclinic connection associated with an  $L_2$  halo orbit in the Earth-Moon system,  $C = 3.0865$ , TOF = 83.1477 days

was not presented in the catalog. The existence of a nearby low-cost transfer from an  $L_2$  halo orbit to a member of the family of DPOs is, again, inferred from the structure of the transfers within the grouping, and a low-cost transfer between an  $L_2$  halo and a DPO appears in Figure 8.130. This transfer requires a  $\Delta v$  of 19.4659 m/s (note that this transfer is not optimized), corresponds to departure and arrival orbit energy levels near that of the homoclinic connection in Figure 8.129, and has a time-of-flight that is roughly half of this homoclinic connection.

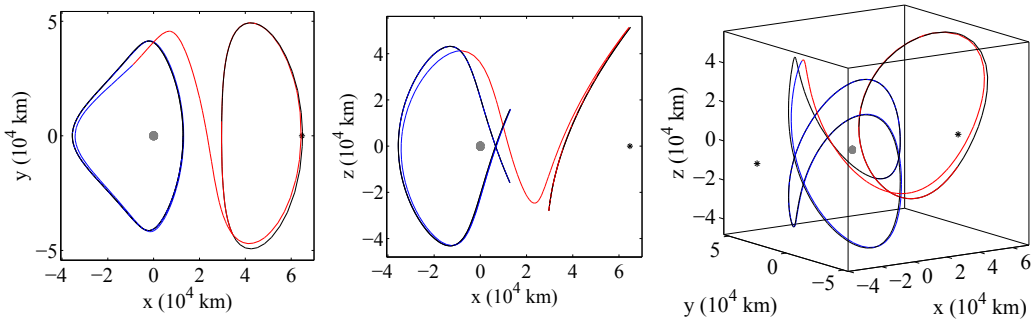


Figure 8.130. Transfer from an  $L_1$  halo orbit to a distant prograde orbit in the Earth-Moon system,  $C_1 = 3.0848$ ,  $C_2 = 3.0898$ , tof = 41.3846 days,  $\Delta v = 19.4659$  m/s (not optimized)

There are many other examples of transfer groupings in the catalog. Eleven sample groupings are listed below in Tables 8.8–8.9. It is likely that any transfers that are not associated with a grouping in this catalog would be associated with a grouping if the boundaries of the catalog were expanded, i.e., if the TOF and  $\Delta v$  limits were increased. Several notable features of transfer groupings are apparent upon inspection of Tables 8.8–8.9. Transfer groupings generally come in “partners” (e.g., partner groupings 8 and 9) or contain partner transfers (e.g., grouping 6). Here, the transfers from Figures 8.119–8.123 and those in Figures 8.125–8.129 comprise “partner groupings” 4 and 5, respectively. Each of the transfers in grouping 4 possess a partner that is contained within grouping 5, and vice versa. Conversely, grouping 6 is composed of three pairs of partner transfers, in addition to one low-cost transfer.

Table 8.8 Transfer Groupings 1–5

Grouping No.	Transfer	$C_1$	$C_2$	TOF (days)	Figures
1	V1-23 ( $\Delta v = 21.3$ )	3.0469	3.0469	65.2842	8.113
	H2-19	3.0485	3.0485	65.5675	8.67
	V1H2-3	3.0571	3.0468	40.5559	8.107
2	V2-22	3.0315	3.0315	69.6960	8.36
	H1-19	3.0366	3.0366	63.1381	8.53
	H1V2-3	3.0338	3.0538	41.1473	8.111
3	V1-10	3.1126	3.1126	63.9845	8.8
	V2-10 ( $\Delta v = 18.2$ )	3.1131	3.1131	71.5102	8.112
	V1V2-4	3.1139	3.1073	54.9474	8.94
4	H1-11	3.0763	3.0763	52.9703	8.45
	H1-14	3.0723	3.0723	65.9529	8.48
	HH1-9	3.0779	3.0779	65.9390	8.79
	HH1-11	3.0723	3.0723	40.1881	8.81
5	H2-11	3.0820	3.0820	58.3090	8.58
	H2-14	3.0687	3.0687	75.1186	8.63
	HH2-9	3.0850	3.0850	70.6057	8.85
	HH2-11	3.0686	3.0686	47.7498	8.87

Table 8.9 Transfer Groupings 6–11

Grouping No.	Transfer	$C_1$	$C_2$	TOF (days)	Figures
6	V1-16	3.0897	3.0897	55.3035	8.13
	V1-17	3.0885	3.0885	38.7444	8.14
	V1-18	3.0870	3.0870	47.0461	8.15
	V2-16	3.0876	3.0876	60.1932	8.29
	V2-17	3.0852	3.0852	45.2766	8.30
	V2-18	3.0827	3.0827	52.7960	8.31
	V1V2-8	3.0849	3.0884	33.1433	8.98
7	V1-14	3.1008	3.1008	51.4635	8.11
	V1-15	3.0947	3.0947	67.9682	8.12
	V2-14	3.0999	3.0999	58.4020	8.28
	V2-15	3.1045	3.1045	70.6015	8.26
	V1V2-5	3.0986	3.0951	41.2976	8.95
8	H1-10	3.0766	3.0766	65.1147	8.44
	HH1-10	3.0768	3.0768	43.9812	8.80
9	H2-10	3.0746	3.0746	72.0334	8.62
	HH2-10	3.0742	3.0742	50.6271	8.86
10	H1-17	3.0584	3.0584	70.6021	8.51
	H1-18	3.0498	3.0498	62.5695	8.52
	H1-19	3.0366	3.0366	63.1381	8.53
	H2-17	3.0663	3.0663	75.1945	8.64
	H2-18	3.0616	3.0616	66.4187	8.66
	H2-19	3.0485	3.0485	65.5675	8.67
11	H2-2	3.1517	3.1517	45.0669	8.54
	H2-5	3.1510	3.1510	57.1765	8.55

To represent all entries in the transfer catalog, each is plotted by its associated time-of-flight and Jacobi constant value(s) and the resulting chart is presented in Figure 8.131. In this chart, all free transfers are plotted by colored markers, where a

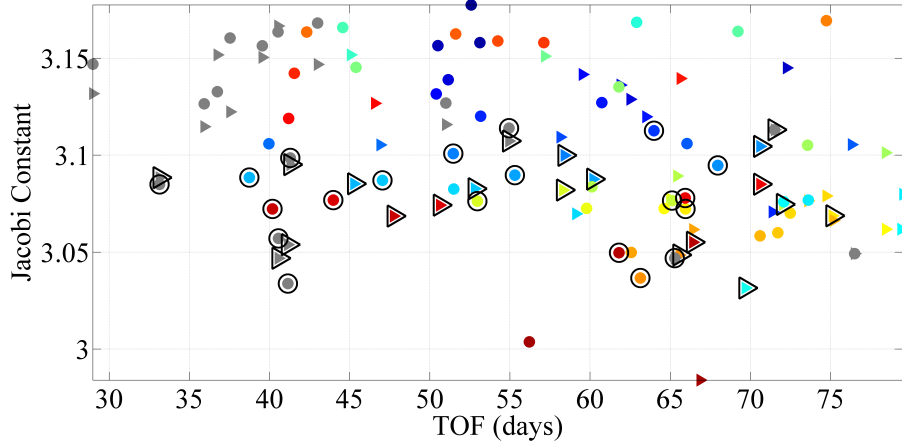


Figure 8.131. Catalog transfers are represented via their associated time-of-flight and Jacobi constant values

particular color is associated with a particular pair of partner transfers. The  $L_1$  orbit transfers are indicated by solid colored dots, and  $L_2$  transfers by solid triangles. Each low-cost transfer between a pair of  $L_1$  and  $L_2$  orbits is represented via a gray dot and a gray triangle, both possessing the same TOF value. Here, the dot is associated with the  $L_1$  orbit Jacobi constant value, and the triangle with the Jacobi constant value of the  $L_2$  orbit. The transfers that appear within the groupings listed in Tables 8.8–8.9 are additionally outlined in black. From this representation, it is evident that the transfers in the groupings correspond to lower values of Jacobi constant, i.e., higher energy levels. Recall that, for the larger values of  $C$ , fewer partner transfers exist in general. As many of the transfer groupings are associated with partner transfers, this could be the reason that the transfers associated with lower Jacobi constant values are more likely to be members of a transfer grouping. The transfers also appear to cluster within TOF bands. For example, transfers generally appear to

clump near the values  $\text{TOF} = 41, 46,$  and  $51$  days. One of the main distinguishing features between two solutions is the number of revolutions incorporated about the Moon during the transfer, which is a discrete quantity. While the TOF required to complete a revolution about the Moon depends on the energy level of the transfer, this TOF will generally fall within a range of values. Thus, it might be expected that the transfers will appear to cluster densely within certain TOF bands.

As a final observation, an association between libration point orbit transfers and periodic orbits is apparent. It was previously noted that periodic orbits from the family of DPOs exist in the vicinity of the transfers from groupings 4 and 5 and that the transfers from the grouping and nearby periodic orbits within the family of DPOs are associated with similar physical attributes. In fact, periodic orbits can be located in the vicinity of all of the transfer groupings listed in Tables 8.8–8.9. Some sample orbits are computed and appear in blue in Figures 8.132–8.133 with the nearby transfer included in black. For example, a member from the family of

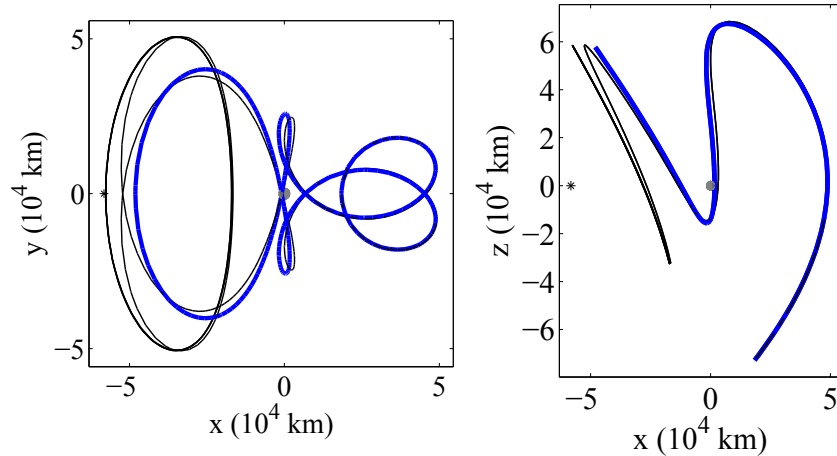


Figure 8.132. H1-19 Group 2,  $C = 3.0366$ , period = 31.4358 days

butterfly orbits [34] exists for the energy level corresponding to transfer V2-17 and is plotted in Figure 8.133. It should be noted that more than one periodic orbit may exist possessing similar geometry to a particular transfer grouping. Periodic orbits

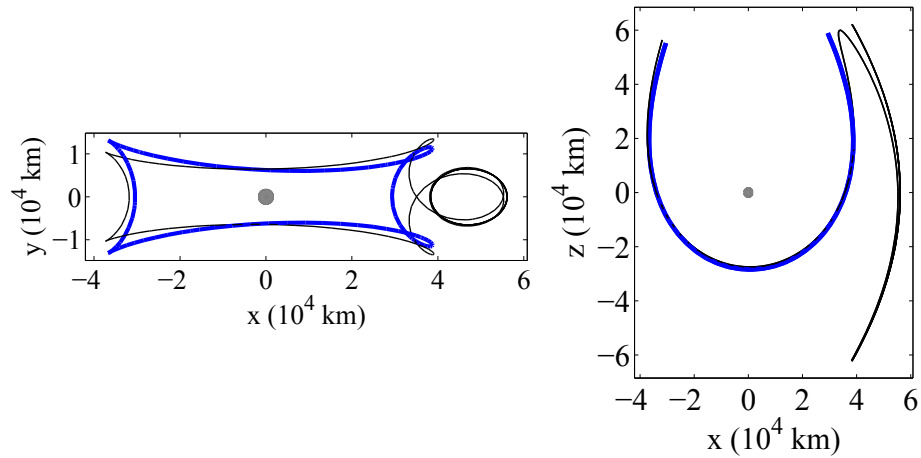


Figure 8.133. V2-17 Group 7,  $C = 3.0852$ , period = 18.359 days

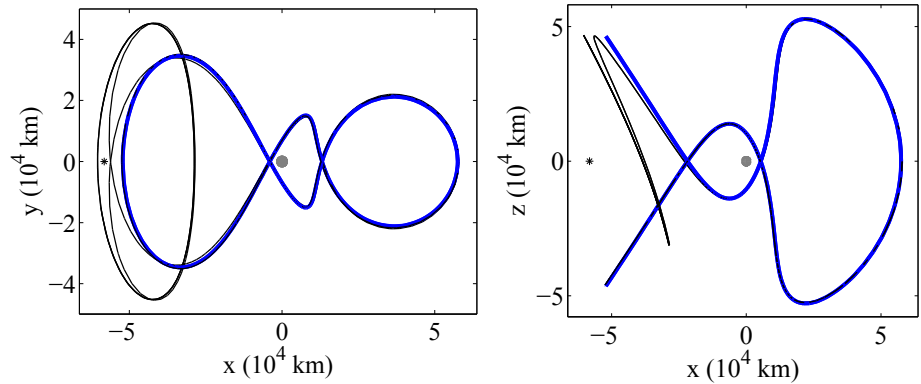


Figure 8.134. H1-10 Group 9,  $C = 3.0766$ , period = 42.2254 days

can also be located in the vicinity of transfers that are not associated with a grouping in this catalog. As an example, a periodic solution with geometry similar to V1-9 is computed and is displayed in Figure 8.137. Note again, however, that it is likely that transfers that are not associated with a grouping in this catalog could be associated with a grouping if the catalog boundaries are expanded.

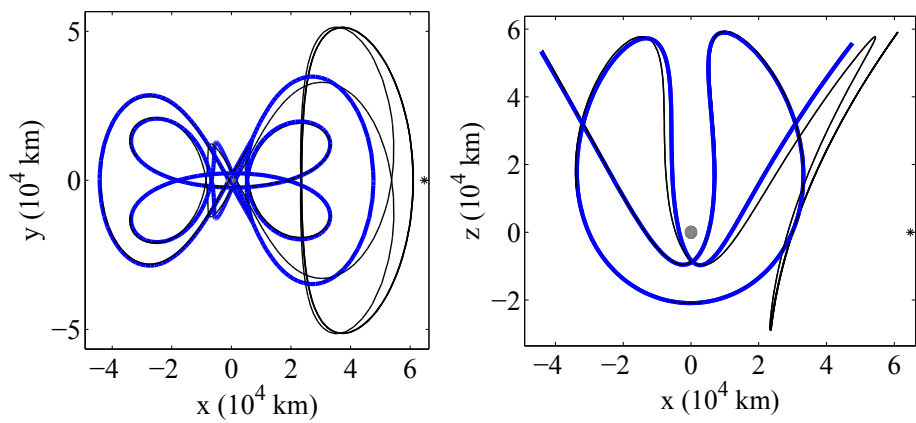


Figure 8.135. H1-17 Group 11,  $C = 3.0663$ , period = 43.1169 days

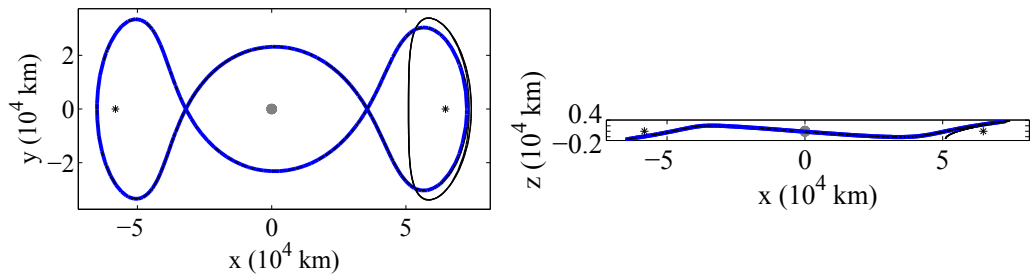


Figure 8.136. H2-2 Group 12,  $C = 3.1518$ , period = 28.4862 days

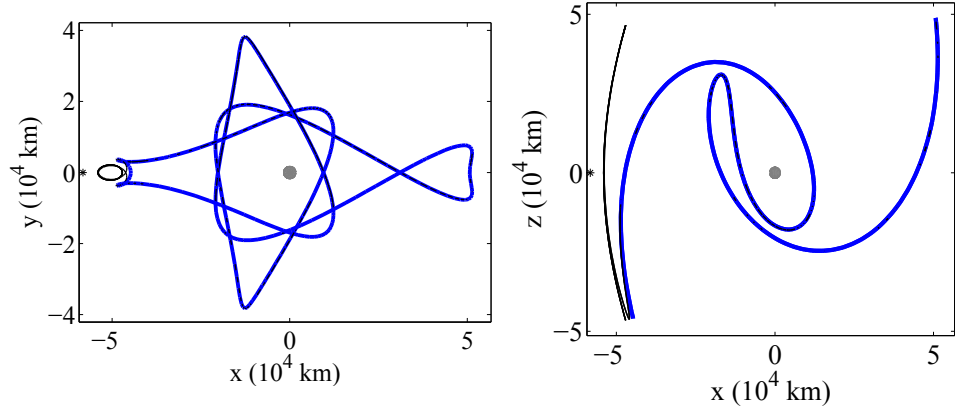


Figure 8.137. V1-9,  $C = 3.1201$ , period = 38.0188 days

### 8.7.6 Charting the Solution Space to Locate Transfers

While the interactive design tool demonstrated in Chapter 7 is useful to search the solution space for transfers between libration point orbits, automated methods are also of interest. Mondelo et al. [94] employ Poincaré maps and invariant manifolds to search for free transfers between quasi-periodic libration point orbits. These authors consider the angles,  $\theta_1$  and  $\theta_2$ , that define the departure location along a two-dimensional torus, as described in Chapter 3.4.2. By varying these angles along a departure and an arrival torus, different arcs along the associated invariant manifolds are defined. These manifold arcs are propagated, and crossings with a surface of section are recorded. A search algorithm is employed to locate nearest neighbors on the map, and the magnitude of the minimum discontinuity to the nearest neighbor is displayed for each manifold arc using a heat map. Here, the manifold arcs are represented by their associated angles  $\theta_1$  and  $\theta_2$  on the torus and the locations of free transfers are indicated by “hot spots” on the map.

Here, techniques demonstrated by Mondelo et al. are modified and are employed to perform an automated scan for transfers between periodic libration point orbits. Rather than parameterizing transfers by the departure location of the manifold arcs from the periodic orbit, solutions are defined by their associated Jacobi constant value and time-of-flight. Using these variables, a chart is made for transfers spanning a range of energy levels and transfer times. Selecting departure and arrival orbit types, an automated search algorithm steps through a range of  $C$  values, computes the associated periodic orbits from within the orbit families, and defines initial conditions for  $N$  manifold arcs along the unstable manifold associated with the departure orbit and along the stable manifold asymptotic to the arrival orbit. The manifolds are propagated for a specified time interval and all crossings of a surface of section are recorded. In this investigation, 1000 arcs are integrated for 50 days to search for all transfers except those of type A1, A2, AA1, AA2, or A1A2; for the axial transfers 1500 arcs are

propagated for 50 days. Here,  $\Sigma = \{\bar{x} | x = 1 - \mu\}$  is selected as the surface of section. Define  $M_U$  as the array containing all crossings of the propagated unstable manifold arcs with  $\Sigma$  and  $M_S$  as the array in which crossings of the stable manifold arcs are stored, where all manifold arcs are computed for a particular value of  $C$ . The nearest neighbor search proceeds as follows. The state  $\bar{x}_{U,i}$ , corresponding to the  $i$ -th row in  $M_U$ , is compared to each state  $\bar{x}_{S,j}$  in  $M_S$ , and the position and velocity discontinuities are computed by as  $\Delta r_{ij} = \sqrt{(x_{U,i} - x_{S,j})^2 + (y_{U,i} - y_{S,j})^2 + (z_{U,i} - z_{S,j})^2}$ , and  $\Delta v_{ij} = \sqrt{(\dot{x}_{U,i} - \dot{x}_{S,j})^2 + (\dot{y}_{U,i} - \dot{y}_{S,j})^2 + (\dot{z}_{U,i} - \dot{z}_{S,j})^2}$ . For each value of  $i$ , the minimum values of  $\Delta r_{ij}$  and  $\Delta v_{ij}$  are recorded, yielding vectors  $\bar{R}_i$  and  $\bar{V}_i$  containing  $i$  entries that define the minimum discontinuity between each manifold crossing in  $M_U$  and the set of manifold crossings in  $M_S$ .

To display the resulting heat map, boundaries on the magnitudes of  $\Delta r$  and  $\Delta v$  are assumed. Here,  $\Delta r = 10000$  km and all recorded values in  $\bar{V}_i$  for which the associated value  $\bar{R}_i > \Delta r$  are discarded. Then, selecting  $\Delta v = 2$  m/s, the remaining transfers are plotted in batches, where the  $k$ -th batch satisfies  $(k-1)\Delta v \leq \bar{V}_i \leq (k)\Delta v$  for  $k = 1-50$ . The batches associated with smaller→larger values of  $\bar{V}_i$  appear bluer→redder. The resulting maps appear for transfers of type V1 and V2 in Figures 8.138–8.139. The transfers of these types that are computed from the catalog, as listed in Table 8.2, are included as black markers overlaid on the map. The solutions of type V1 are plotted in Figure 8.138, while transfers of type V2 appear in Figure 8.139. The homoclinic connections of types V1 and V2 clearly lie within the blue regions on the respective maps. However, there also appear blue regions for which no homoclinic connection appears. This is because, while low-cost transfers are available in these regions, a maneuver-free transfer is not available. Expanding the catalog of V1 and V2 transfers to include solutions that require maneuvers, markers would appear in these regions. There are also, however, homoclinic connections that appear in isolated regions of the map where a blue region does not exist. Thus, while an automated method provides a useful guide to search for maneuver-free or low-cost transfers, a

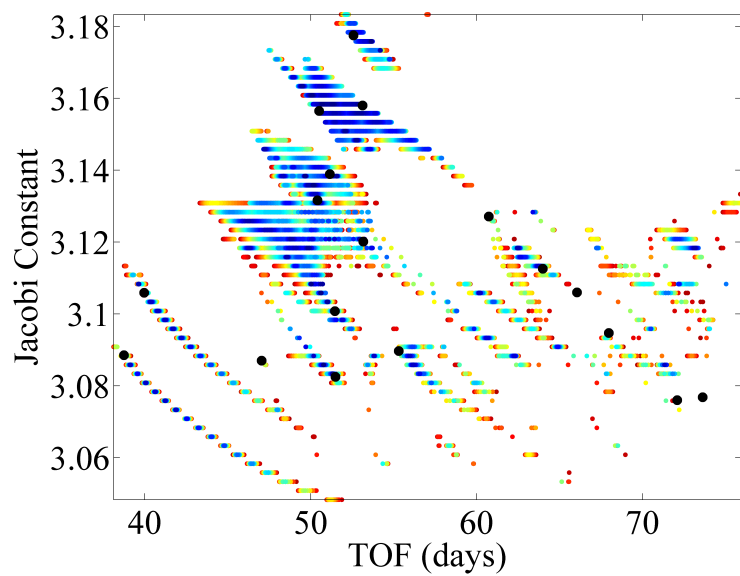


Figure 8.138. Heat map for transfers of type V1

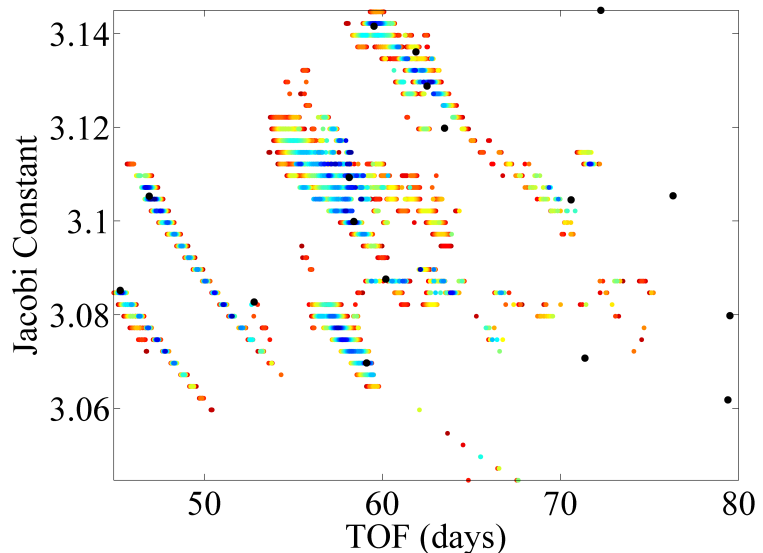


Figure 8.139. Heat map for transfers of type V2

combination of automated and interactive methods is perhaps most useful to ensure the full solution space is considered.

### 8.7.7 Evolution of Low-Cost Transfers with Mass Parameter

All transfers in this catalog are computed for the Earth-Moon system, however, many of these solutions exist for other values of the mass parameter. As a solution evolves with  $\mu$ , the shape of and time-of-flight along the transfer are modified. Any maneuvers along the transfer may also change in magnitude. A free transfer in one system may require a nonzero maneuver for another value of  $\mu$ .

To demonstrate how solutions change with  $\mu$ , the transfers H1H2-2 and V1V2-8 from the Earth-Moon catalog are re-computed for the Sun-Earth system and for the Hill problem. The Earth-Moon, Sun-Earth ( $\mu = 3.0038961 \times 10^{-6}$ ), and H3BP ( $\mu \rightarrow 0$ ) solutions appear in Figures 8.100, and 8.140 for transfer H1H2-2. For transfer V1V2-8, the Earth-Moon, Sun-Earth, and H3BP solutions appear in Figures 8.98 and 8.141. The solutions in the Earth-Moon and Sun-Earth problems are locally optimal

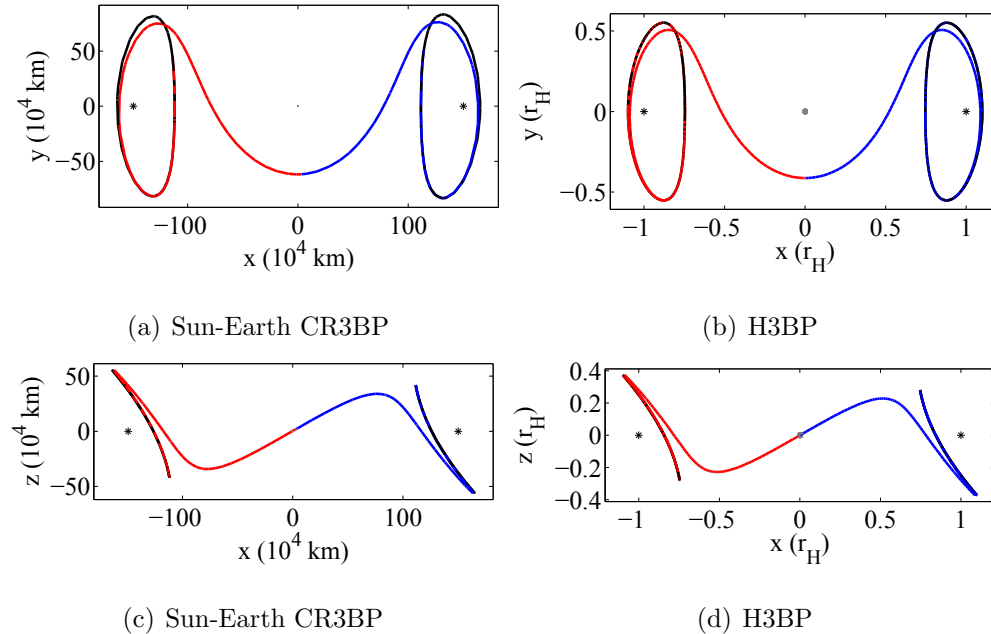


Figure 8.140. H1H2-2 in the (a),(c) Sun-Earth CR3BP,  $C_1 = 3.0007425$ ,  $C_2 = 3.0007387$ , TOF = 401.9274 days,  $\Delta v = 2.2331$  m/s; (b),(d) Hill 3BP,  $C = 3.6156$  TOF = 11.2451 dimensionless,  $\Delta v = 0$

with respect to the  $\Delta v$ . Clearly, the  $\Delta v$  required to complete the transfer reduces with mass parameter for these solutions. For the H3BP, where the  $L_1$  and  $L_2$  families of orbits are symmetric across the  $y-z$  plane at the  $x$ -location of the smaller primary, a heteroclinic ( $\Delta v = 0$ ) connection is available. The dimensions of the coordinates in the H3BP are Hill radii ( $r_H = 3^{(-1/3)}$  dimensionless). Note, again, that the axis labels  $x, y, z$  in the H3BP plots correspond to the coordinates  $\xi, \eta, \zeta$ , respectively, from the equations of motion (D.13)–(D.15).

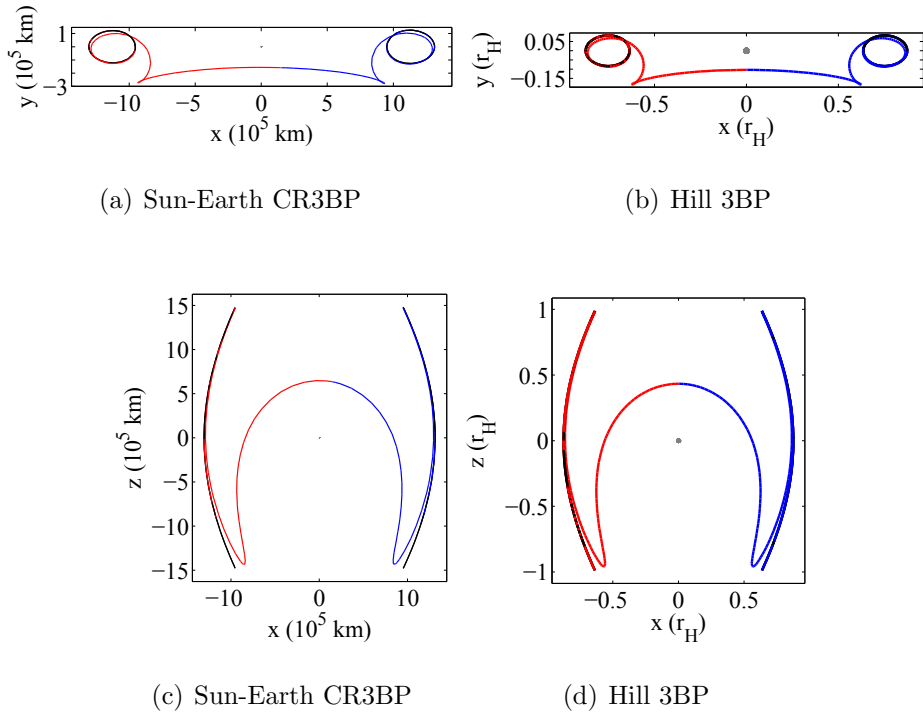


Figure 8.141. V1V2-8 in the (a),(c) Sun-Earth system,  $C_1 = 3.0005$ ,  $C_2 = 3.0005$ , TOF = 464.4181 days,  $\Delta v = 0.6859$  m/s; (b),(d) V1V2-8 in the Hill problem,  $C = 2.5296$ , TOF = 13.061 dimensionless,  $\Delta v = 0$

The symmetry properties of the H3BP appear to provide favorable conditions for free transfers between  $L_1$  and  $L_2$  orbits. Given a state

$$\bar{\xi}_{u,1} = \left[ \xi_u, \eta_u, \zeta_u, \dot{\xi}_u, \dot{\eta}_u, \dot{\zeta}_u \right]^T$$

along the unstable manifold associated with an  $L_1$  libration point orbit, the symmetry properties of the system equations require that the state

$$\bar{\xi}_{u,2} = \left[ -\xi_u, -\eta_u, \zeta_u, -\dot{\xi}_u, -\dot{\eta}_u, \dot{\zeta}_u \right]^T$$

is associated with the unstable manifold asymptotic to the symmetric  $L_2$  orbit. To locate the analogous state along the  $L_2$  orbit stable manifold, the symmetry in time is exploited to yield

$$\bar{\xi}_{s,2} = \left[ -\xi_u, \eta_u, \zeta_u, \dot{\xi}_u, -\dot{\eta}_u, -\dot{\zeta}_u \right]^T.$$

Considering crossings of  $\Sigma = \{\bar{\xi}|\xi = 0\}$ , then the first elements of  $\bar{\xi}_{u,1}$  and  $\bar{\xi}_{s,2}$  are both set to zero. If  $\dot{\eta} = \dot{\zeta} = 0$  at the crossing of  $\Sigma$ , then the states  $\bar{\xi}_{u,1}$  and  $\bar{\xi}_{s,2}$  are identical. This condition is satisfied by the solution V1V2-8 in the Hill problem, thus, this transfer requires zero  $\Delta v$ . If the additional symmetry with respect to the  $\xi$ - $\eta$  plane is included, then the state

$$\bar{\xi}_{s,2}^{-z} = \left[ -\xi_u, \eta_u, -\zeta_u, \dot{\xi}_u, -\dot{\eta}_u, \dot{\zeta}_u \right]^T$$

is along the stable manifold surface asymptotic to the  $L_2$  orbit as reflected across the  $\xi$ - $\eta$  plane. Then, if  $\zeta = \dot{\eta} = 0$  at  $\Sigma$ , the states  $\bar{\xi}_{u,1}$  and  $\bar{\xi}_{s,2}^{-z}$  are identical. The transfer H1H2-2 in the H3BP possesses a crossing of this configuration.

## 8.8 Existence of Transfers in an Ephemeris Model

The solutions in the Earth-Moon catalog are computed in the simplified model of the CR3BP. However, these transfers generally transition to an ephemeris model while maintaining the significant characteristics of the orbits. To demonstrate the effect of perturbations such as the Earth-Moon eccentricity and solar gravity, sample solutions from the catalog are transitioned to a Sun-Earth-Moon ephemeris model.

### 8.8.1 Transitioning to an Ephemeris Model

To validate the trajectory design tools employed in this investigation, it is useful to demonstrate the existence of solutions from the Earth-Moon transfer catalog within a higher-fidelity ephemeris model. This is accomplished by first discretizing the arcs along a transfer to enable multiple-shooting. The individual arcs are numerically integrated in the  $N$ -body model, yielding discontinuities between subsequent arcs. To construct a feasible solution in the ephemeris model, a differential corrections process is employed [90].

Before transitioning a solution to the ephemeris model, the solution is modified to include some number of revolutions along both the departure and arrival orbits, and an initial epoch is selected to define the orientation of the bodies in the  $N$ -body system. Sample transfers from the catalog are modified to include the following arcs:

- five revolutions along the departure and arrival orbits
- a bridge arc linking the initial condition along the departure orbit to the initial condition along the unstable manifold
- a bridge arc linking the final state along the stable manifold to the initial condition along the arrival orbit

Thus, the final solution contains the following sequence of segments:

1. five revolutions along the departure orbit
2. bridge arc linking the departure orbit to the unstable manifold

3. unstable manifold arc
4. stable manifold arc
5. bridge arc linking the stable manifold to the arrival orbit
6. five revolutions along the arrival orbit

Each solution is continuous in the CR3BP, except for two small discontinuities that exist between segments 2 and 3 and between segments 4 and 5. These discontinuities are 20 km in position and are on the order of  $\sim 1 \times 10^{-5}$  km/s in velocity. To combat numerical sensitivities, nodes are distributed along each of the segments to reduce the integration times. Numerical integration of these nodes in the ephemeris model proceeds via the relative 4-body equations of motion as expressed in Moon-centered J2000 inertial coordinates. The second-order equations of motion are written as

$$\bar{R}_{23}'' = -G(m_3 + m_2) \frac{\bar{R}_{23}}{R_{23}^3} + \sum_{i=1,4} Gm_i \left( \frac{\bar{R}_{3i}}{R_{3i}^3} - \frac{\bar{R}_{2i}}{R_{2i}^3} \right), \quad (8.1)$$

where  $m_1$ ,  $m_2$ , and  $m_4$  represent the masses of the Earth, Moon, and Sun, respectively. The vector  $\bar{R}_{23}$  locates the spacecraft relative to the Moon, and  $\bar{R}_{ij} = \bar{R}_j - \bar{R}_i$  locates the  $i^{th}$  body relative to the  $j^{th}$  body. The respective distances are obtained via the planetary and lunar ephemeris file DE 421 [89]. The integrated solution possesses discontinuities between each resulting arc, and a differential corrections process is employed to reduce these discontinuities below a prescribed tolerance. The magnitude of the discontinuities varies depending on the selected initial epoch. Here, the epoch is arbitrarily chosen to be the first of the month for a particular month in the year 2020, and is allowed to vary during the differential corrections process. The month is determined by propagating the solution in the ephemeris model and searching for the month that minimizes the sum of the discontinuities along the initial guess, where the discontinuities include both position and velocity states.

To determine the effect the Earth-Moon eccentricity and solar gravity on transfers between libration point orbits, it is useful to consider both free and low-cost transfers. Here, the transfers V1-19, HH2-11, H1H2-2, V1H2-3, and H1V2-3 are transitioned to

the Sun-Earth-Moon model via a differential corrections process. Full-state continuity is enforced between each arc along the transfers to within a tolerance of  $1 \times 10^{-9} = 0.39 \text{ m} = 1.0 \times 10^{-6} \text{ m/s}$ , although the converged solutions, generally, meet a tighter nondimensional tolerance of roughly  $1 \times 10^{-11}$ . The resulting solutions appear in Figures 8.142–8.146, where the ephemeris path is plotted in black and the stable and unstable manifolds along the original CR3B transfers are additionally included in blue and red, respectively. For the solutions in Figures 8.143–8.146, the initial epoch

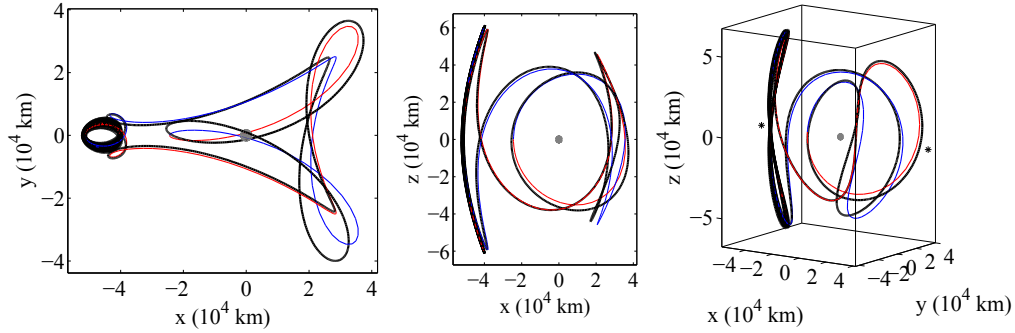


Figure 8.142. V1-19 in the Sun-Earth-Moon ephemeris model for initial epoch July 31 2020 23:37:26.4

is selected as previously described, that is, by selecting the initial epoch associated with the smallest cumulative discontinuity along the initial guess. For the transfer in Figure 8.142, the minimum discontinuity occurs for November 1, 2020. However, convergence of the corrections process is improved and the general characteristics of the CR3B solution are better maintained in the ephemeris model for V1-19 by selecting the initial epoch (August 1, 2020) associated with the *largest* cumulative discontinuity along the initial guess. For the November 1 epoch, the magnitude of the error chatters between  $\sim 10^{-3}$  and  $\sim 0.1$  for the first 20 iterations and requires 24 iterations to converge to a tolerance of  $1.9 \times 10^{-11}$ , while, for the August 1 epoch, the error decreases monotonically and the solution converges to a tolerance of  $2.2 \times 10^{-11}$  in 9 iterations. Clearly, the relationship between convergence and the total initial

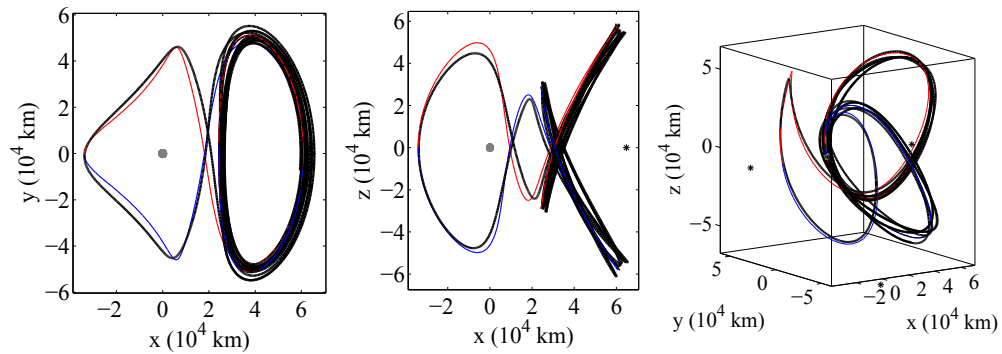


Figure 8.143. HH2-11 in the Sun-Earth-Moon ephemeris model for initial epoch June 30 2020 23:23:50.5

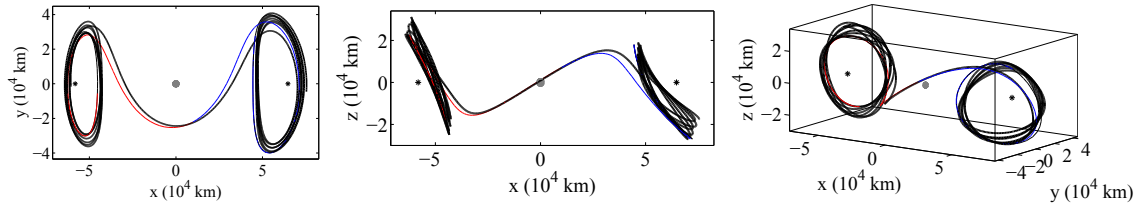


Figure 8.144. H1H2-2 in the Sun-Earth-Moon ephemeris model for initial epoch December 1 2020 0:42:48.2

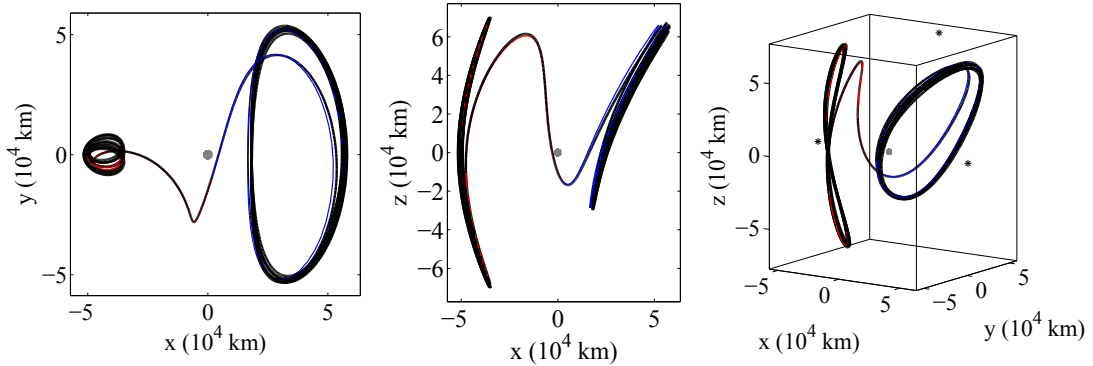


Figure 8.145. V1H2-3 in the Sun-Earth-Moon ephemeris model for initial epoch August 31 2020 23:14:58.9

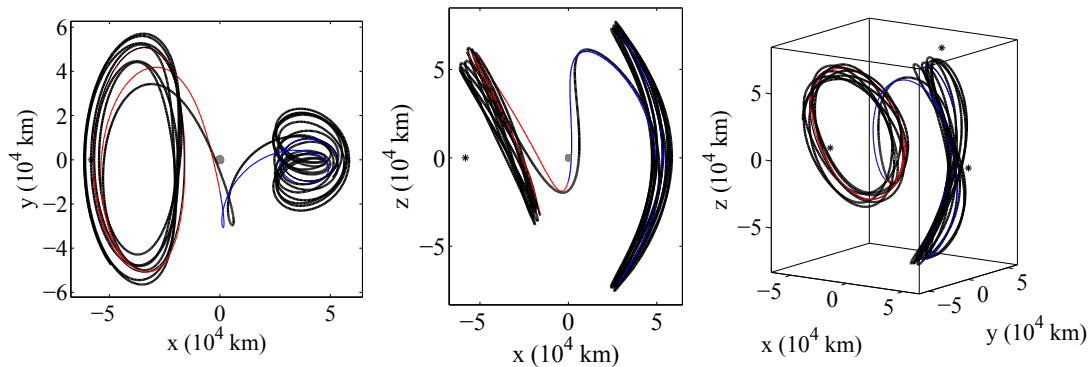


Figure 8.146. H1V2-3 in the Sun-Earth-Moon ephemeris model for initial epoch November 1 2020 1:13:52.1

error is not linear. Again, the initial epoch is allowed to vary within the corrections process for all solutions. Because no periodic solutions exist in the ephemeris model, all of the converged transfers depart from nonperiodic orbits in the vicinity of the original periodic orbits from the CR3B. For some solutions, such as V1-19 and V1H2-3, the nonperiodic orbits remain quite close to the periodic solution while for others, such as H1V2-3, the nonperiodic orbits spread further from the original solution. One factor contributing to the larger difference in the orbits in H1V2-3 is that the  $\Delta v$  is also removed during the transition to the ephemeris model. Including one or more maneuvers within the differential corrections process could help to yield final orbits that remain more closely bound to their original periodic solutions. In general, the solutions from the CR3BP transition to the Sun-Earth-Moon ephemeris model while maintaining the significant characteristics of the transfer.

### 8.8.2 Transitioning Solutions to GMAT

For further validation and to demonstrate that catalog transfer solutions may be accessed via the currently available mission design tools, the solutions from the previous section are transitioned to NASA's General Mission Analysis Tool (GMAT)

[102, 103], version 2013a. Here, a Sun-Earth-Moon ephemeris is employed, and solar radiation pressure (SRP) is also included.

The ephemeris paths from the previous section are transitioned to GMAT by employing the available optimization routines within GMAT. To affect this transition, a script file is generated that defines a spacecraft object and a mission sequence in GMAT. The spacecraft object is associated with an initial state and epoch to be numerically integrated in the Sun-Earth-Moon ephemeris model including SRP. The states and epochs provided to GMAT are associated with the nodes that are distributed along the final converged ephemeris paths computed in the previous section. All states correspond to dimensional units in the Earth-Moon rotating frame. Because the rotating frame in GMAT is a pulsating frame defined for each instant along the spacecraft trajectory, the states are dimensionalized according to their associated instantaneous values of  $\ell^*$ , available from the DE 421 ephemeris file. Assume the ephemeris path to be transitioned to GMAT is comprised of  $(m - 1)$  segments and  $m$  nodes, where nodes  $1-(m - 1)$  are individually propagated within the multiple-shooting algorithm and node  $m$  defines the final state along the transfer. Then, the mission sequence to be implemented within GMAT is specified as follows: (1) the first node that defines the first arc along the transfer is numerically integrated for the specified time-of-flight, (2) all subsequent arcs are propagated, and an optimization algorithm is employed to minimize the  $\Delta v$  between the current arc and the previous arc. Within (2), the initial velocities along the  $i$ -th segment ( $i = 2, \dots, m - 1$ ) are allowed to vary to target the initial position along the  $(i + 1)$ -th segment. The associated  $\Delta v$  is computed as  $\sqrt{(\dot{x}_i - \dot{x}_{i-1})^2 + (\dot{y}_i - \dot{y}_{i-1})^2 + (\dot{z}_i - \dot{z}_{i-1})^2}$  and is minimized within the mission sequence for each arc. The resulting solutions are plotted in Figure 8.147–8.148, where Figure 8.147 contains the maneuver-free transfers from the CR3BP, and the solutions in Figure 8.148 require a  $\Delta v$  in the CR3BP. The converged ephemeris paths are plotted in red in Moon-centered coordinates, with the Earth appearing on the left. An orange path near the Earth is visible and indicates

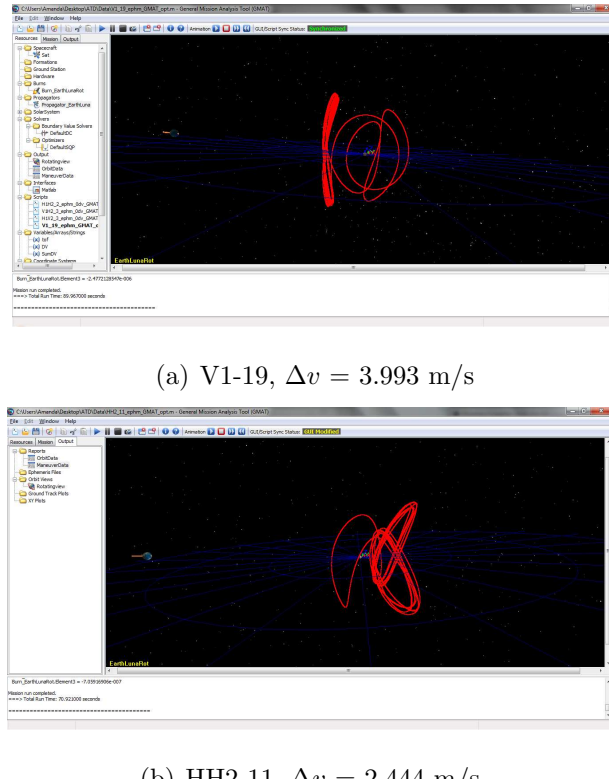


Figure 8.147. Transfers are transitioned to GMAT assuming a Sun-Earth-Moon ephemeris model with SRP

all positions of the Earth along the Earth-Moon line during the propagation; this line represents the pulsation of the Earth-Moon rotating frame. Note that, in the plots in Figures 8.142–8.146, the pulsation of the frame is removed so that the Earth and Moon are in fixed locations. The total  $\Delta v$  required for the converged solution in GMAT with SRP is included in the figure captions. Considering the solutions propagated *without* SRP, the total  $\Delta v$  values are as follows: V1-19  $\Delta v = 3.994 \text{ m/s}$ , HH2-11  $\Delta v = 2.437 \text{ m/s}$ , H1H2-2  $\Delta v = 3.280 \text{ m/s}$ , V1H2-3  $\Delta v = 2.879 \text{ m/s}$ , H1V2-3  $\Delta v = 2.806 \text{ m/s}$ . Clearly, the inclusion of perturbations due to solar radiation pressure has a small affect on the total  $\Delta v$  required to complete these transfers, and can cause either a reduction or an increase in this cost.

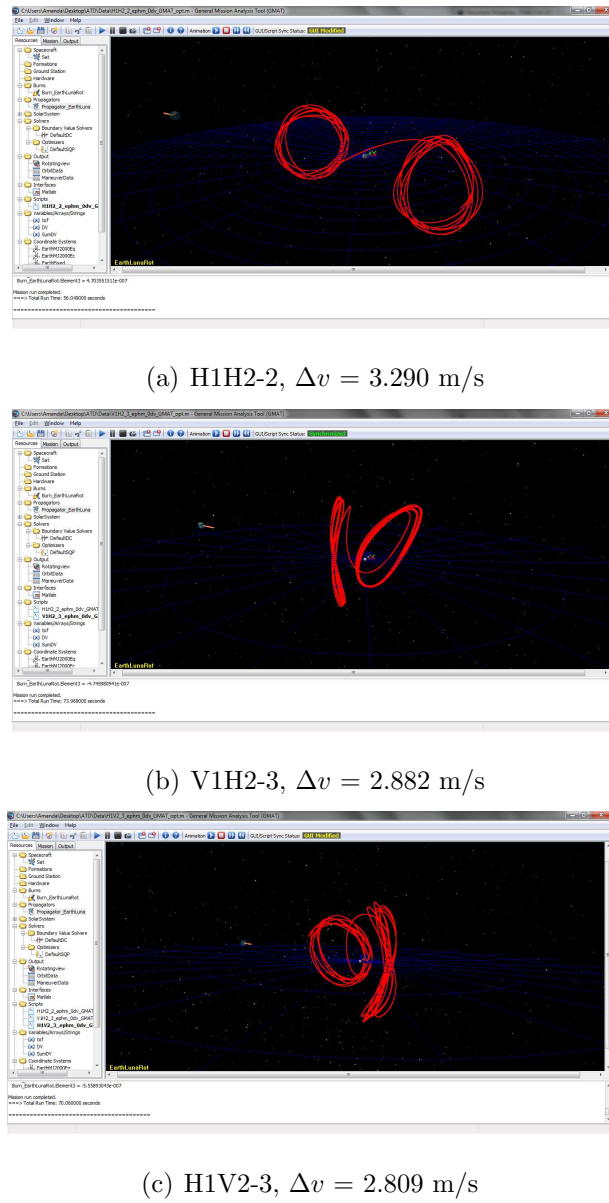


Figure 8.148. Transfers are transitioned to GMAT assuming a Sun-Earth-Moon ephemeris model with SRP

Converging the CR3BP libration point orbit transfers within an ephemeris model returns solutions that preserve the qualitative characteristics of the original transfer. The ephemeris solutions are transitioned to GMAT, demonstrating that the catalog transfers may be accessed via the currently available mission design tools. The in-

clusion of perturbations from the Sun and SRP has a small affect on the behavior of these transfers.

## 8.9 Catalog Conclusions

As a result of the computation of the catalog of transfers in the Earth-Moon system, observations are made about the relationships between transfers in the Earth-Moon CR3BP and Hill 3BP that provide insight into the existence of the transfers in the catalog. Many of the homoclinic and heteroclinic connections in the Earth-Moon catalog emerge as partners within the limiting case as  $\mu \rightarrow 0$ , and persist as  $\mu$  evolves to the Earth-Moon mass parameter value. Indeed, 66 of the 90 heteroclinic and homoclinic connections computed correspond to partner transfers. Noting that all transfers in the H3BP are associated with a partner, due to the symmetry properties of the model, a search for transfers in the H3BP is performed. Those transfers without partners in the Earth-Moon system either

1. do not exist as partners in the H3BP, and either the  $L_1$  or  $L_2$  orbit transfer emerges as  $\mu$  evolves away from 0,
2. do exist as partners in the H3BP, and either the  $L_1$  or  $L_2$  orbit transfer becomes extinct as  $\mu$  evolves away from 0, or
3. do exist as partners in the H3BP, but evolve very differently as  $\mu$  evolves away from 0 so that they no longer appear nearly symmetric in the Earth-Moon system.

For the cases considered, examples of all three causes are found to lead to the nonexistence of partner transfers in the Earth-Moon catalog, although the second cause is the most prevalent. Likewise, maneuver-free transfers between  $L_1$  and  $L_2$  orbits are available for low times-of-flight in the H3BP due to the inherent symmetries of the model. Again, evolving  $\mu$  toward the Earth-Moon system value, many of these solutions persist but require a small  $\Delta v$  to complete the transfer due to the loss of symmetry.

Automated methods to search the solution space for maneuver-free and low-cost transfers are considered in addition to a manual, interactive search. The automated

techniques explored in this investigation prove useful as a guide in the search for transfers; however, some transfers located via the manual search are not readily identified within the automated search. Thus, a combination of interactive and automated search strategies is likely most useful.

Finally, to demonstrate the applicability of employing strategies to locate transfers in the idealized CR3B model for real mission design scenarios, arbitrarily selected solutions from the Earth-Moon catalog are transitioned to a Sun-Earth-Moon ephemeris model. The qualitative characteristics associated with the CR3B solutions are well maintained in the high-fidelity model, and the inclusion of solar radiation pressure appears to have a nearly negligible effect. Thus, a preliminary investigation of solutions in the CR3BP is useful to gain insight into the available solution space. The process to transition solutions of interest to a higher-fidelity model is straightforward.

## 9. CONCLUDING REMARKS

As mission requirements become increasingly complex, tools that exploit knowledge about the available dynamics are vital. The natural dynamics that emerge in the three-body problem yield an expanded range of trajectory options, including libration point orbits and their associated invariant manifolds. These structures have been employed for a number of missions; however, incorporation of these types of solutions into a mission design is nontrivial. Poincaré maps reduce the dimension of the problem, and the incorporation of maps into trajectory design strategies improves the tractability of mission design in multi-body regimes. These maps are frequently higher-dimensional, however, and are difficult to represent visually. Thus, the focus of this investigation is an expansion of the available strategies for incorporating higher-dimensional Poincaré maps into the mission design process. Here, the results of this work are summarized and recommendations for future work are offered.

### 9.1 Incorporating Higher-Dimensional Poincaré Maps into the Trajectory Design Process

Existing techniques to employ higher-dimensional Poincaré maps for trajectory design generally serve to reduce the dimension of the map to two so that it may be represented by the projection onto a plane. To achieve this reduction in dimension, these strategies may require that additional constraints be placed on the data set. Thus, data that do not satisfy these constraints are eliminated and only a subset of the data is examined for a particular map. As an alternative, strategies to visually represent the higher-dimensional map allow the user to view the full data set simultaneously.

In this investigation, the currently available techniques to incorporate higher-dimensional maps into the design process are first explored. The techniques considered are useful to facilitate the computation of transit trajectories as well as maneuver-free transfers between libration point orbits in the spatial CR3B problem. New applications for these strategies are additionally considered. The process to design transit trajectories in the spatial problem is applied to examine the relationship between the behavior of comets that experience temporary capture by Jupiter and the invariant manifold structures associated with the collinear points in the Sun-Jupiter system. Using Poincaré maps, it is demonstrated that the behavior of these comets during temporary capture is governed by the invariant manifolds of the CR3BP. An additional application for the approach demonstrated by previous researchers is the search for periodic orbits in the spatial problem. By exploiting known symmetry properties, Poincaré maps prove useful to locate for symmetric periodic orbits and to examine their relationship to the invariant manifolds associated with libration point orbits in the vicinity of the collinear libration points.

Several of the currently available strategies to incorporate higher-dimensional Poincaré maps into the design process require that additional constraints be enforced to reduce the dimension of the map. In this investigation, techniques from the field of data visualization are employed to develop a graphical representation for higher-dimensional Poincaré maps, allowing the user to view the full data set simultaneously. Up to three coordinates may be expressed via a traditional orthographic projection. The inclusion of color allows a fourth dimension to be represented. Alternatively, glyphs, graphical objects whose physical characteristics are determined by the variables of a data set, prove useful to visualize multidimensional data. In this investigation, glyphs that serve to represent three- and four-dimensional maps are developed and are employed for transfer design applications. Rather than presenting a map as a puncture plot, crossings of a map are indicated using vectors, where the basepoint coordinates, length, and orientation of the vector serve to indicate four vari-

ables simultaneously. Such a representation is convenient because it is viewed in one plane, rather than considering orthographic projections. Thus, all of the information is represented in one image without requiring rotation of the view. Representations for higher-dimensional maps employing glyphs are demonstrated to generate transfers between libration point orbits. System transfers, in which the spacecraft departs from a libration point orbit in one three-body system and connects to an orbit in another system, are also enabled.

## 9.2 Interactive Design Environments and a Catalog of Libration Point Orbit Transfers

Representations for higher-dimensional Poincaré maps offer the opportunity for implementation within an interactive mission design environment. Such an environment offers several advantages from the perspective of mission design. Real time computation and propagation of solutions, such as invariant manifolds, enables the designer to explore the space while gaining intuition about the available solutions. The ability to simultaneously consider different design options and interactively select between them allows the user to adapt solutions based on the insight gained and to select a design that best meets the mission requirements. In this investigation, an interactive design environment is demonstrated to construct transfers between libration point orbits. Characteristics associated with the transfer are specified by the user, and various map definitions and representations may be explored. An initial guess for a transfre is located using Poincaré maps within this interactive environment, and may be passed to a is differential corrections environment. A corrections method is offered to compute a feasible transfer with a number of options available to constrain the total required  $\Delta v$ . These environments represent design modules that can be incorporated within the ongoing effort to expand trajectory design tools, and

are intended to demonstrate one possible implementation of Poincaré maps within an interactive design tool exploiting multi-body dynamics.

An interactive design environment employing Poincaré maps proves useful in the search for transfers between libration point orbits employing invariant manifolds. The lunar libration points have been proposed as destinations in the next step of the development of the human presence in space. Thus, an understanding of the available transfers between the lunar libration point orbits is useful to assess transport options to, from, and between these orbits. Employing the previously discussed interactive design tools, a catalog of transfers between orbits in the vicinity of  $L_1$  and  $L_2$  is established for the Earth-Moon system. Within this catalog, novel transfers, including maneuver-free heteroclinic and homoclinic connections, are computed between libration point orbits in the vicinity of  $L_1$  and  $L_2$ . Observations about the structure of solutions within the catalog reveals insight into the dynamics responsible for many of these transfers. Many transfers occur in “partners” consisting of one solution associated with an  $L_1$  orbit, and a second, nearly symmetric transfer associated with an  $L_2$  orbit. These partners appear to emerge from the Hill 3BP, the limiting case in which the system mass parameter approaches zero, where the  $L_1$  and  $L_2$  families of libration point orbits are symmetric. As the mass parameter evolves away from zero, many of the these transfers persist yielding partner transfers that exist for the Earth-Moon system. In addition to partners, “groupings” of transfers emerge in which many solutions appear to employ similar dynamical structures to affect the transfer. The existence of nearby periodic orbits is explored, and leads to the discovery of additional transfers between these periodic solutions and the libration point orbits considered in the catalog.

### 9.3 Recommendations for Future Work

As space exploration advances to increasingly complex dynamical regimes, continued development of tools for trajectory analysis and design is necessary. Potential areas for future research development are as follows:

- Poincaré maps are employed to analyze the behavior of comets that experience temporary capture in the vicinity of Jupiter. The analysis is performed from the perspective of invariant manifolds in the CR3BP; however, the comet path is clearly not subject to the restrictions assumed in this simplified model. For example, the Jacobi integral is not precisely maintained along a comet path, but fluctuates along the trajectory. In this investigation, Poincaré maps are defined for the Jacobi constant value associated with one particular instant along the comet path, and are employed to determine the relationship between the invariant manifolds of the CR3BP and the behavior of the comet. It may also be of interest to observe how the Poincaré map evolves with the osculating Jacobi constant value associated with the comet trajectory, and to determine if the relationship between the comet behavior and the invariant manifolds is maintained over the entire duration of temporary capture.
- Methods to reduce the dimension of higher-dimensional maps are applied to search for periodic orbits in the vicinity of the Moon. Specifically, a “perpendicular crossing” map is employed to search for quasi-periodic structures that indicate the existence of nearby stable periodic orbits. However, by the definition of the constraints associated with the perpendicular crossing map, no quasi-periodic orbit can intersect the map twice in finite time. Thus, clearly defined structures are not visible on the map. While a three-dimensional torus cannot delineate the five-dimensional space defined for a particular energy level, alternative surfaces of section should be explored in an effort to capture the dis-

tinct quasi-periodic structures that are commonly visible on Poincaré maps in the planar CR3BP.

- Further development of applications for the representation of Poincaré maps employing glyphs is of interest. The applications explored in this work include maneuver-free and low-cost connections between libration point orbits, as well as transfers between periodic orbits in different three-body systems. Thus, the maps in this investigation are employed to represent the crossings of invariant For example, glyphs are employed by Haapala and Howell [55] to represent background maps employed for the computation of transit trajectories in the spatial problem. New glyph definitions may prove useful to represent different maps, depending on the initial conditions and surface of section considered.
- Methods to represent Poincaré maps in nonautonomous sytems are of interest to observe the dynamical structures available within an ephemeris model. It is generally beneficial to develop solutions within the context of the CR3BP and transition these trajectories to a higher-fidelity model. With the ability to represent higher-dimensional maps, however, it may be of interest to explore the role of Poincaré maps in trajectory design within an ephemeris model.
- In this investigation, a catalog of maneuver-free and low-cost transfers between libration point orbits is developed within the Earth-Moon CR3BP. Many of these transfers are related to the existence of analogous transfers in the Hill three-body problem. To further explore this relationship, the development of a catalog of heteroclinic and homoclinic connections in the Hill problem would be of interest. Comparing this catalog with the available solutions in the Earth-Moon system may provide additional insight into the existence and emergence of the Earth-Moon transfers.

## LIST OF REFERENCES

## LIST OF REFERENCES

- [1] NASA, ISEE-3 Overview, [Accessed November 19, 2014].  
<http://heasarc.gsfc.nasa.gov/docs/heasarc/missions/isee3.html>
- [2] NASA, SOHO Overview, [Accessed November 19, 2014].  
<http://soho.nascom.nasa.gov/about/about.html>
- [3] NASA, Missions, [Accessed November 19, 2014].  
<http://www.nasa.gov/missions/index.html>
- [4] NASA, WMAP Mission, [Accessed November 19, 2014].  
<http://map.gsfc.nasa.gov/mission/>
- [5] ESA, Herschel and Planck Overview, [Accessed November 19, 2014].  
<http://www.esa.int/esaMI/herschelplanck/index.html>
- [6] D. Folta, and T. Sweetser, “ARTEMIS mission overview: From concept to operations,” AAS/AIAA Astrodynamics Specialist Conference, Girdwood, Alaska, July, 2011. Paper No. AAS 11-510.
- [7] IAU Minor Planet Center. <http://www.cfa.harvard.edu/iau/lists/Trojans.html>, October 2014.
- [8] G.W. Hill, Researches in the Lunar Theory, *American Journal of Mathematics*, **1**, 5–26, 1878.
- [9] J. Barrow-Green, *History of Mathematics: Poincaré and the Three Body Problem*. American Mathematical Society, Providence, Rhode Island, 1997.
- [10] V. Szebehely, *Theory of Orbits: The Restricted Problem of Three Bodies*. Academic Press, New York, United States, 1967.
- [11] C.C. Conley, Low energy transit orbits in the restricted three-body problem, *Society for Industrial and Applied Mathematics Journal on Applied Mathematics*, **16**, 732–746, 1968.
- [12] W.S. Koon, M.W. Lo, J.E. Marsden, and S.D. Ross, Heteroclinic connections between periodic orbits and resonance transitions in celestial mechanics, *Chaos*, **10**, 427–469, 2000.
- [13] G. Gómez, W.S. Koon, M.W. Lo, and J.E. Marsden, Connecting orbits and invariant manifolds in the spatial restricted three-body problem, *Nonlinearity*, **17**, 1571–1606, 2004.

- [14] A.F. Haapala, "Trajectory Design using Periapse Maps and Invariant Manifolds," M.S. Thesis, School of Aeronautics and Astronautics, Purdue University, West Lafayette, Indiana, 2010.
- [15] D. Craig Davis, "Multi-Body Trajectory Design Strategies Based on Periapsis Poincaré Maps," Ph.D. Dissertation, School of Aeronautics and Astronautics, Purdue University, West Lafayette, Indiana, 2011.
- [16] C. Froeschlé, Numerical study of dynamical systems with three degrees of freedom, *Astronomy and Astrophysics*, **4**, 115–128, 1970.
- [17] C. Froeschlé, Numerical study of a four-dimensional mapping, *Astronomy and Astrophysics*, **16**, 172–189, 1972.
- [18] L. Martinet, and P. Magnenat, Invariant surfaces and orbital behaviour in dynamical systems with 3 degrees of freedom, *Astronomy and Astrophysics*, **96**, 68–77, 1981.
- [19] G. Contopoulos, L. Martinet, and P. Magnenat, Invariant surfaces and orbital behaviour in dynamical systems with 3 degrees of freedom II, *Physica D*, **6D**, 126–136, 1982.
- [20] P.A. Patsis, and L. Zachilas, Using color and rotation for visualizing four-dimensional Poincaré cross-sections: With applications to the orbital behavior of a three-dimensional Hamiltonian system, *International Journal of Bifurcations and Chaos*, **4**, 1399–1424, 1994.
- [21] C. Geisel, "Spacecraft Orbit Design in the Circular Restricted Three-Body Problem Using Higher Dimensional Poincaré Maps," Ph.D. Dissertation, School of Aeronautics and Astronautics, Purdue University, West Lafayette, Indiana, 2013.
- [22] Á. Jorba, and J. Masdemont, Dynamics in the center manifold of the collinear points of the restricted three body problem, *Physica D*, **132**, 189–213, 1999.
- [23] G. Gómez, M. Marcote, and J.M. Mondelo, The invariant manifold structure of the spatial Hills problem,, *Dynamical Systems: An International Journal*, **20**, 115–147, 2005.
- [24] G. Gómez, W.S. Koon, M.W. Lo, and J.E. Marsden, J. Masdemont, and S.D. Ross, Invariant manifolds, the spatial three-body problem and space mission design, *AAS/AIAA Astrodynamics Specialist Conference*, Quebec City, Canada, July, 2001. Paper No. AAS 01-301.
- [25] M.E. Paskowitz and D.J. Scheeres, Robust capture and transfer trajectories for planetary satellite orbiters, *Journal of Guidance, Control, and Dynamics*, **29**, 342–353, 2006.
- [26] GSL — GNU Scientific Library, [Accessed November 26, 2014]. <http://www.gnu.org/software/gsl/>
- [27] D.C. Davis, and K.C. Howell, Trajectory evolution in the multi-body problem with applications in the Saturnian system, *Acta Astronautica*, **69**, 1038–1049, 2011.

- [28] D.C. Davis, and K.C. Howell, Characterization of trajectories near the smaller primary in the restricted problem for applications, *Journal of Guidance, Control, and Dynamics*, **35**, 116–128, 2012.
- [29] A.E. Roy, *Orbital Motion*. Institute of Physics, Bristol, United Kingdom, 2005.
- [30] A.M. Ozorio de Almeida, *Hamiltonian Systems: Chaos and Quantization*. Cambridge University Press, Cambridge, England, 1988.
- [31] J.E. Guckenheimer, L. Sirovich, and F. John, *Nonlinear Oscillations, Dynamical Systems, and Bifurcations of Vector Fields*. Springer, New York, United States, 1983.
- [32] L. Perko, *Differential Equations and Dynamical Systems*. Springer, New York, United States, 2001.
- [33] S. Wiggins, L. Wiesenfeld, C. Jaffé, and T. Uzer, Impenetrable barriers in phase-space, *Physical Review Letters*, **86**, 5478–5481, 2001.
- [34] D. Grebow, “Generating Periodic Orbits in the Circular Restricted Three-Body Problem with Applications to Lunar South Pole Coverage,” M.S. Thesis, School of Aeronautics and Astronautics, Purdue University, West Lafayette, Indiana, 2006.
- [35] V.A. Yakubovich and V.M. Starzhinskii, *Linear Differential Equations with Periodic Coefficients*, Volume 1. John Wiley & Sons, New York, United States, 1975.
- [36] B.A. Steves, A.J. Maciejewski, and M. Hendry, editors, *Chaotic Worlds: From Order to Disorder in Gravitational N-Body Dynamical Systems, II. Mathematics, Physics and Chemistry — Volume 227*. Springer & Sons, Dordrecht, The Netherlands, 2006.
- [37] T.S. Parker and L.O. Chua, *Practical Numerical Algorithms for Chaotic Systems*. Springer-Verlag, Berlin, 1989.
- [38] A.H. Nayfeh and B. Balachandran, *Applied Nonlinear Dynamics: Analytical, Computational, and Experimental Methods*. John Wiley & Sons, Inc., New York, 1995.
- [39] E.J. Doedel, R.C. Paffenroth, H.B. Keller, D.J. Dichmann, J. Galán-Vioque, and A. Vanderbauwhede, Computation of periodic solutions of conservative systems with application to the 3-body problem, *International Journal of Bifurcation and Chaos*, **13**, 2003.
- [40] E. Campbell, “Bifurcations from Families of Periodic Solutions in the Circular Restricted Problem with Application to Trajectory Design,” Ph.D. Dissertation, School of Aeronautics and Astronautics, Purdue University, West Lafayette, Indiana, 1999.
- [41] E. Castellá, and Á. Jorba, On the vertical families of two-dimensional tori near the triangular points of the bicircular problem, *Celestial Mechanics and Dynamical Astronomy*, **76**, 35–54, 2000.

- [42] K.C. Howell, and H.J. Pernicka, Numerical determination of Lissajous trajectories in the restricted three-body problem, *Celestial Mechanics*, **41**, 107–124, 1988.
- [43] E. Kolemen, J. Kasdin, P. Gurfil, Quasi-periodic orbits of the restricted three-body problem made easy, *New Trends in Astrodynamics and Applications III, AIP Conference Proceedings*, **886**, 68–77, Princeton, New Jersey, August 16–18, 2007.
- [44] Z. Olikara and D. Scheeres, Numerical method for computing quasi-periodic orbits and their stability in the restricted three-body problem, *1st IAA/AAS Conference on the Dynamics and Control of Space Systems*, Porto, Portugal, March, 2012.
- [45] B. Barden, “Application of Dynamical Systems Theory in Mission Design and Conceptual Development for Libration Point Missions,” Ph.D. Dissertation, School of Aeronautics and Astronautics, Purdue University, West Lafayette, Indiana, 2000.
- [46] G. Gómez, Á. Jorba, J. Masdemont, and C. Simó, Study of the transfer from the Earth to a halo orbit around the equilibrium point  $L_1$ , *Celestial Mechanica and Dynamical Astronomy*, **56**, 541–562, 1993.
- [47] B.F. Villac and D.J. Scheeres, Escaping trajectories in the Hill three-body problem and applications, *Journal of Guidance, Control, and Dynamics*, **26**, 224–232, 2003.
- [48] M. Hénon, Numerical exploration of the restricted three-body problem, *Academie des Sciences Paris Comptes Rendus Serie B Sciences Physiques*, **268**, 223–238, 1966.
- [49] M. Hénon, Numerical exploration of the restricted problem. V. Hill’s case: Periodic orbits and their stability, *Astronomy and Astrophysics*, **1**, 223–238, 1969.
- [50] M. Hénon, Numerical exploration of the restricted problem. VI. Hill’s case: Non-periodic orbits, *Astronomy and Astrophysics*, **9**, 24–36, 1970.
- [51] E. Barrabés, J.M. Mondelo, J.M., and M. Ollé, Numerical continuation of families of homoclinic connections of periodic orbits in the RTBP, *Nonlinearity*, **22**, 2901–2918, 2009.
- [52] E. Barrabés, J.M. Mondelo, and M., Ollé, Dynamical aspects of multi-round horseshoe-shaped homoclinic orbits in the RTBP, *Celestial Mechanics and Dynamical Astronomy*, **105**, 197–210, 2009.
- [53] J.S. Parker, K.E. Davis, and G.H. Born, Chaining periodic three-body orbits in the EarthMoon system, *Acta Astronautica*, **67**, 623–638, 2010.
- [54] A.F. Haapala, and K.C. Howell, Trajectory design using periapse Poincaré maps and invariant manifolds, *21st AAS/AIAA Space Flight Mechanics Meeting*, New Orleans, Louisiana, February, 2011. Paper No. AAS 11-131.

- [55] A.F. Haapala, and K.C. Howell, Trajectory design strategies applied to temporary comet capture including Poincaré maps and invariant manifolds, *Celestial Mechanics and Dynamical Astronomy*, **116**, 299–323, 2013.
- [56] K.C. Howell, D.C. Davis, and A.F. Haapala, Application of periapse maps for the design of trajectories near the smaller primary in multi-body regimes, *Journal of Mathematical Problems in Engineering*, Special Issue: Mathematical Methods Applied to the Celestial Mechanics of Artificial Satellites, **2012**, 1–22, 2012. DOI: <http://dx.doi.org/10.1155/2012/3517592001b>. Article ID 351759.
- [57] A. Carusi, and G.B. Valsecchi, Temporary satellite captures of comets by Jupiter, *Astronomy and Astrophysics*, **94**, 226–228, 1981.
- [58] K.C. Howell, B.G. Marchand, and M.W. Lo, Temporary satellite capture of short-period Jupiter family comets from the perspective of dynamical systems, *Journal of Astronautical Sciences*, **49**, 539–557, 2001.
- [59] E. Helin, R. Helin, B. Roman, R. Crockett, T. Seki, T. Kobayashi, K. Endate, K. Watanabe, C.Y. Shao, and D. Levy, Comet Helin-Roman-Crockett (1989b), *International Astronomical Union Circular*, **4714**, 1, 1989.
- [60] K. Ohtsuka, T. Ito, M. Yoshikawa, D.J. Asher, and H. Arakida, Quasi-Hilda comet 147P/Kushida-Muramatsu. Another long temporary satellite capture by Jupiter, *Astronomy and Astrophysics*, **489**, 1355–1362, 2008.
- [61] G. Tancredi, M. Lindgren, and H. Rickman, Temporary satellite capture and orbital evolution of comet P/Helin-Roman-Crockett, *Astronomy and Astrophysics*, **239**, 375–380, 1990.
- [62] M. Michalodimitrakis, Hill’s problem: families of three-dimensional periodic orbits (part I), *Astrophysics and Space Science*, **68**, 253–268, 1980.
- [63] M. Lara and R.P. Russell, On the family ‘g’ of the restricted three-body problem, *IX Jornadas de Trabajo en Mecánica Celeste*, Jaca, Huesca, Spain, June, 2006.
- [64] A. Inselberg, The plane with parallel coordinates, *The Visual Computer*, **1**, 69–91, 1985.
- [65] R.A. Becker, W.S. Cleveland, and M. Shyu, The visual design and control of trellis display, *Journal of Computational and Graphical Statistics*, **5**, 123–155, 1996.
- [66] K.C. Howell, and M. Kakoi, Transfers between the Earth-Moon and Sun-Earth systems using manifolds and transit orbits, *Acta Astronautica*, **59**, 367–380, 2006.
- [67] M.O. Ward, A taxonomy of glyph placement strategies for multidimensional data visualization, *Information Visualization*, **1**, 194–210, 2002.
- [68] E. Anderson, A semigraphical method for the analysis of complex problems, *Technometrics*, **2**, 387–391, 1960.
- [69] J.H. Siegel, E.J. Farrell, R.M. Goldwyn, and H.P. Friedman, The surgical implications of physiologic patterns in myocardial infarction shock, *Surgery*, **72**, 126–141, 1972.

- [70] H. Chernoff, The use of faces to represent points in k-dimensional space graphically, *Journal of the American Statistical Association*, **68**, 361–368, 1973.
- [71] R. Pickett and G. Grinstein, Iconographic displays for visualizing multidimensional data, *Proceedings IEEE Conference on Systems, Man, and Cybernetics*, **1**, 514–519, 1988.
- [72] “Motor Trend’s 1980 Car of the Year,” *Motor Trend*, **32**, 66–77, February 1980.
- [73] “Dishonorable mention: The 10 most embarrassing award winners in automotive history,” [Accessed November 13, 2014]. <http://www.caranddriver.com/features/dishonorable-mention-the-10-most-embarrassing-award-winners-in-automotive-history>
- [74] “The exploration of the Earth’s magnetosphere, An educational web site by David P. Stern and Mauricio Peredo” [Accessed November 28, 2014]. <http://www-spof.gsfc.nasa.gov/Education/whfldns.html>
- [75] W.D. Niven, editor, “On Faraday’s Lines of Force.” *The Scientific Papers of James Clerk Maxwell*. Dover Publications, Inc., New York, 1965.
- [76] R.P. Feynman, R.B. Leighton, M. Sands, *The Feynman Lectures on Physics*, Volume II. Addison-Wesley Publishing Company, Massachusetts, 1964.
- [77] A.F. Haapala, and K.C. Howell, Representations of higher-dimensional Poincaré maps with application to spacecraft trajectory design, *IAF 63rd International Astronautical Congress*, Naples, Italy, October, 2012. Paper No. IAC-12.C1.7.2.
- [78] A.F. Haapala, and K.C. Howell, Representations of higher-dimensional Poincaré maps with application to spacecraft trajectory design, *Acta Astronautica*, **96**, 23–41, 2014.
- [79] M. Vaquero, “Spacecraft Transfer Trajectory Design Exploiting Resonant Orbits in Multi-Body Environments,” Ph.D. Dissertation, School of Aeronautics and Astronautics, Purdue University, West Lafayette, Indiana, 2013.
- [80] J.J. Masdemont, High-order expansions of invariant manifolds of libration point orbits with applications to mission design, *Dynamical Systems: An International Journal*, **20**, 59–113, 2005.
- [81] J. Stuart, M. Ozimek, and K.C. Howell, Optimal, low-thrust, path-constrained transfers between libration point orbits using invariant manifolds, *AIAA/AAS Astrodynamics Specialist Conference*, Toronto, Canada, August, 2010.
- [82] J. Senent, C. Ocampo, and A. Capella, Low-thrust variable-specific-impulse transfers and guidance to unstable periodic orbits, *Journal of Guidance, Control, and Dynamics*, **28**, 280–290, 2005.
- [83] E.A. Belbruno, and J.K. Miller, Sun-perturbed Earth-to-Moon transfers with ballistic capture, *Journal of Guidance, Control, and Dynamics*, **16**, 770–775, 1993.
- [84] M.W. Lo, B.G. Williams, W.E. Bollman, D. Han, Y. Hahn, J.L. Bell, E.A. Hirst, R.A. Corwin, P.E. Hong, K.C. Howell, B. Barden, and R. Wilson, Genesis mission design, *The Journal of the Astronautical Sciences*, **49**, 169–184, 2001.

- [85] W.S. Koon, M.W. Lo, J.E. Marsden, and S.D. Ross, Shoot the Moon, *AAS/AIAA Space Flight Mechanics Meeting*, Clearwater, Florida, January, 2000. Paper No. AAS 00-166.
- [86] W.S. Koon, M.W. Lo, J.E. Marsden, and S.D. Ross, Low energy transfer to the Moon, *Celestial Mechanics and Dynamical Astronomy*, **81**, 63–73, 2001.
- [87] W.S. Koon, M.W. Lo, J.E. Marsden, and S.D. Ross, Constructing a low energy transfer between Jovian moons, *Contemporary Mathematics*, **292**, 129–145, 2002.
- [88] J.S. Parker, and M.W. Lo, Shoot the Moon 3D, *AAS/AIAA Astrodynamics Specialist Conference*, Lake Tahoe, California, August 2005. Paper No. AAS 05-383.
- [89] W.M. Folkner, J.G. Williams, and D.H. Boggs, “The Planetary and Lunar Ephemeris DE 421,” IPN Progress Report 42-178, August 15, 2009.
- [90] T.A. Pavlak, “Trajectory Design and Orbit Maintenance Strategies in Multi-Body Dynamical Regimes,” Ph.D. Dissertation, School of Aeronautics and Astronautics, Purdue University, West Lafayette, Indiana, 2013.
- [91] K.C. Howell, and J.P. Anderson, “Generator’s User’s Guide, Version 3.0.2,” IOM AAE-0140-012, July, 2001.
- [92] K.C. Howell, and J.J. Guzmán, “Generator,” IOM AAE-0140-010, 2001.
- [93] M. Lo, “LTool Version 1.0G Delivery,” JPL, IOM 00-2147, September, 2000.
- [94] J.M. Mondelo, E. Barrabés, G. Gómez, and M. Ollé, “Numerical parametrizations of libration point trajectories and their invariant manifolds,” 23rd AAS/AIAA Space Flight Mechanics Meeting, Kauai, Hawaii, February, 2013. Paper No. AAS 07-321.
- [95] E.J. Doedel, and B.E. Oldeman, “AUTO-07P: Continuation and bifurcation software for ordinary differential equations,” January, 2012.
- [96] W. Schlei, “An Application of Visual Analytics to Spacecraft Trajectory Design,” M.S. Thesis, School of Aeronautics and Astronautics, Purdue University, West Lafayette, Indiana, 2011.
- [97] A.F. Haapala, M. Vaquero, T.A. Pavlak, K.C. Howell, and D.C. Folta, Trajectory selection strategy for tours in the Earth-Moon system, *AAS/AIAA Astrodynamics Specialist Conference*, Hilton Head, South Carolina, August 10–15, 2013. Paper No. AAS 13-782.
- [98] D. Folta, N. Bosanac, D. Guzzetti, and K. Howell, An Earth-Moon system trajectory design reference catalog, *Acta Astronautica*, in press, 2014. DOI <http://www.sciencedirect.com/science/article/pii/S0094576514002938>
- [99] D. Guzzetti, N. Bosanac, and K.C. Howell, A framework for efficient trajectory comparison in the Earth-Moon design space, *AIAA/AAS Astrodynamics Specialist Conference*, San Diego, CA, August 4–7, 2014.

- [100] M.W. Lo, and S.D. Ross, “The Lunar L1 gateway: Portal to the stars and beyond,” AIAA Space Conference and Exposition, Albuquerque, New Mexico, August, 2001.
- [101] J.M. Mondelo, M. Ollé, P.A. de Sousa-Silva, and M.O. Terra, “Families of heteroclinic connections Between quasi-periodic libration point trajectories,” 65th International Astronautical Congress, Toronto, Canada, September, 2014. Paper No. IAC-14-C1.1.9.
- [102] D.J. Conway, and S.P. Hughes, “The General Mission Analysis Tool (GMAT): Current Features and Adding Custom Functionality,” 4th International Conference on Astrodynamical Tools and Techniques, Madrid, Spain, May, 2010.
- [103] General Mission Analysis Tool Wiki, [Accessed August 1, 2013]. [GMATcentral.org](http://GMATcentral.org).

## APPENDICES

## A. DERIVING THE CR3B EQUATIONS OF MOTION

In this section, the equations of motion associated with the Circular Restricted Three-Body Problem are derived with respect to the rotating frame.

Recall the equations of motion for the Circular Restricted Three-Body Problem, as written in the inertial frame:

$$\bar{R}'' = -\frac{Gm_1}{R_{13}^3}\bar{R}_{13} - \frac{Gm_2}{R_{23}^3}\bar{R}_{23}, \quad (\text{A.1})$$

where  $\bar{R} = X\hat{X} + Y\hat{Y} + Z\hat{Z} = x_d\hat{x} + y_d\hat{y} + z_d\hat{z}$ , and  $x_d = x\ell^*$ ,  $y_d = y\ell^*$ ,  $z_d = z\ell^*$ ,  $x'_d = \dot{x}\frac{\ell^*}{t^*}$ ,  $y'_d = \dot{y}\frac{\ell^*}{t^*}$ ,  $z'_d = \dot{z}\frac{\ell^*}{t^*}$ . The derivatives of  $\bar{R}$  with respect to the inertial and rotating frames are related in terms of rotating frame coordinates as follows:

$$\bar{R}'_I = \bar{R}'_R + \theta'\hat{z} \times \bar{R}, \quad (\text{A.2})$$

$$= [x'_d, y'_d, z'_d]^T + [-\theta'y_d, \theta'x_d, 0]^T, \quad (\text{A.3})$$

$$= [x'_d - \theta'y_d, y'_d + \theta'x_d, z'_d]^T, \quad (\text{A.4})$$

where  $\theta = N\tau$  and  $\theta' = N$ . Similarly, the second derivatives of  $\bar{R}$  with respect to the inertial and rotating frames are related as follows:

$$\bar{R}''_I = \bar{R}''_R + \theta'\hat{z} \times \bar{R}'_I, \quad (\text{A.5})$$

$$= [x''_d - \theta'y'_d, y''_d + \theta'x'_d, z''_d]^T + \theta' \cdot [-y'_d - \theta'x_d, x'_d - \theta'y_d, 0]^T, \quad (\text{A.6})$$

$$= [x''_d - 2\theta'y'_d - \theta'^2x, y''_d + 2\theta'x'_d + -\theta'^2y, z''_d]^T. \quad (\text{A.7})$$

The expression in equation (A.1) is written in terms of rotating frame coordinates as

$$\bar{R}''_I = -\frac{Gm_1}{R_{13}^3} \cdot [x_d + \mu\ell^*, y_d, z_d]^T - \frac{Gm_2}{R_{23}^3} \cdot [x_d - (1-\mu)\ell^*, y_d, z_d]^T. \quad (\text{A.8})$$

Then, solving for  $\bar{R}_R''$  yields the dimensional equations of motion

$$x_d'' - 2\theta'y_d' - \theta'^2x = -\frac{Gm_1}{R_{13}^3}(x_d + \mu\ell^*) - \frac{Gm_2}{R_{23}^3}(x_d - (1 - \mu)\ell^*), \quad (\text{A.9})$$

$$y_d'' + 2\theta'x_d' - \theta'^2y = -\frac{Gm_1}{R_{13}^3}y_d - \frac{Gm_2}{R_{23}^3}y_d, \quad (\text{A.10})$$

$$z_d'' = -\frac{Gm_1}{R_{13}^3}z_d - \frac{Gm_2}{R_{23}^3}z_d. \quad (\text{A.11})$$

The nondimensional equations of motion are obtained by dividing both sides of equations (A.9) by the quantity  $\frac{\ell^*}{t^{*2}}$  as follows:

$$\ddot{\tilde{r}} = (\ddot{x} - 2\dot{y} - x)\hat{x} + (\ddot{y} + 2\dot{x} - y)\hat{y} + \ddot{z}\hat{z}. \quad (\text{A.12})$$

$$\ddot{x} = 2\dot{\theta}\dot{y} + \dot{\theta}^2x - \frac{(1 - \mu)(x + \mu)}{r_{13}^3} - \frac{\mu(x - (1 - \mu))}{r_{23}^3}, \quad (\text{A.13})$$

$$\ddot{y} = -2\dot{\theta}\dot{x} + \dot{\theta}^2y - \frac{(1 - \mu)y}{r_{13}^3} - \frac{\mu y}{r_{23}^3}, \quad (\text{A.14})$$

$$\ddot{z} = -\frac{(1 - \mu)z}{r_{13}^3} - \frac{\mu z}{r_{23}^3}. \quad (\text{A.15})$$

## B. DERIVING THE JACOBI CONSTANT

### B.1 Derivation of the Jacobi Integral

To obtain a relationship between the Jacobi constant and the Hamiltonian, it is necessary to derive the expression for the Jacobi constant. The following derivation is based on that presented by Szebehely [10]:

$$\begin{aligned}\dot{x}\ddot{x} + \dot{y}\ddot{y} + \dot{z}\ddot{z} &= \Omega_x\dot{x} + \Omega_y\dot{y} + \Omega_z\dot{z}, \\ \frac{1}{2}\frac{d}{dt}(\dot{x}^2 + \dot{y}^2 + \dot{z}^2) &= \Omega_x\frac{dx}{dt} + \Omega_y\frac{dy}{dt} + \Omega_z\frac{dz}{dt}, \\ \frac{1}{2}d(\dot{x}^2 + \dot{y}^2 + \dot{z}^2) &= \Omega_x dx + \Omega_y dy + \Omega_z dz \\ \frac{1}{2}v^2 &= \Omega(x, y, z) - \frac{1}{2}C, \\ C &= 2\Omega(x, y, z) - v^2.\end{aligned}$$

Recall the following expression for the Hamiltonian associated with the CR3BP,

$$H = \frac{1}{2}v^2 - \Omega(x, y, z). \quad (\text{B.1})$$

Thus, the relationship between the Hamiltonian function and Jacobi constant is  $H = -\frac{1}{2}C$ .

## B.2 Second Partial Derivatives of the Pseudo-Potential

The second partial derivatives of the pseudo-potential function are as follows,

$$\Omega_{xx} = 1 - \frac{(1-\mu)}{r_{13}^3} - \frac{\mu}{r_{23}^3} + \frac{3(1-\mu)(x+\mu)^2}{r_{13}^5} + \frac{3\mu(x-1+\mu)^2}{r_{23}^5}, \quad (\text{B.2})$$

$$\Omega_{xy} = \frac{3(1-\mu)(x+\mu)y}{r_{13}^5} + \frac{3\mu(x-1+\mu)y}{r_{23}^5}, \quad (\text{B.3})$$

$$\Omega_{xz} = \frac{3(1-\mu)(x+\mu)z}{r_{13}^5} + \frac{3\mu(x-1+\mu)z}{r_{23}^5}, \quad (\text{B.4})$$

$$\Omega_{yy} = 1 - \frac{(1-\mu)}{r_{13}^3} - \frac{\mu}{r_{23}^3} + \frac{3(1-\mu)y^2}{r_{13}^5} + \frac{3\mu y^2}{r_{23}^5}, \quad (\text{B.5})$$

$$\Omega_{yx} = \Omega_{xy}, \quad (\text{B.6})$$

$$\Omega_{yz} = \frac{3(1-\mu)yz}{r_{13}^5} + \frac{3\mu yz}{r_{23}^5}, \quad (\text{B.7})$$

$$\Omega_{zz} = -\frac{(1-\mu)}{r_{13}^3} - \frac{\mu}{r_{23}^3} + \frac{3(1-\mu)z^2}{r_{13}^5} + \frac{3\mu(x-1+\mu)^2}{r_{23}^5}, \quad (\text{B.8})$$

$$\Omega_{zx} = \Omega_{xz}, \quad (\text{B.9})$$

$$\Omega_{zy} = \Omega_{yz}. \quad (\text{B.10})$$

These functions are necessary to compute the linear equations of motion relative to the libration points.

## C. EIGENSTRUCTURE ASSOCIATED WITH THE LIBRATION POINTS

### C.1 Eigenvalues Associated with the Collinear Points

From the linear system described in Section 3.1 by equation (3.2), with matrix  $A$  defined by equations (3.6), (3.7), the following characteristic polynomial is computed,

$$(\lambda^2 - \Omega_{zz0}) (\lambda^4 + (4 - \Omega_{xx0} - \Omega_{yy0})\lambda^2 + (\Omega_{xx0}\Omega_{yy0} - \Omega_{xy0}^2)) = 0. \quad (\text{C.1})$$

To gain insight into the stability of the collinear points, more information about the terms in equation (C.1) is required. In particular, the signs of the terms  $\Omega_{xx0}$ ,  $\Omega_{yy0}$  and  $\Omega_{zz0}$  must be determined, where the expressions for  $\Omega_{pq}$  are summarized in equations (B.2)–(B.10), and  $\Omega_{pq0}$  indicates that the partial derivative  $\frac{\partial^2 \Omega}{\partial p \partial q}$  is evaluated at the equilibrium point of interest. Clearly the term  $\Omega_{zz0}$  is negative for each of the five libration points, thus, two roots of equation (C.1) are

$$\lambda_5 = i\omega = \sqrt{\Omega_{zz0}}, \quad (\text{C.2})$$

$$\lambda_6 = -i\omega = -\sqrt{\Omega_{zz0}}. \quad (\text{C.3})$$

Examining the expressions for  $\Omega_{xx}$  and  $\Omega_{yy}$ , from equations (B.2), (B.5), respectively, it is clear that, at the collinear libration points, these expressions are reduced to the form

$$\Omega_{xx}(x, 0) = 1 + \frac{2(1-\mu)}{r_{13}^3} + \frac{2\mu}{r_{23}^3}, \quad (\text{C.4})$$

$$\Omega_{yy}(x, 0) = 1 - \frac{(1-\mu)}{r_{13}^3} - \frac{\mu}{r_{23}^3}, \quad (\text{C.5})$$

and it is readily apparent that  $\Omega_{xx0} > 0$ . Now, the terms  $\Omega_{yy0}$  for each of the collinear points are evaluated separately to determine the sign of for each. In the following

discussions, recall that the libration points are defined such that  $\Omega_{x0} = \Omega_{y0} = \Omega_{z0} = 0$ , where  $\Omega_{q0}$  is the partial derivative  $\frac{\partial\Omega}{\partial q}$ , given in equations (2.18)–(2.20), evaluated at the equilibrium point. The subsequent results are based on discussions by Szebehely in his *Theory of Orbits: The Restricted Problem of Three Bodies* [10].

### The $L_1$ and $L_2$ Points

For collinear points  $L_1$  and  $L_2$ , the radial distances to the primaries are  $r_{13} = x + \mu$  and  $r_{23} = x - 1 + \mu < 1$ . Then,

$$\Omega_{x0} = 0 = x - \frac{(1 - \mu)}{r_{13}^2} - \frac{\mu}{r_{23}^2}, \quad (\text{C.6})$$

$$\frac{(1 - \mu)}{r_{13}^2} = x - \frac{\mu}{r_{23}^2}, \quad (\text{C.7})$$

and  $\Omega_{yy}(x, 0)$  is expressed as follows,

$$\Omega_{yy}(x, 0) = 1 - \frac{1}{r_{13}} \left( x - \frac{\mu r_{23}}{r_{23}^3} + \frac{\mu r_{13}}{r_{23}^3} \right), \quad (\text{C.8})$$

$$= 1 - \frac{1}{r_{13}} \left( x + \frac{\mu}{r_{23}^3} \right). \quad (\text{C.9})$$

Substituting  $x = r_{13} - \mu$ , this expression reduces to the form

$$\Omega_{yy0} = \frac{\mu}{r_{13}} \left( 1 - \frac{1}{r_{23}^3} \right), \quad (\text{C.10})$$

and, because  $r_{23} < 1$ ,  $\Omega_{yy} < 0$  at the both  $L_1$  and  $L_2$  collinear points.

### The $L_3$ Point

For  $L_3$ , the radial distance to each of the primaries is  $r_{13} = -(x + \mu)$  and  $r_{23} = -(x - 1 + \mu) > 1$ . Then,

$$\Omega_{x0} = 0 = x + \frac{(1 - \mu)}{r_{13}^2} + \frac{\mu}{r_{23}^2}, \quad (\text{C.11})$$

$$\frac{(1 - \mu)}{r_{13}^2} = - \left( x + \frac{\mu}{r_{23}^2} \right), \quad (\text{C.12})$$

and  $\Omega_{yy}(x, 0)$  is, then, expressed as follows,

$$\Omega_{yy}(x, 0) = 1 - \frac{1}{r_{13}} \left( -x - \frac{\mu r_{23}}{r_{23}^3} + \frac{\mu r_{13}}{r_{23}^3} \right) \quad (\text{C.13})$$

$$= 1 - \frac{1}{r_{13}} \left( -x - \frac{\mu}{r_{23}^3} \right). \quad (\text{C.14})$$

Substituting  $x = -(r_{13} + \mu)$ , this expression reduces to the form

$$\Omega_{yy0} = \frac{\mu}{r_{13}} \left( \frac{1}{r_{23}^3} - 1 \right),$$

and, because  $r_{23} > 1$ ,  $\Omega_{yy} < 0$  at  $L_3$ .

Thus,  $\Omega_{xx0} > 0$  and  $\Omega_{yy0} < 0$  for each of the collinear libration points. The roots for equation (C.1) associated with out-of-plane motion are given by equations (C.2)–(C.3). Recalling that, for the collinear points,  $\Omega_{xy0} = \Omega_{yx0} = 0$ , the characteristic polynomial of the planar variational equations of motion is written

$$\Lambda^2 + (4 - \Omega_{xx0} - \Omega_{yy0})\Lambda + (\Omega_{xx0}\Omega_{yy0} - \Omega_{xy0}^2) = 0, \quad (\text{C.15})$$

where  $\Lambda = \rho^2$ . Define the following quantities,

$$\beta_1 = 2 - \frac{\Omega_{xx0} + \Omega_{yy0}}{2}, \quad (\text{C.16})$$

$$\beta_2 = \sqrt{-\Omega_{xx0}\Omega_{yy0}} > 0. \quad (\text{C.17})$$

The roots of equation (C.15) are

$$\Lambda_1 = -\beta_1 + \sqrt{\beta_1^2 + \beta_2^2} > 0, \quad (\text{C.18})$$

$$\Lambda_2 = -\beta_1 - \sqrt{\beta_1^2 + \beta_2^2} < 0, \quad (\text{C.19})$$

and the eigenvalues associated with the collinear points are

$$\lambda_1 = \rho = \sqrt{\Lambda_1}, \quad (\text{C.20})$$

$$\lambda_2 = -\rho = -\sqrt{\Lambda_1}, \quad (\text{C.21})$$

$$\lambda_3 = i\nu = \sqrt{\Lambda_2}, \quad (\text{C.22})$$

$$\lambda_4 = -i\nu = -\sqrt{\Lambda_2}. \quad (\text{C.23})$$

Of course, the eigenvectors associated with  $\lambda_{1-6}$  are obtained by solving the equation  $A\bar{v}_i = \lambda_i\bar{v}_i$ .

## C.2 General Solution for a Center

For a linear system,  $\dot{\bar{x}} = A\bar{x}$ , with eigenvalues  $\pm\rho$ , such that  $\rho \in \mathbb{C}$ , consider a solution of the form

$$\bar{x}(t) = \alpha e^{\rho t} \bar{v} + \alpha^* e^{\rho^* t} \bar{v}^*, \quad (\text{C.24})$$

where  $q^*$  denotes the complex conjugate of  $q$ . Define  $\alpha_1 = \text{Real}(\alpha)$ ,  $\alpha_2 = \text{Imag}(\alpha)$ ,  $a = \text{Real}(\rho)$ ,  $b = \text{Imag}(\rho)$ ,  $\bar{u} = \text{Real}(\bar{v})$ ,  $\bar{w} = \text{Imag}(\bar{v})$ , such that  $\alpha = \alpha_1 + i\alpha_2$ ,  $\rho = a + ib$  and  $\bar{v} = \bar{u} + i\bar{w}$ . Then, the terms in equation (C.24) are substituted as follows,

$$\bar{x}(t) = e^{at}[(\alpha_1 + i\alpha_2)(\cos(bt) + i \sin(bt))(\bar{u} + i\bar{w}) + \quad (\text{C.25})$$

$$(\alpha_1 - i\alpha_2)(\cos(bt) - i \sin(bt))(\bar{u} - i\bar{w})]. \quad (\text{C.26})$$

Expanding this expression, the imaginary terms cancel yielding

$$\bar{x}(t) = 2e^{at}[\alpha_1(\cos(bt)\bar{u} - \sin(bt)\bar{w}) - \alpha_2(\sin(bt)\bar{u} + \cos(bt)\bar{w})]. \quad (\text{C.27})$$

Thus, the general solution described by equation (C.24) is equivalent to the expression

$$\bar{x}(t) = 2\text{Real}(\alpha e^{\rho t} \bar{v}), \quad (\text{C.28})$$

and is elliptical in nature.

## C.3 General Solution for a Saddle Point

For an  $n$ -dimensional linear system,  $\dot{\bar{x}} = A\bar{x}$ , with eigenvalues  $\pm\rho$ , such that  $\rho \in \mathbb{R}$ , consider a solution of the form

$$\bar{x}(t) = \alpha e^{\rho t} \bar{v} + \alpha' e^{-\rho t} \bar{v}', \quad (\text{C.29})$$

Define  $\alpha = \alpha_1 + \alpha_2$ ,  $\alpha_{1,2} \in \mathbb{R}$ , and  $\bar{v} = \bar{u} + \bar{w}$ ,  $\bar{u}, \bar{w} \in \mathbb{R}^n$ . Then,  $\alpha' = \alpha_1 - \alpha_2$ , and  $\bar{v}' = \bar{u} - \bar{w}$ . Then, the terms of equation (C.29) are substituted as follows,

$$\bar{x}(t) = (\alpha_1 + \alpha_2)(\cosh(\rho t) + \sinh(\rho t))(\bar{u} + \bar{w}) + \quad (C.30)$$

$$(\alpha_1 - \alpha_2)(\cosh(\rho t) - \sinh(\rho t))(\bar{u} - \bar{w}), \quad (C.31)$$

$$= (\alpha_1 + \alpha_2)(\cosh(\rho t)\bar{u} - \sinh(\rho t)\bar{w} + \sinh(\rho t)\bar{u} + \cosh(\rho t)\bar{w}) + \quad (C.32)$$

$$(\alpha_1 - \alpha_2)(\cosh(\rho t)\bar{u} + \sinh(\rho t)\bar{w} - \sinh(\rho t)\bar{u} - \cosh(\rho t)\bar{w}), \quad (C.33)$$

$$= 2\alpha_1(\cosh(\rho t)\bar{u} + \sinh(\rho t)\bar{w}) + 2\alpha_2(\sinh(\rho t)\bar{u} + \cosh(\rho t)\bar{w}), \quad (C.34)$$

and is hyperbolic in nature.

## D. HILL'S THREE-BODY PROBLEM

### D.1 Deriving Hill's Equations of Motion

In this section, the equations of motion associated with Hill's three-body problem (H3BP) are derived, following Szebehely [10]. The derivation of the H3BP equations of motion begins from the CR3BP, where a shift in coordinates translates the rotating frame so that it is centered at the smaller primary. Then, it proves useful to scale the distance unit of the coordinates by a factor of  $\mu^\alpha$ . Selecting  $\alpha = \frac{1}{3}$ , the gravitational terms from the smaller primary are reduced so that they are no longer a function of the mass parameter. Finally, allowing  $\mu \rightarrow 0$ , the Hill equations of motion are obtained.

The previously derived Circular Restricted Three-Body Problem equations of motion are written as

$$\ddot{x} = 2\dot{y} + x - \frac{(1-\mu)(x+\mu)}{r_{13}^3} - \frac{\mu(x-1+\mu)}{r_{23}^3}, \quad (\text{D.1})$$

$$\ddot{y} = -2\dot{x} + y - \frac{(1-\mu)y}{r_{13}^3} - \frac{\mu y}{r_{23}^3}, \quad (\text{D.2})$$

$$\ddot{z} = -\frac{(1-\mu)z}{r_{13}^3} - \frac{\mu z}{r_{23}^3}, \quad (\text{D.3})$$

where  $r_{13} = \sqrt{(x+\mu)^2 + y^2 + z^2}$  and  $r_{23} = \sqrt{(x-1+\mu)^2 + y^2 + z^2}$ . The coordinates are redefined relative to the smaller primary,  $P_2$ , so that  $x_2 = x - 1 + \mu$ ,  $y_2 = y$ ,  $z_2 = z$ . The resulting equations are

$$\ddot{x}_2 = 2\dot{y}_2 + x_2 + (1-\mu) - \frac{(1-\mu)(x_2+1)}{r_{13}^3} - \frac{\mu x_2}{r_{23}^3}, \quad (\text{D.4})$$

$$\ddot{y}_2 = -2\dot{x}_2 + y_2 - \frac{(1-\mu)y_2}{r_{13}^3} - \frac{\mu y_2}{r_{23}^3}, \quad (\text{D.5})$$

$$\ddot{z}_2 = -\frac{(1-\mu)z_2}{r_{13}^3} - \frac{\mu z_2}{r_{23}^3}. \quad (\text{D.6})$$

Here,  $r_{13} = \sqrt{(x_2 + 1)^2 + y_2^2 + z_2^2}$  and  $r_{23} = \sqrt{x_2^2 + y_2^2 + z_2^2}$ . Next, the variables are rescaled such that  $\xi = x_2/\mu^\alpha$ ,  $\eta = y_2/\mu^\alpha$ , and  $\zeta = z_2/\mu^\alpha$ . The scaled equations of motion are given as

$$\ddot{\xi} = 2\dot{\eta} + \xi + (1 - \mu)\mu^{-\alpha} - \frac{(1 - \mu)(\mu^\alpha\xi + 1)\mu^{-\alpha}}{r_{13}^3} - \frac{\mu^{1-3\alpha}\xi}{r^3}, \quad (\text{D.7})$$

$$\ddot{\eta} = -2\dot{\xi} + \eta - \frac{(1 - \mu)\eta}{r_{13}^3} - \frac{\mu^{1-3\alpha}\eta}{r^3}, \quad (\text{D.8})$$

$$\ddot{\zeta} = -\frac{(1 - \mu)\zeta}{r_{13}^3} - \frac{\mu^{1-3\alpha}\zeta}{r^3}, \quad (\text{D.9})$$

where  $r_{13} = \sqrt{(\mu^\alpha\xi + 1)^2 + \mu^{2\alpha}\eta^2 + \mu^{2\alpha}\zeta^2}$ ,  $r_{23} = \mu^{3\alpha}\sqrt{\xi^2 + \eta^2 + \zeta^2}$ , and

$r = \sqrt{\xi^2 + \eta^2 + \zeta^2}$ . Selecting the value of  $\alpha$  to be  $1/3$ , the  $P_2$  gravitational acceleration terms reduce to  $\frac{\xi}{r^3}$ ,  $\frac{\eta}{r^3}$ , and  $\frac{\zeta}{r^3}$  and are no longer a function of the mass parameter  $\mu$ . Assuming  $\alpha = \frac{1}{3}$ , the equations are written as

$$\ddot{\xi} = 2\dot{\eta} + \xi + (1 - \mu)\mu^{-\frac{1}{3}} - \frac{(1 - \mu)(\xi + \mu^{-\frac{1}{3}})}{r_{13}^3} - \frac{\xi}{r^3}, \quad (\text{D.10})$$

$$\ddot{\eta} = -2\dot{\xi} + \eta - \frac{(1 - \mu)\eta}{r_{13}^3} - \frac{\eta}{r^3}, \quad (\text{D.11})$$

$$\ddot{\zeta} = -\frac{(1 - \mu)\zeta}{r_{13}^3} - \frac{\zeta}{r^3}, \quad (\text{D.12})$$

where  $r_{13} = \sqrt{\mu^{\frac{2}{3}}r^2 + 2\mu^{\frac{1}{3}}\xi + 1}$ .

At this step in the derivation, the coordinates are shifted and scaled but no assumptions are made that alter the dynamics from the original CR3BP. The final step in the derivation is to take the limit of equations (D.10)–(D.12) as  $\mu \rightarrow 0$ . The mass parameter appears in the third and fourth terms in equation (D.10). Consider the binomial expansion  $(1 + a)^n = [1 + na + \frac{n(n-1)}{2!}a^2 + \frac{n(n-1)(n-2)}{3!}a^3 + \dots]$ . Recalling that  $r_{13} = \sqrt{\mu^{\frac{2}{3}}r^2 + 2\mu^{\frac{1}{3}}\xi + 1}$ ,  $r_{13}^3$  is represented by the expansion

$$r_{13}^3 = \left[ 1 + \frac{3}{2}(\mu^{\frac{2}{3}}r^2 + 2\mu^{\frac{1}{3}}\xi) + \frac{3}{8}(\mu^{\frac{2}{3}}r^2 + 2\mu^{\frac{1}{3}}\xi)^2 + \dots \right].$$

Clearly, all higher-order terms in the expansion are multiples of  $\mu$  and the limit of  $r_{13}^3$  is unity as  $\mu \rightarrow 0$ . Computing the limit of equation (D.10) as  $\mu \rightarrow 0$  from the individual terms yields

$$\begin{aligned} \lim_{\mu \rightarrow 0} \left[ (1 - \mu)\mu^{-\frac{1}{3}} - \frac{(1-\mu)(\xi + \mu^{-\frac{1}{3}})}{r_{13}^3} \right] &= \\ \lim_{\mu \rightarrow 0} \left[ -\frac{(1-\mu)\xi}{r_{13}^3} + \frac{(1-\mu)}{r_{13}^3} \frac{(r_{13}^3 - 1)}{\mu^{\frac{1}{3}}} \right] &= \\ \lim_{\mu \rightarrow 0} \left[ -\frac{(1-\mu)\xi}{r_{13}^3} + \frac{(1-\mu)}{r_{13}^3} \frac{(1 + [\frac{3}{2}(\mu^{\frac{2}{3}}r^2 + 2\mu^{\frac{1}{3}}\xi) + \frac{3}{8}(\mu^{\frac{2}{3}}r^2 + 2\mu^{\frac{1}{3}}\xi)^2 + \dots] - 1)}{\mu^{\frac{1}{3}}} \right] &= \\ -\xi + 3\xi. \end{aligned}$$

Considering equations (D.11) and (D.12), the mass parameter appears in the third and first terms, respectively. Taking the limit of these terms as  $\mu \rightarrow 0$  yields

$$\begin{aligned} \lim_{\mu \rightarrow 0} -\frac{(1-\mu)\eta}{r_{13}^3} &= -\eta, \\ \lim_{\mu \rightarrow 0} -\frac{(1-\mu)\zeta}{r_{13}^3} &= -\zeta. \end{aligned}$$

Thus, the equations of motion for Hill's problem are written as

$$\ddot{\xi} = 2\dot{\eta} + 3\xi - \frac{\xi}{r^3}, \quad (\text{D.13})$$

$$\ddot{\eta} = -2\dot{\xi} - \frac{\eta}{r^3}, \quad (\text{D.14})$$

$$\ddot{\zeta} = -\zeta - \frac{\zeta}{r^3}. \quad (\text{D.15})$$

## D.2 Equilibrium Points and the Jacobi Constant

The search for equilibrium points of equations (D.13)–(D.15) yields two libration points. Clearly, from equations (D.14)–(D.15),  $\eta = \zeta = 0$  for all equilibrium solutions. Solving for the  $\xi$ -locations corresponding to equilibrium yields  $\xi = \pm 3^{(-1/3)}$ . Thus, the  $L_1$  and  $L_2$  points are the only libration points for the H3BP and are located at  $(-3^{(-1/3)}, 0, 0)$  and  $(3^{(-1/3)}, 0, 0)$ , respectively. From the locations of the libration points, the Hill radius is defined as  $r_H = 3^{(-1/3)}$ . Note that this is a dimensionless quantity.

The Jacobi integral is derived for the H3BP following the same steps, demonstrated in Appendix B.1, as for the CR3BP. Define  $\tilde{\Omega} = \frac{3}{2}\xi^2 - \frac{1}{2}\zeta^2 + \frac{1}{r}$  as the pseudo-potential function for the Hill problem. Then, the equations of motion (D.13)–(D.15) may be rewritten as

$$\ddot{\xi} = 2\dot{\eta} + \tilde{\Omega}_\xi, \quad (\text{D.16})$$

$$\ddot{\eta} = -2\dot{\xi} + \tilde{\Omega}_\eta, \quad (\text{D.17})$$

$$\ddot{\zeta} = -\zeta + \tilde{\Omega}_\zeta, \quad (\text{D.18})$$

where  $\tilde{\Omega}_q = \frac{\partial \tilde{\Omega}}{\partial q}$  represents the partial derivative of the pseudo-potential function with respect to a variable  $q$ . Following the derivation in Appendix B.1 for the H3BP equations of motion yields

$$\begin{aligned} \dot{\xi}\ddot{\xi} + \dot{\eta}\ddot{\eta} + \dot{\zeta}\ddot{\zeta} &= \tilde{\Omega}_\xi \dot{\xi} + \tilde{\Omega}_\eta \dot{\eta} + \tilde{\Omega}_\zeta \dot{\zeta}, \\ \frac{1}{2} \frac{d}{dt} \left( \dot{\xi}^2 + \dot{\eta}^2 + \dot{\zeta}^2 \right) &= \tilde{\Omega}_\xi \frac{d\xi}{dt} + \tilde{\Omega}_\eta \frac{d\eta}{dt} + \tilde{\Omega}_\zeta \frac{d\zeta}{dt}, \\ \frac{1}{2} d \left( \dot{\xi}^2 + \dot{\eta}^2 + \dot{\zeta}^2 \right) &= \tilde{\Omega}_\xi d\xi + \tilde{\Omega}_\eta d\eta + \tilde{\Omega}_\zeta d\zeta, \\ \frac{1}{2} \tilde{v}^2 &= \tilde{\Omega}(\xi, \eta, \zeta) - \frac{1}{2} \tilde{C} \\ \tilde{C} &= 2\tilde{\Omega}(\xi, \eta, \zeta) - \tilde{v}^2, \end{aligned}$$

where  $\tilde{v}^2 = (\dot{\xi}^2 + \dot{\eta}^2 + \dot{\zeta}^2)$ . Thus, The Jacobi integral is of the same form for the H3BP and the CR3BP, with differing pseudo-potential functions.

### D.3 Symmetry Properties

Inherent in the equations of motion associated with Hill's problem is a symmetry across the  $\eta$ -axis. Given a solution  $\xi = \xi(t), \eta = \eta(t), \zeta = \zeta(t)$ , the symmetry properties of the system equations also yield a solution of the form  $\tilde{\xi} = -\xi(t), \tilde{\eta} =$

$-\eta(t), \tilde{\zeta} = \zeta(t)$ . Consider the equations of motion (D.13)–(D.15). The transformation,  $\tilde{\xi} \rightarrow -\xi(t), \tilde{\eta} \rightarrow -\eta(t)$ , yields

$$-\ddot{\xi} = -2\dot{\eta} - 3\xi + \frac{\xi}{r_{23}^3}, \quad (\text{D.19})$$

$$-\ddot{\eta} = +2\dot{\xi} - \frac{\eta}{r_{23}^3}, \quad (\text{D.20})$$

$$\ddot{\zeta} = -\zeta - \frac{\zeta}{r_{23}^3}. \quad (\text{D.21})$$

The form of these solutions is exactly the same as the previously derived equations of motion, thus, for any solution  $\xi = \xi(t), \eta = \eta(t), \zeta = \zeta(t)$ , there exists a symmetric solution  $-\xi = -\xi(t), -\eta = -\eta(t), \zeta = \zeta(t)$ . As a consequence of this symmetry, families of periodic orbits in the vicinity of  $L_1$  and  $L_2$  are exactly symmetric. Thus, for an initial state  $\bar{\xi}_1 = [\xi_1, \eta_1, \zeta_1, \dot{\xi}_1, \dot{\eta}_1, \dot{\zeta}_1]^T$  along a  $T_1$ -periodic  $L_1$  orbit, the complementary state along an  $L_2$  orbit is computed as  $\bar{\xi}_2 = [-\xi_1, -\eta_1, \zeta_1, -\dot{\xi}_1, -\dot{\eta}_1, \dot{\zeta}_1]^T$ . The resulting  $L_2$  orbit corresponds to the same period and value of the Jacobi integral  $\tilde{C}$  as the original  $L_1$  orbit.

The H3BP also possesses a symmetry in time, consistent with the symmetry of the CR3B equations of motion as described in Chapter 2.3. Given a solution

$$[\xi(t), \eta(t), \zeta(t), \dot{\xi}(t), \dot{\eta}(t), \dot{\zeta}(t)]^T,$$

the symmetry properties of the system equations also yield a solution of the form

$$[\xi(-t), -\eta(-t), \zeta(-t), -\dot{\xi}(-t), \dot{\eta}(-t), -\dot{\zeta}(-t)]^T.$$

This result is apparent if the equations are allowed to evolve in negative time, that is,  $t \rightarrow -t$ . Consider the second-order equations (D.13)–(D.15). The time transformation yields  $\frac{d}{d(-t)} = -\frac{d}{dt}$ , and  $\frac{d^2}{d(-t)^2} = \frac{d^2}{dt^2}$ , thus,

$$\frac{d^2\xi}{d(-t)^2} = 2\frac{d(-\eta)}{d(-t)} + 3\xi - \frac{\xi}{r^3}, \quad (\text{D.22})$$

$$\frac{d^2(-\eta)}{d(-t)^2} = -2\frac{d\xi}{d(-t)} - \frac{(-\eta)}{r^3}, \quad (\text{D.23})$$

$$\frac{d^2\zeta}{d(-t)^2} = -\zeta - \frac{\zeta}{r^3}. \quad (\text{D.24})$$

The form of these solutions is exactly the same as the equations of motion (D.13)–(D.15) given suitable substitutions. Thus, for any solution, a second solution, reflected across the  $\hat{\xi}$ -axis, also exists.

VITA

## VITA

Amanda Fay Haapala was born to Daniel Haapala and Katherine Denniston in Silver Spring, Maryland on May 26, 1984. She graduated from Towson High School in 2002 and received her Associate of Applied Science degree in Automotive Technology from the Community College of Baltimore County, Catonsville in 2004. She continued her undergraduate studies at Towson University and completed her Bachelor of Science degree in Physics with a minor in Mathematics in the fall of 2007. As an undergraduate, Amanda was involved in research investigating the environments of quasars under the guidance of Dr. Jennifer Scott.

After graduating from Towson University, Amanda studied for one semester at the University of Maryland before coming to Purdue University in the fall of 2008. She joined Professor Kathleen Howell's Multi-Body Dynamics Research Group in January 2009 and received her Master of Science degree in December of 2010. After graduation, Amanda entered the doctoral program at Purdue. During this program, she spent several summers at NASA Goddard Space Flight Center working to develop Adaptive Trajectory Design<sup>©</sup> software under the guidance of Mr. David Folta. Amanda has accepted a position with the Space Exploration Group at the Johns Hopkins University Applied Physics Laboratory.